Magnetic Properties of Mesoporous and Nano-particulate Metal Oxides

Adrian H. Hill

A thesis submitted in fulfilment of the requirements
for the degree of Doctor of Philosophy
to the
University of Edinburgh
2009

Abstract

The magnetic properties of the first row transition metal oxides are wide and varied and have been studied extensively since the 1930's. Observations that the magnetic properties of these material types change with the dimension of the sample have stimulated many theoretical and experimental studies of the systems involved. As sample sizes decrease towards the nanoscale long range crystallographic order is no longer possible. However, the application of mesoporous silica samples as hard exo-templates to direct the formation of mesoporous metal oxides has provided a new opportunity to explore the influence of scale of crystallographic order further. These types of samples have pore systems running through the material on the mesoscale (diameter between 2 nm to 50 nm) with pore walls truly in the nanoscale region (7 nm to 9 nm thick) crystallographically ordered over large scale distances.

The work presented in this thesis presents magnetic and crystallographic studies of a variety of the first row transition metal oxides from chromium to nickel in three dimensional mesoporous forms predominantly using SQUID magnetometry and neutron powder diffraction. Rietveld refinements of diffraction data from hematite and eskolaite (α-Fe_2O_3 and Cr_2O_3) show that the samples have space groups identical to their bulk counterparts, however slight differences in lattice parameters are observed. Refinement of magnetic properties has also been performed and compared to magnetic property measurements. Of particular interest are results from a mesoporous hematite which show suppression of a well defined first-order magnetic phase transition (the Morin transition). This suppression has been studied extensively with neutron powder diffraction and preliminary inelastic neutron spectroscopic measurements. Comparisons with hematite nanoparticles which also show the suppression of the Morin transition can be drawn. Parametric neutron powder diffraction studies on Co_3O_4 and NiO samples shows that the Néel ordering temperatures are lowered as the mesoporous structure is imposed. This too was observed in eskolaite.

Other studies have been carried out on mesoporous α-MnO_2 (magnetometry) and nanoscale $Li_{1+x}Mn_{2-x}O_4$ (X-ray photo electron spectroscopy) with comparisons to their bulk counterparts and finally nanoparticulate hausmannite Mn_3O_4 (magnetometry and muon spin relaxation) which exhibits spin-glass type behaviour.

Declaration

I do hereby declare that this thesis was composed by myself and that the work described within is my own, except where explicitly stated otherwise. The work has not been submitted for any other degree or professional qualification.

Adrian H. Hill
April 2009

Acknowledgements

I would like to thank my PhD supervisors, Professor Andrew Harrison and Dr Philippe Monthoux for finding funding for this research from the Engineering and Physical Sciences Research Council (EPSRC), through the Schools of Chemistry and Physics respectively. I would particularly like to thank Andrew for allowing/trusting me to "get on" with my research and providing support and advice when required. I would also like to thank my secondary supervisors who have provided advice in the absence of Andrew, Professor J. Paul Attfield and Dr Gordon McDougall.

This research would not have been possible without the generous provision of samples from two groups within the School of Chemistry at the University of St Andrews, part of the Edinburgh and St Andrews Research School of Chemistry (EaStCHEM). Those groups are led by Professor Peter Bruce and Dr Wuzong Zhou. In particular, I would like to thank; Dr Feng Jiao (currently at the Lawrence Berkeley National Laboratory, California, USA), Mr Yu Ren, Mrs Jianli Bao, Dr Calum Dickinson (currently at the University of Limerick, Limerick, Ireland), and Mr Wenbo Yue.

Essential to this research are the instrument scientists and technicians who have helped me run my experiments at the various central facilities used. At ISIS I would particularly like to thank; Dr Winfried Kockelmann (OSIRIS and GEM), Dr Richard Ibberson (HRPD), and Dr James Lord (MuSR). At the ILL I would like to thank; Dr Clemens Ritter (D1B and D20), Dr J. Ross Stewart (IN6), and Dr Inés Puente Orench (D1B). At the HZB I would like to thank; Dr Michael Tovar (E9), Dr Norbert Stüßer (E6), and Dr Simon Kimber (E9 and E6). At the PSI I would like to thank Dr Alex Amato (GPS).

From the University of Edinburgh I would like to thank all members of the Centre for Science at Extreme Conditions (CSEC) who have helped me along my way, particularly; Mr Gaétan Giriat and Dr Javier Sanchez-Benitez for assisting with remote SQUID measurements, and Dr Tony Williams, Dr Iain Oswald, and Dr Simon Kimber for early

guidance in Rietveld refinements using GSAS, and Dr Ronald Brown for allowing me to use the physisorption apparatus at my whim and the X-ray photoelectron spectrometer.

From Denmark I would like to thank those people with whom I have collaborated with on the inelastic neutron scattering experiments, Professor Kim Lefmann (University of Copenhagen and Risø National Laboratory), Mr Niels Vestergaard Jensen (Risø National Laboratory), and Mrs Sonja Rosenlund Hansen (University of Copenhagen).

Contents

List of Figures

List of Tables

Chapter 1

Introduction

This thesis aims to study the magnetic properties of several transition metal oxides with high surface areas. High surface area materials can be created in the form of very small particles (nano-particles) or by producing voids and channels through the interior of the material (porous structures). The imposition of a high surface area on a material can greatly alter the overall physical properties of the system, such as reactivity and catalytic activity, chemical storage capabilities, and magnetic properties. Throughout this thesis, comparisons are made between standard bulk materials and their (novel) high surface area counterparts, in particular with regard to their crystallographic and magnetic properties.

1.1 Mesoporous materials

Porous materials can be placed into one of three (sub)categories. Microporous (or nanoporous) materials have pores whose width does not exceed about 2.0 nm (20 Å). Macroporous materials have pores whose widths exceed 50 nm (500 Å). All those materials with an intermediate pore width of 2 nm to 50 nm (20 Å to 500 Å) are classed as mesoporous materials [1]. Prior to the early 1990's materials with the largest pore systems fell into the microporous category (zeolites with pores up to 5.2 nm [2]), however, this has changed with the discovery of a form of mesoporous silica (SiO_2) [3, 4].

1.1.1 Mesoporous silica

The first family of mesoporous silica materials produced were entitled M41S, and discovered by the Mobil Corporation [3, 4]. It was observed that, by varying the synthetic conditions slightly, different properties such as pore size and wall thickness could be imposed on the material. One such member, MCM-41 has a typical pore diameter of 2.5 nm, a wall thickness of 1.8 nm, and a surface area of $\approx 1000\,\mathrm{m^2\,g^{-1}}$. This exists as one-dimensional hexagonal array of unconnected pores. The synthesis involves creating micelles using an organic surfactant template which self assemble as a soft aggregate. Addition of a silica source coats the aggregate structure (known as soft

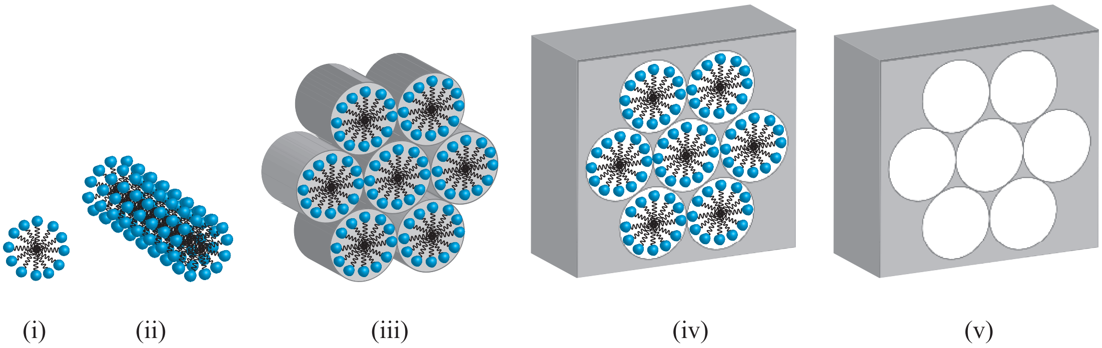

Figure 1.1: The synthetic process of creating MCM type mesoporous silicas: (i) a surfactant micelle self assembles into, (ii) a micellar rod, which itself assembles into, (iii) a hexagonal array; (iv) addition of silica encapsulates the micelles, and (v) after calcination the final mesoporous product is produced.

templating), and after maturing at elevated temperature and pressure (hydrothermal synthesis) produces a silica structure with the organic material creating pores. The organic material can then be removed by calcination to produce the mesoporous material (Figure 1.1).

This class of material do not have ideal stability due to the thickness of the walls between the pores. Stability was improved by preparation of materials (with a very similar technique) with thicker walls and also larger pores. This material (also a one-dimensional pore system), known as SBA-15 [5] has been widely used in experiments and has more recently been used to prove the synthetic process outlined in Figure 1.1 with small angle neutron diffraction (SANS) [6].

There is, however, an issue with pore blockage due to the one-dimensional nature of the pore system in these materials, leading to inefficient use of all the surface available during thermodynamic or kinetic processes. This has led to the development of three-dimensional mesoporous structures, such as KIT-6 [7]. This material typically has a surface area of $\approx 800\,\mathrm{m^2\,g^{-1}}$, a wall thickness of $\approx 4\,\mathrm{nm}$, and a pore diameter of $\approx 7\,\mathrm{nm}$. The structure consists of two sets of individual pores interwoven in three-dimensions throughout the material.

1.1.2 Beyond mesoporous silica

Since the development of mesoporous silica, there has been considerable effort to apply the synthesis method to non-silica materials, such as mesoporous carbon, transition metal oxides and even metals. Mesoporous transition metal oxides are a particularly exciting class of material due to their incomplete *d*-electron shells. The resultant materials may well exhibit interesting properties in catalysis, electron transfer processes, and magnetic properties to name but a few [8–14]. The first reported synthesis of a mesoporous transition metal oxide was presented in 1995, using long chain alkyl amines as a template [9]. Since then various other metal oxides have been produced, such as Nb_2O_5, TiO_2, ZrO_2, SnO_2, Ta_2O_5, WO_3, and MnO_x [8, 15, 16]. The synthesis of such materials is generally by a soft templating approach, similar to that used to make mesoporous silica. This leads to materials with high surface areas but there are issues with poor crystallinity within the pore walls, and poor thermal stability. A second synthetic method, using a mesoporous silica as a template (hard templating) to produce mesoporous carbon was then reported in 1999 [17].

Mesoporous silica as a hard template

The hard templating method uses the pore structure of mesoporous silica to create a new mesoporous material (also known as nanocasting). A precursor to the desired end material is allowed to infuse into the mesoporous structure of the silica. This is then heated to a suitable temperature for thermal degradation to form the required product. The silica can then be removed by dissolving in either 10 % aqueous HF or 2 M NaOH. This method was used to create various mesoporous carbon structures, such as CMK-1, CMK-3, and CMK-6 [7, 17–20]. This method of hard templating was first applied to transition metal oxides in 2003 [21], where a silica template SBA-15 was used to create mesoporous Cr_2O_3 with highly ordered pores and crystalline walls. Since then large numbers of mesoporous transition metals have been created, using the wide diversity of mesoporous silica templates to control the final pore size and surface area of the end product. Of key interest is the development of mesoporous structures in three dimensions. Using a three-dimensional mesoporous silica, such as KIT-6 (Figure 1.2) a wide variety of metal oxides with large surfaces areas have been synthesised with a crystal structure that truly extends in three dimensions [22–27].

1.1.3 Mesoporous 3d transition metal oxides

First row (3d) transition metal oxides are a fascinating class of materials with a wide range of physical properties. Since the early theories of magnetism these metal oxides have been the subject of intensive experimental and theoretical studies [28, 29]. The wide variety of oxides possible and their physical properties are fairly well defined and understood, however it is known that as the length scale of the materials is reduced their properties can be greatly altered due to (but not limited to): increasing surface to volume ratio [30], altered exchange energies due to structural surface distortions [31], and imbalance of spin alignments on surfaces [32–34]. Surface disorder on particles can lead to phenomena throughout the total particle volume, such as superparamagnetism

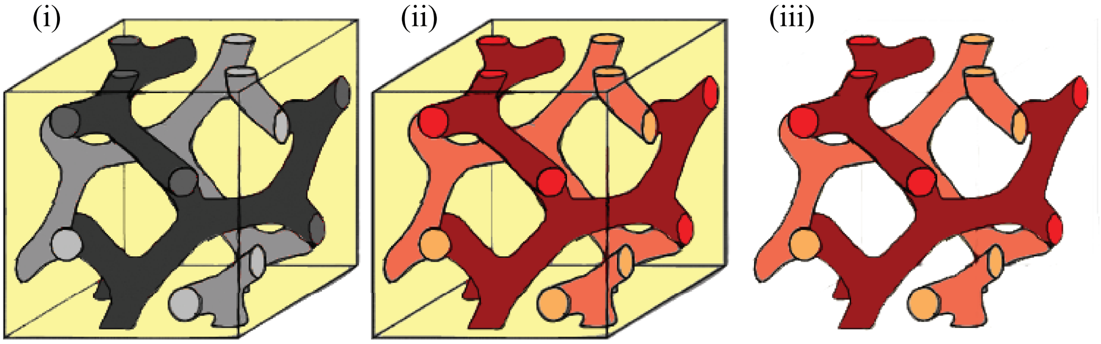

Figure 1.2: The hard templating technique illustrated with, (i) three-dimensional mesoporous KIT-6 template (note the two independent pore systems), (ii) filled with a precursour (such as iron nitrate) and thermally decomposed (to iron oxide), and (iii) the final mesoporous structure after dissolving away the silica template, (after reference 7).

and spin glass states. These effects have largely been observed in 2 dimensional thin films or nanoscale particles. These systems, however, do not display long range crystallographic order in three dimensions. The possibility of making three dimensional materials with these surface effects is therefore a fascinating opportunity. The early research into crystalline mesoporous metal oxides [35] have focussed upon the 3*d* transition metals due to the wide variety of materials possible and the ease in which thermal decomposition from precursors (such as nitrates) to oxides occur.

Preliminary measurements upon one such mesoporous material, α-Fe_2O_3 (hematite) have shown magnetic properties that differ greatly from the bulk material [23], and are instead similar to those seen in nanoparticles. It is from this observation that the (vast) majority of research carried out in this thesis has progressed.

Chapter 2

Instrumentation and analysis techniques

The instrumentation and analysis techniques used throughout the research presented in this thesis are relatively common within the fields of magnetism and solid state chemistry. Therefore the techniques are only summarised here. Where necessary, greater detail has been entered into in the derivation of formulae to ensure a clear and transparent definition of the terms used when describing experiments and results. This chapter has been divided into two: a section on scattering techniques which covers the vast majority of this work; and a section on other instrumentation used throughout the course of the thesis.

2.1 Scattering techniques

Scattering of waves by matter is a concept well understood, and plays a huge part in materials chemistry and solid state physics. From the de Broglie relationship (Equation 2.1) and the value of Planck's constant, h we know that all particles of mass m, and velocity ν have a wavelength λ. Therefore anything with a suitable wavelength or energy for the system being studied can be used for scattering experiments (depending upon the penetration of the probe into the material being studied). For example, if one desires to study the crystal structure of matter, a probe with a wavelength in the same region as the atomic spacing is required (ångström scale). To study dynamic processes in matter such as magnons and phonons, the probe will ideally have a similar energy to the process being studied to enable effective resolution of energy changes (0.01 eV to 0.1 eV).

$$\lambda = \frac{h}{m\nu} \tag{2.1}$$

$$E = \frac{p^2}{2m} = \frac{\hbar^2 k^2}{2m} = \frac{m\nu^2}{2} \tag{2.2}$$

To understand scattering processes in general, it is important to cover several formalisms [36, 37]. The incoming wave has a wavevector, $\boldsymbol{k}_i$ and will undergo an interaction with

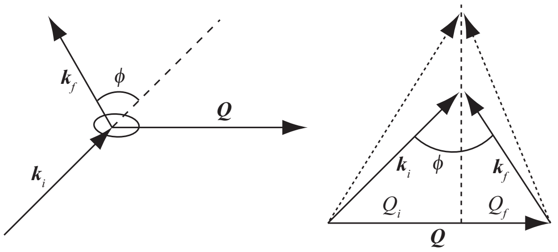

Figure 2.1: A scattering event in real (left) and reciprocal space (right). Q_i and Q_f are projections of $\boldsymbol{k}_i$ and $\boldsymbol{k}_f$ onto $\boldsymbol{Q}$. ϕ is the scattering angle.

the matter being studied which leads to a scattering process that can be elastic or inelastic. This results in a new outgoing wavevector, $\boldsymbol{k}_f$. From the wavevector, we can calculate a wave's momentum p, energy E and in the case of matter with mass m, velocity ν (Equation 2.2). Values of interest in scattering are the energy transfer $\hbar\omega$ and momentum (or wavevector) transfer $\boldsymbol{Q}$ (Equations 2.3 and 2.4).

$$\hbar\omega = E_f - E_i \tag{2.3}$$

$$\boldsymbol{Q} = \boldsymbol{k}_f - \boldsymbol{k}_i \tag{2.4}$$

This can be illustrated by a diagram of scattering event in real and reciprocal space (Figure 2.1). From this it can be seen that given specific values of $\hbar\omega$ and $\boldsymbol{Q}$, any combinations of $\boldsymbol{k}_i$ and $\boldsymbol{k}_f$ that lie within the outer dotted arrows are possible. For elastic experiments where there is no energy transfer ($E_i = E_f$), the projections of $\boldsymbol{k}_i$ and $\boldsymbol{k}_f$ onto $\boldsymbol{Q}$ will be equal. In a scattering experiment detectors are placed at particular positions in ($\boldsymbol{Q}$,ω) space around a sample. With energy analysis of the scattered waves, this gives the double differential cross section, (Equation 2.5). That is the number of waves scattered into a solid angle $d\Omega$ per second with an energy between E and $E + dE$, which is related to a form factor, f and the dynamic structure factor $S(\boldsymbol{Q}, \omega)$. All scattering that we observe (inelastic or elastic) is contained within the dynamic structure factor.

$$\frac{d\sigma^2}{d\Omega dE} = \frac{\boldsymbol{k}_f}{\boldsymbol{k}_i} f^2 S(\boldsymbol{Q}, \omega) \tag{2.5}$$

The $\boldsymbol{Q}$ dependence of $S(\boldsymbol{Q}, \omega)$ gives information on where the atomic positions are within cells (diffraction). The ω dependence of $S(\boldsymbol{Q}, \omega)$ gives information on dynamics within the structure (spectroscopy), such as vibrations. Measuring both $\boldsymbol{Q}$ and ω simultaneously tells us where particular atoms are and and how fast they are moving. These dependencies can also be applied to magnetic scattering, providing information about the structure and movement of electronic spins.

Property	Value
charge	0
spin, S	$\frac{1}{2}$
mass, m	1.675×10^{-27} kg

Table 2.1: Basic properties of the neutron. After reference 36.

	Energy E / meV	Temperature T / K	Wavelength λ / Å
Cold	0.1–10	1–120	30–4
Thermal	5–100	60–1000	4–1
Hot	100–500	1000–6000	1–0.4

Table 2.2: Approximate neutron energies, temperatures, and wavelengths for cold, thermal and hot neutrons. After reference 36.

The scattering techniques used in this research are wide and low angle X-ray powder diffraction (XRD) from a laboratory source, neutron powder diffraction (NPD) and inelastic neutron scattering (INS). Neutron scattering techniques require the use of large scale central facilities such as ISIS, UK, and the Institut Laue-Langevin (ILL), France, and the Berlin Neutron Scattering Center (BENSC), Germany.

Neutron scattering

At ISIS, (which is a pulsed neuron spallation source) neutrons are produced by pulsing a high intensity beam of protons into a heavy metal target (tantalum) which creates a burst of neutrons of a wide range of energies. The ILL and BENSC are both examples of nuclear reactors that produce neutrons for research. These utilise the natural radioactivity of ^{235}U, which undergoes fission to produce a continuous flux of neutrons. Neutrons are particularly useful for studying solid state matter because of their physical properties such as mass, charge and spin (Table 2.1). These properties lead to four very useful aspects which are utilised in neutron scattering.

The velocity (and hence wavelength) of neutrons can be altered during the production phase by allowing them to reach thermal equilibrium with a moderator, giving a Maxwell-Boltzmann distribution with a peak around the moderator temperature (such as graphite at 2000 K for hot neutrons, water for thermal neutrons and liquid methane for cold neutrons). This provides large numbers of neutrons with particular ranges of wavelengths (Table 2.2). The wavelength of thermal neutrons is on a scale similar to interatomic distances within matter, enabling effective probing of the crystallographic structure of a material being studied. Secondly, as neutrons are uncharged they can

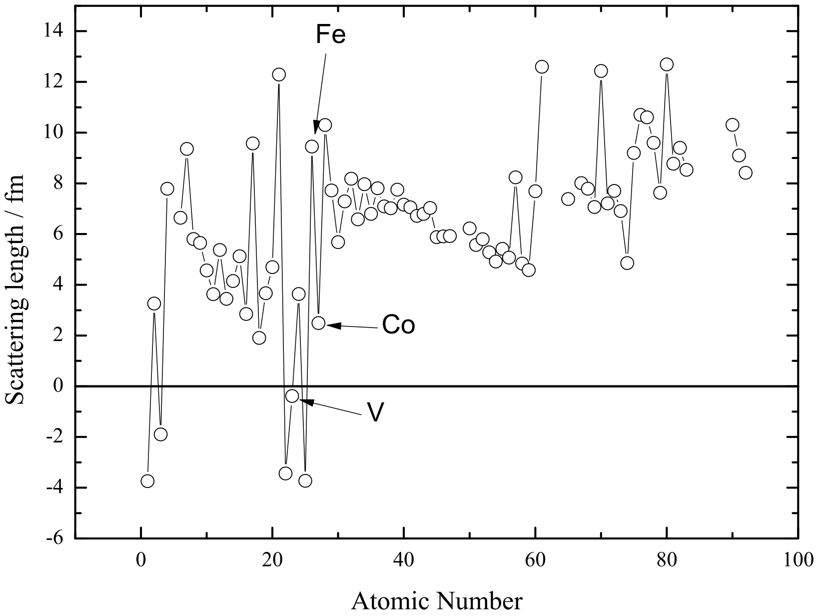

Figure 2.2: Nuclear scattering length for neutrons as a function of atomic number. Values represent the mean values of b for natural isotopic distribution. Key nuclei marked are, iron and cobalt, showing the differences in their scattering lengths, and vanadium, which is often used as sample holder due to its small scattering length.

pass through the vast majority of space that matter takes up (they are not affected by Coulombic interactions from electron clouds). Therefore the neutron passes very close to atomic nuclei, where nuclear forces cause scattering. The scattering strength of the nuclei (which alters the scattering length, b) depends upon the element causing the scattering (the composition of nuclear spins), with different elements possessing a wide range of different scattering lengths (Figure 2.2). This is a very useful feature, particularly when examining systems with elements that would be very difficult to distinguish with X-rays, such as iron and cobalt which have very similar scattering lengths due to only one electron difference. Thirdly, as the neutron has a spin (from its proportions of up and down quarks) it can interact with atoms which also have a spin from unpaired electrons (magnetic atoms) or even nuclear spins at very low temperatures. The magnitude of this scattering is similar to that of nuclear scattering, and enables the probing of both nuclear and magnetic structures simultaneously. Finally, the energy of cold and thermal neutrons is similar to that of excited states in matter. Inelastic scattering of the neutron will result in a change in neutron energy (Equation 2.3). Analysis of the outgoing neutron allows one to probe the energetics of these excitations.

Modern neutron detectors are generally ^{3}He detectors. The interaction of a neutron with ^{3}He creates a nuclear fission process which produces hydrogen, tritium and energy.

$$\underset{\text{thermal}}{{}^1_0n} + {}^3_2\text{He} \longrightarrow {}^1_1\text{H} + {}^3_1\text{H} + 0.764\,\text{MeV}$$

2.1.1 Powder diffraction

Diffraction is a very common technique in analysis of solid state matter made up of either a single crystal or a polycrystalline powder. Diffraction of waves by a crystal occurs due to scattering (Thomson scattering) from different planes of the crystal [38]. When diffracted waves (wavelength λ) from identical lattice planes (wave striking plane at an angle θ) with a particular spacing (d) between them, interfere with each other they lead to constructive interference and the production of a Bragg reflection (with a specific index hkl) in a diffraction pattern. This is the fulfilment of the Bragg relationship.

$$\lambda = 2d\sin\theta \tag{2.6}$$

The position of Bragg reflections in a diffraction pattern can then be compared with known patterns to provide phase identification. Diffraction patterns are collected as a function of 2θ. However for ease of comparison between different instruments, where wavelengths may differ, it is customary to plot diffraction patterns as a function of d (Å) or Q (Å^{-1}).

$$d = \frac{\lambda}{2\sin\theta} \tag{2.7}$$

$$Q = \frac{2\pi}{d} \tag{2.8}$$

As well as phase identification from diffraction patterns there is a great deal more information that can be obtained from the intensity and shapes of the Bragg peaks. The intensity of a Bragg peak (I_{hkl}) is dependent upon a number of parameters (Equation 2.9): the structure factor, S_{hkl} ($\boldsymbol{Q}$ dependence of the dynamic structure factor, $S(\boldsymbol{Q},\omega)$); the multiplicity, (M_{hkl}); the Lorentz polarisation factor, ($LP(\theta)$); and the atomic displacement parameter, ($TF(\theta)$)).

$$I_{hkl} = |S_{hkl}|^2 \times M_{hkl} \times LP(\theta) \times TF(\theta) \tag{2.9}$$

The structure factor, S_{hkl} (Equation 2.10) is constructed from the atomic coordinates and atomic form factors of all atoms in the crystallographic unit cell. Of crucial importance in this equation is the atomic form factor, f_j. In neutron scattering, the form factor takes the scattering length term b (in the case of X-rays, the form factor

Figure 2.3: Diffraction of multiple reflections with identical *d*-spacing (left) leading to individual Bragg reflections for the single crystal case (centre), and Debeye-Scherrer rings for the polycrystalline case (right).

drops off with increasing 2θ due to scattering from a cloud of electrons as opposed to the case of neutrons, where scattering is from a single point, the atomic nucleus).

$$S_{hkl} = \sum_j f_j \exp[2\pi i(hx_j + ky_j + lz_j)] \tag{2.10}$$

The multiplicity term in Equation 2.9 accounts for the 1 dimensional reperesentation of a 3 dimensional object when carrying out powder diffraction. It is often the case, particularly at higher Q vector, that d spacings for inequivalent reflections are identical. For example, the (100) reflection from a cubic crystal is actually equivalent to the (010), (001), $(\bar{1}00)$, $(0\bar{1}0)$, and $(00\bar{1})$ reflections, so there is a 6-fold equivalency. This is because in a polycrystalline sample, all crystal grains are randomly orientated, therefore any hkl reflections of a specific d-spacing will have intensity around the edge of a cone rather than a specific point in space (as is the case with single crystals), causing a Debeye-Scherrer ring. If two or more reflections have identical d-spacings, then they will be superimposed upon each other (Figure 2.3).

The Lorentz polarisation factor accounts for specifics such as the preferred orientation of crystallites, diffraction at angles just off fulfilling Braggs law, and instrumental geometry (Lorentz). The polarisation factor is only relevant for X-ray diffraction, as the X-ray has an electric field perpendicular to its propagation vector which will be scattered differently. The atomic displacement factor (sometimes listed as a thermal factor, TF) takes into account thermal vibrations of atoms and their mean squared displacement (B) from equilibrium positions. These can be modelled as isotropic (spherical) or anisotropic (eliptical).

$$TF(\theta) = \exp(B[sin\theta/\lambda]^2) \tag{2.11}$$

In the case of magnetic diffraction of neutrons, the intensity of a Bragg peak in

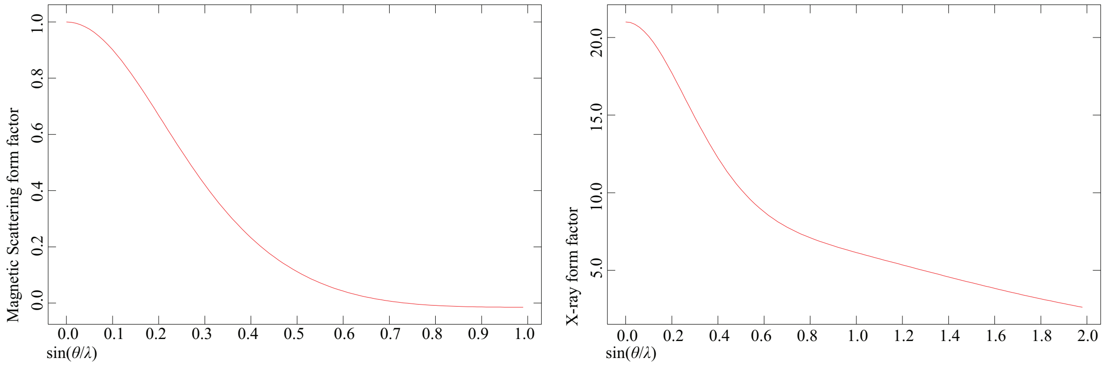

Figure 2.4: Form factor curves for the Cr^{3+} ion. The magnetic form factor on the left and the X-ray form factor on the right (note the different scales). The nuclear form factor, b would be constant over the entire 2θ range with a value of 0.363.

Equation 2.9 will also depend upon a further structure factor, $\left|S_{hkl}^{mag}\right|^2$. This term takes a form very similar to the nuclear structure factor (Equation 2.10), but drops off with increasing 2θ, similar to the form factor for X-ray scattering (Figure 2.4). This is because as with XRD, magnetic scattering is from the electrons about the nuclei rather than a single point. Laboratory XRPD has been used in these studies to carry out the phase identification of the materials, whereas neutron diffraction has been used for full strucutral analysis using a technique know as Rietveld refinement [39].

Rietveld Refinement

Analysis of neutron powder diffraction is generally carried out using a method known as the Rietveld method. This involves creating a model structure of the sample being studied and creating an ideal theoretical scattering pattern. As well as structural information, the pattern also contains information on the instrument, microscopic sample details, and background (a function to model the intensity of all in-elastic and incoherent scattering). The two patterns (real and model) are then compared. A least squares procedure is then carried out to minimise the differences between the two patterns by slightly altering parameters in the original model. This is continued until the residual, S_y is minimised (Equation 2.12, where w_i is a weighting factor, and y_{oi} and y_{ci} are the observed and calculated intensities at the ith step respectively) [40].

$$S_y = \sum_i w_i (y_{oi} - y_{ci})^2 \tag{2.12}$$

The goodness of fit of the Rietveld refinement is best observed by plotting observed and calculated profiles together and examining their agreement with a plot of a difference curve. Several statistical parameters can also be reported enabling a quick idea of the

Parameter	Name
$R_{wp} = \left[\frac{\sum_i w_i (y_{oi} - y_{ci})^2}{\sum_i w_i (y_{oi})^2}\right]^{\frac{1}{2}}$	R-weighted pattern
$R_p = \left[\frac{\sum_i \lvert y_{oi} - y_{ci} \rvert}{\sum_i y_{oi}}\right]$	R-pattern
$R_e = \left[\frac{N - P}{\sum_i w_i y_{oi}^2}\right]^{\frac{1}{2}}$	R-expected
$\chi^2 = \left[\frac{R_{wp}}{R_e}\right]^2$	Reduced chi-squared

Table 2.3: Often used numerical criteria of Rietveld fits. Parameters are discussed in the text.

goodness of fit. These are listed in Table 2.3, where N is the number of observations and P is the number of parameters refined.

The R_{wp} is often considered the best guide to how well a refinement is going, as it contains the residual, S_y. The R_e value is a measure of how good an R_{wp} value could theoretically get. The ratio squared of these values (χ^2), can indicate how well the refinement is going. However, the parameters strongly depend upon the background in a diffraction pattern: a high background (as is the case with materials with small amounts of disorder) leads to artificially low numerical values. This shows the importance of visually checking the refinement profiles.

The program used in this research for Rietveld refinement was the "General Structure Analysis System", (GSAS) [41] with the EXPGUI graphical user interface [42].

2.1.2 Low angle X-ray diffraction

As the typical mesoporous structure of the materials presented in this thesis has a unit cell length in the 200 Å to 300 Å range, the d-spacing of Bragg reflections will be very large. To view these reflections using standard geometry XRD, an incident wavelength in the regions of 100's of ångströms would be required. This is unrealistic (photons of that wavelength would actually be in the ultraviolet rather than X-ray part of the electromagnetic spectrum), so the alternative is to look at low angle X-ray diffraction (LAXRD), 0° to 2° 2θ. Measurements at low angles were carried out using a customised instrument built at the School of Physics, Edinburgh with Cu K_α radiation.

2.1.3 Inelastic neutron scattering

Annihilation or creation of excitations in matter by neutrons will result in a change in energy of the interacting neutron of a scale similar to its original energy. This makes

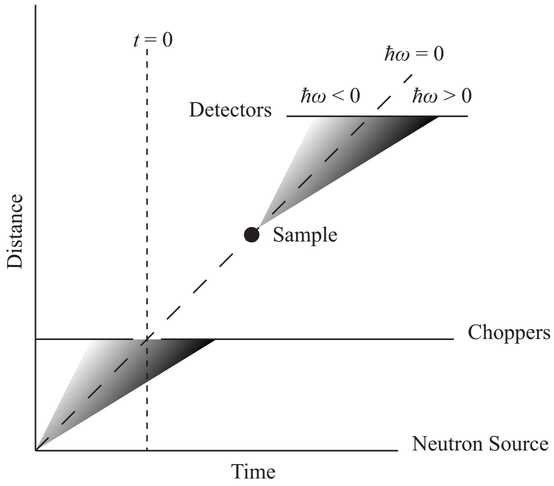

Figure 2.5: Distance-time plot for a direct geometry spectrometer such as IN6 and MARI.

energy resolution relatively simple. Using X-rays with wavelengths of a suitable size for interatomic distances requires much higher resolution as their original energy will be in the KeV range and the change will be minimal compared to this, (although sub eV events can now be seen).

It is, however, very difficult to directly measure the energy of a neutron as it is detected by a secondary process. One way of analysing a neutron's energy is to measure the time it takes to get from point A to point B. This is known as time-of-flight (TOF) spectrometry. The source of neutrons needs to be pulsed, so that the exact starting time of a neutron at point A is known. This is fine for a spallation source such as ISIS; however, for a continuous fission source, the neutron beam has to be chopped into pulses. For a spectrometer such as IN6 (ILL) and MARI (ISIS), a series of choppers select neutrons of specific energy and turn the neutrons into pulses where necessary (Figure 2.5).

Neutrons which are elastically scattered (i.e. no energy change, E_f) will arrive at detectors at a pre-determined time specific to the instrument and energy of the incident neutron (E_i). The energy transfer ($\hbar\omega$, Equation 2.3) will be equal to zero. Neutrons which lose energy to the sample (creating an excitation) will slow down, so take longer to arrive (Stokes scattering). Their energy transfer will be positive. Neutrons which gain energy from the sample (destroying an excitation) will speed up, so take a shorter time to arrive (anti-Stokes scattering). Their energy transfer will be negative. At very low temperatures, the sample can't give any energy to the neutrons so no anti-Stokes scattering will be observed. As temperatures are raised more and more anti-Stokes scattering occurs, until at high T, the signals of Stokes and anti-Stokes are

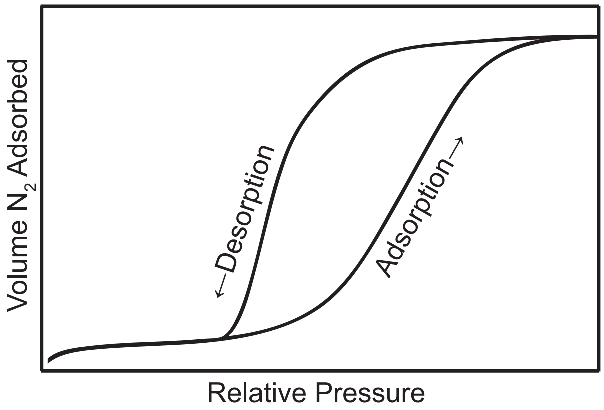

Figure 2.6: A typical type IV isotherm.

approximately equal. The relative intensities of the ($\hbar\omega < 0$) and ($\hbar\omega > 0$) scattering signals is known as the detailed balance condition (Equation 2.13)

$$S(-\boldsymbol{Q}, -\omega) = \exp^{-\hbar\omega/k_B T} S(\boldsymbol{Q}, \omega) \tag{2.13}$$

2.2 Other techniques

Other techniques used in the characterisation of the materials presented in this thesis include: surface area measurements, magnetometry, microscopy, X-ray photoelectron spectroscopy, and muon spin relaxation studies.

2.2.1 Surface area and pore size distribution

Physisorption measurements are widely used (particularly within the catalyst industry) to determine surface area and pore size distribution of porous materials. The basis of the measurements is in the physical adsorption (van der Waals Forces only) of a gas onto the surface of the porous material at a particular temperature. Surface area and pore size distribution measurements in this research were carried out using nitrogen adsorption/desorption on a NOVA 3000 surface area analyser from Quantachrome. Typical isotherms obtained (Figure 2.6) show an opening between the adsorption and desorption branches (hysteresis) indicating behaviour of an absorbent with large pores [43]. Surface area values were calculated using the Brunauer-Emmett-Teller (BET) method [43, 44]. Pore size distributions were estimated using the Barrett-Joyner-Halenda (BJH) technique [45]. Relatively recent studies on large pore MCM-41 type structures have shown these techniques to be robust on the mesoporous scale [46].

2.2.2 Magnetometry

Various magnetometry techniques were used throughout this work to determine the magnetic properties of the materials under investigation. These were carried out in what is known as a superconducting quantum interface device (SQUID) magnetometer. This device measures the change in current induced in a superconducting coil when a magnetic sample in close proximity is moved relative to it. The sample can also be subjected to magnetic fields by application of external superconducting magnets. Measurements carried out in this work consist of direct current (DC) susceptibility, hysteresis loop measurements, and alternating current (AC) susceptibility.

The magnetic properties of materials studied in this work were measured using a Quantum Design Magnetic Property Measurement System (MPMS) SQUID, (the MPMS-1 and MPMS-XL models). Weighed samples were placed in a gelatine capsule and held in place by adding molten eicosane wax, $C_{20}H_{42}$ (melting point 310 K). These were then mounted in a plastic straw and placed in the sample measuring position of the magnetometer.

Direct current susceptibility

DC susceptibility measures the ease in which a material is magnetised (M) in a specific magnetic field ($\mathbf{H}$). From the temperature dependence of the magnetisation in one specific field the magnetic moment in the material can be determined. Measurements were carried out using the following procedure to acquire zero field cooled (ZFC) and field cooled (FC) magnetisation temperature dependencies. Samples were initially cooled in zero field down to approximately 2 K. A field of 100 Oe (approximately $8000\,\mathrm{A\,m^{-1}}$, see Appendix A for units used in magnetometry) was then applied and the magnetisation measured. The samples were then heated up to room temperature with magnetisation measurements taken at specific points. With the field still applied the samples were cooled again and the temperature dependence of the magnetisation was re-measured.

Plots of inverse susceptibility against temperature above the ordering temperature in the paramagnetic region generally show linear behaviour, so can therefore be modelled with a modified Curie-Weiss law (Equation 2.14).

$$\chi_{\mathrm{m}} = \chi_0 + \frac{C}{T-\theta} \tag{2.14}$$

$$\frac{1}{\chi_{\mathrm{m}}} = \frac{T-\theta}{\chi_0(T-\theta)+C} \tag{2.15}$$

Here, χ_0 represents any temperature independent contributions, such as diamagnetism,

C is the Curie constant, and θ is the Weiss temperature. Negative Weiss temperatures predominantly indicate an antiferromagnetic material, whereas the opposite is predominantly indicative of a ferromagnetic material. Determination of the Curie constant enables a calculation of the effective magnetic moment of the material, μ_{eff} using either Equation 2.16 or Equation 2.17 depending upon the units used (Appendix A).

$$\mu_{\mathrm{eff}} = 797.8\sqrt{\chi_{\mathrm{m}}^{\mathrm{SI}} T} = 797.8\sqrt{C^{\mathrm{SI}}} \tag{2.16}$$

$$\mu_{\mathrm{eff}} = 2.827\sqrt{\chi_{\mathrm{m}}^{\mathrm{cgs}} T} = 2.827\sqrt{C^{\mathrm{cgs}}} \tag{2.17}$$

The measured effective magnetic moment can be compared to the theoretical moment of the ground state ion in question. For an ion with orbital degeneracy, the theoretical moment is shown in Equation 2.18, where J is the sum of the orbital (L) and spin (S) angular momentum (for electronic shells less than half full, $J = L - S$), and g is the g-Landé factor, Equation 2.19. For atoms where there is no orbital degeneracy, usually $L = 0$ and $g = 2$. The theoretical moment is therefore given by Equation 2.20.

$$\mu_{\mathrm{p}} = g\mu_{\mathrm{B}}\sqrt{J(J+1)} \tag{2.18}$$

$$g = 1 + \frac{J(J+1) + S(S+1) - L(L+1)}{2J(J+1)} \tag{2.19}$$

$$\mu_{\mathrm{p}} = 2\mu_{\mathrm{B}}\sqrt{S(S+1)} \tag{2.20}$$

Hysteresis loops

Hysteresis loops ($M(H)$) are obtained to determine several physical properties of ferromagnetic materials. A hysteresis loop shows the relationship between the induced magnetisation (M) and the magnetising field (H), (Figure 2.7). Typical measurements involve cooling a sample down to a desired temperature, then applying increasing field strengths (whilst measuring response) until saturation is obtained (M_{s}). The field is then reduced back to zero, where any remaining magnetisation in the sample is called the remanent magnetisation, (M_{r}). A negative field is then applied to reverse the magnetisation in the sample. The field at which this occurs is called the coercive field (H_{c}). Negative saturation is achieved and the process repeats itself back to a positive field to close the hysteresis loop. Analysis of the hysteresis loop's shape and size can provide information on the type of magnetic material being studied (e.g. a hard or soft magnetic material).

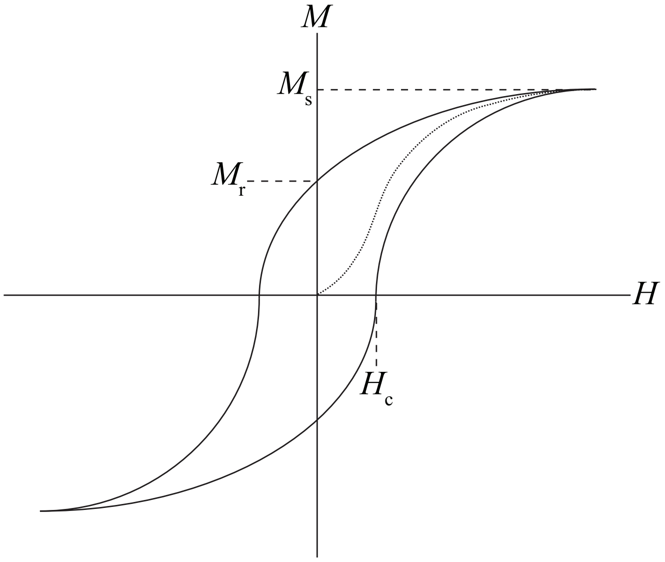

Figure 2.7: A schematic magnetic hysteresis loop. The saturisation magnetisation, M_{s}, remanent magnetisation, M_{r}, and coercive field, H_{c} are marked. The dotted line within the loop is the initial measurements expected for a de-magnetised ferromagnetic sample.

Alternating current susceptibility

Alternating current (AC) susceptibility is often referred to as dynamic susceptibility. It is a useful probe of dynamics occurring at typical values within magnetic materials. In this technique, a very small alternating magnetic field is applied to a sample. This induces a time dependent moment in the sample, which is in turn picked up by the superconducting measurement coils [47]. At low frequencies any dynamics occurring in the material will have time to relax during measurement, so the magnetisation will follow a standard DC $M(H)$ curve. The AC moment (M_{AC}) at a particular time, t, is a function of the driving amplitude (H_{AC}), the driving frequency (ω), and the slope ($\frac{dM}{dH} = \chi$) of the susceptibility curve ($M(H)$). As the AC measurement is dependent upon the slope rather than the absolute value of $M(H)$, small magnetic shifts can be detected even in systems where the absolute moment is large, making AC measurements very sensitive to small changes in $M(H)$.

$$M_{AC} = \frac{dM}{dH} H_{AC} \sin(\omega t) \tag{2.21}$$

At higher frequencies, the material will not be able to relax, so the AC signal will not follow the $M(H)$ curve. This time lag is detected by the magnetometer. Therefore the AC measurements will provide us with a susceptibility χ, and a phase shift φ. These two components can be manipulated to give what is known as an in-phase, real component

χ' and an out of phase, imaginary component χ''.

$$\chi' = \chi \cos \varphi \tag{2.22}$$

$$\chi'' = \chi \sin \varphi \tag{2.23}$$

Analysis of the χ' and χ'' curves for a variety of frequencies over a range of temperatures can provide valuable information on the dynamics of materials, particularly in the cases of spin glass and superparamagnetic materials.

2.2.3 Transmission electron microscopy

Transmission electron microscopy (TEM) and high resolution transmission electron microscopy (HRTEM) involves the imaging of samples with electrons, rather than light. The advantage of this technique over standard optical microscopy is a much higher resolution. With classical light microscopy, the smallest distance between two points that can be resolved (δ) is dependent upon the wavelength (λ).

$$\delta = \frac{0.61\lambda}{\mu \sin \beta} \tag{2.24}$$

Where μ is the refractive index of the viewing medium and β is the half-angle of the maximum cone of light that can enter or exit the lens [48]. The resolution obtained from optical microscopy is generally no greater than 200 nm. However, much smaller wavelengths can be achieved by application of the de Broglie relationship to electrons. By varying their energy desired wavelengths are obtained which can provide much greater resolution, typically down to 1 Å (100 pm).

$$\lambda \approx \frac{1.22}{E^{0.5}} \tag{2.25}$$

TEM studies during this research were carried out at the University of St Andrews Electron Microscope Facility in the School of Chemistry, using a Jeol JEM 2011 HRTEM, (HRTEM can refer to the microscopy technique and the microscope).

2.2.4 X-ray photoelectron spectroscopy

X-ray photoelectron spectroscopy [49] (XPS) is a technique used to determine the oxidation state of elements in a material's surface. An incoming monochromatic X-ray beam ($h\nu$) displaces a core electron, which is then detected (Figure 2.8). The energy of this electron (E_{kinetic}) is used to determine its original binding energy (E_{binding}) by combining the input energy, output energy, and the workfunction (Φ) of the element in

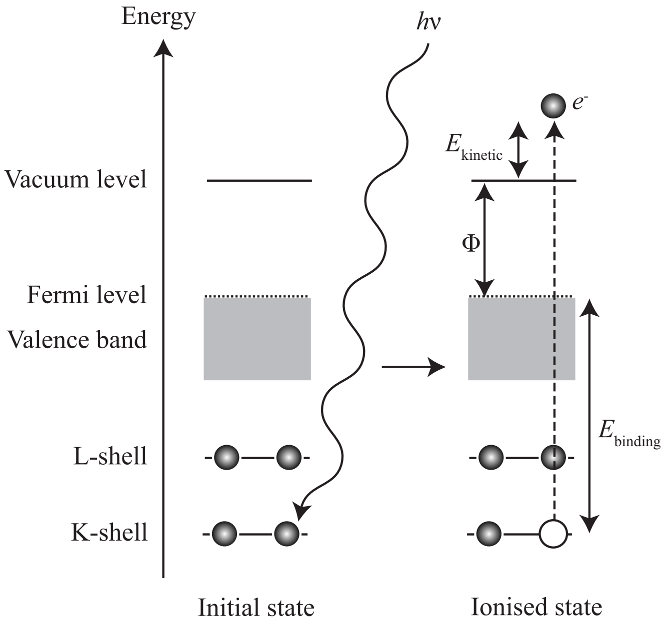

Figure 2.8: The X-ray photoelectron spectroscopy (XPS) process.

question (Equation 2.26).

$$E_{\text{binding}} = h\nu - E_{\text{kinetic}} + \Phi \tag{2.26}$$

Many different electrons will be detected, coming from different shells and sub-shells of the elements present. The binding energies of these electrons enable the oxidation states to be determined. XPS measurements were made with monochromatic Al light ($K_\alpha = 1486.6\,\text{meV}$) at room temperature using a Thermo VG Sigma Probe XPS spectrometer.

2.2.5 Muon spin relaxation

Muon spin relaxation, (also know as muon spin rotation or muon spin resonance) [50] μSR is a spectroscopic technique which provides a site specific probe of structure within a material. As this is a fairly uncommon technique, the basic principles will be described here. More comprehensive reviews may be consulted for further information [50–52].

The muon is a subatomic particle of approximately $\frac{1}{9}$ the mass of a proton, with a charge of ±1. The muon has spin $\frac{1}{2}$, and a magnetic moment 3.18 times that of a proton. It is therefore ideal for studying local magnetic order within a material. The mechanism of muon production for spectroscopic techniques is rather complicated and involves various decay pathways. The facilities used in this research have been the MuSR [53] instrument at the ISIS faciltiy [54] at the Rutherford Appleton Laboratory, UK and the GPS [55] instrument at the Paul Scherrer Institut (PSI), Switzerland. These two facilities produce muons from a proton source.

A high energy pulse of protons (p^+) is aimed at a sheet of material composed of light atoms (typically graphite), causing the production of pions (π^+) and neutrons (n). The pion, which has a very short lifetime ($\tau = 26\,\text{ns}$), then decays into a muon (μ^+) and muon neutrino (ν_μ). Due to the very short lifetime of the pions, they effectively decay in the graphite target. This gives rise to 100 % spin polarised muons [51]. The muons then implant themselves in the sample of interest for a certain time before then decaying ($\tau = 2.2\,\mu\text{s}$) to give a positron (e^+), an electron neutrino (ν_e), and muon antineutrino ($\overline{\nu}_\mu$). This is summarised in the following scheme.

$$p^+ + p^+ \longrightarrow p^+ + \pi^+ + n$$

$$\pi^+ \longrightarrow \mu^+ + \nu_\mu$$

$$\mu^+ \longrightarrow e^+ + \nu_e + \overline{\nu}_\mu$$

It is the production of the positron that is of interest in this type of experiment. As the incoming muon beam is 100 % spin polarised, all muons going into the sample will originally have their spin pointing in the same direction (back in the direction they came from). If the muon were to the decay immediately, it would give off the positron in the same direction of its spin. During their lifetime, however, the muons can precess around local magnetic moments (Larmor precession) within the material with a particular frequency (ω_μ), which is dependent upon the field B, and the gyromagnetic ratio of the muon. This will alter their spin polarisation, giving off positrons in different directions (Figure 2.9). By detecting positrons in the forward (N_F) and backward (N_B) directions (relative to the incoming muon beam) it is possible to observe different relaxation patterns (Figure 2.10). This is known as the time-dependent positron asymmetry function, $G(t)$ (Equation 2.27). Careful analysis of the observed relaxation pattern above and below a magnetic transition (such as a blocking temperature in nanoparticles) can provide critical information as to the local magnetic ordering in the material of interest.

$$G(t) = \frac{N_\text{F}(t) - N_\text{B}(t)}{N_\text{F}(t) + N_\text{B}(t)} \tag{2.27}$$

The main difference between the MuSR instrument at ISIS and the GPS instrument at the PSI is in the way the muons are produced and then used experimentally. For

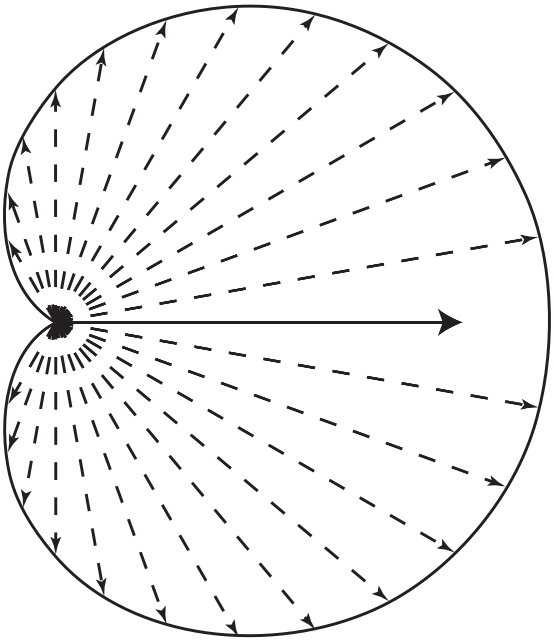

Figure 2.9: The probability of a positron resulting from a muon decay emerging at different directions with respect to the initial muon-spin direction (large horizontal arrow), after reference 51.

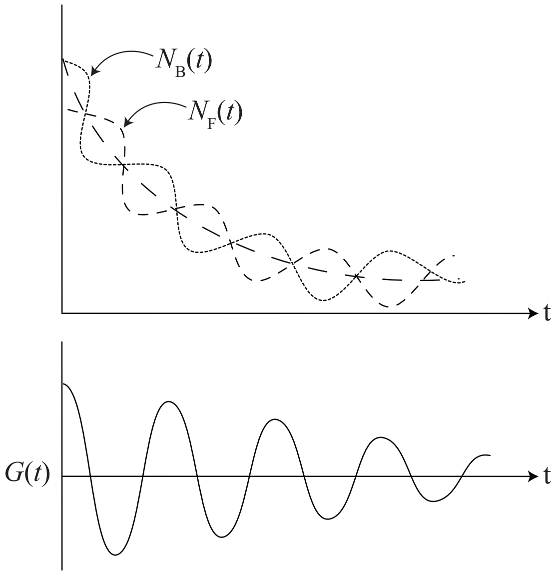

Figure 2.10: A schematic of the number of positrons detected in the forward and backward detectors and the overall asymmetry function with time.

good statistics and reliable data analysis many thousands of positrons are detected. At the ISIS facility the muon beam is pulsed, therefore a cluster of muons are implanted each time. These will arrive within a specific (albeit very small) time frame, with a half width at half maximum of typically 70 ns. There will therefore be uncertainty in whether the positrons detected came from the earlier or later muons implanted. This is critical to know for high frequency precessions, but not so critical at longer timescales. At the PSI facility however, the muon beam is continuous but with a flux capable of being reduced to limit the number of muons arriving at the sample within a specified time frame. Therefore the time resolution at PSI is much greater than at ISIS. The analytical functions used in this research are presented in Chapter 10 where the μSR technique is used.

Chapter 3

Synthesis and preliminary characterisation

As outlined in Chapter 1, the synthesis of mesoporous metal oxides is a multi stage process, starting with the preparation of a hard silica host which is then impregnated with a guest material, followed by removal of the silica host. The synthetic details of materials made are provided here.

3.1 Mesoporous silica

Throughout this research the form of mesoporous silica used in the synthesis part is known as KIT-6 (Figure 1.2) [7]. To make this, the following typical procedure was carried out.

3.1.1 Synthesis

Six grams of Pluronic P123 (a tri-bloc co-polymer, $EO_{20}PO_{70}EO_{20}$, where EO = ethylene oxide and PO = propylene oxide, molecular weight = 5800) were completely dissolved by stirring in 217 mL of distilled H_2O with 11.8 g of concentrated HCl (35 %) at 35 °C. This created micelles, micellar rods, and micellar arrays. Once complete dissolution had occurred, 6 g of butanol was added to cause swelling of the micellar arrays by infusing into the hydrophobic interior (propylene oxide) of the tri-block micelles. After 1 hour of stirring at 35 °C, 12.9 g of TEOS (tetraethyloxysilane) was added (the source of silica). The solution was left stirring for 24 hours at 35 °C (turning to an opaque milky white), and subsequently transferred to a polypropylene bottle and sealed. This was then heated at 100 °C for 24 hours under static conditions (hydrothermal treatment). The white solid product obtained was then filtered (no washing) and dried at 100 °C. The final stage of the mesoporous silica template preparation was the extraction of the organic template. This was achieved by washing in a dilute ethanol—HCl solution [56], followed by calcination at 550 °C under atmospheric conditions.

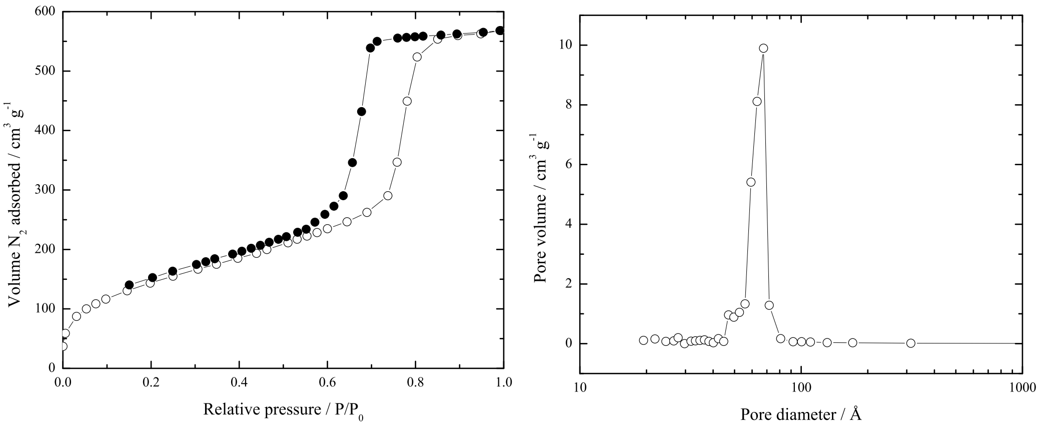

(a) Adsorption—desorption isotherm (empty—filled symbols).

(b) Pore size distribution.

Figure 3.1: N_2 adsorption—desorption isotherm for mesoporous silica, KIT-6 and corresponding pore size distribution derived from the BJH method.

3.1.2 Characterisation

Synthesised samples of KIT-6 were analysed for surface area and pore size distribution (PSD) by measuring the N_2 adsorption—desorption isotherm at 77 K and using the BET and BJH methods (Chapter 2). A typical isotherm observed is shown in Figure 3.1(a), along with the PSD, Figure 3.1(b). Using the BET method (adsorption branch within the limits, $0.15 \leq P/P_0 \leq 0.30$), the surface area from this particular isotherm is calculated as $517\,\mathrm{m^2\,g^{-1}}$. The pore size distribution using the desorption branch of the isotherm is centred around 6.5 nm.

Low angle X-ray powder diffraction patterns were obtained (Figure 3.2) which show three distinct reflections. These can be indexed upon the $Ia\bar{3}d$ space group, enabling a determination of the unit cell dimension, $a_0 = 21.1\,\mathrm{nm}$.[1]

TEM was performed on the samples of KIT-6 (Figure 3.3). These images taken at various magnifications show an ordered porous system (Figure 3.3(a)) which can be seen to be cubic (in agreement with literature). The image taken with greater magnification (Figure 3.3(b)) clearly shows a cubic ordering, however in this particular image the pore system cannot easily be seen due to the observed sample being too thick on the carbon backing disk.

---

[1]
$$\sin^2\theta = \frac{\lambda^2}{4a^2}(h^2+k^2+l^2) \tag{3.1}$$

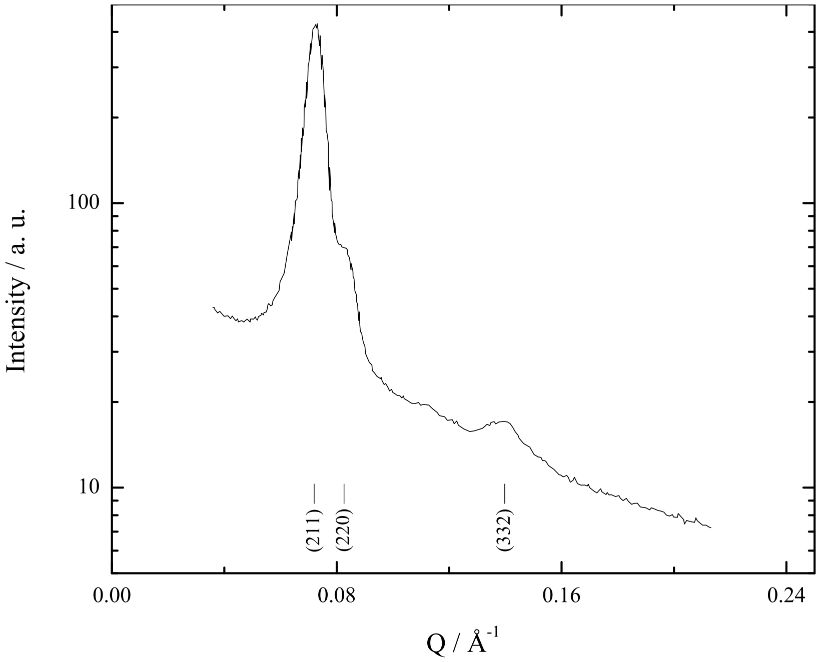

Figure 3.2: Low angle X-ray (Cu K$_\alpha$)powder diffraction pattern of mesoporous silica, KIT-6. Reflections indexed upon the cubic $Ia\bar{3}d$ space group give a unit cell parameter, $a_0 = 21.1\,\text{nm}$.

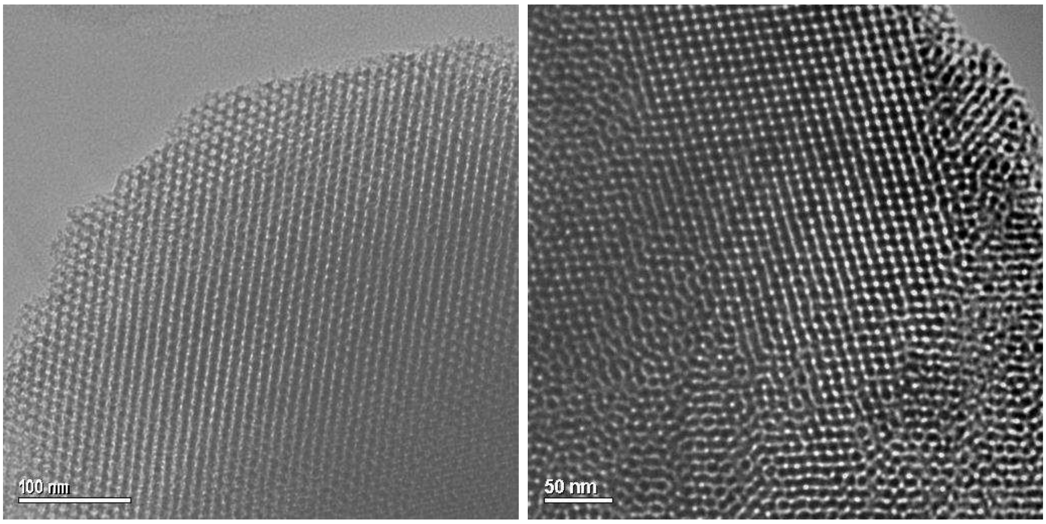

(a) KIT-6, 100 nm.

(b) KIT-6, 50 nm.

Figure 3.3: TEM images of mesoporous silica, KIT-6.

3.2 Mesoporous hematite

To ensure correct procedures were being followed, it was decided to try to replicate the synthesis of crystalline mesoporous hematite, α-Fe_2O_3 by Jiao *et al.* [23]. This met with mixed success, and requires careful synthesis steps.

3.2.1 Synthesis

Typically, 1.5 g of iron III nitrate nonahydrate ($Fe(NO_3)_3 \cdot 9\,H_2O$) was dissolved in 20 mL of ethanol, with the addition of 1 g of mesoporous silica, KIT-6. The solution was then stirred at room temperature until completely dry to allow infusion of the iron nitrate into the pores, and evaporation of the ethanol. The sample was then heated slowly to 600 °C and calcined at that temperature for 6 hours to decompose the nitrate to oxide. The resulting powder was then washed in hot 2 M NaOH to remove the silica template and centrifuged to provide the solid product. This was subsequently washed several times with a water—ethanol mixture followed by centrifugation, and finally dried in air at 100 °C.

3.2.2 Characterisation

Adsorption—desorption isotherms (Figure 3.4(a)) of synthesised mespoporous hematite samples do not show hysteresis characteristic of a type IV isotherm [43]. Despite this, there is clearly an opening of the adsorption—desorption branches. This indicates that the material does have a porous system, albeit with a lower surface area than more standard materials (such as KIT-6). The surface area calculated from the BET method (adsorption branch within the limits, $0.15 \leq P/P_0 \leq 0.30$) is shown to be $154\,m^2\,g^{-1}$. The plot of pore size distribution (Figure 3.4(b)) shows that there is a broad range of pore sizes, from 3 nm to 100 nm. This suggests that the material is not as crystallographically ordered as the KIT-6 template.

Wide angle XRPD (Figure 3.5) of the mesoporous hematite sample shows that the material is far from crystalline. The main Bragg reflections are barely distinguishable above the amorphous baseline, however they do occur at positions expected for bulk hematite. This again shows a lack of crystalline order in the sample.

TEM images of the mesoporous hematite (Figure 3.6) at various magnifications show the material is largely disordered and amorphous (Figure 3.6(a)) with some parts having an ordered mesoporous structure (Figure 3.6(b) and Figure 3.6(c)).

Because of the disordered nature of the mesoporous hematite samples, no LAXRD measurements were made.

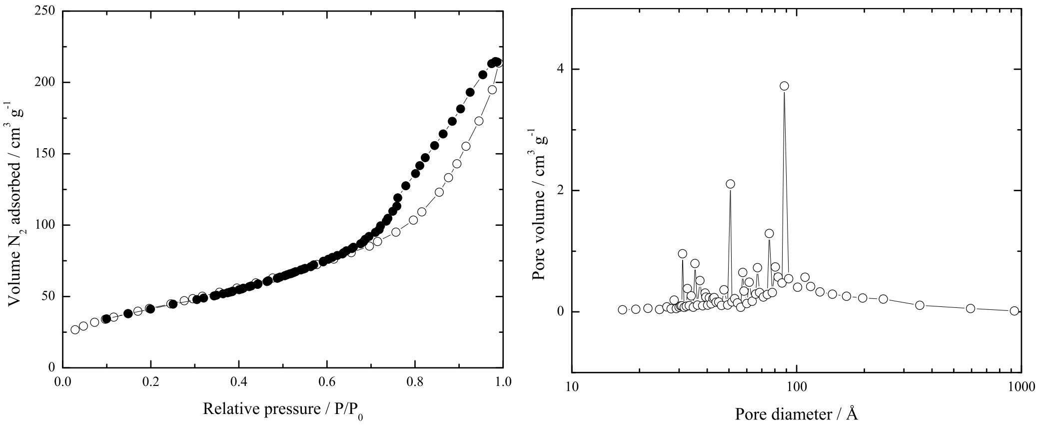

(a) Adsorption—desorption isotherm (empty—filled symbols).

(b) Pore size distribution.

Figure 3.4: N_2 adsorption—desorption isotherm for mesoporous α-Fe_2O_3 and corresponding pore size distribution derived from the BJH method.

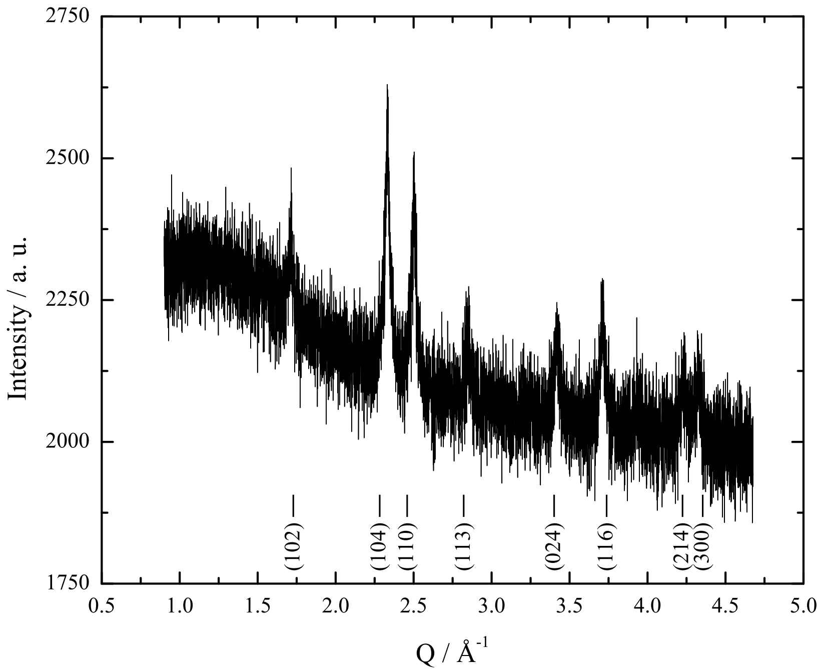

Figure 3.5: X-ray (Cu K_α) powder diffraction of synthesised mesoporous α-Fe_2O_3.

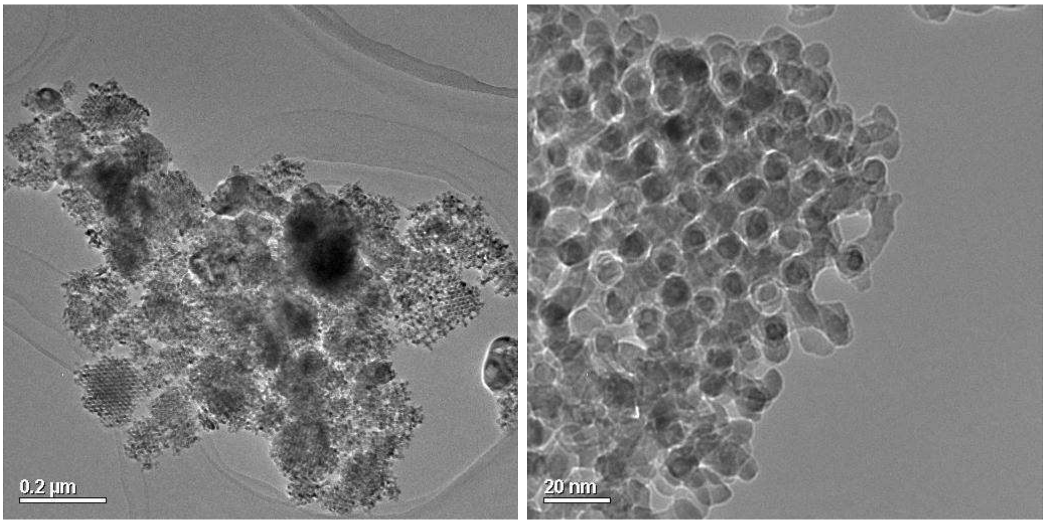

(a) α-Fe_2O_3, 200 nm.　(b) α-Fe_2O_3, 20 nm.

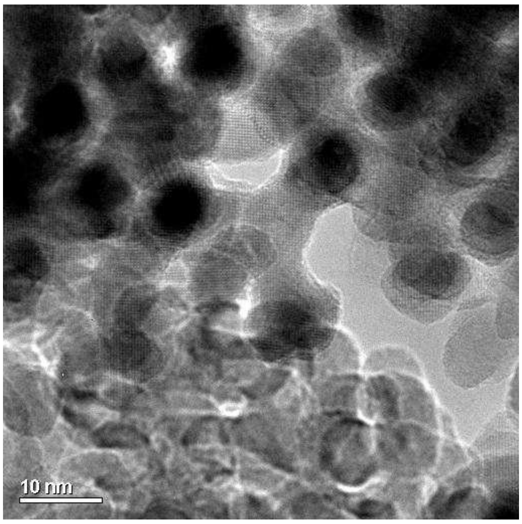

(c) α-Fe_2O_3, 10 nm.

Figure 3.6: TEM images of mesoporous hematite, α-Fe_2O_3.

3.3 Discussion of synthesis

It can be seen that the synthesis of mesoporous silica such as KIT-6 is easily reproducible and follows simple experimental steps. The next step to synthesise materials using the mesoporous silica as a hard template is not so simple. There are many stages in the synthesis where slight variations in the environmental and synthetic conditions can alter the outcome greatly, such as producing amorphous mesoporous rather than crystalline material, as demonstrated by Jiao *et al.* [23]. What seems to be of importance in the synthesis is determining the correct percentage weight of oxide precursor (e.g. weight of iron III nitrate) to fill the pores, and ensuring the sample is completely dry before heating to decompose the precursor. Due to difficulties in obtaining reliable syntheses (the reasons for which are not known), samples were provided by two external groups (University of St Andrews) to enable magnetic and crystallographic studies to be carried out.

Chapter 4

Mesoporous hematite, α-Fe_2O_3

Previous work on a synthesised sample of mesoporous α-Fe_2O_3 has shown that a particular magnetic transition present in bulk material (the Morin transition) is not observed upon cooling. Measurements were made with SQUID magnetometry and preliminary room temperature neutron powder diffraction [23]. The work carried out here (some of which is published in *Chemistry of Materials* [57] — see Appendix B) expands upon these initial measurements.

The sample, prepared by Dr Feng Jiao (School of Chemistry, University of St Andrews), was the same one that previous measurements had been made upon. The synthesis is briefly summarised here.

> An initial mesoporous silica template, KIT-6 was prepared as described by Kleitz and co-workers [7]. This has a three dimensional pore structure with a cubic $Ia\bar{3}d$ asymmetric unit. Iron (III) nitrate was allowed to diffuse into the pore structure and heated to decompose into iron (III) oxide. The silica template was subsequently removed by dissolving in NaOH, leaving a three dimensional negative image Fe_2O_3 framework of the original mesoporous silica. Transmission electron microscopy images (previously published) show a cubic structure of space group $Ia\bar{3}d$. Low angle X-ray powder diffraction showed a peak corresponding to the (211) reflection, a_0 of 229 Å. Pore diameter (centred at 38.5 Å) and surface area ($139\,\mathrm{m^2\,g^{-1}}$) were calculated from physisorption isotherms. XRPD measurements confirm the phase as that corresponding to hematite, α-Fe_2O_3. A second sample of hematite with a regular mesoporous structure, but an amorphous wall structure rather than crystalline was also synthesised in a similar manner (surface area of $210\,\mathrm{m^2\,g^{-1}}$ and a pore size centred at 37.8 Å).

4.1 NPD measurements

Measurements were performed upon the time of flight spectrometer/diffractometer, OSIRIS[58] at the ISIS facility between 2 K to 300 K on both the crystalline and amorphous mesoporous hematite samples. Due to difficulty in refining the isotropic thermal parameters from the OSIRIS data, further measurements were conducted with a bulk sample of hematite from Acros Organics, 99.999 %, 100 mesh (diameter $< 150\,\mu$m) on the GEM diffractometer [59] (collects data over a greater Q range) at the ISIS facility. The temperature dependence of the key magnetic Bragg peaks in the bulk sample were also studied by collecting data on the high flux D1B diffractometer at the ILL.

4.1.1 Bulk hematite data

Rietveld refinements of the NPD data were carried out as follows. A $R\bar{3}c$ (hexagonal setting) hematite model was fitted to the data for the crystallographic unit cell, with Fe and O atoms on the 12c and 18e Wyckoff sites respectively. A second phase consisting of 12 Fe atoms set at the positions generated by the symmetry operations of the $R\bar{3}c$ phase was added with $P1$ symmetry for refinement of the magnetic structure, following the two-phase fit without magnetic symmetry approach summarised by Cui et al. [60]. Rietveld refinement of the model was then carried out using the GSAS suite of programs [41] with the EXPGUI interface [42], typically using a 10–12 point shifted Chebyschev background polynomial for each diffraction pattern. Patterns obtained from all 6 detector banks of the GEM diffractometer at 300 K and 10 K are shown in Figure 4.2 and Figure 4.3 whilst OSIRIS patterns are shown in Figure 4.4. Refined parameters are shown in Table 4.1 and Table 4.2.

The key observation from these patterns is the change in intensity of the purely magnetic (003) Bragg peak[1] at lowest Q-spacing (≈ 1.37 Å), visible in the first 3 collector banks of the GEM diffractometer. At high temperatures, this is the most intense

---

[1] The rhombohedral space groups can either be described in a hexagonal or rhombohedral setting. In the latter, $a = b = c$, $\alpha = \beta = \gamma \neq 90°$. In the former, $a = b \neq c$, $\alpha = \beta = 90°$, $\gamma = 120°$. The Miller indices h_R, k_R, l_R of the rhombohedral setting are related to the hexagonal Miller indices h_H, k_H, l_H by the following relationships (where $i_H = -h_H - k_H$). Therefore the (003) hexagonal peak corresponds to the (111) rhombohedral peak.

$$\begin{aligned} h_H &= k_R - l_R & h_R &= \frac{1}{3}(-k_H + i_H + l_H) \\ k_H &= l_R - h_R & k_R &= \frac{1}{3}(h_H - i_H + l_H) \\ i_H &= h_R - k_R & h_R &= \frac{1}{3}(-h_H + k_H + l_H) \\ l_H &= h_R + k_R + l_R & & \end{aligned}$$

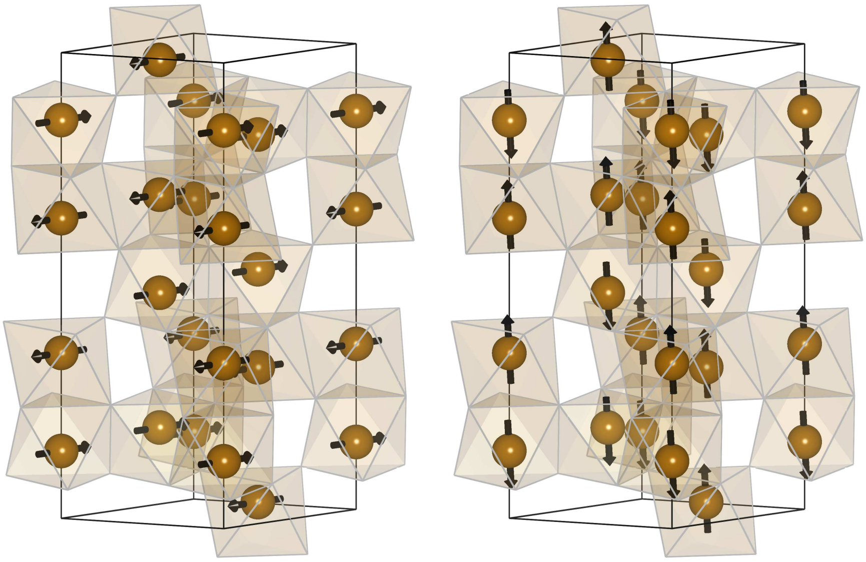

(a) $T > T_{\mathrm{M}}$.

(b) $T < T_{\mathrm{M}}$.

Figure 4.1: The magnetic structure of α-Fe_2O_3 above and below the Morin transition.

magnetic Bragg peak, but at low temperatures this peak has a very small intensity. The intensity of this peak corresponds to the proportion of magnetic moment from the Fe^{3+} ions lying in the hexagonal *ab* (basal) plane. At high temperatures the intensity of the peak is greatest, showing that the majority (if not all) of the moment is lying in the basal plane, whereas at low temperatures, the small intensity suggests that the majority of the moment has re-orientated into the hexagonal *c* axis (Figure 4.1). This first-order transition is known as the Morin transition and the temperature at which this occurs is denoted by T_{M} [61]. To enable stable Rietveld refinements, magnetic moments were allowed to refine only in the x direction (x and y directions are equivalent in the hexagonal cell) above T_{M}. Below this transition, a component of magnetic moment was also allowed to refine in the z direction. The intensity of the (003) Bragg peak provides an accurate calculation of the component of magnetic moment tilted out of the [003] direction. The components of magnetic moment in the x and z directions at 2 K allow an accurate calculation of this tilting angle as $10.7(2)^\circ$. This is in good agreement with, and far more accurate than previously reported values of $15(10)^\circ$ [62]. Data obtained from the D1B diffractometer show the intensity change of the key magnetic Bragg peaks as a function of temperature (Figure 4.5).

T / K	a / Å	c / Å	Fe^{3+} z coordinate	O^{2-} x coordinate
300	5.035128(4)	13.75809(10)	0.355322(16)	0.30618(6)
250	5.034778(3)	13.74857(9)	0.355266(14)	0.30616(6)
200	5.034516(4)	13.74145(10)	0.355169(15)	0.30615(6)
150	5.034321(4)	13.73618(11)	0.355155(17)	0.30609(7)
100	5.034172(4)	13.73210(11)	0.355082(17)	0.30605(7)
50	5.034172(4)	13.73213(12)	0.355131(18)	0.30615(7)
10	5.034171(4)	13.73210(11)	0.355080(17)	0.30602(7)

T / K	Fe^{3+}	O^{2-}	m_x / μ_B	m_z / μ_B	m / μ_B	$R_{(\mathrm{wp})}$	$R_{(\mathrm{p})}$
	U_iso / $\times$ 10^2 Å^2						
300	0.250(5)	0.339(7)	4.118(6)	—	4.118(6)	0.0438	0.0419
250	0.198(4)	0.311(6)	1.607(10)	4.026(7)	4.165(7)	0.0411	0.0496
200	0.160(4)	0.301(7)	0.826(14)	4.101(7)	4.183(7)	0.0435	0.0516
150	0.103(5)	0.276(8)	0.785(16)	4.133(8)	4.207(8)	0.0493	0.0549
100	0.057(4)	0.247(7)	0.783(16)	4.164(8)	4.237(8)	0.0503	0.0487
50	0.060(5)	0.266(8)	0.762(18)	4.153(9)	4.223(9)	0.0554	0.0598
10	0.067(5)	0.263(8)	0.781(17)	4.149(9)	4.222(9)	0.0529	0.0520

Table 4.1: Rietveld refinement parameters for bulk α-Fe$_2$O$_3$ from the GEM diffractometer.

T / K	a / Å	c / Å	Fe^{3+} z coordinate	O^{2-} x coordinate
300	5.03431(8)	13.7479(3)	0.35494(5)	0.3061(2)
150	5.03095(4)	13.7370(2)	0.35502(4)	0.30508(17)

T / K	Fe^{3+}	O^{2-}	m_x / μ_B	m_z / μ_B	m / μ_B	$R_{(\mathrm{wp})}$	$R_{(\mathrm{p})}$
	U_iso / $\times$ 10^2 Å^2						
300	0.35(3)	0.86(3)	4.073(14)	—	4.073(14)	0.0813	0.0482
150	0.38(2)	0.88(3)	0.816(13)	3.975(11)	4.165(7)	0.0690	0.0598

Table 4.2: Structural and magnetic parameters obtained by Rietveld refinement of bulk α-Fe$_2$O$_3$ NPD patterns from the OSIRIS instrument.

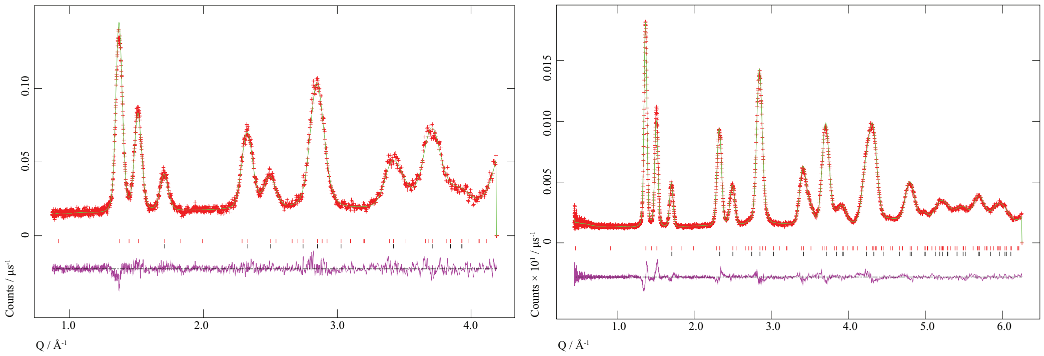

(a) Bank 1.

(b) Bank 2.

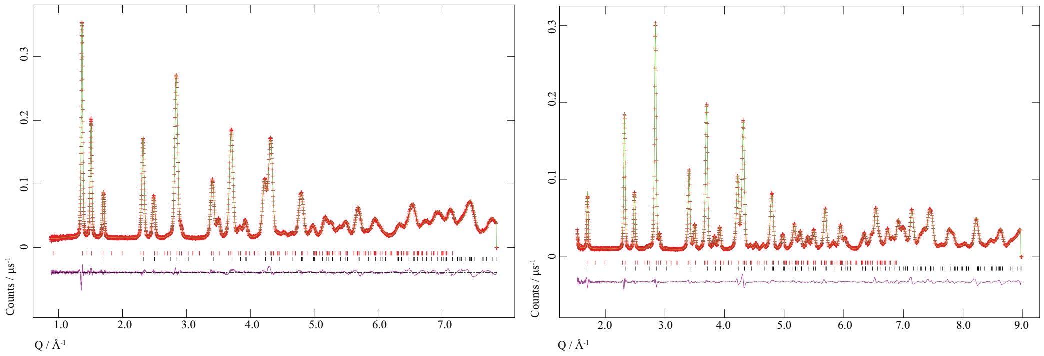

(c) Bank 3.

(d) Bank 4.

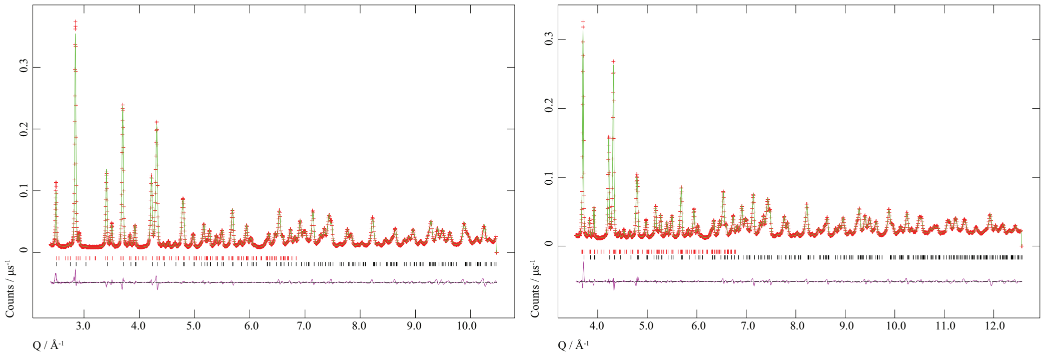

(e) Bank 5.

(f) Bank 6.

Figure 4.2: Rietveld refinements of diffraction patterns of bulk α-Fe_2O_3 from the GEM diffractometer at 300 K. The red marks are observed points, with the green line the calculated pattern from the refined model, with expected Bragg peak positions shown with red and black tick-marks from the magnetic and crystallographic cells respectively. The magnetic Bragg peak positions (upper tick-marks) are only calculated to $\approx 6.9\,\text{Å}^{-1}$ due to the magnetic form factor having very little intensity after this point (Figure 2.4). The purple line is the difference between the observed and calculated profile.

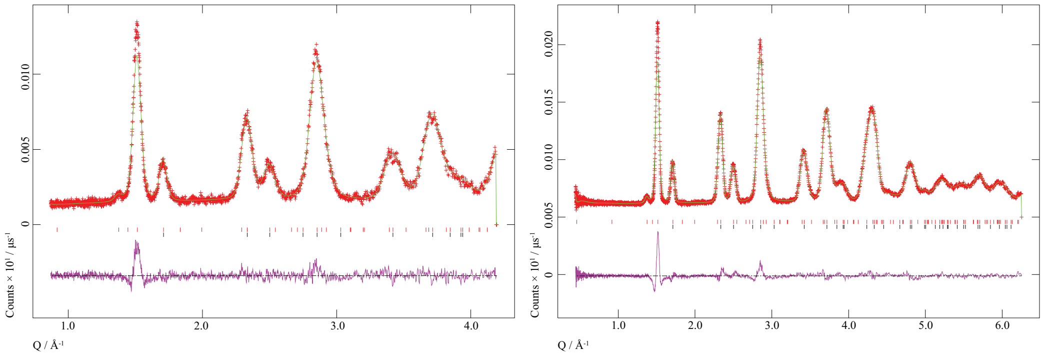

(a) Bank 1.
(b) Bank 2.

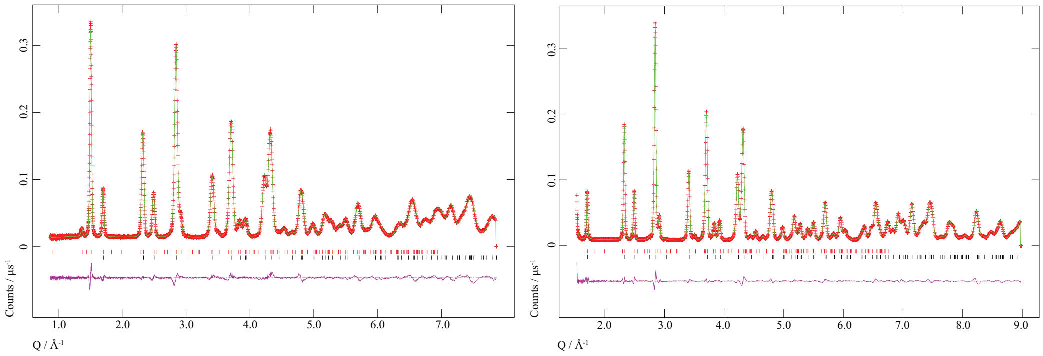

(c) Bank 3.
(d) Bank 4.

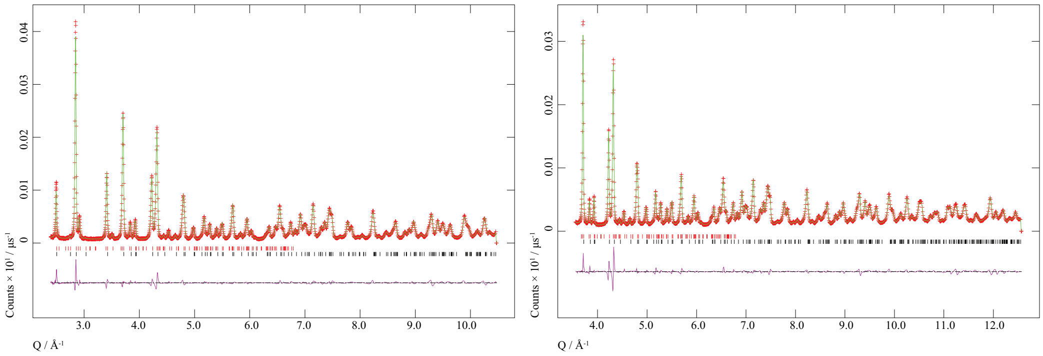

(e) Bank 5.
(f) Bank 6.

Figure 4.3: Rietveld refinements of diffraction patterns of bulk α-Fe_2O_3 from the GEM diffractometer at 10 K. The red marks are observed points, with the green line the calculated pattern from the refined model, with expected Bragg peak positions shown with red and black tick-marks from the magnetic and crystallographic cells respectively. The purple line is the difference between the observed and calculated profile.

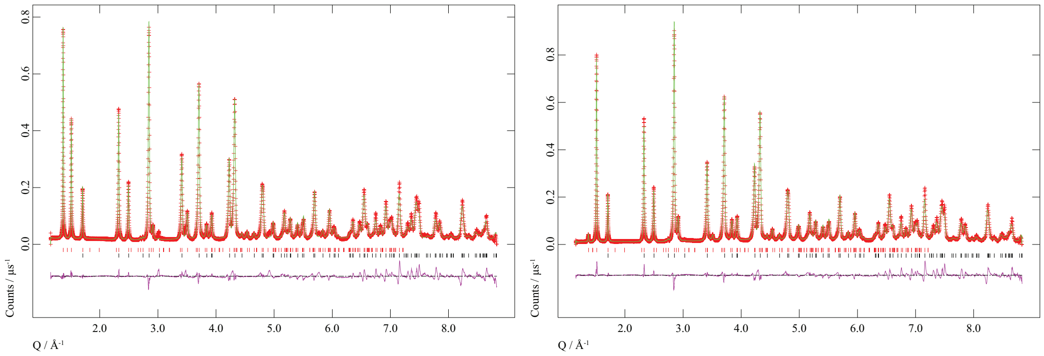

(a) 300 K.

(b) 150 K.

Figure 4.4: Rietveld refinements of diffraction patterns of bulk α-Fe_2O_3 from the OSIRIS instrument at 300 K and 150 K. The red marks are observed points, with the green line the calculated pattern from the refined model, with expected Bragg peak positions shown with red and black tick-marks from the magnetic and crystallographic cells respectively. The purple line is the difference between the observed and calculated profile.

4.1.2 Amorphous mesoporous hematite data

Diffraction patterns were collected on the OSIRIS diffractometer from 1.5 K to 300 K (Figure 4.6(a)). Due to the amorphous nature of the mesoporous walls, Bragg reflections are not well defined. A clear drop in the background can be seen with increasing Q-vector. This will be in part due the magnetic form factor dropping with increasing Q. The most noticeable feature is the reduction in background at low Q with decreasing temperature in the region where the most prominent magnetic Bragg reflections occur in the bulk material. This suggests that as cooling occurs, the magnetic moments are becoming more ordered, and the paramagnetic background is decreasing. Bragg peaks in all the diffraction patterns are poorly resolved and have very broad FWHM (full width at half maximum), making any form of structure refinement very difficult, therefore no physical parameters are reported here.

4.1.3 Crystalline mesoporous hematite data

Rietveld refinements of the data collected from OSIRIS on mesoporous crystalline hematite were performed in the same manner as that utilised for the bulk data on GEM. These are shown in Figure 4.7. Due to the way that data is collected using OSIRIS (chopper frequencies are changed to obtain different wavelengths) the overall histogram is a combination of several measurements. These are then binned together to make one continuous file. This has led to an error in the 150 K histogram which is most noticeable in the region of $Q = 2.1\,\text{Å}^{-1}$ (Figure 4.7(d)), therefore refined

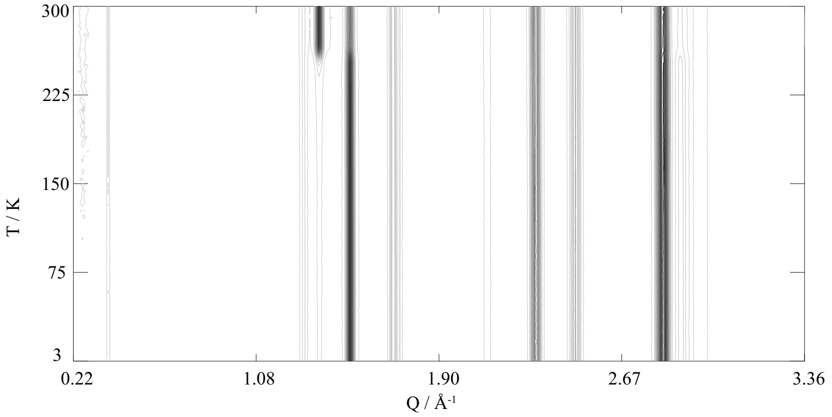

(a) Full Q-range of the D1B diffractometer as a function of T. The intensity of Bragg peaks are shown by the contours on the plots.

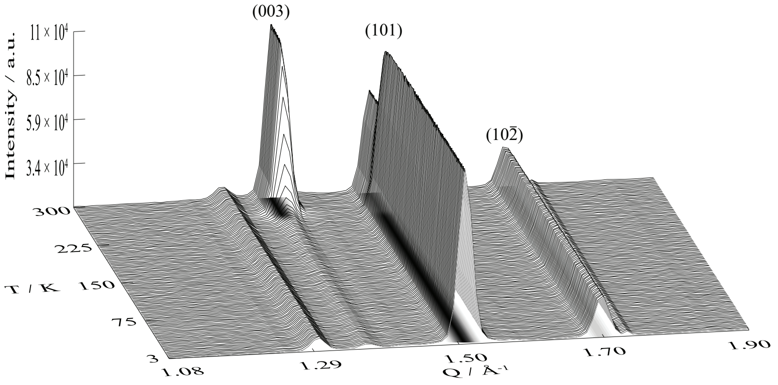

(b) Three-dimensional image showing, Q, T and peak intensity for the primary magnetic Bragg peaks.

Figure 4.5: Neutron powder diffraction patterns from D1B of bulk α-Fe_2O_3. The peak at 1.29 $\mathring{A}^{-1}$ is believed to arise from a low concentration of impurity, but does not affect the intensity of the (003) reflection.

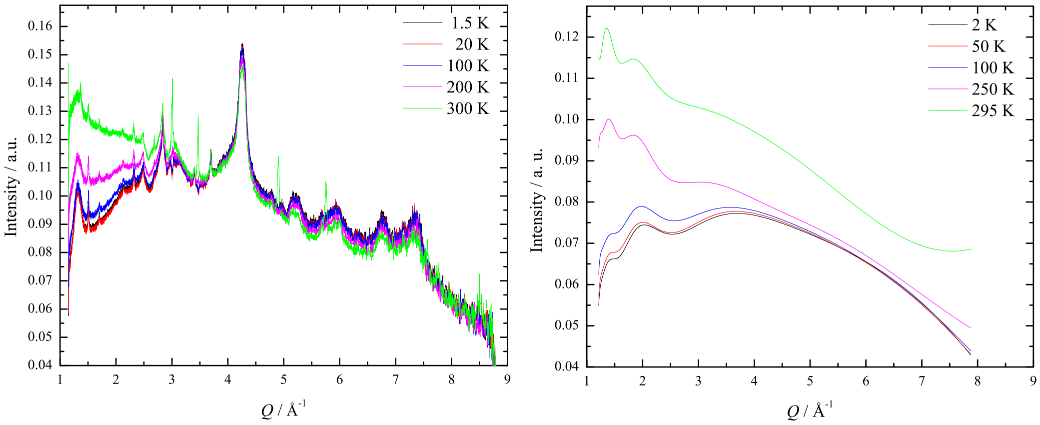

(a) Diffraction patterns of amorphous mesoporous hematite.

(b) Background functions from refinements of crystalline mesoporous hematite.

Figure 4.6: Comparison of the elastic backgrounds observed in amorphous and crystalline mesoporous hematite.

parameters for this temperature are not reported here. The remaining results are presented in Table 4.3. What is immediately obvious from the diffraction patterns is that the intensity of the (003) magnetic Bragg peak does not decrease suddenly at the expected Morin transition temperature. This suggests that there is no first-order phase transition occurring, and that the magnetic moments are remaining perpendicular to the [003] direction. Therefore refinements were carried out only allowing magnetic moment in the x direction. The background parameters have been extracted from the Rietveld refinements and are shown in Figure 4.6(b). It should be noted here that the 295 K data were collected without an orange cryostat so the background function is slightly different, (although it displays the same trends as the data collected at lower temperatures).

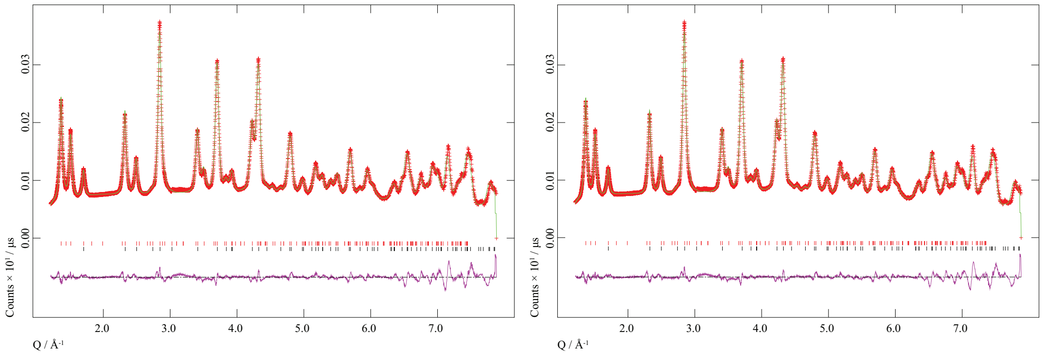

(a) 2 K. (b) 50 K.

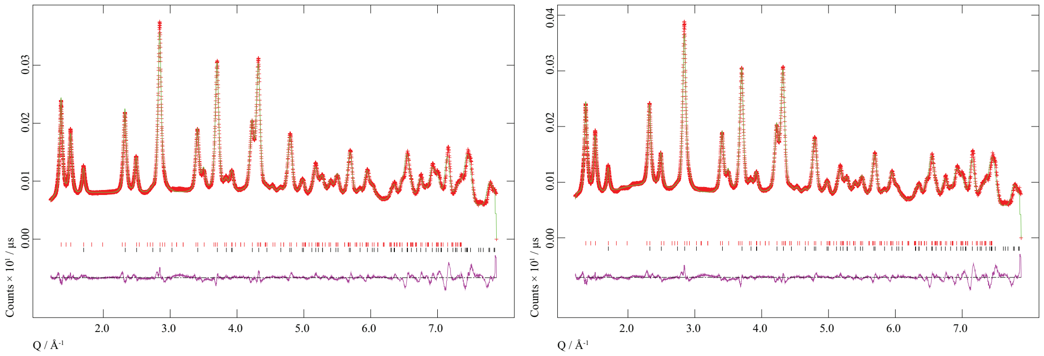

(c) 100 K. (d) 150 K.

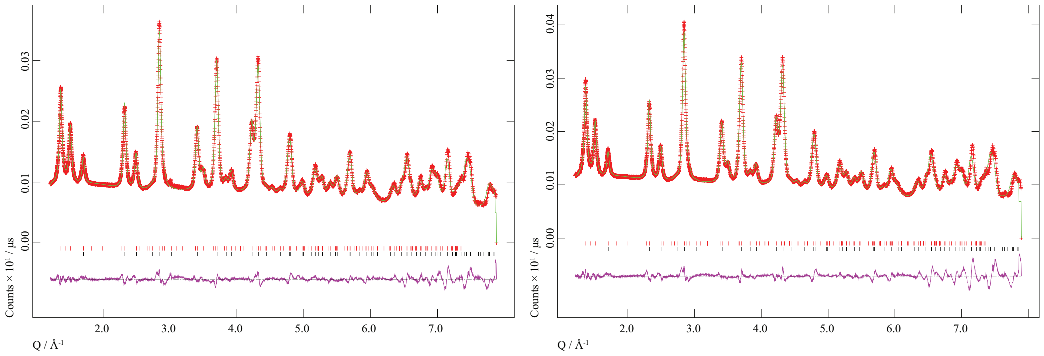

(e) 250 K. (f) 295 K.

Figure 4.7: Rietveld refinements for diffraction patterns of crystalline mesoporous α-Fe_2O_3 from the OSIRIS diffractometer. The red marks are observed points, with the green line the calculated pattern from the refined model, with expected Bragg peak positions shown with red and black tick-marks from the magnetic and crystallographic cells respectively. The purple line is the difference between the observed and calculated profile.

T / K	a / Å	c / Å	Fe^{3+} z coordinate	O^{2-} x coordinate
295	5.03599(3)	13.7816(9)	0.35510(6)	0.3090(3)
250	5.036201(17)	13.7873(5)	0.35493(5)	0.3098(3)
100	5.035521(16)	13.7687(4)	0.35493(5)	0.3100(2)
50	5.035469(16)	13.7673(4)	0.35485(5)	0.3097(2)
2	5.035476(16)	13.7676(4)	0.35485(5)	0.3097(3)

T / K	Fe^{3+}	O^{2-}	m_x / μ_B	m_z / μ_B	m / μ_B	$R_{(wp)}$	$R_{(p)}$
	U_{iso}[a]/ Å^2 × 10^2						
295	—	—	4.05(2)	—	4.05(2)	0.0248	0.0188
250	—	—	3.98(2)	—	3.98(2)	0.0265	0.0190
100	—	—	4.192(18)	—	4.192(18)	0.0266	0.0224
50	—	—	4.208(18)	—	4.208(18)	0.0271	0.0231
2	—	—	4.224(18)	—	4.224(18)	0.0274	0.0235

[a] Isotropic thermal parameters not refined. Set from bulk GEM refinements.

Table 4.3: Structural and magnetic parameters obtained by Rietveld refinement of mesoporous α-Fe_2O_3 NPD patterns from the OSIRIS instrument.

4.2 Magnetic property measurements

Further magnetic property measurements (in addition to preliminary measurements carried in the previous work [23]) were made upon bulk and crystalline mesoporous hematite samples with a SQUID magnetometer. Fine resolution ZFC DC susceptibility measurements were performed upon the bulk sample to determine accurately T_M and compared with; integrated magnetic Bragg peak areas determined from the D1B data, and refined magnetic moment from the GEM data (Figure 4.8). All three data sets show the onset of the Morin transition at the same temperature points. This is determined to be (from the temperature at which the magnetic susceptibility is half it's maximum value) 259.1(1) K.

Magnetic hysteresis measurements were taken upon bulk (Figure 4.9) and crystalline mesoporous (Figure 4.10) hematite samples at a variety of temperatures. Linear fits of the magnetic response at high fields ($> 4 \times 10^6$ A m^{-1}) have been performed to determine the remnant magnetisation ($\mathbf{M}_r$) due to the weak ferromagnetic spin canting. These values along with the estimated coercive fields ($\mathbf{H}_c$) and calculated canting angles (calculated using the remnant magnetisation and refined magnetic moment from corresponding temperature NPD) are presented in Table 4.4.

4.3 Discussion

The magnetic moments determined from Rietveld refinements are lower than those expected for the quantised z-component of the spin only moment of Fe^{3+}, $5.00\,\mu_B$, but are of a similar value to previously refined values [63]. This is due to the α-Fe_2O_3 system being a charge transfer insulator rather than a Mott—Hubbard insulator [64, 65] with a p-d band gap. Hence there is a small amount of Fe$-$O σ type bonding due to charge back transfer $2p(O^{2-}) \longrightarrow 3\,d(Fe^{3+})$. This therefore increases the effective charge on the Fe^{3+} ions, producing a lower magnetic moment (number of unpaired spins is reduced). This charge transfer has been directly observed with spherical neutron polarimetry in the case of isostructural eskolaite, Cr_2O_3 [66]. No net magnetization is seen on the oxygen anions, due to an equal fraction of up and down spin gain from the up and down spin chromium cation neighbours. Examination of the magnetic moments observed in the mesoporous sample show that unlike the bulk material, the magnetic moment increases upon cooling (Figure 4.11). This increase in magnetic moment occurs far below the antiferromagnetic Néel transition observed in bulk hematite ($T_N \approx 955\,K$). It therefore

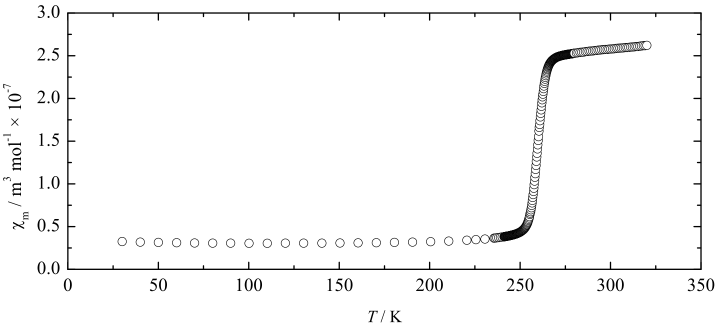

(a) χ_m vs. T.

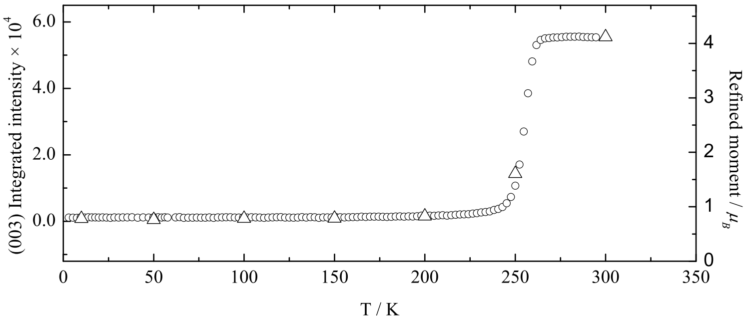

(b) (003) Bragg peak intensity (circles) and refined magnetic moment (triangles).

Figure 4.8: Comparison of magnetic susceptibility, (003) Bragg peak intensity, and refined magnetic moment of bulk α-Fe_2O_3.

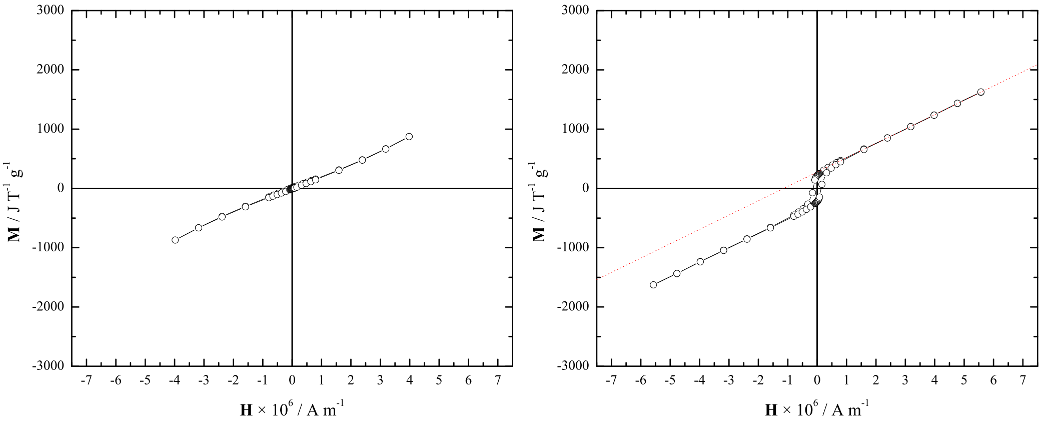

(a) 12 K.

(b) 295 K.

Figure 4.9: Magnetic hysteresis of bulk hematite above and below T_M. A linear fit to the high field response in the weak ferromagnetic phase (b) has been performed and extrapolated.

Sample	$\mathbf{H}_\mathrm{c} \times 10^6$ / A m^{-1}	$\mathbf{M}_\mathrm{r}$ / J T^{-1} g^{-1}	θ / °	m_y / μ_B	m_x / μ_B
Bulk 295 K	0.133	276(9)	0.0550(19)	0.00395(15)	4.118(6)
Meso 300 K	0.022	553(17)	0.112(4)	0.0079(3)	4.05(2)
Meso 250 K	0.027	640(90)	0.132(19)	0.0092(13)	3.98(2)
Meso 200 K	0.046	656(18)	—	—	—
Meso 150 K	0.064	667(17)	—	—	—
Meso 100 K	0.072	727(17)	0.142(4)	0.0104(3)	4.192(18)
Meso 50 K	0.105	727(17)	0.141(4)	0.0104(3)	4.207(18)
Meso 10 K	0.344	750(50)	—	—	—
Meso 2 K	0.453	797(18)	0.155(4)	0.0114(3)	4.224(18)

Table 4.4: Values of coercivity and remnance calculated from $\mathbf{M}(\mathbf{H})$ curves along with calculated canting angle, θ, and m_x and m_y components for hematite samples.

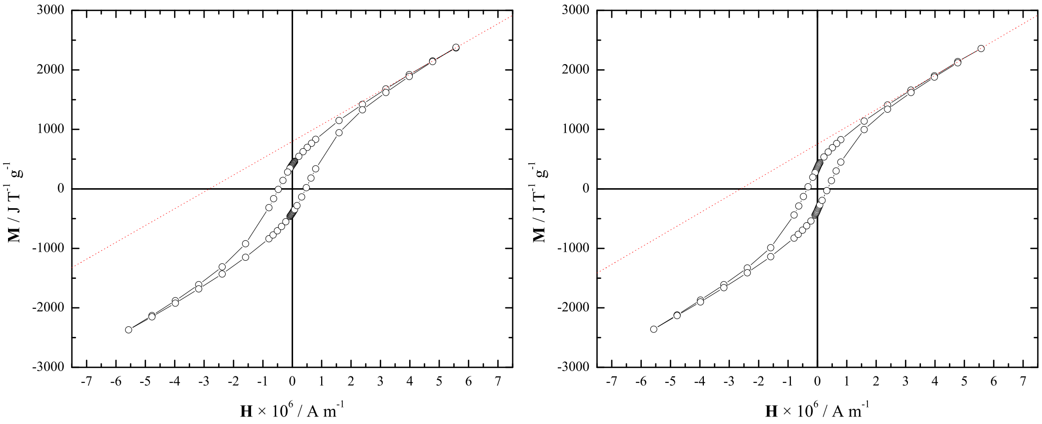

(a) 2 K.

(b) 10 K.

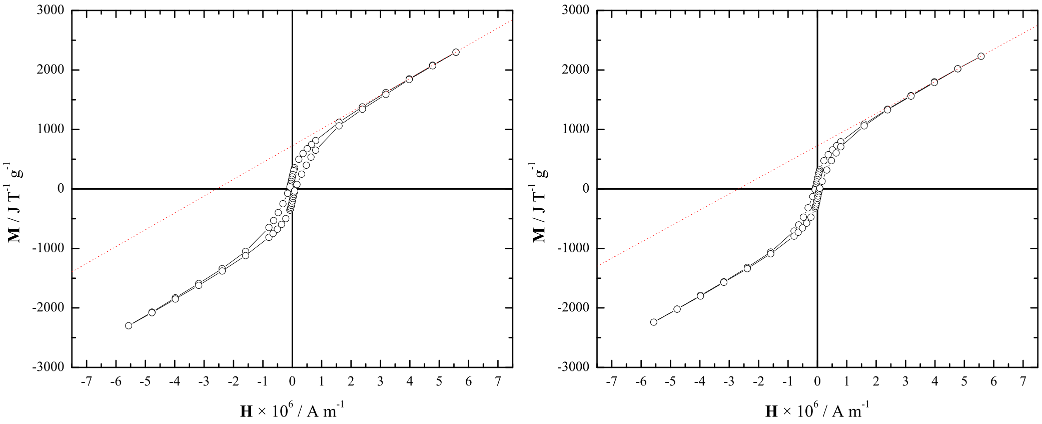

(c) 50 K.

(d) 100 K.

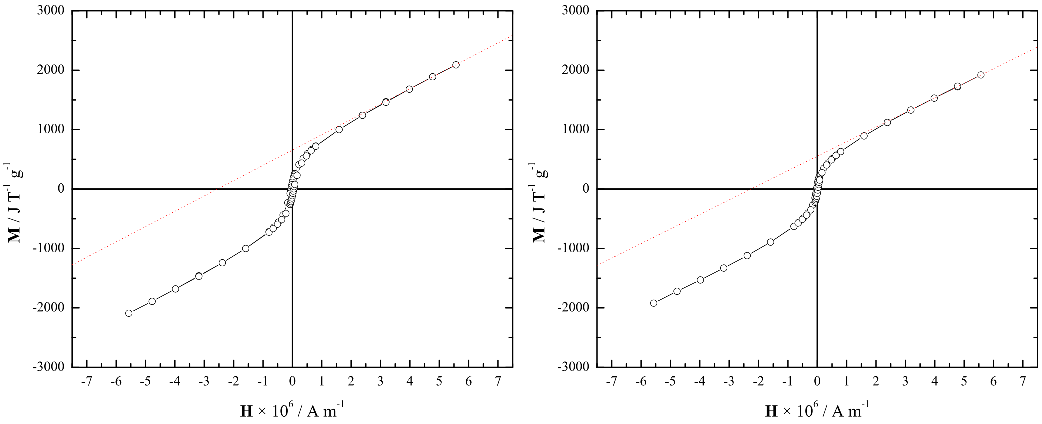

(e) 200 K.

(f) 300 K.

Figure 4.10: Magnetic hysteresis of crystalline mesoporous hematite. Linear fits to the high field response have been performed and extrapolated.

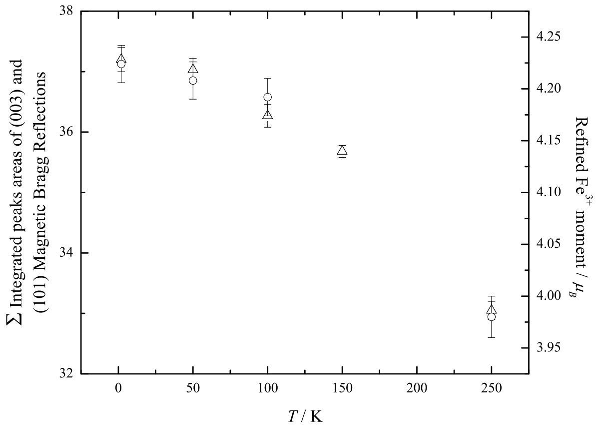

Figure 4.11: Sum of extracted (003) and (101) Bragg peak intensities (triangles) and refined magnetic moments (circles) in mesoporous hematite.

points to a considerable amount of magnetic disorder present in the mesoporous sample, even at temperatures close to 300 K, which are slowly becoming more ordered upon cooling. This is also shown in the decrease in background in Figure 4.6(b), particularly at lower Q, where the magnetic scattering is strongest and the magnetic Bragg peaks are present.

Magnetic hysteresis loops of bulk hematite (Figure 4.9) carried out below and above T_{M} at 12 K and 295 K show what is expected for the material. A lack of hysteresis at 12 K indicates a simple antiferromagnet (the curve is not horizontal due to suspected paramagnetic impurities in the sample), at 295 K, hysteresis is observed, due to the weak ferromagnetic state of the material. The extrapolated spontaneous magnetization ($\mathbf{M}_r$) in Table 4.4 is in close agreement to previous studies [67–70]. Combination of the hysteresis data and NPD refinements allows the determination of the canting angle within the hexagonal basal plane responsible for the weak ferromagnetism above T_{M}. The value of 0.06° and a canted moment of 0.004 μ_{B} is in good agreement with accepted literature values [71].

The diffraction patterns of the mesoporous hematite show broadened Bragg peaks, known as Scherrer broadening. This is likely to be due to disruption of the repetition of the crystallographic and magnetic cell over long ranges by the meso-structure. Using TOF profile 2 in GSAS (an incorporation of the Ikeda-Carpenter function [72] with a pseudo-Voigt linear combination of a Lorentzian and a Gaussian function) the γ_2 variables of the Lorentzian part of the peak profile were allowed to refine independently between the nuclear and magnetic phases, whilst the Gaussian parts were constrained between phases. This enabled an estimation of correlation lengths in the material, using Equation 4.1 where p is the correlation length (Å), C is the diffractometer constant

T / K	p_{nuc} / Å	p_{mag} / Å
295	154.5(15)	139.4(16)
250	150.9(13)	137.0(15)
100	152.5(12)	135.7(12)
50	152.9(12)	136.9(12)
2	153.3(13)	140.0(12)

Table 4.5: Estimated nuclear and magnetic correlation lengths in mesoporous Fe_2O_3. from OSIRIS data.

DIFC, characteristic of the particular geometry of the instrument used, and K is the Scherrer constant. The Scherrer equation has a dependence on the shapes of the objects concerned (spheres, platelets, rods etc.), this is accounted for in the value of K. In the case of mesoporous materials of this type, it is not clear as to what value of K is appropriate. For spheres, K $\approx$ 0.9, and it is this value which has been used here. This will give a ball park estimate of the correlation lengths present in the material.

$$p = \frac{\mathrm{CK}}{\gamma_2} \tag{4.1}$$

Nuclear and magnetic correlation lengths have been calculated for mesoporous Fe_2O_3, (Table 4.5. Both the nuclear and magnetic correlation length in mesoporous Fe_2O_3 are shown to be approximately 150 Å at base temperature. A similar approach was applied to the bulk Fe_2O_3 data, where correlation lengths of $\approx$ 500 Å to 600 Å were observed at the temperatures studied for both the nuclear and magnetic contributions. These *estimates* show that the magnetic and nuclear correlation lengths in the mesoporous material are around $\frac{1}{4}$ the length of the correlation lengths in the bulk material. The particle sizes of the mesoporous hematite observed with TEM are approximately 1000 Å to 2000 Å in diameter.

Analysis of the refined unit cell parameters from the bulk and mesoporous samples show that both samples exhibit similar unit cell contractions upon cooling ($\approx 0.02\,\%$ in a and $\approx 0.2\,\%$ in c for bulk materials and $\approx 0.01\,\%$ in a and $\approx 0.1\,\%$ in c for the mesoporous material). The mesoporous sample has a slightly larger unit cell ($\approx 0.03\,\%$ in a and $\approx 0.3\,\%$ in c) in comparison to the bulk sample at equivalent temperatures (Figure 4.12). Similar expansions in the lattice parameters have been noted in microcrystalline hematite particles, where a suppression of the Morin transition was also observed [73–75].

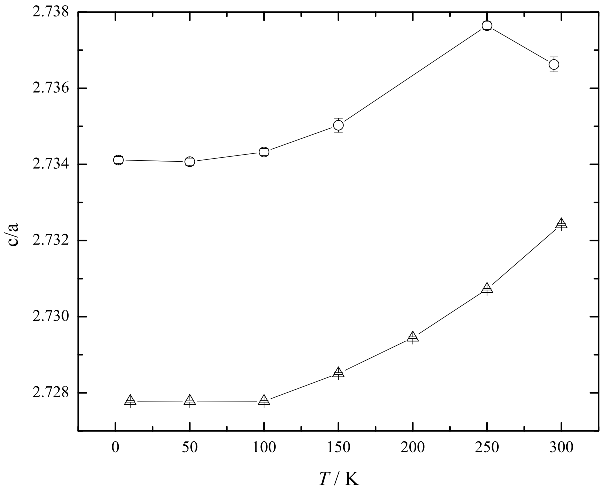

Figure 4.12: Variation of c/a with temperature for bulk (triangles) and mesoporous (circles) hematite.

4.4 Inelastic neutron scattering

Some of the properties, such as the expanded lattice and lack of Morin transition in the mesoporous hematite sample bear striking resemblance to properties displayed by hematite nanoparticles. Various studies of such hematite nanoparticles have been performed with inelastic neutron scattering to try to understand some of the dynamic processes (e.g. magnons) occurring in the samples [76–81]. By looking at the inelastic interactions near the purely antiferromagnetic (003) and (101) Bragg reflections ($Q \approx 1.37\,\text{Å}^{-1}$ and $\approx 1.50\,\text{Å}^{-1}$ respectively) information regarding the magnetic anisotropy and dynamics in the hematite nanoparticles was obtained. Preliminary measurements upon the mesoporous hematite sample using the MARI and IN6 inelastic neutron spectrometers at ISIS and the ILL have been carried out to try to emulate these results.

Measurements on the MARI spectrometer (Figure 4.13) showed that there was indeed an inelastic feature occurring at the (101) Bragg reflection. This is shown in Figure 4.14, where a Q cut has been made at $\approx 1.51\,\text{Å}^{-1}$. This shows what could be a small up-scattering interaction at $\approx 1.2\,\text{meV}$, however the resolution of the instrument and the broad elastic line prevent a similar observation on the down scattering side.

Further measurements on the IN6 spectrometer (Figure 4.15) were performed from 300 K down to 1.5 K at 0 T and 2.5 T. These show a high intensity and broad elastic line, probably due to intercalated water within the pore structure contributing to a large amount of incoherent scattering. Q-cuts have been performed at a wavevector values corresponding to the (003) and (101) purely antiferromagnetic Bragg reflections as well as the $(10\bar{2})$ magnetic and structural reflection. Plots of these cuts in 0 T and 2.5 T are

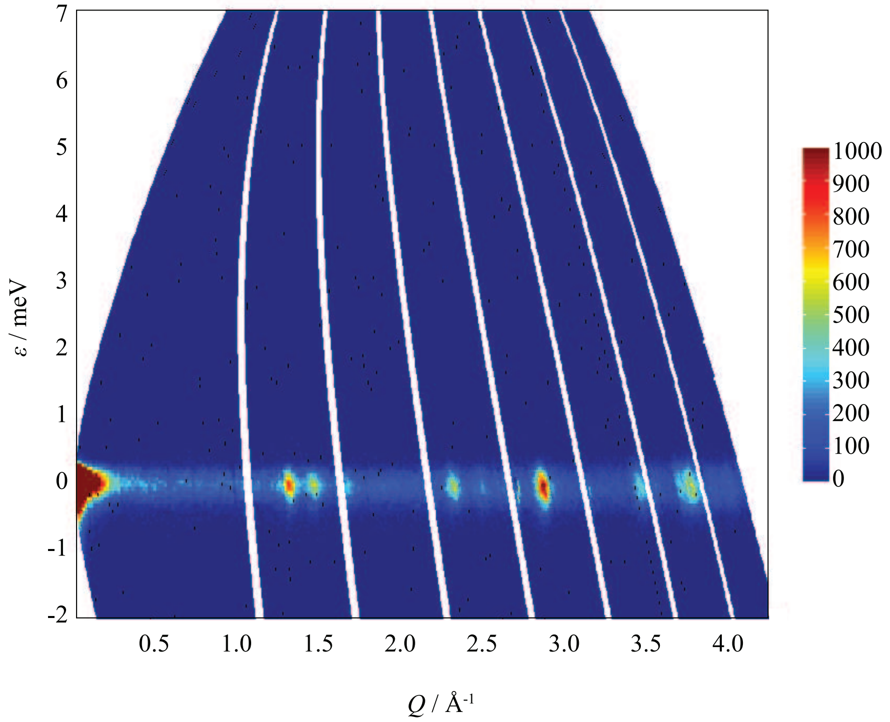

Figure 4.13: Spectrogram of mesoporous hematite from MARI taken at 300 K.

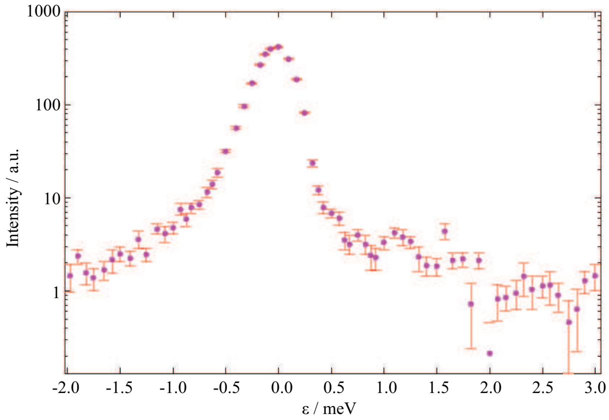

Figure 4.14: A cut in Q at $1.51\,\mathring{A}^{-1}$ from the MARI spectrometer.

shown in Figure 4.16. From the $(10\bar{2})$ reflection at $Q = 1.70\,\text{Å}^{-1}$ we can clearly see a sharp shoulder to the elastic line at approximately 0.2 meV. This is a known intrinsic effect of the resolution function of the IN6 spectrometer. This can be seen throughout the entire spectrum with different Q cuts.

The cuts at the (003) reflection show a broad extension to the elastic line on the Stokes and anti-Stokes sides. This broadening decreases as the temperature reduces down to 1.5 K. Application of the small 2.5 T field reduces this inelastic interaction but does not seem to pull the energy values further away from the elastic line as seen with nanoparticles in fields up to 6 T [76], which was attributed to collective magnetic excitations in the nanoparticles which are precession states of the sublattice magnetisations.

The (101) reflection cut at $Q = 1.51\,\text{Å}^{-1}$ shows a clearly localised magnetic excitation at an energy transfer of ≈ 1.1 meV at room temperature. As the temperature decreases, this excitation lowers in energy and becomes less intense. This is shown in Figure 4.17, where the anti-Stokes scattering has been focussed upon. A similar trend is shown on the Stokes side, but are considerably harder to see due to a shoulder at 0.2 meV, intrinsic to the IN6 instrument. This too was observed in nanoparticles [79], and was described as a discrete spin wave with an anisotropy gap. The application of magnetic fields, although lowering the intensity of this excitation, also seems to move it to higher energies, (as shown in the nanoparticles). The next steps to take in the analysis of this data is to correct for detailed balance (Equation 2.13), and perform a correct background subtraction (large amounts of water in the mesopores create a high background due to incoherent scattering of the ^{1}H nuclei).

These comparisons with nanoparticles are very promising and provide a valuable insight into the reasons for suppression of the Morin transition. Plots of the interaction near the (101) reflection from the nanoparticle study (Figure 4.18(a)) show that the position (ϵ_0) of the inelastic peak increases in energy away from the elastic line with temperature from ≈ 1.03 meV up to 1.27 meV at 300 K. Initial analysis of the peak position in the mesoporous hematite data (just from judging by eye the peak maximum) show that the inelastic peak is at smaller energies, ranging from 0.65 meV to 1.15 meV (superimposed onto Figure 4.18(a)). In the nanoparticle work the energy of the movement in the inelastic peak was related to a coefficient κ_1, which is related to the anisotropy of the [001] direction. This enabled a plot of the anisotropy of the system to be produced (Figure 4.18(b)). This plot shows bulk hematite to undergo a change in sign in anisotropy at the Morin transition (positive for the pure antiferromagnetic phase below T_{M} and negative for the weakly ferromagnetic phase above T_{M}). The nanoparticulate hematite however, which stays in the weakly ferromagnetic state at all times show a negative anisotropy value throughout the temperature range. As the

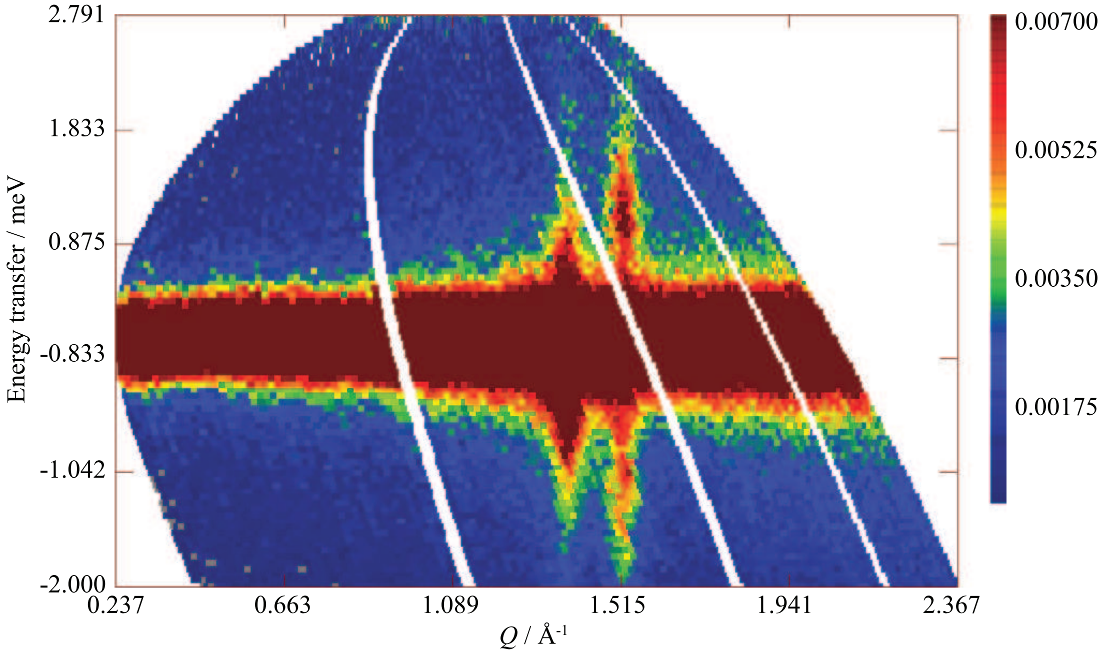

(a) 300 K, 0 T.

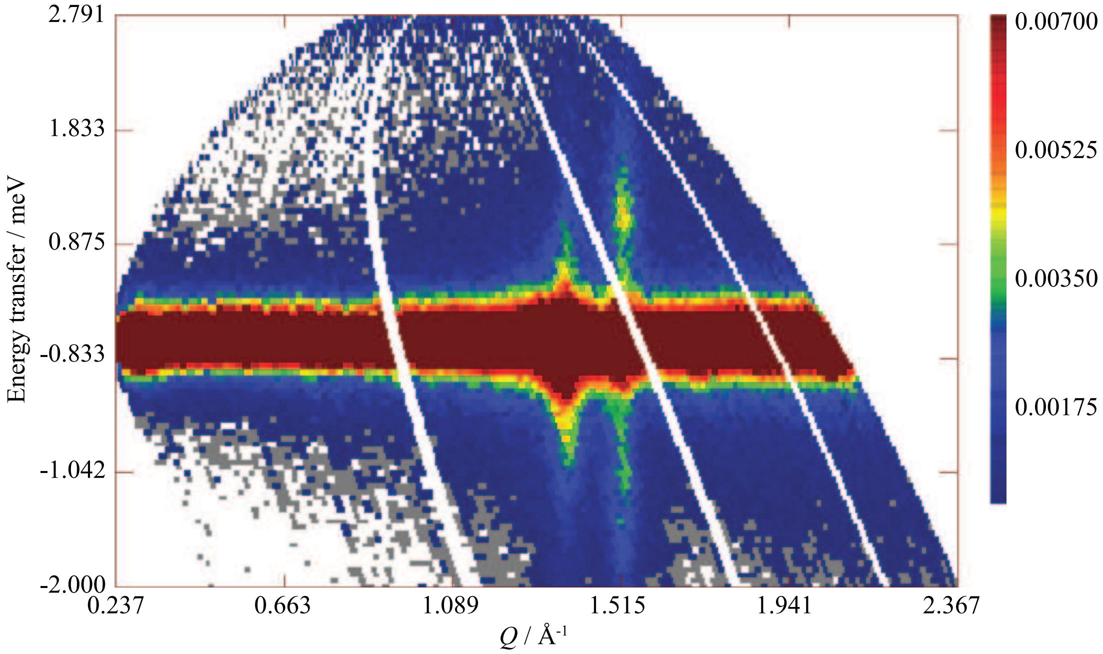

(b) 300 K, 2.5 T.

Figure 4.15: Spectrograms of mesoporous hematite from IN6 taken at 300 K with applied fields of 0 T and 2.5 T.

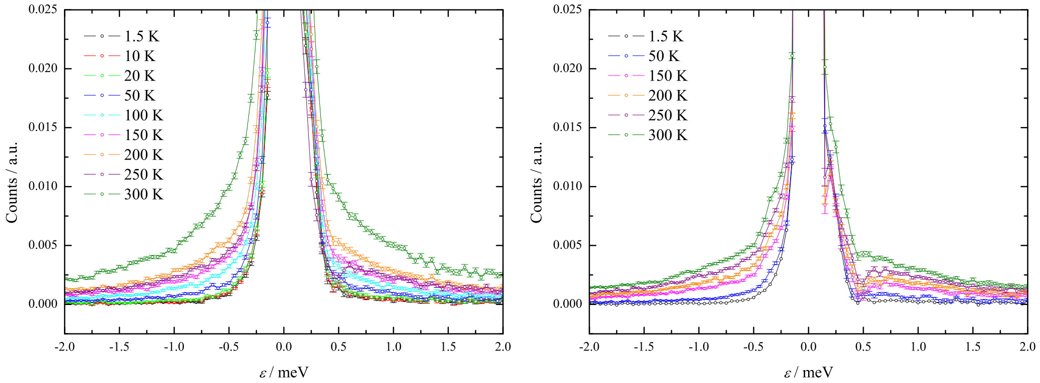

(a) $Q = 1.37\,\text{Å}^{-1}$, $\mathbf{B} = 0\,\text{T}$.

(b) $Q = 1.37\,\text{Å}^{-1}$, $\mathbf{B} = 2.5\,\text{T}$.

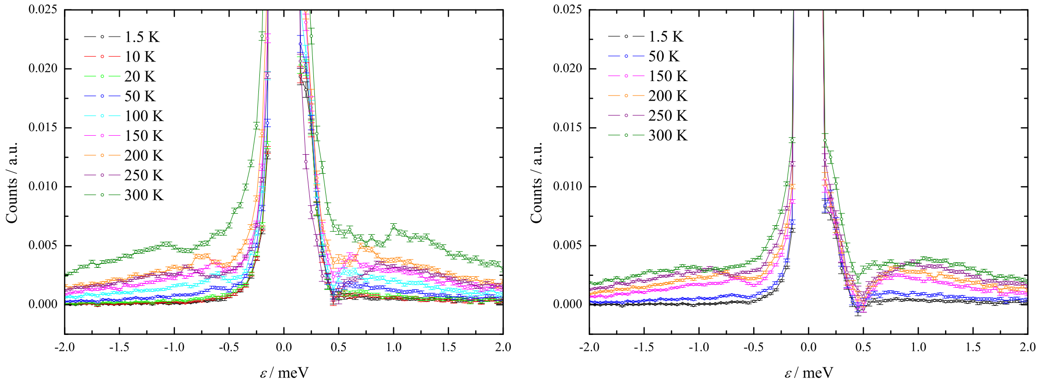

(c) $Q = 1.51\,\text{Å}^{-1}$, $\mathbf{B} = 0\,\text{T}$.

(d) $Q = 1.51\,\text{Å}^{-1}$, $\mathbf{B} = 2.5\,\text{T}$.

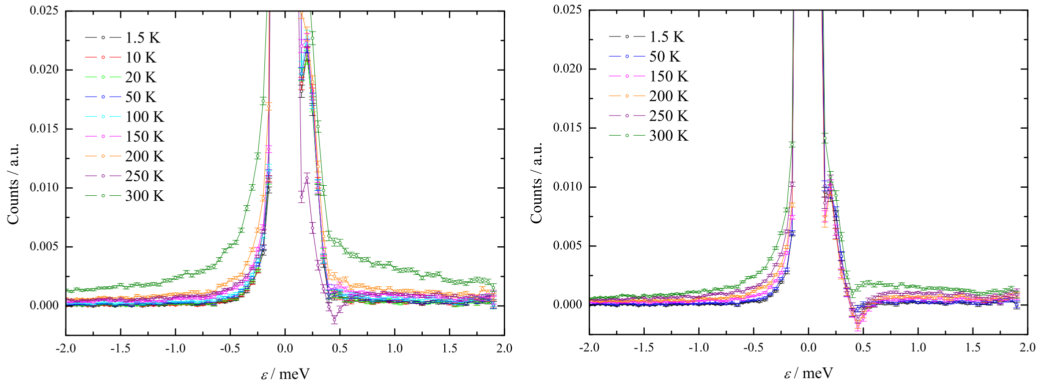

(e) $Q = 1.70\,\text{Å}^{-1}$, $\mathbf{B} = 0\,\text{T}$.

(f) $Q = 1.70\,\text{Å}^{-1}$, $\mathbf{B} = 2.5\,\text{T}$.

Figure 4.16: Q-cuts on the (003), (101), and $(10\bar{2})$ Bragg peaks ($Q = 1.37\,\text{Å}^{-1}$, $1.51\,\text{Å}^{-1}$, and $1.70\,\text{Å}^{-1}$ respectively) of mesoporous hematite from the IN6 spectrometer at 0 T and 2.5 T.

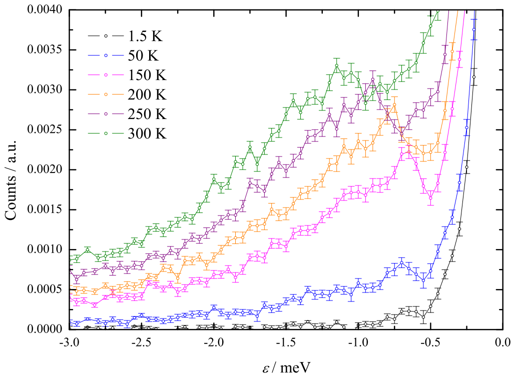

Figure 4.17: Close up of the $Q = 1.51\,\mathring{A}^{-1}$ cut on the anti-Stokes side.

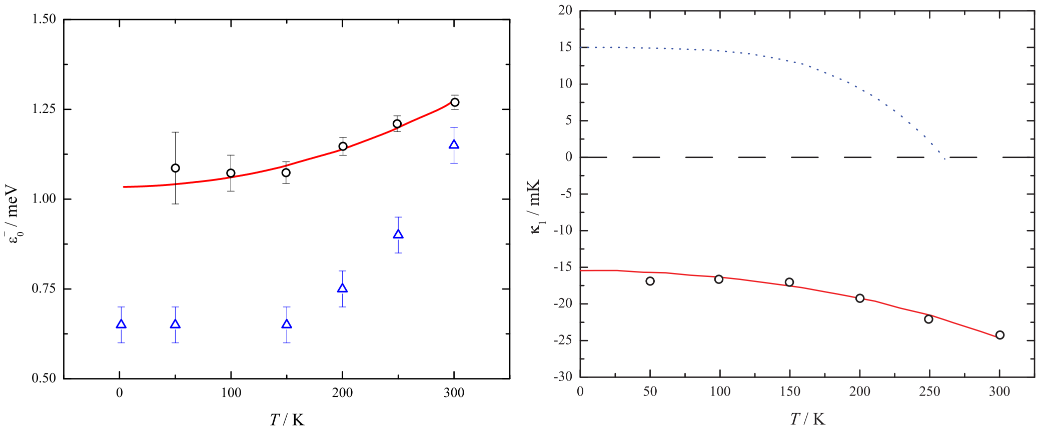

(a) Position of the inelastic peak vs. T.

(b) Temperature dependence of κ_1.

Figure 4.18: Graphs of peak position and magnetic anisotropy term κ_1 (solid line represents nanoparticles, dotted line represents bulk hematite). After reference 79. Initial peak positions from the mesoporous hematite data are shown in (a) with triangles.

size of the nanoparticles decreases (and the surface area increases) the value of κ_1 became increasingly negative. By comparing the energies of the inelastic interaction in the nanoparticle and mesoporous hematite, we can assume that the κ_1 coefficient in mesoporous hematite stays negative throughout the temperature range too, but probably sits closer to zero (the surface area of mesoporous hematite sits between bulk and nanoparticle materials), particularly at very low temperatures.

Instrumental factors such as the shoulder at 0.2 meV to the elastic line for IN6 limit our ability to perform a detailed analysis of the excitations. Further studies with a higher resolution instrument such as IN5 at the ILL would be required for a much more detailed analysis of the dynamics occurring in the mesoporous system.

4.5 Summary

From the variable temperature neutron diffraction of crystalline mesoporous α-Fe_2O_3, we can see that the material does not undergo the first-order spin re-orientation Morin transition even at temperatures as low as 2 K. This is clearly evident from the intensity of the (003) magnetic Bragg peak intensity at low temperatures. Bulk hematite undergoes the transition from the weak ferromagnetic state to the pure antiferromagnetic state upon cooling through 259.1(2) K. It the latter state the magnetic moments are canted out of the hexagonal c-axis at an angle of 10.7(2)°. Above the Morin transition in both the bulk and crystalline hematite samples, the tilting angle within the hexagonal ab plane responsible for the weak ferromagnetism has been calculated by combining magnetic hysteresis and Rietveld refinement data. These show the mesoporous material to be a harder magnet, with a tilt angle of 0.112(4)° compared to 0.0550(19)° in bulk material (both at 300 K). There is a clear breakdown in long range crystallographic and magnetic order within the mesoporous sample, as illustrated by significant Bragg peak broadening. However magnetic ordering can be seen to increase significantly upon cooling within the mesoporous samples as demonstrated by a sizeable reduction in the measured paramagnetic background.

Inelastic neutron scattering measurements on the crystalline mesoporous sample show significant similarities to measurements taken upon nanoparticulate hematite samples. This provides information on the fine balance of energies in the system being studied and how they can be affected by increases in surface area and local disorder. Further studies of the inelastic interactions are therefore warranted.

Chapter 5

Mesoporous eskolaite, Cr_2O_3

Eskolaite, Cr_2O_3 has the same corundum structure as α-Fe_2O_3. However the magnetic structure within this material is somewhat different to hematite. Below the Néel temperature (T_N) of approximately 315 K to 320 K, it adopts an antiferromagnetic structure, this has a magnetic propagation vector $k = (0, 0, 0)$, in reference to the crystallographic unit cell, (infact, the magnetic unit cell is half the size as the structural cell). The ordering of the moments (Figure 5.1) is of the form $+ - +-$ along the [003] axis (c axis) [82, 83]. Mesoporous Cr_2O_3 was prepared by Dr Calum Dickinson (School of Chemistry, University of St Andrews) using the KIT-6 silica template [84]. The synthesis is briefly summarised here.

> Chromium (III) nitrate nonahydrate (in ethanol) was allowed to infuse into a powder sample of mesoporous silica, KIT-6 [7]. Once dried, this was then heated to convert the chromium nitrate to chromium oxide. The silica template was then removed by dissolving in aqueous hydrofluoric acid. This left behind a 3 dimensional mesoporous Cr_2O_3 structure, based upon the pore structure of the KIT-6 silica template. The mesoporous sample has a specific surface area and pore volume of $74\,m^2\,g^{-1}$ and $0.456\,cm^3\,g^{-1}$ respectively. The pore size is distributed over a large range, up to 200 Å, with pores believed to be centred at 40 Å and 90 Å [85]. Wall thickness within the mesoporous sample is approximately 80 Å.

5.1 Magnetic property measurements

Magnetic measurements on a polycrystalline sample of mesoporous Cr_2O_3 were performed using a MPMS Quantum Design SQUID magnetometer. Samples (held in eicosane wax in gelatin capsules) were initially cooled to 2 K in zero applied field, then measurements were taken upon heating in 100 Oe. A second set of measurements were then obtained by cooling the sample in 100 Oe (Figure 5.2). The response of the material to changing magnetic fields at a constant temperature was also measured at 10 K, 200 K and 300 K (Figure 5.3).

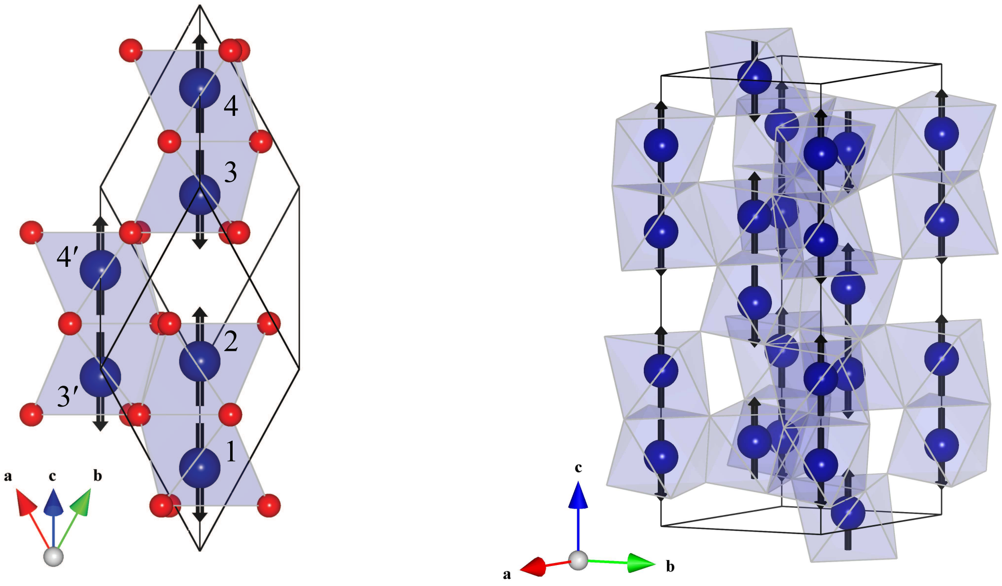

(a) Rhombohedral. (b) Hexagonal.

Figure 5.1: The rhombohedral (fractional co-ordinates between; $x = 0$ & 1; $y = -0.5$ & 1; and $z = 0$ & 1) and hexagonal unit cell of Cr_2O_3 showing the magnetic moment arrangement.

The magnetic susceptibility of bulk Cr_2O_3 (Figure 5.2(a)) is typical of an antiferromagnetic material. The plot of inverse molar susceptibility (Figure 5.2(b)) shows a clear transition occurring at 310 K to 320 K. This is very close to the expected Néel transition [82, 86], and can be assumed to be the ordering temperature for this particular sample. The susceptibility of the mesoporous form, however displays a very different profile. Analysis of the ZFC-FC curves shows a maximum in ZFC susceptibility at 77 K. The ZFC and FC data sets differ (from a difference plot not shown here) in the entire temperature range studied, suggesting that the bifurcation point occurs above 330 K. This suggests that there is a small amount of ferromagnetic component present in the sample. This could either be due to uncompensated surface spins on the high surface area of the mesoporous sample, or the presence of a small amount of ferromagnetic CrO_2, which has a Curie temperature (T_C) of ≈ 386 K to 394 K [87, 88]. The inverse susceptibility profile (Figure 5.2(d)) does not provide any information on what the ordering temperature may be. Magnetic hysteresis measurements show that at 300 K the sample is almost paramagnetic (Figure 5.3(a)). As the temperature is cooled down to 10 K, it can be seen that hysteresis sets in (Figure 5.3(c)). A close examination of the hysteretic parts of the data (Figure 5.3(d)) show that the feature is symmetric around the field axis and hysteresis only occurs at low temperatures, this points towards

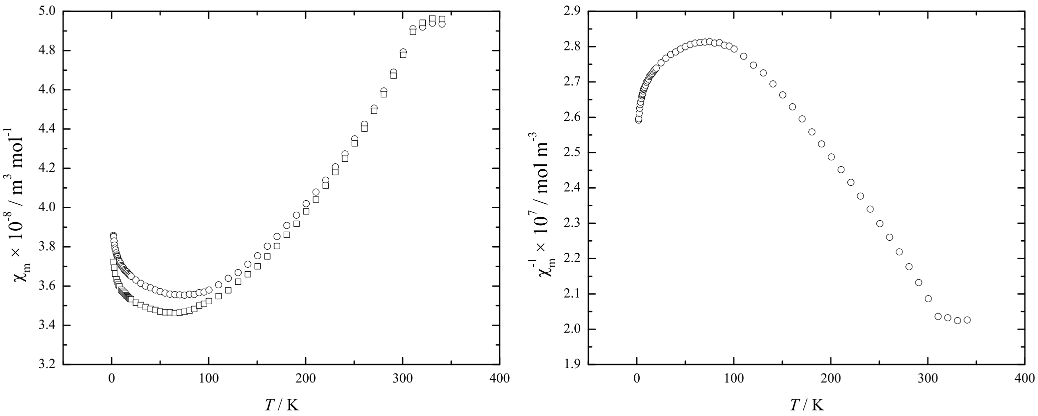

(a) Bulk Cr_2O_3 molar susceptibility.

(b) Bulk Cr_2O_3 inverse molar susceptibility.

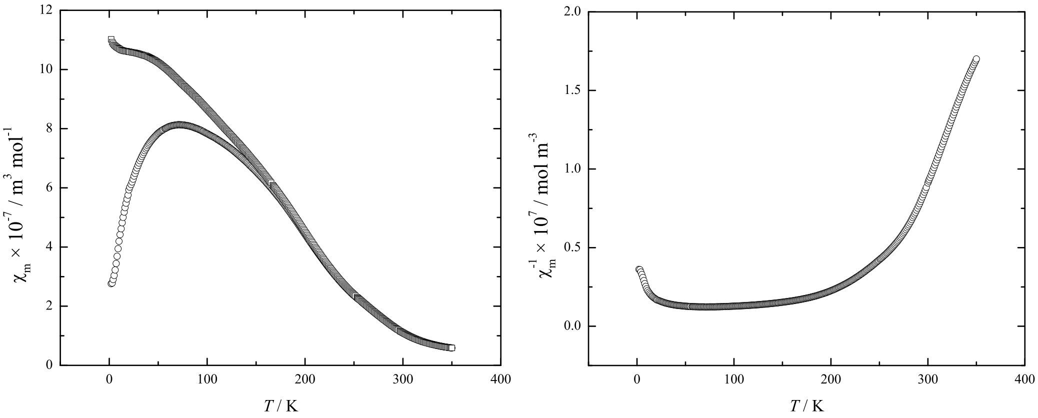

(c) Mesoporous Cr_2O_3 molar susceptibility.

(d) Mesoporous Cr_2O_3 inverse molar susceptibility.

Figure 5.2: Magnetic susceptibility measurements (ZFC, ○ and FC, □) of bulk and mesoporous Cr_2O_3.

the exclusion of any ferromagnetic components in the sample, such as CrO_2, which would cause hysteresis at higher temperatures. It can therefore be assumed that the ferromagnetic component is due to uncompensated surface spins on the mesoporous Cr_2O_3.

5.2 NPD measurements

Measurements were performed upon the time of flight spectrometer/diffractometer,OSIRIS[58] (standard orange cryostat) and the GEM diffractometer[59] (closed cycle refrigerator) at ISIS from 2 K to 315 K on a bulk eskolaite reference sample and a sample of the crystalline mesoporous Cr_2O_3.

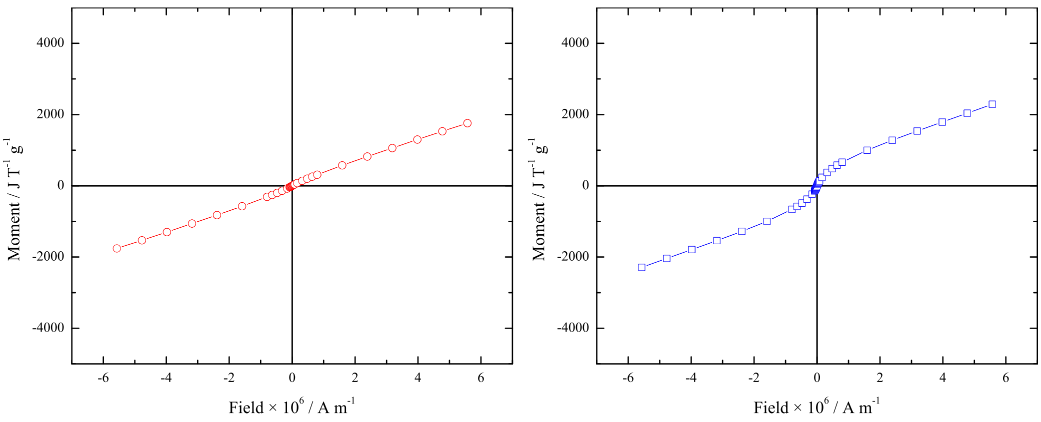

(a) 300 K.

(b) 200 K.

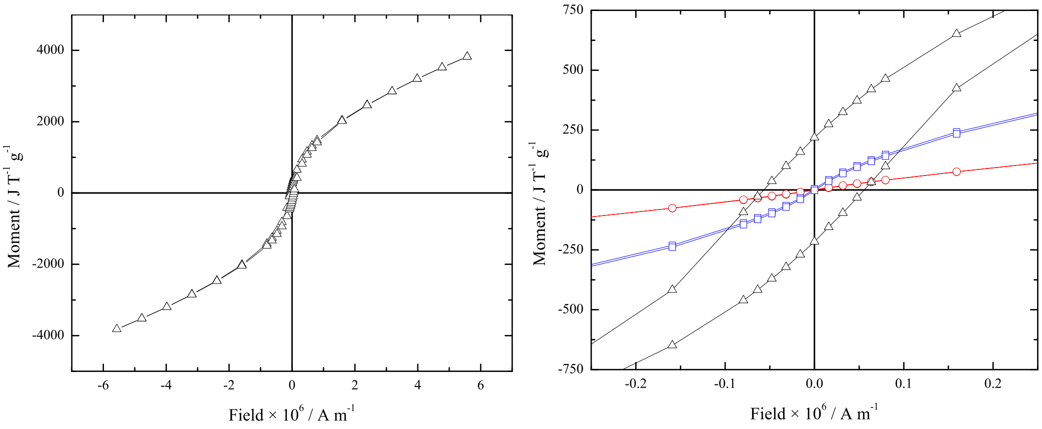

(c) 10 K.

(d) Expanded low field region.

Figure 5.3: Magnetic hysteresis curves of mesoporous Cr_2O_3.

Rietveld refinements of the NPD data using GSAS and EXPGUI were carried out as follows. A $R\bar{3}c$ (hexagonal setting) eskolaite model was fitted to the data for the crystallographic unit cell, with Cr^{3+} and O^{2-} atoms on the 12c and 18e Wyckoff sites respectively. A second phase with a magnetic space group[1] $R\bar{3}'c'$ with a Cr^{3+} ion at the same position as in the crystallographic phase was added for the refinement of the magnetic structure, following the two-phase fit with magnetic symmetry approach summarised by Cui et al. [60]. The magnetic form factor used for the Cr^{3+} ion was that programmed into GSAS, the values of which are tabulated in reference 90. This symmetry allows a component of magnetic moment in the hexagonal [003] direction. Refinement of the model was then carried out, typically using a 8 point shifted Chebyschev background polynomial for each diffraction pattern. Typical patterns observed and their Rietveld fits are shown in Figure 5.5. Refined lattice parameters, atomic co-ordinates, isotropic thermal parameters, and magnetic moments from the various instruments and samples used are shown in Table 5.1, Table 5.2, and Table 5.3.

5.3 Discussion

Comparison between the four data sets (bulk and mesoporous samples measured on GEM and OSIRIS) is rather complex due to the different instrument designs. Lattice parameters are most accurately determined with the GEM diffractometer, whereas the OSIRIS instrument has several problems when it comes to determination of lattice

---

[1] Magnetic space groups were first proposed in 1951 by A.V. Shubnikov [89]. By combining an anti-identity operation $1'$ with normal symmetry elements, we obtain a new symmetry operation, the anti-operation. The new operation has identical properties to the original with the addition of spin flip. This is shown in Figure 5.4, where the effects of having a reflection and anti- reflection operation are shown upon a magnetic moment and its associated current loop (the current loop must always rotate anticlockwise around an upward pointing moment).

Normal operations act upon the current loop, whereas the anti operation will flip the moment, causing the current loop to be reversed. The $\bar{3}'$ causes an anti- threefold rotation inversion and the c' an anti-c-glide.

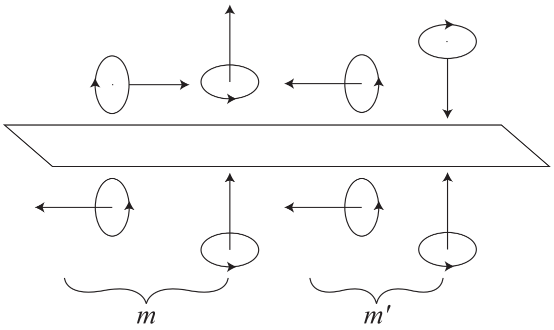

Figure 5.4: Effect of a reflection operation, m and the reflection anti-operation, m' upon a magnetic moment and current loop.

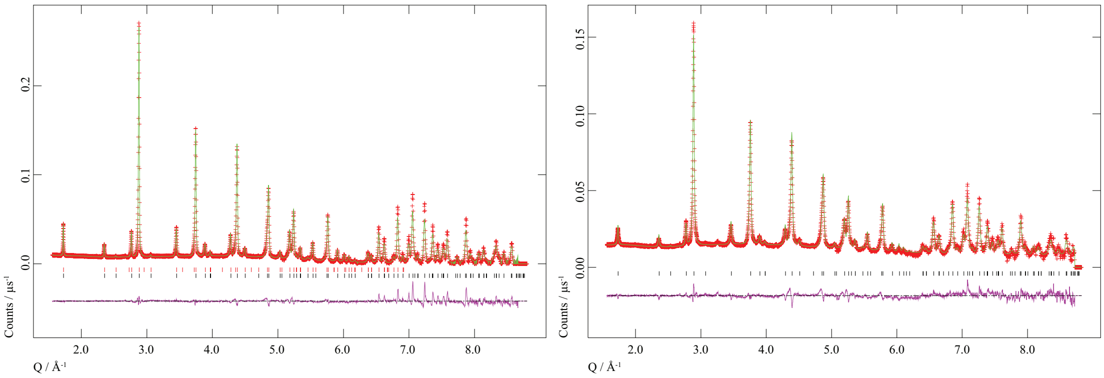

(a) Bulk Cr_2O_3 at 315 K.

(d) Mesoporous Cr_2O_3 at 315 K.

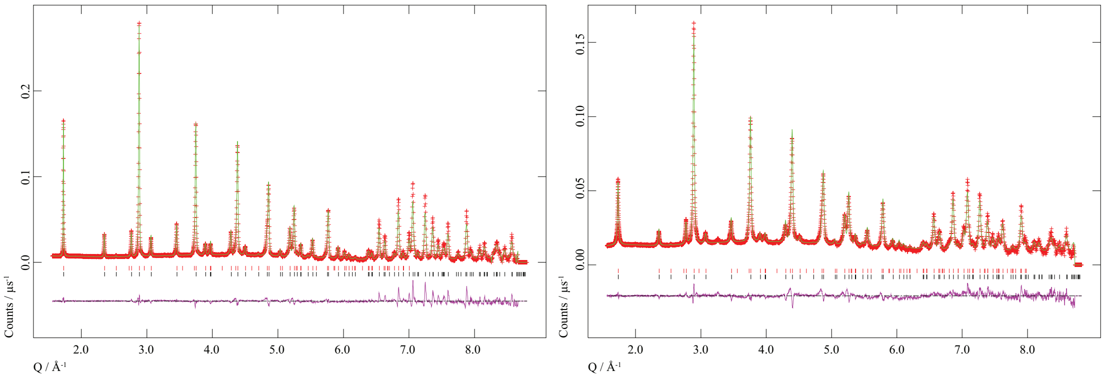

(b) Bulk Cr_2O_3 at 188 K.

(e) Mesoporous Cr_2O_3 at 195 K.

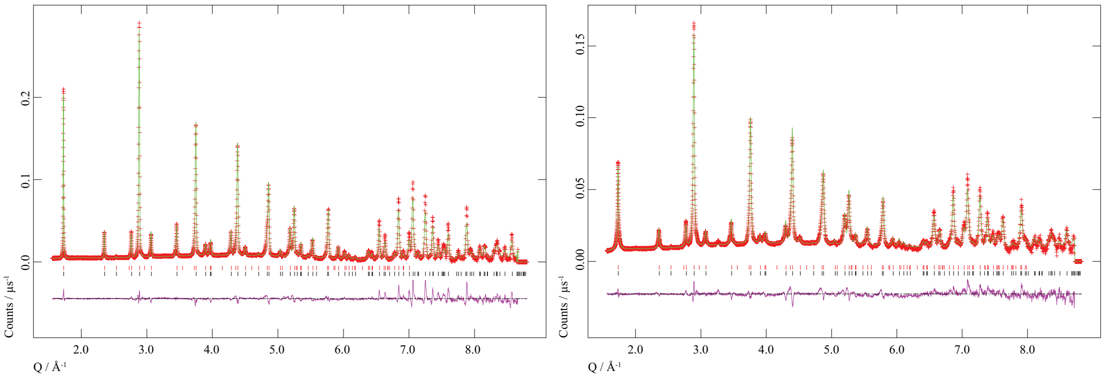

(c) Bulk Cr_2O_3 at 2 K.

(f) Mesoporous Cr_2O_3 at 2 K.

Figure 5.5: Powder diffraction patterns and Rietveld refinement of bulk ((a)–(c)) and mesoporous ((d)–(e)) Cr_2O_3 from the OSIRIS diffractometer.

T / K	a / Å	c / Å	Cr^{3+} z coordinate	O^{2-} x coordinate
300[a]	4.95721(3)	13.59170(10)	0.34734(3)	0.30569(3)
315	4.95825(3)	13.59224(15)	0.34824(9)	0.30565(13)
300	4.95688(3)	13.59349(15)	0.34823(8)	0.30585(13)
284	4.95555(3)	13.59450(15)	0.34813(8)	0.30598(13)
265	4.95398(3)	13.59580(15)	0.34816(8)	0.30624(13)
229	4.95189(3)	13.59721(15)	0.34802(8)	0.30631(13)
188	4.95027(3)	13.59807(15)	0.34762(8)	0.30647(13)
135	4.94890(3)	13.59905(15)	0.34759(7)	0.30665(14)
75	4.94847(3)	13.59932(16)	0.34725(8)	0.30670(14)
2	4.94844(3)	13.59952(16)	0.34721(8)	0.30663(14)

T / K	Cr^{3+}	O^{2-}	m_z / μ_B	$R_{(\mathrm{wp})}$	$R_{(\mathrm{p})}$
	U_{iso} / $\times 10^2$ Å^2				
300[a]	0.263(4)	0.372(4)	1.056(7)	0.0356	0.0376
315	0.51(3)	0.46(2)	0.51(3)	0.0510	0.0503
300	0.55(3)	0.50(2)	1.157(9)	0.0506	0.0511
284	0.51(3)	0.45(2)	1.511(8)	0.0529	0.0534
265	0.42(3)	0.38(2)	1.769(7)	0.0525	0.0531
229	0.36(3)	0.35(2)	2.069(7)	0.0522	0.0527
188	0.34(3)	0.31(2)	2.328(7)	0.0531	0.0525
135	0.29(3)	0.27(2)	2.504(7)	0.0551	0.0554
75	0.31(3)	0.28(2)	2.625(8)	0.0585	0.0594
2	0.29(3)	0.26(2)	2.652(8)	0.0603	0.0617

[a] Data from the GEM diffractometer.

Table 5.1: Rietveld refinement parameters for bulk Cr_2O_3 from the OSIRIS diffractometer.

T / K	a / Å	c / Å	Cr^{3+} z coordinate	O^{2-} x coordinate
300	4.964737(9)	13.5917(3)	0.34640(9)	0.30786(12)
200	4.958340(11)	13.5975(3)	0.34632(10)	0.30834(14)
100	4.956648(11)	13.5969(3)	0.34627(11)	0.30846(15)
10	4.955794(9)	13.5991(2)	0.34647(8)	0.30845(11)

T / K	Cr^{3+}	O^{2-}	m_z / μ_B	$R_{(\mathrm{wp})}$	$R_{(\mathrm{p})}$
	U_{iso} / $\times 10^2$ Å^2				
300	0.363(15)	0.487(10)	0.99(5)	0.0362	0.0294
200	0.288(17)	0.382(12)	1.97(3)	0.0448	0.0411
100	0.205(16)	0.384(12)	2.25(2)	0.0478	0.0433
10	0.220(13)	0.366(9)	2.312(18)	0.0378	0.0313

Table 5.2: Rietveld refinement parameters for mesoporous Cr_2O_3 from the GEM diffractometer.

T / K	a / Å	c / Å	Cr^{3+} z coordinate	O^{2-} x coordinate
315	4.95441(5)	13.58346(3)	0.34738(13)	0.31018(2)
303	4.95435(6)	13.58293(3)	0.34713(13)	0.30910(2)
289	4.95314(6)	13.58395(3)	0.34692(13)	0.30937(2)
273	4.95204(5)	13.58442(3)	0.34699(13)	0.30953(2)
255	4.95088(5)	13.58508(3)	0.34697(12)	0.30953(2)
244	4.95016(5)	13.58525(3)	0.34673(13)	0.30958(2)
195	4.94786(5)	13.58616(3)	0.34689(12)	0.31006(2)
150	4.94625(5)	13.58754(3)	0.34693(12)	0.31058(2)
75	4.94509(5)	13.58744(3)	0.34717(11)	0.31095(2)
2	4.94535(5)	13.58836(3)	0.34723(11)	0.31094(2)

T / K	Cr^{3+}	O^{2-}	m_z / μ_B	$R_{(wp)}$	$R_{(p)}$
	U_{iso} / × 10^2 Å^2 [b]				
315	0.36	0.49	—	0.0412	0.0336
303	0.36	0.49	0.54(6)	0.0410	0.0331
289	0.36	0.49	0.90(2)	0.0401	0.0317
273	0.34	0.46	1.204(16)	0.0419	0.0331
255	0.33	0.43	1.402(14)	0.0403	0.0323
244	0.33	0.43	1.542(13)	0.0404	0.0323
195	0.29	0.38	1.890(11)	0.0418	0.0336
150	0.22	0.38	2.082(10)	0.0461	0.0380
75	0.22	0.38	2.250(10)	0.0372	0.0297
2	0.22	0.37	2.313(9)	0.0505	0.0424

[b] Isotropic thermal parameters not refined.

Table 5.3: Rietveld refinement parameters for mesoporous Cr_2O_3 from the OSIRIS diffractometer.

parameters: OSIRIS diffraction patterns are constructed from several sections for different chopper settings, and errors could occur in binning the data together; the sample is held on the end of a very long cryo-stick, so errors in sample displacement could be significant. This will be a particular issue where the Bragg peaks are considerably broadened, as is the case with the mesoporous sample and systematic differences will occur. We can therefore assume that the lattice parameters obtained from the GEM diffractometer are more reliable; however to observe trends in lattice parameter variation the OSIRIS data will be used, due to a greater number of data points.

Comparison of the lattice parameters between bulk and mesoporous Cr_2O_3 refined using GEM data show that the mesoporous sample has a slightly expanded a parameter, whereas the c values are identical. This expanded lattice parameter in a can be seen in all the datasets obtained at various temperatures by comparing bulk OSIRIS data with mesoporous GEM data. Both bulk and mesoporous samples show that upon cooling, a contracts and c expands slightly. This trend is shown in Figure 5.6. The a and c axes change by approximately the same amount in both the mesoporous and bulk Cr_2O_3 samples. The expansion in c and contraction in a upon cooling is expected [91, 92], as more and more magnetic moments align antiferromagnetically along the [003] (c) axis (Figure 5.1), creating magnetostatic repulsions between the moments in c and attractions in a. The increase in magnetic moment upon cooling is shown in Figure 5.7. The values calculated from both the GEM and OSIRIS data sets for the mesoporous sample agree closely with each other, providing a numerical value of $\approx 2.3\,\mu_B$. This is approximately 15 % lower than the value calculated from bulk eskolaite data ($\approx 2.7\,\mu_B$) from the OSIRIS instrument. This suggests that there is a considerable amount of magnetic disorder within the mesoporous sample, which is illustrated by a higher (paramagnetic) background in the diffraction patterns in Figure 5.5. The value obtained from bulk eskolaite, ($\approx 2.7\,\mu_B$) agrees with values obtained in early studies of eskolaite [83], and is quite close to the expected $3.0\,\mu_B$ for the quantised z-component of the spin only moment of a $3d^3$ Cr^{3+} ion (term symbol, $^4F_{3/2}$). The slightly lower observed moment is due to a small amount of Cr−O π^* type bonding due to charge back transfer, $2p(O^{2-}) \longrightarrow 3\,d(Cr^{3+})$. The effective charges on the Cr^{3+} ions are therefore reduced, producing a lower magnetic moment. This has been observed with spherical neutron polarimetry in the particular case of Cr_2O_3 [66].

The magnetic ordering of Cr_2O_3 will depend upon the exchange interactions between the Cr^{3+} ions. The four principal exchange interactions (from inelastic scattering [93, 94]) between cations 1–2, 2–3′, 3–4′, and 2–4′ are illustrated in Figure 5.1(a), and summarised in Table 5.4. Typically $J_1 \approx 2J_2 \approx 25J_3 \gg J_4$. Graphs of how these interactions vary with temperature can be seen in Figure 5.8. Generally the angles and lengths of the exchange interactions follow the same trends in the bulk and mesoporous

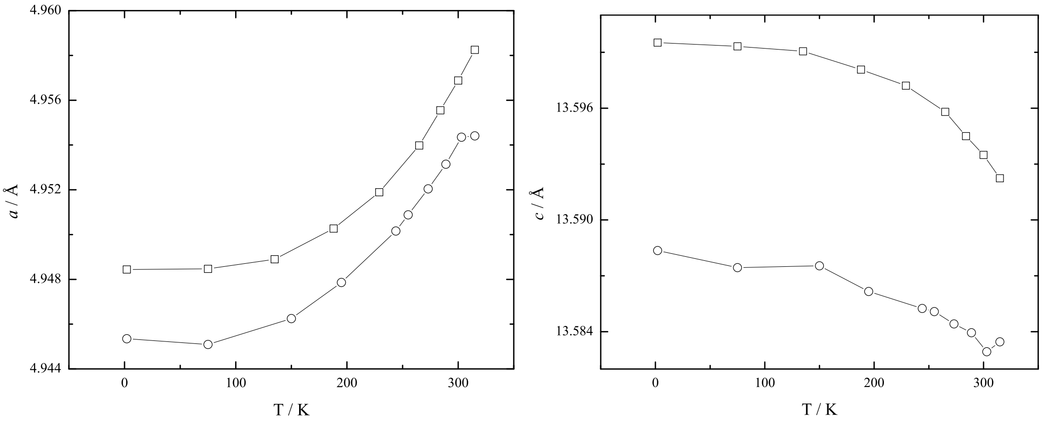

(a) Lattice parameter a.

(b) Lattice parameter c.

Figure 5.6: Plots of refined lattice parameters of mesoporous (circles) and bulk (squares) Cr_2O_3 determined from OSIRIS. Error bars are of a size smaller than the data markers. Note the discussion in the text about the reliability of the relative values between samples.

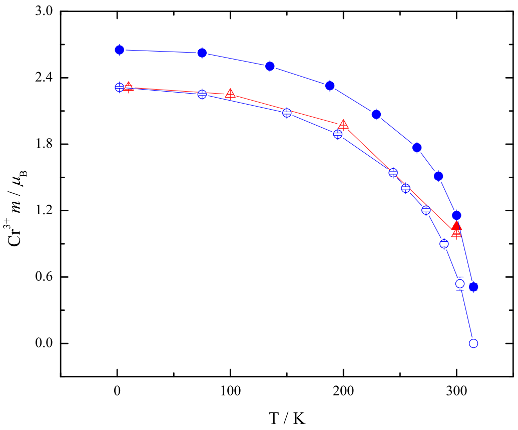

Figure 5.7: Refined magnetic moment of Cr_2O_3 samples. OSIRIS values are shown with blue open (mesoporous) and filled (bulk) circles, GEM values are shown with red open (mesoporous) and filled (bulk) triangles.

materials, the obvious exception being J_4. Here, the exchange angle increases for bulk Cr_2O_3, but decreases in the case of mesoporous Cr_2O_3. The exchange interactions J_1 and J_2 occur between face and edge sharing octahedra, this allows direct exchange (antiferromagnetic) between the cations [95]. The relative magnitude of J_1 and J_2 compared to $J_{\geq 3}$ suggest that this direct exchange is of the most importance in Cr_2O_3. The Cr−Cr distances for J_1 and J_2 in the bulk material decrease with temperature, increasing orbital overlap and therefore making the anitferromagnetic interactions stronger (the observed increase in ordered magnetic moment is a consequence of this). In the mesoporous material the Cr−Cr distance for J_1 does not change significantly (over the entire temperature range), but the J_2 distance follows the same trend as in the bulk material. Overall this would increase the antiferromagnetic ordering, but not as significantly as in the bulk material. The Cr−Cr distances for the J_3 and J_4 exchange interactions are too far apart for direct exchange and orbital overlap. These therefore follow the Goodenough-Kanamori [96] rules for super-exchange, and the Cr−O−Cr angle is important. As there are only 3 t_{2g} electrons present on each Cr^{3+} ion, antiferromagnetic exchange will be greatest at 180°, whereas ferromagnetic exchange will be favoured at 90°. However the exact nature of these rules are not rigidly set in stone, particularly for angles in the 120° to 140° region. The J_3 angle increases by approximately the same amount in both the mesoporous and bulk samples. The J_4 angle seems to increase in the bulk sample, but decrease in the mesoporous sample. The reasons for this discrepancy are at this time unclear. However, it is important to bear in mind the mentioned earlier issues with determining the lattice parameters from the OSIRIS data, and how this will have a knock-on affect on the absolute values of angles and distances, although the relative trends in these parameters are useful to observe.

Close examination of the unit cell dimensions and exchange parameters reveals an anomaly in the mesoporous data between 303 K and 315 K. The abrupt change in a and c is ascribed to the Néel transition, and the effect of magnetic ordering upon the lattice parameters [92, 97, 98]. We can therefore assume that the Néel transition is between 315 K and 303 K for the mesoporous sample, and just above 315 K for the bulk material. Pressure studies on bulk eskolaite have noticed that an increase in hydrostatic pressure reduces not only the lattice parameters, but also T_{N} at a rate of $dT_{\mathrm{N}}/dP = -16\,\mathrm{K\,GPa^{-1}}$ [99]. This agrees with our findings on the unit cell parameters of mesoporous eskolaite, which are smaller than bulk material, in effect an imaginary pressure is present in the mesoporous sample.

The diffraction patterns of mesoporous eskolaite show clear Scherrer broadening of the Bragg peaks. This could be due to disruption of the repetition of the crystallographic and magnetic cell over long ranges by the meso-structure (as observed with mesoporous hematite [57]). Using TOF profile 2 in GSAS (an incorporation of the Ikeda-Carpenter

Exchange interaction	Spin (ion) pair	Neighbours	Typical Cr−Cr distance^c/ Å	Typical Cr−O−Cr angle^c/ °
J_1	$+-(1\text{–}2)$	1	2.66	82.4
J_2	$+-(2\text{–}3')$	3	2.89	93.2
J_3	$+-(3\text{–}4')$	3	3.41	121.1
J_4	$++(2\text{–}4')$	6	3.66	133.0

^{c} Values taken from bulk Cr_2O_3 measured at 1.9 K on OSIRIS.

Table 5.4: The principle exchange pathways in Cr_2O_3.

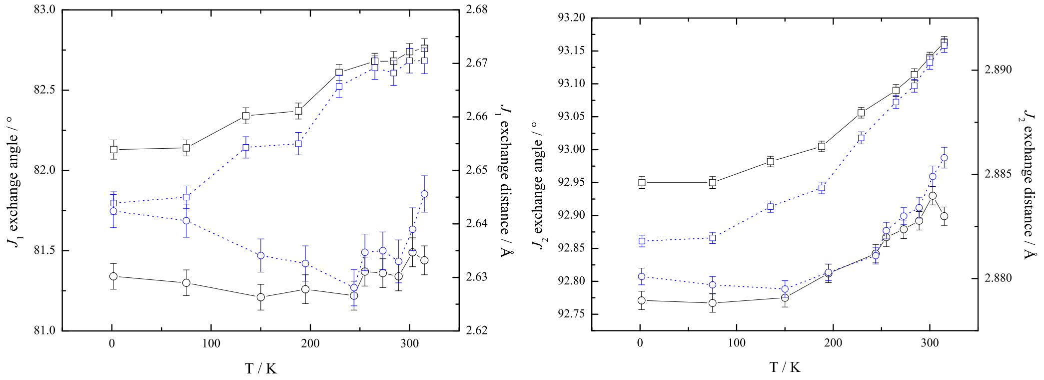

(a) J_1. (b) J_2.

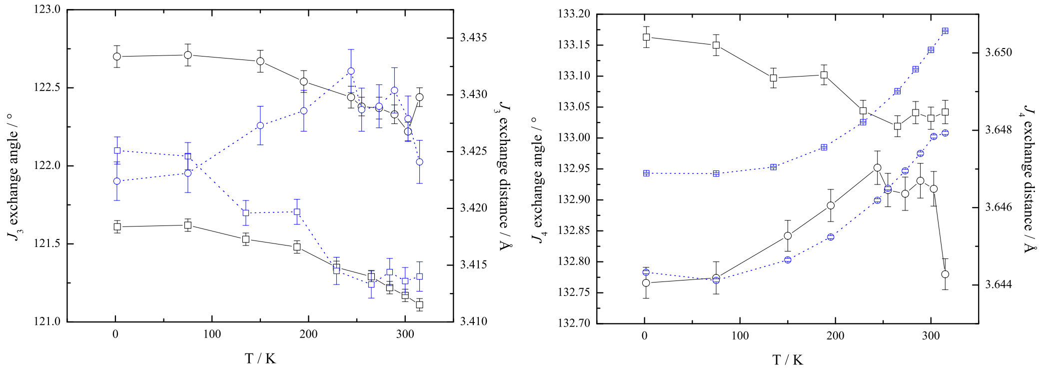

(c) J_3. (d) J_4.

Figure 5.8: Plots of variation with temperature of the exchange interaction angles (black solid lines) and distances (blue dotted lines) for bulk (squares)and mesoporous (circles) Cr_2O_3.

function [72] with a pseudo-Voigt linear combination of a Lorentzian and a Gaussian function) the γ_2 variables of the Lorentzian part of the peak profile were allowed to refine independently between the nuclear and magnetic phases, whilst the Gaussian parts were constrained between phases. This enables an estimation of correlation lengths in the material, using Equation 5.1 where p is the correlation length (Å), C is the diffractometer constant DIFC, characteristic of the particular geometry of the instrument used, and K is the Scherrer constant (≈ 0.9).

$$p = \frac{\mathrm{CK}}{\gamma_2} \tag{5.1}$$

Both nuclear and magnetic correlation lengths have been calculated for mesoporous Cr_2O_3, (Table 5.5). In the case of the GEM data, correlation lengths were calculated from a similar data range of diffraction pattern as to what was collected from the OSIRIS detector (bank 3 of GEM; $1.2\,\text{Å}^{-1} < Q < 17.5\,\text{Å}^{-1}$). Good agreement can be seen in the calculated correlation lengths between the two diffractometers used. Both the nuclear and magnetic correlation length in mesoporous Cr_2O_3 are shown to be approximately 400 Å at base temperature (OSIRIS data). A similar approach was applied to the bulk Cr_2O_3 data, where correlation lengths of 1200 Å to 1500 Å were observed at the temperatures studied for both the nuclear and magnetic contributions. These *estimates* show that the magnetic and nuclear correlation lengths are of similar magnitudes; however as all the magnetic Bragg peaks in the diffraction patterns also have a structural part, it is difficult to deconvolute the different contributions. The particle sizes of the mesoporous eskolaite have been estimated from TEM imaging at 100 Å to 2000 Å [84]. This is much greater than the estimated correlation lengths. However, from the unit cell size of the KIT-6 template (210 Å) we can see that the correlation extends over an average of ≈ 2 unit cells.

5.4 Summary

Magnetic property measurements and neutron powder diffraction of mesoporous eskolaite have provided valuable information on the magnetic properties of this material. DC susceptibility measurements were rather inconclusive due to the drowning out of signal that is of interest by ferromagnetic components from uncompensated surface spins. NPD shows that the magnetic structure is the same as that of bulk eskolaite, albeit with a lower magnetic moment (again due to random orientation of surface spins). The Néel temperature of mesoporous material ($303\text{ K} < T_\mathrm{N} < 315\,\text{K}$) can be seen to be lower than that of bulk material ($315\,\text{K} < T_\mathrm{N} < 320\,\text{K}$) from the anomalies in unit

OSIRIS data			GEM data[d]		
T / K	p_{nuc} / Å	p_{mag} / Å	T / K	p_{nuc} / Å	p_{mag} / Å
315	303(7)	—			
303	392(3)	388(3)	300	430(40)	180(30)
289	295(5)	130(40)			
273	397(3)	387(3)			
255	296(4)	310(20)			
244	394(3)	384(3)			
195	293(4)	297(11)	200	520(70)	280(20)
150	401(3)	391(3)			
75	290(3)	301(8)	100	450(50)	290(20)
2	393(3)	392(3)	10	480(40)	300(10)

[d] Values calculated from profile co-efficients from bank 3.

Table 5.5: Estimated nuclear and magnetic correlation lengths in mesoporous Cr_2O_3.

cell parameters. The refined magnetic moment in the bulk material ($\approx 2.7\,\mu_{\mathrm{B}}$) is close to the expected figure. The mesoporous sample however has a much lower effective magnetic moment per Cr^{3+} ion of $\approx 2.3\,\mu_{\mathrm{B}}$. This is probably due to the average moment being lowered by surface disorder and uncompensated moments not aligning fully antiferromagnetically, and therefore not contributing fully to the magnetic Bragg reflections. Comparison of the mesoporous GEM data to bulk GEM data (300 K) shows that the mesoporous material is minimally larger (0.15 %) in the a axis, but has no difference in the c axis. This difference can probably be attributed to the mesostructure breaking down the long range crystallographic order (as shown by the short correlation lengths) and reducing the overall lattice energy, so the cell can expand ever so slightly.

Chapter 6

Mesoporous cobalt oxide, Co_3O_4

Mesoporous samples of Co_3O_4 were studied with magnetic susceptibility measurements and NPD. These samples were prepared by templating with 2 different cubic mesoporous silica forms; KIT-6 ($Ia\bar{3}d$) [7], and SBA-16, a body centred cubic (bcc) mesoporous structure ($Im\bar{3}m$) composed of nanospheres connected by small pores [5] (Figure 6.1). The samples were prepared by Dr Calum Dickinson and Mr Wenbo Yue (School of Chemistry, University of St Andrews), and compared to bulk Co_3O_4 by measuring magnetic properties, using SQUID magnetometry and NPD. The surface properties of each material are summarised in Table 6.1.

Mesoporous Co_3O_4 prepared with KIT-6 was prepared in the following way [84].

> 0.50 g of cobalt nitrate hexahydrate ($Co(NO_3)_3 \cdot 6\,H_2O$) was dissolved in $6 \cdot 5$ g ethanol and stirred with 0.15 g of KIT-6 for 2 hours. The ethanol was then evaporated at $\approx$ 40 °C, allowing the metal nitrate to be drawn into the pores by capillary action. The sample was then heated at a rate of 2 °C min^{-1} up to 550 °C and held at constant temperature for 5 hours to allow thermal decomposition of the cobalt nitrate to cobalt oxide within the KIT-6 channels. The KIT-6 silica framework was then removed by dissolving it in aqueous 10 % wt HF. The solution was then centrifuged and washed three times with water (decanting off the clear solution). The final product, mesoporous Co_3O_4-KIT-6 has a surface area of 92 $\mathrm{m}^2\,\mathrm{g}^{-1}$ and a PSD centred at 40 Å and 90 Å. XRPD patterns show the material to have the same space group as bulk Co_3O_4, $Fd\bar{3}m$.

Mesoporous Co_3O_4 prepared with SBA-16 was prepared using the following steps, (Appendix C) [24].

> 0.35 g of $Co(NO_3)_3 \cdot 6\,H_2O$ was mixed with 0.15 g of SBA-16 and ground together lightly. The powder was then heated at a rate of 1 °C min^{-1} up to 500 °C. This allowed the cobalt (III) nitrate to melt (m.p. of 55 °C) before

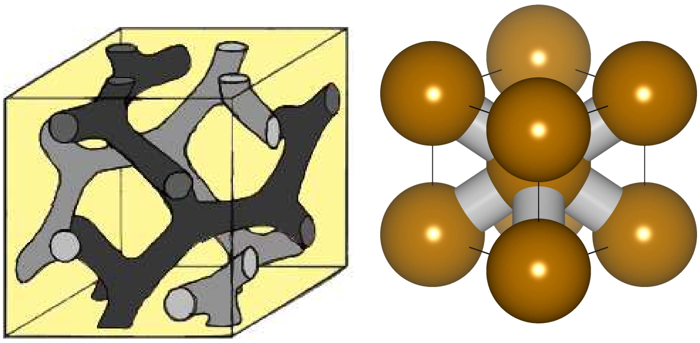

(a) KIT-6. (b) SBA-16.

Figure 6.1: Representations of the pore structures in mesoporous KIT-6 and SBA-16 type silica materials.

Sample	Surface area / $m^2\,g^{-1}$	Pore Size / Å
Mesoporous Co_3O_4 (KIT-6)	92	40 & 90
Mesoporous Co_3O_4 (SBA-16)	122	66

Table 6.1: Surface area and pore size properties of the mesoporous Co_3O_4 samples.

decomposition (74 °C) and infuse into the pore system. The sample was then held at 500 °C for 5 hours before cooling. The silica template was then removed with aqueous 10 % wt HF. A black powder product of mesoporous Co_3O_4-SBA-16 crystals was obtained by centrifugation and washing with distilled water. The final product, mesoporous Co_3O_4-SBA-16 has a surface area of 122 $m^2\,g^{-1}$ and a PSD centred at 66 Å. XRPD patterns show the material to have the same space group as bulk Co_3O_4, $Fd\bar{3}m$.

6.1 Magnetic measurements

Samples of both mesoporous materials and a bulk reference sample of Co_3O_4 were studied with the SQUID magnetometer to determine their magnetic properties. These are shown in Figure 6.2 (bulk Co_3O_4), Figure 6.3 (mesoporous Co_3O_4 templated with KIT-6), and Figure 6.4 (mesoporous Co_3O_4 templated with SBA-16). Modified Curie-Weiss fits (Equation 2.15) were performed on all plots of inverse susceptibility against temperature for three data sets using points above 200 K (the linearity of the Curie-Weiss law breaks down as temperatures approach the Néel transition). Differentiation of the $\chi_m T$ plots provide an estimate of the Néel ordering temperature. These values are presented in Table 6.2. Magnetisation response of the materials to an applied field

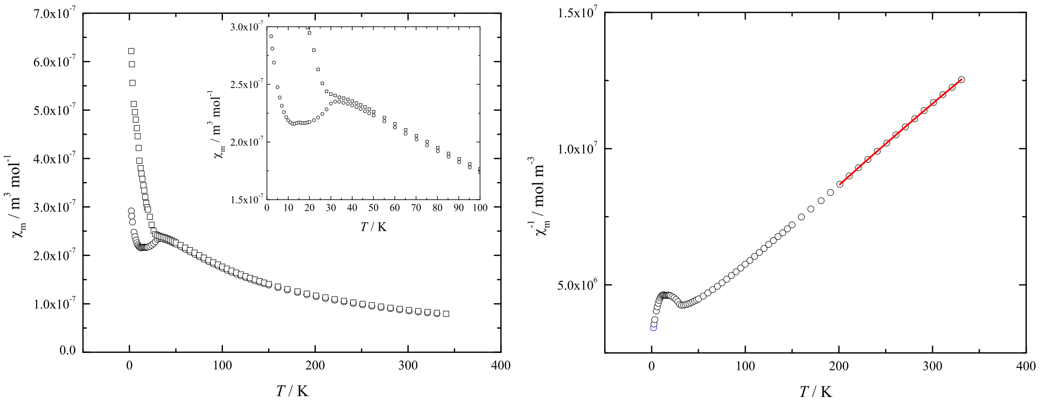

(a) χ_m vs. T. ZFC (circles) and FC (squares).

(b) χ_m^{-1} vs. T with a Curie-Weiss fit for T $\geq$ 200 K.

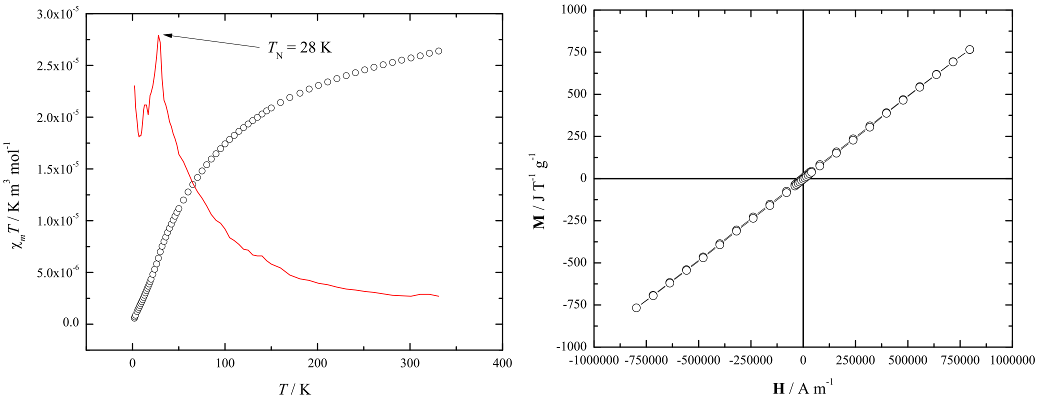

(c) $\chi_m T$ vs. T (data points) and $\frac{d\chi_m T}{dT}$ (line).

(d) $\mathbf{M}$ vs. $\mathbf{H}$ at 6 K.

Figure 6.2: Graphs of magnetic measurements of bulk Co_3O_4.

were also performed at 6 K up to an applied field of 1 T.

The negative Weiss temperature values (θ) obtained from the magnetic property analysis show that the materials are antiferromagnetic as expected (corroborated by the lack of hysteresis loops in the $\mathbf{M}(\mathbf{H})$ plots). The value of T_N of the bulk material is considerably lower than that expected for pure Co_3O_4 (40 K [100]). However, the other studies on bulk Co_3O_4 have reported a Néel point of $\approx$ 40 K from magnetic susceptibility [101] and heat capacity [102] measurements. The 40 K value was determined by taking the maximum in the susceptibility data, however it is believed to be more accurate to take the maximum in the $\frac{d\chi_m T}{dT}$ curves as the transition temperature (the procedure which was used by Dutta et al. in reference 101). The mesoporous materials also exhibit lower ordering temperatures. This has been seen in nanoscale materials of Co_3O_4 [103–105].

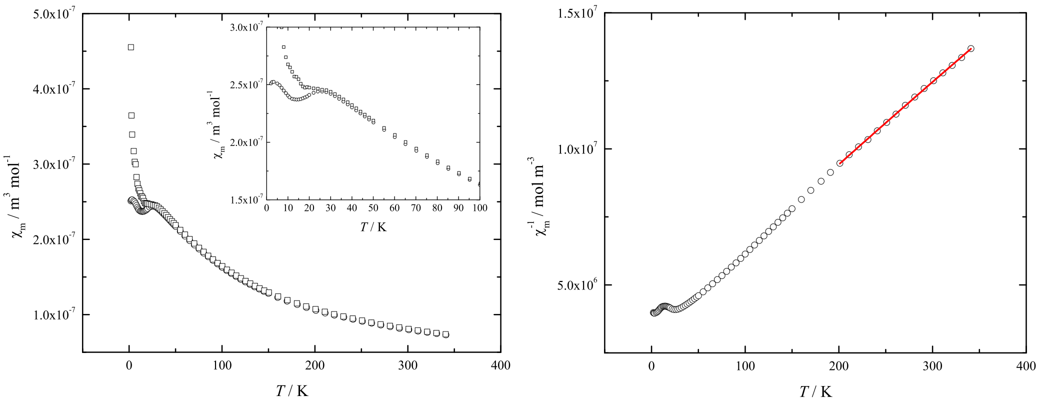

(a) χ_m vs. T. ZFC (circles) and and FC (squares).

(b) χ_m^{-1} vs. T with a Curie-Weiss fit for T $\geq$ 200 K.

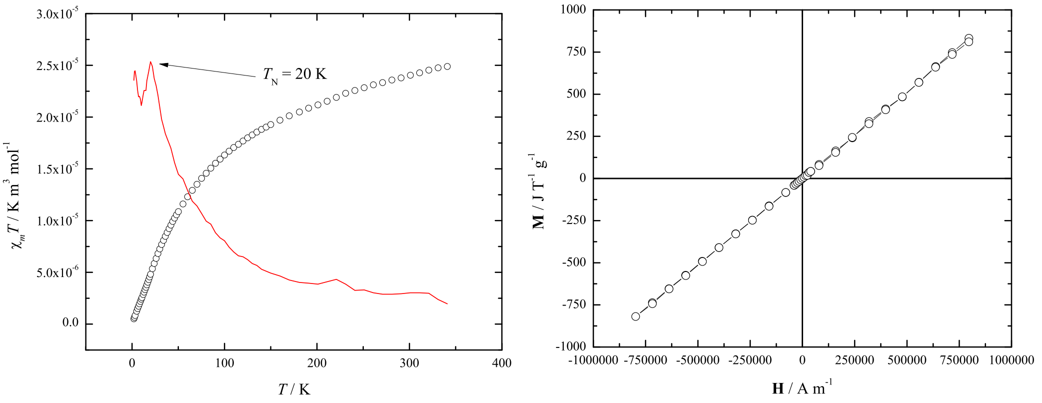

(c) $\chi_m T$ vs. T (data points) and $\frac{d\chi_m T}{dT}$ (line).

(d) **M** vs. **H** at 6 K.

Figure 6.3: Graphs of magnetic measurements of KIT-6 templated mesoporous Co_3O_4.

Sample	T_N / K	$C \times 10^{-5}$ / $m^3\,K\,mol^{-1}$	θ / K	μ_{eff} / μ_B
Bulk Co_3O_4	28(1)	3.70(9)	−56(5)	4.15(7)
Mesoporous Co_3O_4 (KIT-6)	20(1)	3.0(2)	−94(13)	4.36(16)
Mesoporous Co_3O_4 (SBA-16)	26(1)	3.3(3)	−117(17)	4.6(2)

Table 6.2: Magnetic properties of the Co_3O_4 samples from magnetometery measurements.

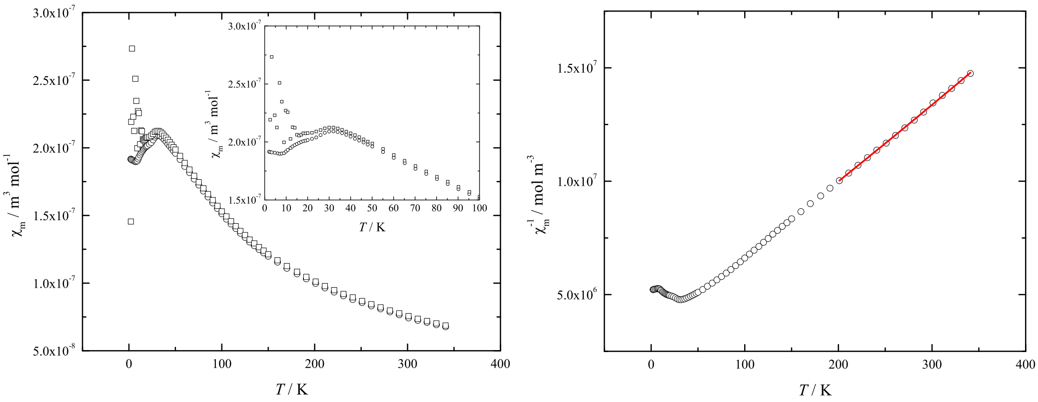

(a) χ_m vs. T. ZFC (circles) and and FC (squares).

(b) χ_m^{-1} vs. T with a Curie-Weiss fit for T $\geq$ 200 K.

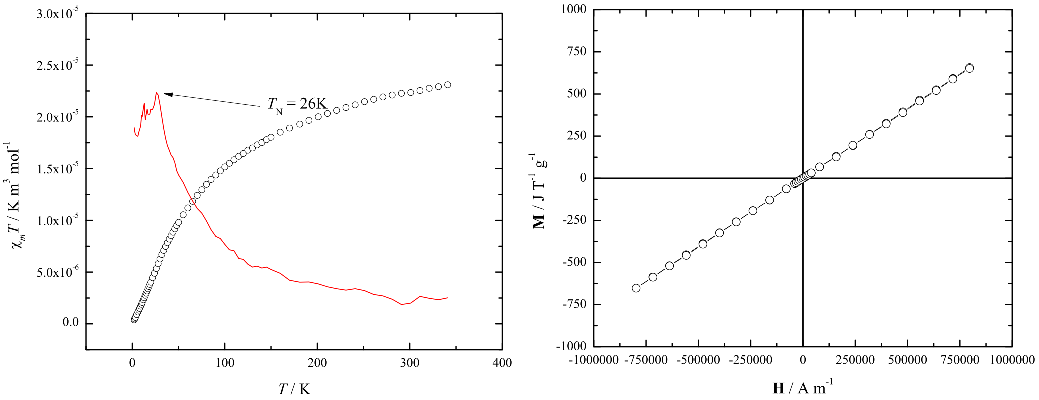

(c) $\chi_m T$ vs. T (data points) and $\frac{d\chi_m T}{dT}$ (line).

(d) **M** vs. **H** at 6 K.

Figure 6.4: Graphs of magnetic measurements of SBA-16 templated mesoporous Co_3O_4.

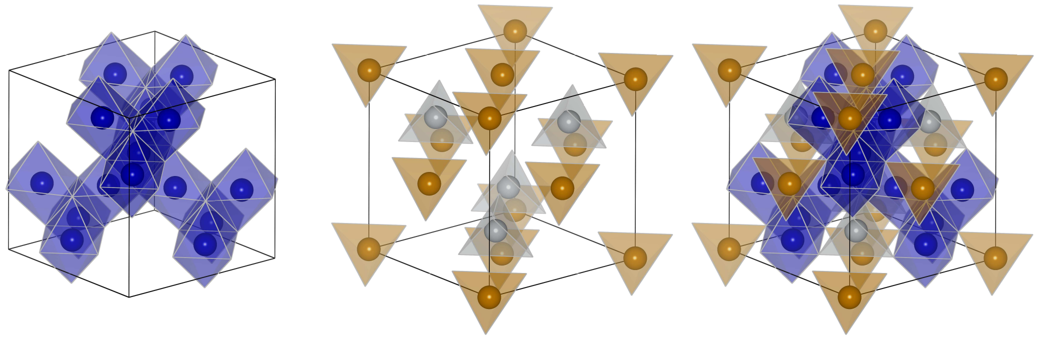

(a) Co^{3+} octahedral (B) sites.

(b) Co^{2+} tetrahedral (A) sites.

(c) $Co^{2+}Co_2^{3+}O_4$ A and B sites.

Figure 6.5: Crystal structure of Co_3O_4, showing the octahedral (B) $S = 0$, Co^{3+}, and tetrahedral (A) $S = \frac{3}{2}$, Co^{2+} sites. The different shading of the B sites represent spin up and spin down ions.

The known structure of Co_3O_4, (Figure 6.5) is a spinel with Co^{3+} ions occupying the B sites (octahedral) and the Co^{2+} ions occupying the A sites (tetrahedral). Due to the splitting of the $3d$ levels, the Co^{3+} ions are low spin ($S = 0$) so do not contribute to the magnetic response [100, 106]. The calculated effective magnetic moments, μ_{eff} of the samples are all of values considerably higher than the theoretical moment derived from spin-only moment contributions ($3.87\,\mu_B$ for Co^{2+}, $3d^7$, term symbol $^4F_{9/2}$). This is because there is some contribution from the orbital angular moment of the $^4F_{9/2}$ ground state. Taking g to be slightly higher at 2.3 provides a theoretical moment of $4.45\,\mu_B$ [107, 108]. The value of $4.45\,\mu_B$ for bulk Co_3O_4 agrees very closely to a previously reported value of $4.14\,\mu_B$ in reference 100. The moments for the mesoporous samples are considerably higher, this could be due to the presence of impurities.

There are two superexchange interactions ($J_{1\text{ex}}$ and $J_{2\text{ex}}$) between Co^{2+} ions in Co_3O_4. These are A–O–A and A–O–B–O–A, with 4 and 12 equivalent pathways (z) respectively. T_N and θ can be expressed by these exchange terms, using molecular field theory [109, 110].

Sample	$J(J+1)$	$J_{1\mathrm{ex}}/k_\mathrm{B}$ / K	$J_{2\mathrm{ex}}/k_\mathrm{B}$ / K
Bulk Co_3O_4	3.26(11)	9.7(7)	1.1(2)
Mesoporous Co_3O_4 (KIT-6)	3.59(12)	11.9(14)	2.6(5)
Mesoporous Co_3O_4 (SBA-16)	4.00(17)	13.4(17)	2.8(5)

Table 6.3: Calculated superexchange constants in Co_3O_4.

$$T_\mathrm{N} = \frac{J(J+1)}{3k_\mathrm{B}}(4J_{1\mathrm{ex}} - 12J_{2\mathrm{ex}}) \tag{6.1}$$

$$-\theta = \frac{J(J+1)}{3k_\mathrm{B}}(4J_{1\mathrm{ex}} + 12J_{2\mathrm{ex}}) \tag{6.2}$$

$$T_\mathrm{N} + \theta = -24J_{2\mathrm{ex}} \times \frac{J(J+1)}{3k_\mathrm{B}} \tag{6.3}$$

$$\mu^2 = g^2 J(J+1)\mu_\mathrm{B}^2 \tag{6.4}$$

The value of $J(J+1)$ (Equation 6.4) can be determined from the calculated effective magnetic moment, μ_eff, and using $g = 2.3(2)$. Using this value with Equation 6.3 alongside observed Néel and Weiss temperatures (Table 6.2) provides values of $J_{1\mathrm{ex}}$ and $J_{2\mathrm{ex}}$ (Table 6.3). The values obtained are all positive, and thus correspond to antiferromagnetic coupling for both exchange interactions (as expected). Comparison with exchange constants calculated in references 111 and 101 for bulk ($7.5/k_\mathrm{B}$ K to $11.7/k_\mathrm{B}$ K and $2.3/k_\mathrm{B}$ K) and 19 nm diameter nanoparticles ($11.5/k_\mathrm{B}$ K and $2.3/k_\mathrm{B}$ K) is favourable.

6.2 Parametric neutron powder diffraction

Samples of both mesoporous Co_3O_4 forms and bulk material (bulk material differed from the SQUID sample) were studied for temperature dependence of the neutron powder diffraction patterns on the D1B diffractometer ($\lambda = 2.52$ Å) at the ILL, using a standard orange cryostat. Data sets were taken from ≈ 3 K to 50 K. Example diffraction patterns collected above and below the Néel temperature are shown for all 3 samples, together with the difference curve (pure magnetic scattering) in Figure 6.6. Bragg peaks arising from CoO were observed in all three samples. Further Bragg peaks were also observed in the mesoporous samples, particularly at low Q. The origin of these is unknown,

Sample	T_N / K	β
Bulk Co_3O_4	25.6(6)	0.13(2)
KIT-6 templated Co_3O_4	24.4(4)	0.185(12)
SBA-16 templated Co_3O_4	26.5(4)	0.220(19)

Table 6.4: Least-squares fit of Equation 6.5 for mesoporous and bulk Co_3O_4 samples.

however, due to the regular periodicity of these peaks, they could be related to the mesoporous structure of the materials. The main magnetic Bragg peaks are the (111) and (200) peaks. The (111) reflection consists of nuclear and magnetic contributions, whereas the (200) reflection is purely magnetic. Integration of this peak area can provide information on the ordering temperature (T_N) of the material.

The integrated area of the (200) peak was determined by performing a least-squares fit with a Gaussian peak shape using ABFFIT software [113]. The normalised (I/I_{max}) peak areas are shown in Figure 6.7, with a least-squares power-law fit of the intensity of the (200) reflection in the critical region given by Equation 6.5. The results of the least-squares fitting are given in Table 6.4.

$$I/I_{\mathrm{max}} = \left(\frac{T_N - T}{T_N}\right)^{2\beta} \tag{6.5}$$

The Néel ordering temperatures of the mesoporous materials (24.4 K and 26.5 K for KIT-6 and SBA-16 templated material) are lower than that expected of bulk material (40 K [100]). The values are also lower than those obtained for nanoparticles of Co_3O_4 (31 K [105]). The exponent values, β of the fits, cannot be compared to known and theoretical critical exponents in Co_3O_4 due to insufficient data points of a suitable δT over the fitted temperature range.

6.3 Summary

DC susceptibility studies show the mesoporous materials to order at 20 K and 26 K (KIT-6 and SBA-16 samples respectively). These are a few Kelvin below the bulk material Néel temperature of 28 K, which is close to values reported for bulk Co_3O_4 from specific heat measurements. The NPD diffraction measurements show that the mesoporous materials have the same magnetic symmetry as that of the bulk material. Integration of the (200) magnetic Bragg peak have enabled a second value of T_N to be determined for each sample. These agree within reason with the susceptibility measurements, although their reliability is not ideal due to lack of sufficient data

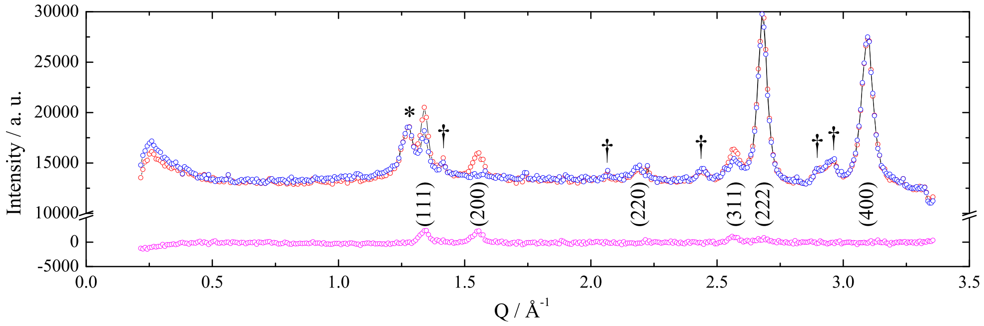

(a) Bulk Co_3O_4.

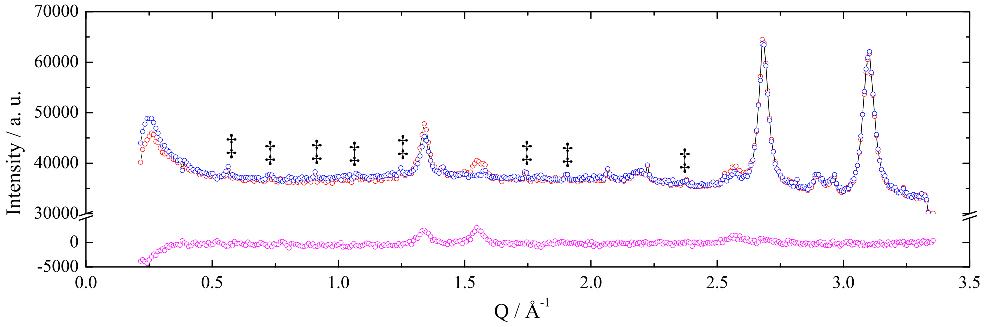

(b) KIT-6 templated Co_3O_4.

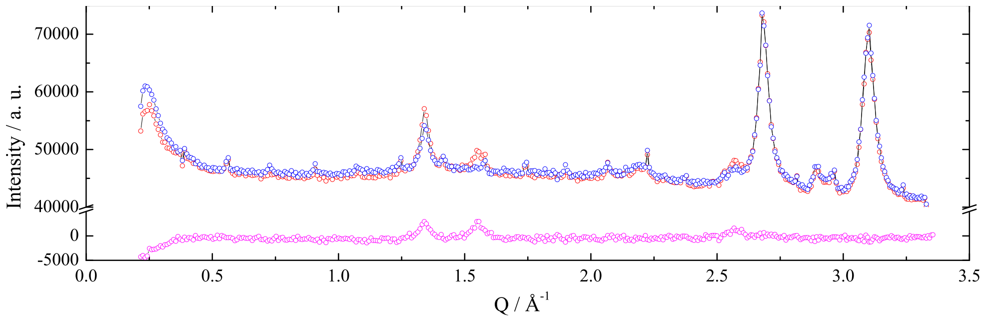

(c) SBA-16 templated Co_3O_4.

Figure 6.6: Neutron powder diffraction patterns of bulk and mesoporous Co_3O_4, collected below and above T_N at $\approx 3\,K$ (red) and $\approx 35\,K$ (blue), with the difference plots shown below (magenta). Bragg reflections are indexed upon the $Fd\bar{3}m$ space group. Impurity peaks seen in all 3 samples marked with a dagger (†) in (a) are identified as originating from a small amount of CoO ($T_N \approx 290\,K$, space group $C2/m$ [112]). An unidentified impurity in the bulk sample is present and indicated with an asterisk. Further Bragg reflections can be seen to be more prominent in the mesoporous samples indicated by double daggers (‡) in (b). The origin of these are unknown.

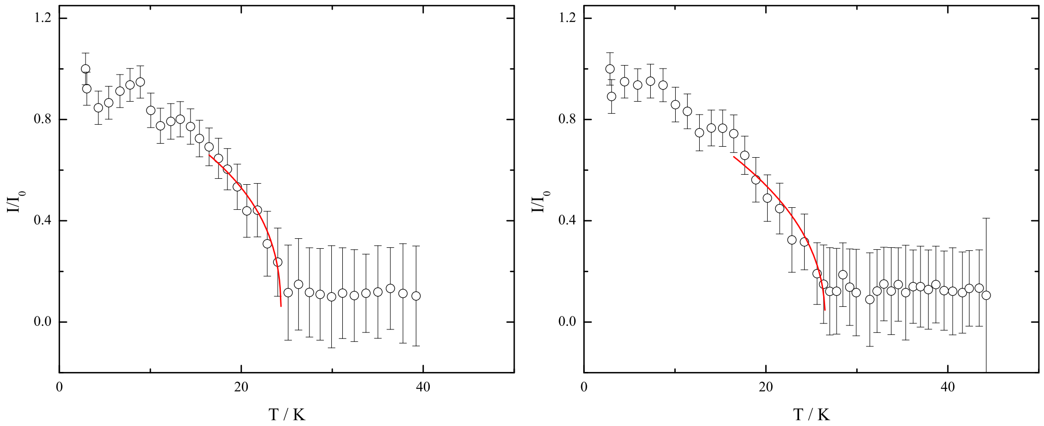

(a) KIT-6 templated Co_3O_4.

(b) SBA-16 templated Co_3O_4.

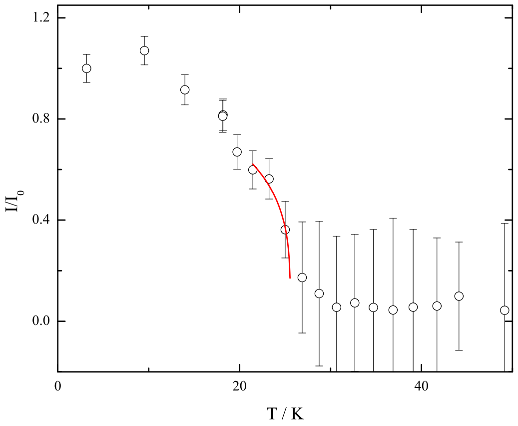

(c) Bulk Co_3O_4.

Figure 6.7: Normalised intensities of the (002) magnetic Bragg peak and the power-law fits in the critical regions.

points near the ordering temperature. The lower Néel transition in the mesoporous materials agrees with measurements taken on nanoscale Co_3O_4 particles. Analysis of the superexchange interactions in the materials using molecular field theory show that the standard A−O−A superexchange interaction has a greater increase in significance over the extended superexchange interaction via the non magnetic B site (A-O-B-O-A) in the mesoporous materials in comparison to the bulk material. This is most likely due to break down of long range order in the mesoporous samples, that is, there will be a higher proportion of near neighbour interactions completed than in the extended superexchange pathway. The KIT-6 templated sample has a bimodal pore system (see Chapter 7), this will produce a further break down of crystallographic ordering in the sample in comparison to the bcc cubic material. This could be an explanation for a slightly lower ordering temperature in the KIT-6 templated sample over the SBA-16 templated sample.

Chapter 7

Mesoporous bunsenite, NiO

Mesoporous samples of bunsenite, NiO were studied by magnetic susceptibility measurements and NPD. These samples were prepared by templating with three different samples of mesoporous KIT-6 (Appendix D). The host KIT-6 templates were prepared under slightly different synthetic conditions, giving rise to a range in pore sizes. The different template samples created samples of mesoporous NiO with differing wall thickness. It is therefore of interest to study these samples to try to link wall, pore, and mesoporous unit cell size with physical properties. The samples were prepared by Dr Feng Jiao (School of Chemistry, University of St Andrews) [27].

> Three different KIT-6 mesoporous silica samples were prepared in the standard way (see Chapter 3), except for the hydrothermal step. The samples were maintained in sealed autoclaves at 80°, 100°, and 130° for the usual 24 hours. The different temperatures give rise to surfactant micelles of different sizes, and subsequently different final pore sizes in the calcined silica: we call these samples KIT-6-80, KIT-6-100, and KIT-6-130. For the preparation of mesoporous NiO, typically 4 g of $Ni(NO_3)_2 \cdot 6\,H_2O$ (96 %, Aldrich) was dissolved in 150 ml of ethanol, and added to 5 g of the particular KIT-6 template. The suspension was then stirred at room temperature until a dry product was obtained. The powder was then redispersed in 100 ml of dry n-hexane and stirred until complete evaporation of the hexane. It was then heated slowly to 550° and held at that temperature for 3 hours to allow decomposition of the nickel nitrate to nickel oxide. To remove the silica host, the material was washed twice with hot aqueous 2 Molar NaOH, followed by washing in water several times, and finally dried at 60°. The NiO samples prepared using the different KIT-6 templates are labeled: NiO-80, NiO-100, and NiO-130. Their surface areas and pore sizes are listed in Table 7.1. The pore size of the NiO-130 sample is in good agreement with the wall thickness of the KIT-6-130 host. The NiO-100 and NiO-80 samples exhibit two different pore sizes, which correspond to a different formation

Sample	BET Surface area / $m^2\,g^{-1}$	Pore diameter / Å	Wall thickness / Å
KIT-6-80	820	53	3.6
KIT-6-100	816	71	3.4
KIT-6-130	787	80	3.3
NiO-80	108.6	31.0 & 111	5.5
NiO-100	94.1	31.5 & 113	6.8
NiO-130	81.8	33.0	7.8

Table 7.1: Different surface parameters of the mesopororous hosts and NiO samples. After reference 27.

mechanism in the silica due to the connectivity of pores in the original host by micropores [114]. The bimodal pore size distribution is therefore a combination of NiO occupying both sets of pores in KIT-6 and occupying just one set (Figure 7.1).

7.1 Magnetic measurements

NiO exists in the rock salt structure, (spacegroup $Fm\bar{3}m$) above its antiferromagnetic ordering temperature, $T_N \approx 523\,\text{K}$ [115–118]. Below this the magnetic moments of the Ni^{2+} ions arrange in ferromagnetic sheets in (111) planes, coupled antiferromagnetically to neighbouring planes. The onset of antiferromagnetic order also induces a small amount of trigonal distortion in the fcc crystal structure, changing it to a rhombohedral crystal structure of space group $R\bar{3}m$ (Figure 7.2) [119, 120]. The arrangement of the magnetic structure has a propagation vector $\vec{k} = \left(0, 0, \frac{1}{2}\right)$, that is the unit cell is doubled along the c axis. The electronic ground state structure of Ni^{2+} in this material is $^3\text{F}_4$, however, despite there being no orbital degeneracy, spin orbit-coupling is important and the orbital moment (L) is not fully quenched. Therefore the total angular momentum, J will be the sum of the spin angular momentum, S and the orbital angular momentum, L. Magnetic measurements on NiO with synchrotron radiation have shown $S = 0.95(10)$ and $L = 0.32(5)$ [121]. This enables the theoretical effective magnetic moment on the nickel site to be calculated, using Equation 2.18 and Equation 2.19.

Using the momenta values determined in reference 121 gives a total angular momentum, J of 1.27(11) and a g factor of 1.74(12). Therefore the expected value of μ_p is $3.0(5)\,\mu_\text{B}$.

Samples of all three mesoporous materials and a bulk reference sample of NiO were studied with the SQUID magnetometer to determine their magnetic properties. The

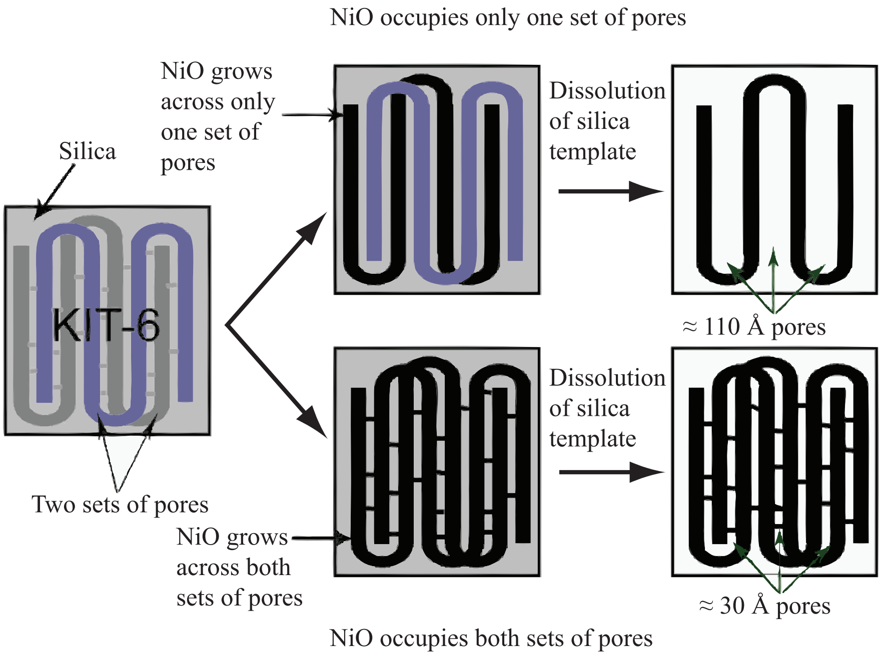

Figure 7.1: Mechanism by which different pore sizes can be obtained in mesoporous KIT-6. After reference 27.

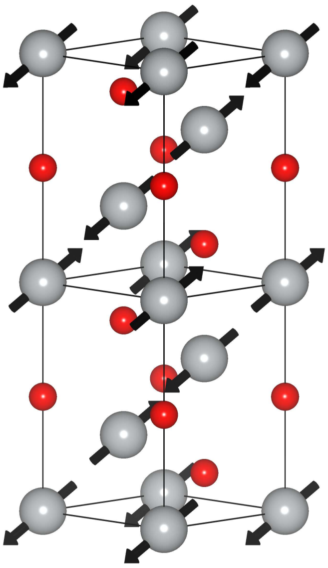

Figure 7.2: The rhombohedral cell of NiO with the magnetic arrangement causing a doubling of the unit cell along *c*.

magnetic susceptibility plots are shown in Figure 7.3. Effective magnetic moments were calculated for each plot by using Equation 2.16 and are plotted in Figure 7.4. Magnetic susceptibility data of standard NiO show a gradual rise with temperature until a plateau is reached at T_{N} [122]. This is what is observed in our bulk measurements (Figure 7.3(a) — the ZFC-FC splitting is minimal) up to 300 K. The mesoporous samples however display different susceptibility profiles. The divergence of the ZFC-FC measurements is similar to observations on 3 nm nanoparticles, where a sharp peak at low temperature (15 K to 17 K) was observed in the ZFC susceptibility [123]. This is believed to be the freezing of uncompensated surface spins on the NiO particles forming a spin glass type system. We too observe a peak in the ZFC susceptibility measurements at ≈ 3 K, 9 K, and 9 K for the NiO-80, NiO-100, and NiO-130 samples respectively. The effective magnetic moments of each sample reduce as expected towards zero with decreasing temperature, (due to better alignment of the antiferromagnetic moments). At higher temperatures the moments increase with varying rates depending upon the samples. The bulk moment increases up to $\approx 1.4\,\mu_{\mathrm{B}}$ at 300 K, but shows little sign of saturation, and would be expected to continue rising up to the theoretical moment of $\approx 3\,\mu_{\mathrm{B}}$. The mesoporous samples however have effective magnetic moment curves which seem to show a faster rate of saturation. This suggests that overall, the average moment on each Ni^{2+} ion is lower compared to the bulk material. The effect is less pronounced as the surface area decreases (NiO-80 → NiO-100 → NiO-130). This is probably due to the material behaving more like bulk material as the surface area (and total pore volume) decreases.

7.2 Neutron powder diffraction

All three mesoporous samples and a bulk reference sample underwent temperature dependent parametric neutron diffraction studies. The aim of this was to track the change in magnetic Bragg peak intensities as the materials passed through the Néel transitions. This would enable us to see any differences in ordering temperatures between the samples and compare to the bulk magnetic ordering temperature. These measurements were carried out upon the high intensity two-axis powder diffractometer, D20 [124] at the ILL with an incident neutron wavelength of 2.4189 Å. The powders were contained in standard cylindrical vanadium cylinders, and placed in a standard orange cryofurnace. NPD patterns were obtained from for mesoporous samples from approximately 300 K up to 550 K, with each pattern collected over 4.5 minutes with $\delta T \approx 5$ K. Patterns for bulk material were collected in a shorter time period (due to better Bragg scattering) of 2.25 minutes per acquisition with $\delta T \approx 1.2$ K.

For all samples, the lowest temperature pattern was used for Rietveld refinements us-

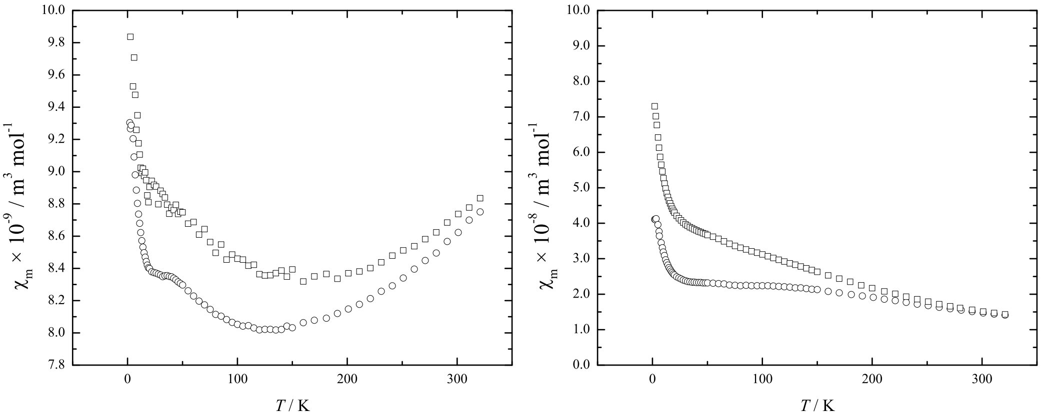

(a) Bulk NiO.

(b) NiO-80.

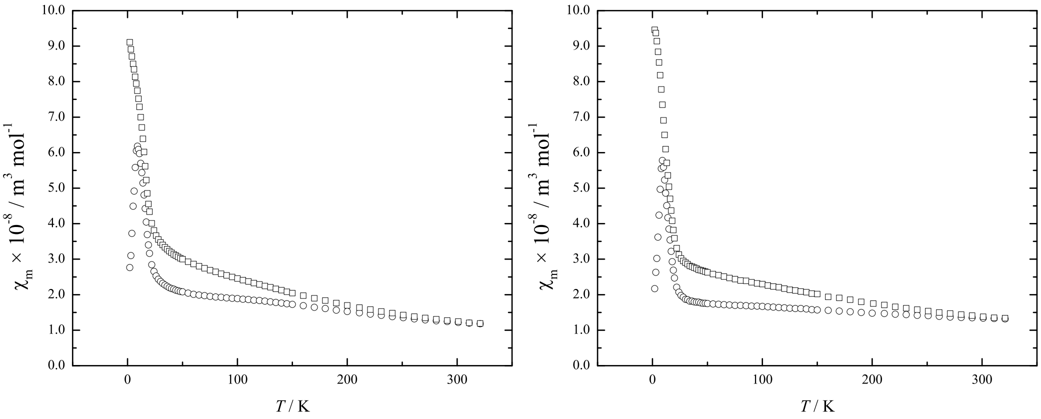

(c) NiO-100.

(d) NiO-130.

Figure 7.3: Magnetic susceptibility plots, χ_m vs. T. of NiO samples. ZFC (circles) and FC (squares).

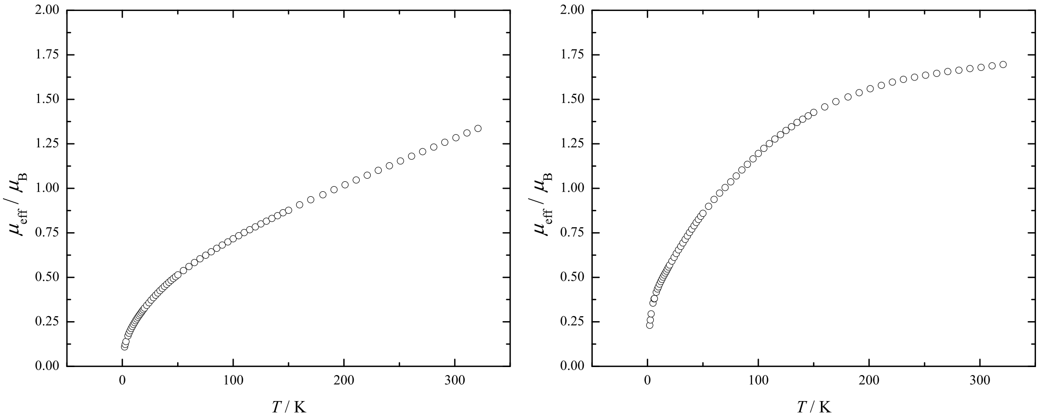

(a) Bulk NiO.

(b) NiO-80.

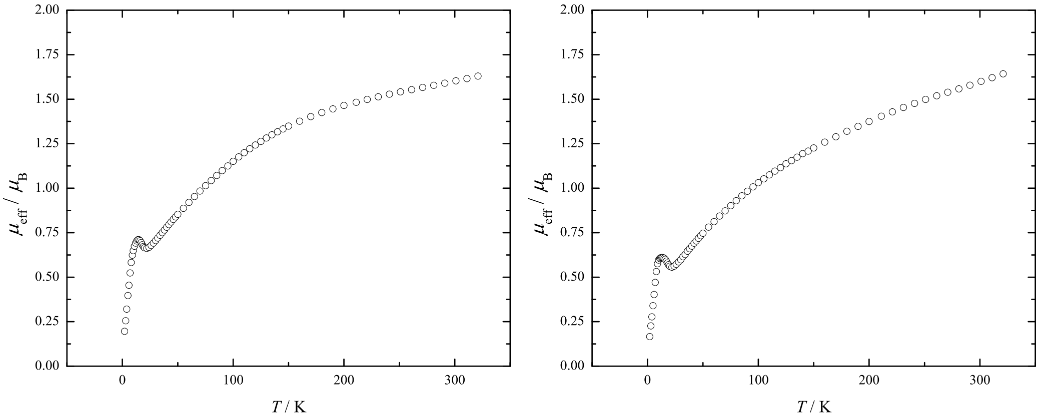

(c) NiO-100.

(d) NiO-130.

Figure 7.4: Effective magnetic moment, μ_{eff} vs. T. of NiO samples from ZFC susceptibility data.

ing GSAS [41]. The refinement was carried using a two phase model; a crystallographic one of space group $R\bar{3}m$, and a magnetic one of space group $P1$. The magnetic cell was doubled in the c axis in relation to the crystallographic cell, with all lattice constants constrained to vary linearly with each other between phases. In the crystallographic cell, the Ni^{2+} ions were placed at the $3a$ Wyckoff site, whilst the O^{2-} ions were placed at the $3b$ $\left(z = \frac{1}{2}\right)$ site. Positions of the Ni^{2+} ions in the magnetic cell were at $6c$ equivalent site $(0, 0, z)$ and $(0, 0, -z)$ for the cell doubled along c $\left(z = \frac{1}{2}\right)$. Magnetic moments were allowed to refine along the x and $-z$ directions with the moments of the $(0, 0, z)$ ions set to be the opposite of the $(0, 0, -z)$ site ions. Refinements were carried out using a six point linear background (GSAS type 7) and a standard Gaussian function for modified peak asymmetry (GSAS constant wavelength type 1 [39]). Once a satisfactory refinement was achieved, a sequential refinement of each data set was carried out for increasing temperature. When the moment in the z direction became sufficiently small, it was set to zero, leaving only the x moment refining. This value too was set to zero when applicable at high temperature. Typical NPD diffraction patterns and refinements of all samples are shown in Figure 7.5. Refined (hexagonal) lattice parameters, a and c for all four samples are shown in Figure 7.6. These indicate a uniform increase of unit cell size with temperature. Using the lattice parameters, it is possible to calculate the rhombohedral angle α (Equation 7.1) [125]. Over the temperature ranges studied, this angle decreases in all four samples by approximately 0.4° upon heating up to the Néel point.

$$\cos\alpha = 1 - \frac{9}{1 + 2\left(\frac{c}{a}\right)^2} \tag{7.1}$$

The refined sublattice magnetic moments for all four samples are shown in Figure 7.7. The m_z component was successfully refined in the bulk material all the way up to T_N. As the surface area of each sample increased the temperature at which the m_z component had to be set to zero to ensure a robust Rietveld refinement decreased. This is due to problems in resolving the $\left(10\frac{1}{2}\right)$ magnetic Bragg peak (indexed with reference to the crystallographic cell). This peak lies at $Q \approx 2.49$ Å, very close to the crystallographic Bragg peaks (101) and (003) at $Q \approx 2.60$ Å. As temperatures increase, the signal gets weaker, and diffuse background scattering increases, causing the peak resolution to reduce. This is a particular issue in the mesoporous patterns, where the Bragg peaks are generally broader than in the bulk material patterns (most likely due to shorter correlation lengths, reducing domain sizes). The magnitude of the m_z component depends upon the intensity of the peak Changes in intensity can easily be lost within the more intense nuclear peaks, due to poor resolution between them. This will result in errors in the peak profile fitting, and difficulties in making robust refinements

Sample	μ_{max} / BM	T_{N} / K	β
Bulk NiO	1.701(19)	525.0(5)	0.287(8)
NiO-80	1.36(7)	502.3(11)	0.39(4)
NiO-100	1.46(5)	520.8(6)	0.399(8)
NiO-130	1.44(5)	503.9(9)	0.341(9)

Table 7.2: Results of least-squares fit of Equation 7.3 for mesoporous and bulk NiO samples.

at higher temperatures when the magnetic Bragg peak intensity is particularly low. The m_x component on the other hand is determined by the intensity of the $\left(\frac{1}{2}0\frac{1}{2}\right)$ magnetic Bragg peak at $Q \approx 1.30\,\text{Å}$, which is well clear of any other reflections, leading to no ambiguity in fitting the peak shape profile. The refined magnetic moments at the lowest temperature measured are presented in Table 7.2. The value obtained for bulk NiO ($1.70\,\mu_{\mathrm{B}}$) agrees very well with the value of $1.77\,\mu_{\mathrm{B}}$ reported for bulk NiO at 295 K in reference 120, and is close to the free ion magnetic moment (Equation 7.2) of $2.2(3)\,\mu_{\mathrm{B}}$ ($g = 1.74$). The magnetic moments of the mesoporous samples are lower, in agreement with the trends observed in the DC susceptibility measurements of μ_{eff} vs. T in Figure 7.4.

$$\mu_{\mathrm{p}} = g\mu_{\mathrm{B}}(J) \tag{7.2}$$

The normalised (M/M_{max}) total magnetic moments observed have been modeled with a least-squares power-law fit of the intensity in the critical region (Equation 7.3). The parameters are given in Table 7.2, where we can see that the calculated critical temperature (T_{N}) of bulk material agrees very well with the accepted literature value of 523 K. The mesoporous materials show a lower ordering temperature, which is an effect observed in NiO nanoparticles, where the transition moved to lower temperatures with smaller NiO particles [126]. The exponent values, β of all the samples can not be compared to theoretical critical exponents due to insufficient data points of a suitable δT over the fitted temperature range.

$$M/M_0 \propto \left(\frac{T_{\mathrm{N}} - T}{T_{\mathrm{N}}}\right)^{\beta} \tag{7.3}$$

7.3 Discussion and summary

DC susceptibility measurements show that the effective magnetic moment in the mesoporous materials are lower than in the bulk reference. This is confirmed by

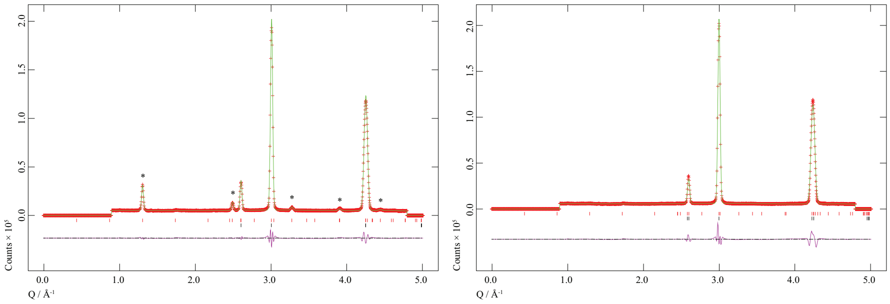

(a) Bulk NiO, $T = 302.3\,\mathrm{K}$.

(b) Bulk NiO, $T = 530.4\,\mathrm{K}$.

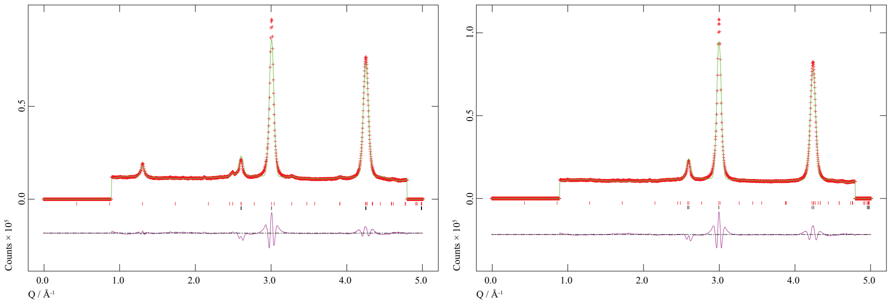

(c) NiO-80, $T = 300.6\,\mathrm{K}$.

(d) NiO-80, $T = 523.1\,\mathrm{K}$.

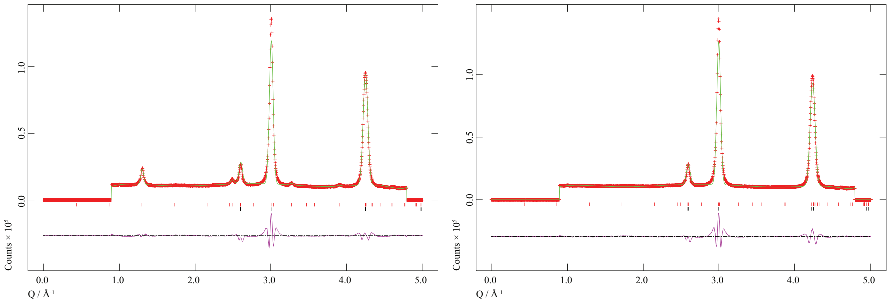

(e) NiO-100, $T = 301.9\,\mathrm{K}$.

(f) NiO-100, $T = 539.0\,\mathrm{K}$.

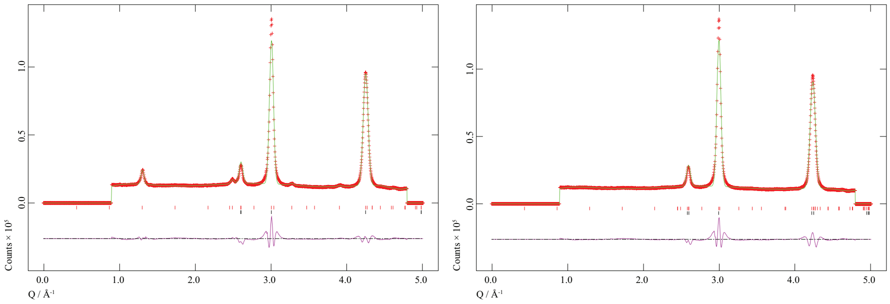

(g) NiO-130, $T = 309.7\,\mathrm{K}$.

(h) NiO-130, $T = 523.3\,\mathrm{K}$.

Figure 7.5: NPD patterns (T_{min} & T_{max}) of NiO samples and the Rietveld refinement patterns of the data. Peaks marked in (a) with asterisks are the purely magnetic Bragg peaks. Patterns refined in the range $0.9 \leq Q \leq 4.8$ Å.

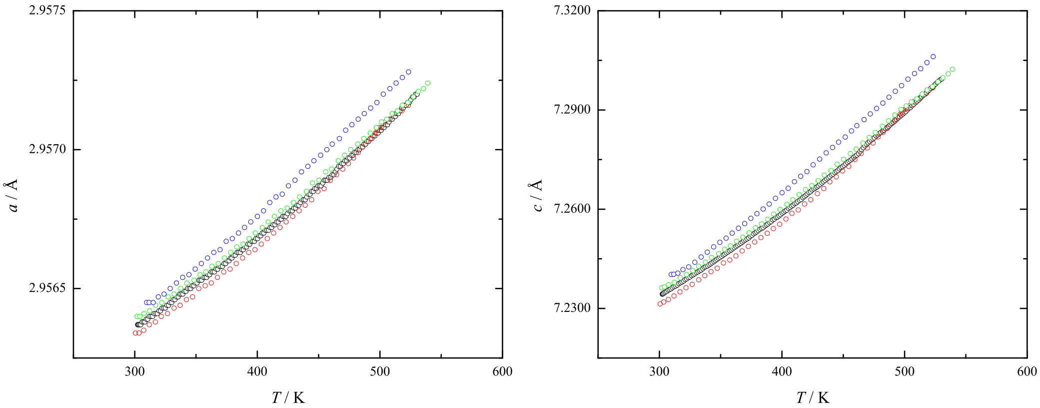

(a) Lattice parameter a.

(b) Lattice parameter c.

Figure 7.6: Graphs of refined lattice parameters, a and c. The colour scheme is black, red, green, and blue for bulk NiO, NiO-80, NiO-100, and NiO-130 respectively.

refinement of NPD data where the magnetic moments are approximately $0.3\,\mu_\mathrm{B}$ lower per Ni^{2+} site. Analysis of the refined moment versus temperature shows a reduced Néel ordering temperature in the mesoporous material, agreeing with data taken from increasingly small NiO particles. The reduced magnetic moment in the mesoporous NiO samples can be attributed to uncompensated surface moments, leading to disorder (of the moments), and therefore a lower $\overline{\mu}$, rather than the presence of higher oxidation state Ni^{3+}, which has been ruled out by XANES (X-ray absorption near edge spectroscopy) measurements by F. Jiao at the Daresbury synchrotron source [27]. These will reduce the average value (that is observed with neutrons) and the susceptibility per unit formula (observed by magnetic susceptibility measurements) of NiO. The uncompensated moments create a spin glass system with randomly fluctuating spins that seem to freeze from 10 K and below. Looking at the NPD patterns we can see that the Bragg peak widths are greater in the mesoporous patterns compared to the sharper peaks in the bulk patterns. This suggests that there are smaller correlation lengths in the mesoporous material. This is expected, as the porosity of the structure will disrupt long range order (for a perfectly ordered material over infinite distance, the Bragg peak would be a δ function).

Comparison of the magnetic properties between the three mesoporous NiO samples seems to be rather more complex. One would expect the ordering temperature to decrease with increasing surface area and decreasing wall size, however the properties of the NiO-100 sample seem to contradict this. This could be due to impurities, or lack of mesoporous structure uniformity throughout the sample. Further analysis may be required.

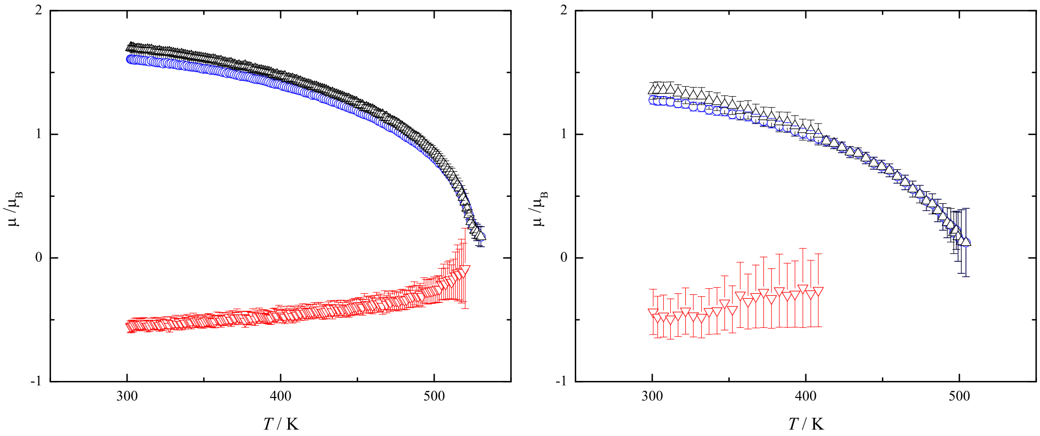

(a) Bulk NiO .

(b) NiO -80.

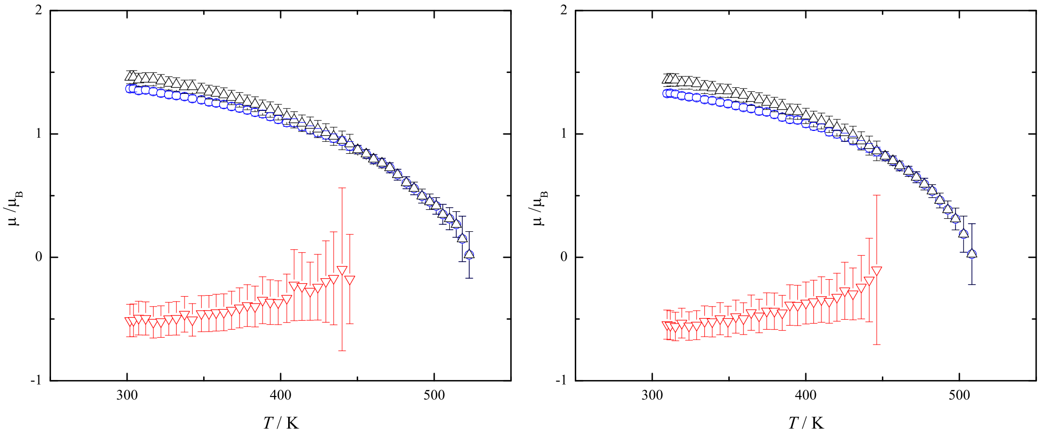

(c) NiO -100.

(d) NiO -130.

Figure 7.7: Graphs of temperature dependence of refined magnetic moments. The colour scheme is black, blue, and red for total moment, m_x, and m_z respectively. The m_z component was not refined at higher temperatures in the mesoporous NiO patterns due to issues in resolving the $\left(10\frac{1}{2}\right)$ magnetic Bragg peak

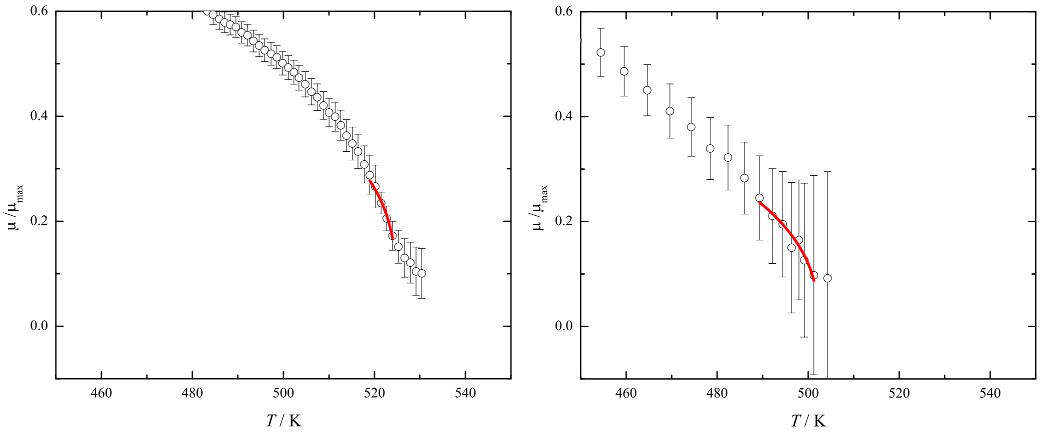

(a) Bulk NiO.

(b) NiO-80.

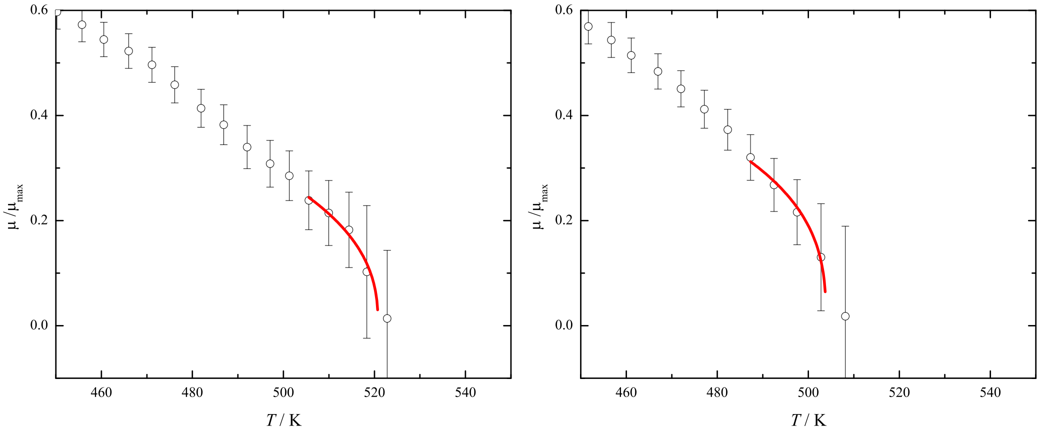

(c) NiO-100.

(d) NiO-130.

Figure 7.8: Fits of Equation 7.3 to the normalised magnetic moments in the NiO samples near the critical region.

Chapter 8

Mesoporous α-MnO_2

Samples of mesoporous and bulk MnO_2 were provided by Mr Yu Ren (School of Chemistry, University of St Andrews) for magnetic properties analysis. The synthetic method for the preparation of these two samples is summarised here.

> In a typical synthesis of mesoporous α-MnO_2, 7.53 g of $Mn(NO_3)_2 \cdot 4\,H_2O$ (98 %, Aldrich) and 1.01 g of KNO_3 were dissolved in $\approx$ 10 ml of water to form a solution with molar ratio of Mn/K = 3.0. 5 ml of this solution were added to 200 ml dried *n*-hexane with 5 g of KIT-6 dispersed in it. The mixture was stirred overnight, filtered and dried at room temperature until a completely dried powder was obtained. The sample was then heated slowly to 500°, and calcined at that temperature for 5 hours. The resulting material was then washed twice with a hot 2 mol dm^{-3} aqueous KOH solution to remove the silica template, followed by several washings in water, and finally dried at 60°.

8.1 Bulk α-MnO_2 properties

Bulk α-MnO_2 is an interesting material in itself. It generally has the hollandite type structure, (space group $I4/m$) which consists of 2 octahedral MnO_6 zigzag chains forming (2×2) tunnels (Figure 8.1) [127–129]. The structure is considered stable in this form, but often has further stabilisation from the presence of cations such as K^+, or water in the (2×2) channels. Consequently the magnetic and physical properties can vary greatly depending upon the presence of absorbed impurities and the local crystallographic structure. α-MnO_2 is an antiferromagnetic compound with a Néel temperature ranging from 25 K (needlelike single crystals [130], and one-dimensional nanostructures [131]), up to 32 K to 40 K (one-dimensional nanoarchitectures with K^+ stabalisation [132]).

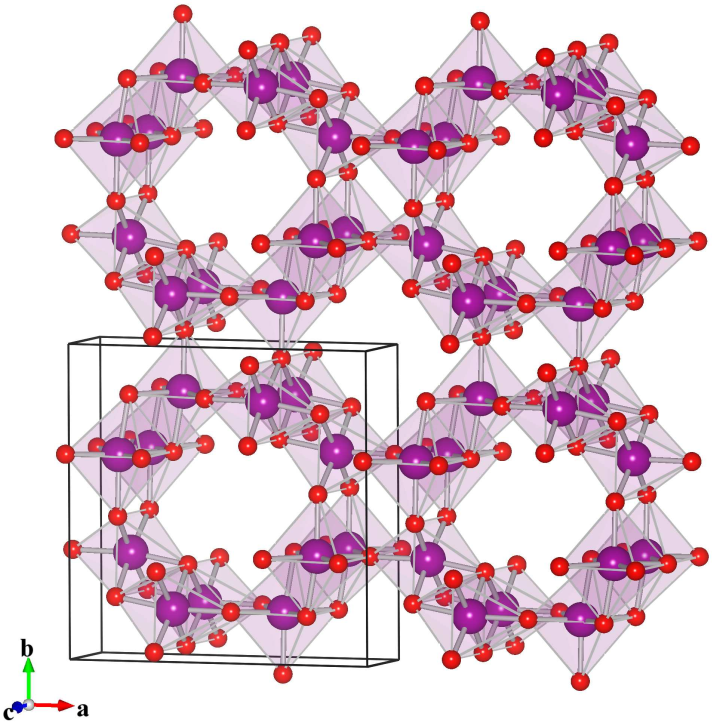

Figure 8.1: The crystal structure of hollandite with unit cell axes of $2a$, $2b$ and c, showing the (2×2) channels along the c axis.

8.2 SQUID magnetometry measurements

Bulk α-MnO$_2$ magnetic susceptibility was measured in the SQUID magnetometer after cooling in zero field (measuring field 100 Oe) and repeated after cooling in 100 Oe. Mesoporous α-MnO$_2$ was analysed by cooling in zero field and measuring in both 100 Oe and 1000 Oe respectively. The measurements were then repeated after cooling in applied fields of 100 Oe and 1000 Oe. Graphs of the magnetic susceptibility (Figure 8.2) show zero field cooled/field cooled divergence. Bulk α-MnO$_2$ shows a divergence at approximateley 46 K. The mesoporous sample diverges at around 50 K (in 100 Oe) and 15 K (in 1000 Oe).

Plots of $\chi_\mathrm{m}T$ against T (Figure 8.3) can yield information about the ordering temperature in these antiferromagnetic materials. The ordering temperature can be taken as the point at which the $\chi_\mathrm{m}T$ slope is greatest [133, 134]. Néel transition temperatures (T_N) where the material changes from an antiferromagnet to a paramagnet are approximately 40(2) K for the bulk sample and 24(2) K for the mesoporous sample. These values are in close agreement to the value of 23 K reported for one-dimensional

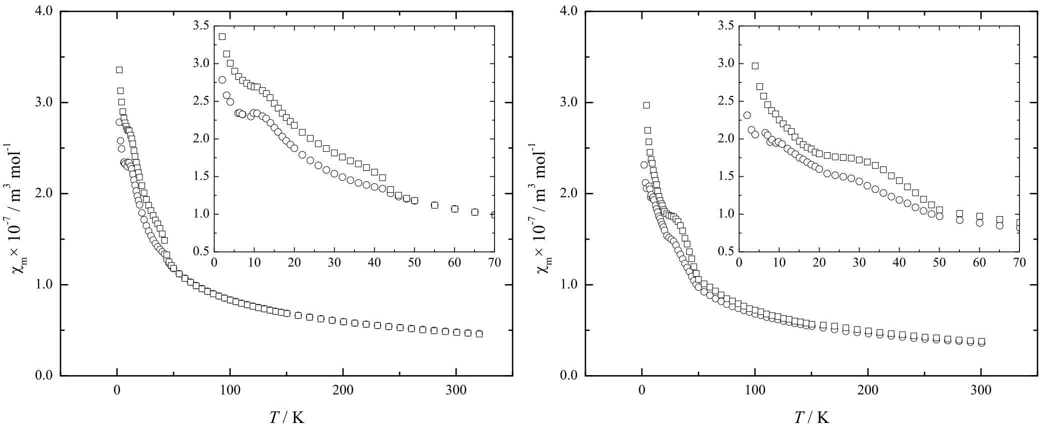

(a) Bulk α-MnO$_2$ 100Oe.

(b) Mesoporous α-MnO$_2$ 100Oe.

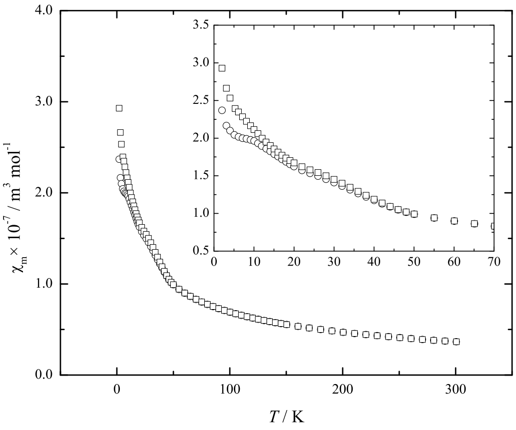

(c) Mesoporous α-MnO$_2$ 1000Oe.

Figure 8.2: Magnetic molar susceptibility (χ_m) of α-MnO$_2$ samples in different fields. Zero field cooled data points are shown with open circles, and the field cooled data points are shown with open squares.

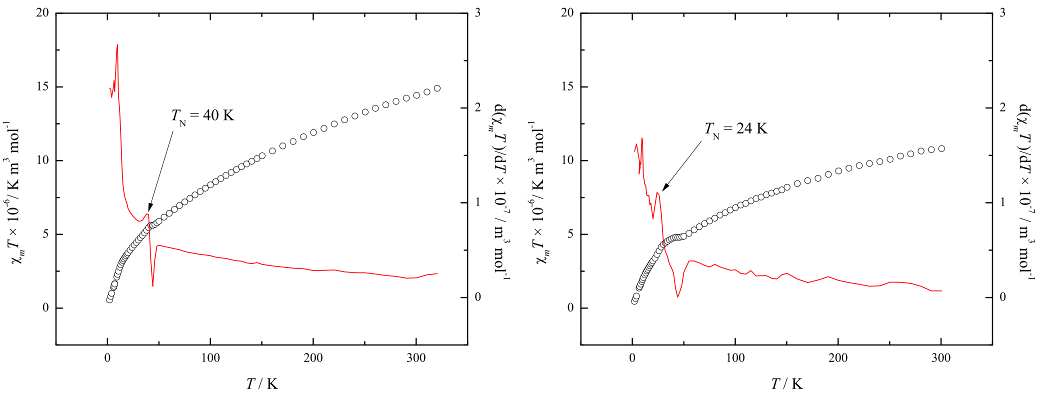

(a) Bulk α-MnO$_2$ 100Oe. (b) Mesoporous α-MnO$_2$ 100Oe.

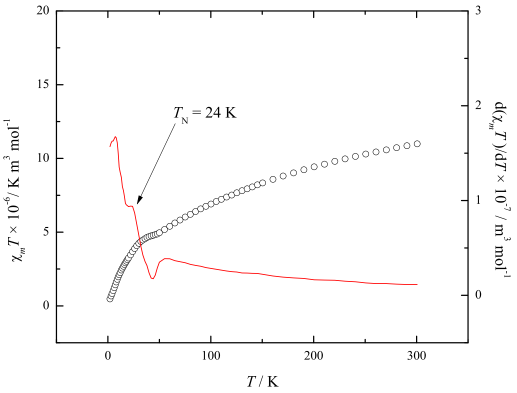

(c) Mesoporous α-MnO$_2$ 1000Oe.

Figure 8.3: $\chi_{\mathrm{m}}T$ (zero field cooled data) against T plots for α-MnO$_2$, with the differential of the graphs plotted as a red line.

nanorods [131], but slightly lower than values of 32–40 K reported for one-dimensional nanoarchitectural arrays with K$^+$ stabalisation in the 2×2 channels [132]. In their analysis of the ordering temperature, T_{N} was taken as the maximum of the χ_{m} plots, (corresponding to the point at which the $\chi_{\mathrm{m}}T$ slope is zero), rather than plotting $\chi_m T$ and $\frac{\mathrm{d}\chi_m T}{\mathrm{d}T}$ against T.

Plots of inverse susceptibility against temperature above the ordering temperature (**??**), in the paramagnetic region generally show linear behaviour, so Curie-Weiss (Equation 2.14) fits have been performed. The temperature independent diamagnetic term, χ_0 ranged from $\approx 2 \times 10^{-9}$ to $\approx 8 \times 10^{-9}$ mol m^{-3}. The Curie-Weiss fit of the mesoporous 100 Oe field data is considered to be a poor fit. The reasons for this are unclear. Therefore, only the values calculated from the 1000 Oe field data will be considered.

Values derived from the Curie-Weiss fits show that the samples are indeed

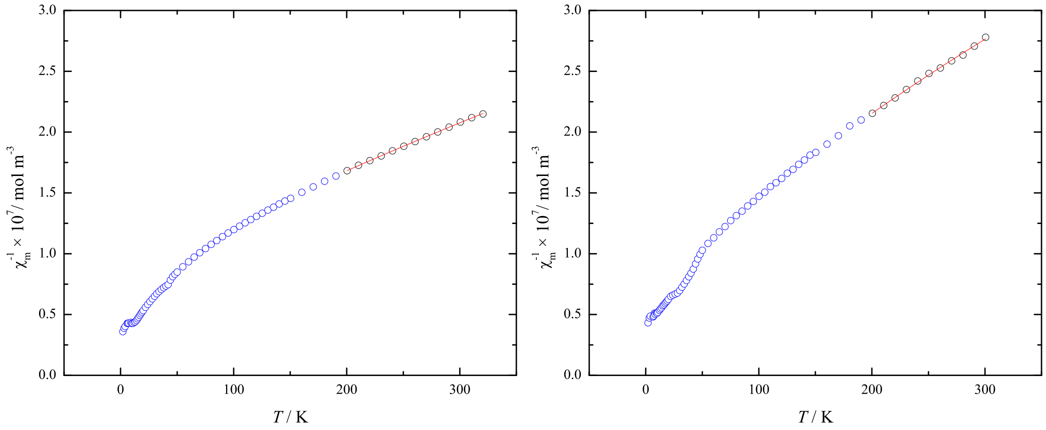

(a) Bulk α-MnO$_2$ 100Oe.

(b) Mesoporous α-MnO$_2$ 100Oe.

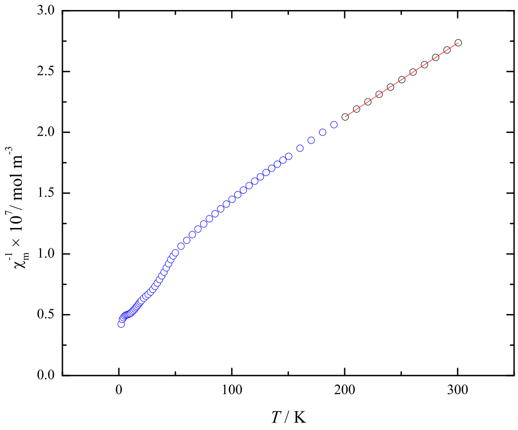

(c) Mesoporous α-MnO$_2$ 1000Oe.

Figure 8.4: χ_{m}^{-1} (zero field cooled data) against T plots for α-MnO$_2$. The Curie-Weiss fits (red lines) were performed above 200 K.

Sample	$C \times 10^{-5}$ / m^3 K mol^{-1}	θ / K	μ_{eff} / μ_{B}
Bulk α-MnO$_2$	1.9(2)	−160(20)	3.44(19)
Mesoporous α-MnO$_2$ (100 Oe)	1.0(4)	−70(60)	2.6(5)
Mesoporous α-MnO$_2$ (1000 Oe)	1.48(7)	−129(9)	3.07(8)

Table 8.1: Magnetic properties of the α-MnO$_2$ samples from Curie-Weiss fits.

antiferromagnetic (negative values of θ). Using the Curie law (Equation 8.1) we can calculate effective magnetic (μ_{eff}) moment per Mn ion present in the samples. Using values of μ_0 (the magnetic constant or permeability of free space), N_{A} (Avogadro constant), μ_{B} (Bohr magneton), and k_b (Boltzmann constant), this can be rearranged to the form shown in Equation 8.2.

$$\chi_m = \frac{\mu_0 N_{\text{A}} \mu_{\text{eff}}^2 \mu_{\text{B}}^2}{3 k_B T} \tag{8.1}$$

$$\mu_{\text{eff}} = 797.8\sqrt{\chi_{\text{m}} T} = 797.8\sqrt{C} \tag{8.2}$$

The values of physical properties calculated from these fits are shown in Table 8.1.

The effective magnetic moments obtained can be compared with theoretical values expected (μ_{p}) for a free ion with only spin angular momentum (Equation 8.3). In stoichiometric α-MnO$_2$ the valence of the manganese ion would be expected to be Mn^{4+}, d^3. The theoretical moment for this ion is 3.87 μ_{B}.

$$\mu_{\text{p}} = g\sqrt{S(S+1)} \tag{8.3}$$

This and the theoretical moment expected for various other states of manganese are listed in Table 8.2. We can see that the effective magnetic moment obtained for the bulk α-MnO $_2$ sample is slightly lower than the Mn^{4+} expected moment. It has been reported in literature that Mn^{3+} is often present in this system, particularly with potassium in the (2×2) channels [131, 135, 136]. This indicates that the sample must have mixed valence states of Mn^{3+} and Mn^{4+}. As the effective magnetic moment is the sum of the magnetic moments from each ion present, the mole fractions of Mn^{3+} and Mn^{3+} can be deduced (Equation 8.4).

$$(\mu_{\text{eff}}) = y(\mu_{\text{p}})_{\text{Mn}^{4+}} + (1-y)(\mu_{\text{p}})_{\text{Mn}^{3+}} \tag{8.4}$$

Normally one would expect high spin Mn^{3+} due to Jahn-Teller distortion, but the presence of higher valence Mn^{4+} can suppress this through broadening of the

Ion	Number of d-electons	Spin quantum number, S	Term symbol	μ_{P} / μ_{B}
Mn^{4+}	3	$\frac{3}{2}$	$^4\mathrm{F}_{3/2}$	3.87
Mn^{3+} (high spin)	4	2	$^5\mathrm{D}_0$	4.90
Mn^{3+} (low spin)[a]	4	1	$^3\mathrm{H}_4$	3.55[b]

[a] Low spin, $S = 1$, $L = 5$, $J = L - S = 4$, $g = 0.8$ (Equation 2.19).

[b] Calculated assuming spin and orbital angular momentum (Equation 2.20).

Table 8.2: Electronic states and theoretical effective magnetic moments of Mn ions.

antibonding *eg** band, making the low spin state more energetically favourable [137]. Assuming that only Mn^{4+} and low spin Mn^{3+} ions are present, this gives a mole fraction 0.59 Mn^{4+}, with an $\mathrm{Mn}^{4+}/\mathrm{Mn}^{3+}$ ratio of 1.42. The average oxidation state is $\mathrm{Mn}^{3.59+}$. From the μ_{eff} value of the mesoporous sample it can be assumed that the average oxidation state is lower, with a higher proportion of low spin Mn^{3+} present. The ratio of $\mathrm{Mn}^{4+}/\mathrm{Mn}^{3+}$ (using the higher field measured value of μ_{eff}) is 0.30, with an average oxidation state of $\mathrm{Mn}^{3.23+}$.

8.3 Summary

Magnetic property measurements of bulk and mesoporous α-MnO_2 have enabled the the Néel transition temperatures of the materials to be determined and the effective magnetic moment per Mn ion in each material to be estimated. Both samples show expected Curie-Weiss behaviour above T_{N}, with a negative Weiss temperature indicating antiferromagnetic ordering. The onset of this antiferromagnetic order has been determined from plots of $\frac{d\chi_m T}{T}$ vs. T. These indicate that the bulk material orders at approximately 40 K, whereas the mesoporous material has a lower ordering temperature at approximately 23 K. This lowering of the phase transition temperature has previously been seen in one-dimensional samples of α-MnO_2. The effective magnetic moments calculated from the Curie-Weiss plots indicates that there may well be a significant presence of low spin Mn^{3+} within the mesoporous sample. This too has been observed in one-dimensional samples. The reasons for this may well be due to the high proportion of surface to volume ratio in the material, causing a noticeable amount of dislocations and non-stoichiometry which is easily detected by SQUID magnetometry.

Chapter 9

Nanoscale lithium manganese oxide spinel, $Li_{1+x}Mn_{2-x}O_4$

$LiMn_2O_4$ spinel is one of the most important intercalation electrodes for rechargeable lithium batteries at the present time. It combines high performance with low cost and toxicity, making it attractive for fuel cell applications [138–141]. Samples of bulk $Li_{1.05}Mn_{1.95}O_4$, bulk $Li_{1.12}Mn_{1.88}O_4$, nanoparticulate $Li_{1.07}Mn_{1.93}O_4$, nanoparticulate $Li_{1.17}Mn_{1.83}O_4$, and mesoporous $Li_{1.12}Mn_{1.88}O_4$ were prepared by Mrs Jianli Bao (School of Chemistry, University of St Andrews) and provided for surface and magnetic property analysis (— see Appendix E [142]).

> Bulk $Li_{1.05}Mn_{1.95}O_4$ and $Li_{1.12}Mn_{1.88}O_4$ were synthesised as follows: stoichiometric ratios of lithium acetate and manganese acetate were ground together before being heated at 400° in air for 3 h. The resulting powder was ground again and then heated at 900°C in air for a further 5 h. The sample was cooled to room temperature at a rate of 3° min^{-1}.
>
> Nanoparticulate $Li_{1.05}Mn_{1.95}O_4$ and $Li_{1.12}Mn_{1.88}O_4$ were synthesised from lithium acetate and manganese acetate following a previously reported procedure [143].
>
> Mesoporous $Li_{1.12}Mn_{1.88}O_4$ was synthesised as follows: by dissolving 30 g of $Mn(NO_3)_2{\cdot}6H_2O$ (98 %, Aldrich) in approximately 20 mL of distilled water. 5 mL of this saturated $Mn(NO_3)_2$ solution were added slowly with stirring to 5 g of mesoporous KIT-6 dispersed in 200 mL of *n*-hexane. The mixture was stirred overnight, filtered and dried at room temperature followed by heating at 600° for 3 hours. The resulting material was treated twice with a $2\,mol\,dm^{-3}$ hot aqueous NaOH solution to remove the silica template, followed by washing with water then drying at 60°. Reduction of mesoporous Mn_2O_3 to Mn_3O_4 was achieved by heating at 280° for 3 hours under a 5:95 H_2:Ar atmosphere. 1 g of the resulting mesoporous Mn_3O_4 was mixed with 1.5 g of $LiOH{\cdot}H_2O$ in 10 mL of water, stirred until dry and then heated

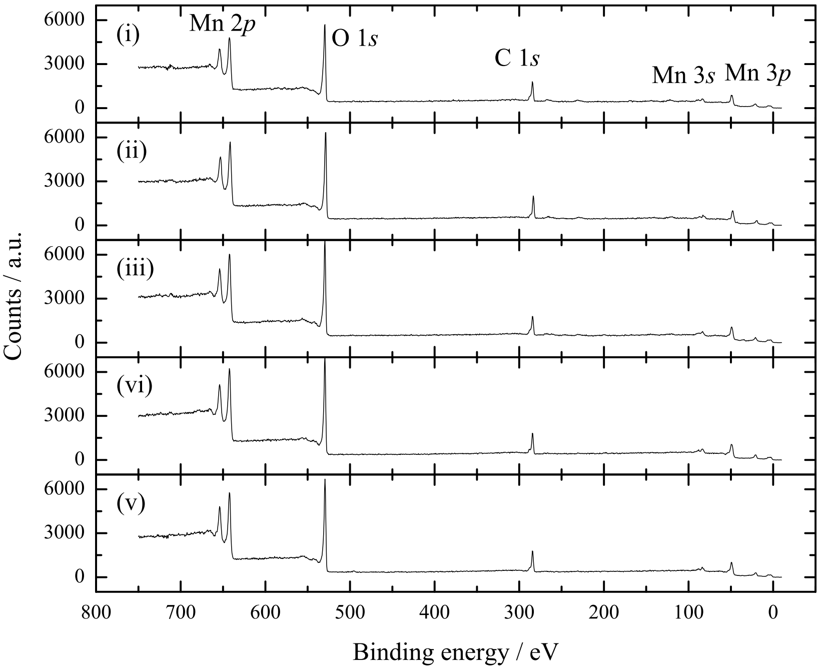

Figure 9.1: Full XPS scans of; (i) bulk $Li_{1.05}Mn_{1.95}O_4$, (ii) bulk $Li_{1.12}Mn_{1.88}O_4$, (iii) nanoparticulate $Li_{1.05}Mn_{1.95}O_4$, (iv) nanoparticulate $Li_{1.12}Mn_{1.88}O\ _4$, and (v) mesoporous $Li_{1.12}Mn_{1.88}O_4$.

slowly at 350° for 1 hour. After the calcination, the sample was cooled to room temperature at a rate of 3° min^{-1}. The resulting material washed with water then dried at 120°.

The mesoporous structure has a surface are of 90 m^2 g^{-1} estimated from the BET isotherm and a pore size distribution from the BJH analysis of the desorption isotherm centred at 4.1 nm.

9.1 X-ray photoelectron spectroscopy

By changing the concentration of Li in these samples, the average oxidation state of the manganese ions will change. To probe this, XPS measurements were taken on all samples using the Sigma Probe XPS spectrometer as described in Chapter 2. An initial full scan (pass energy 80 eV, 0.5 eV steps) was carried out on each sample (Figure 9.1), followed by more detailed scans (pass energy 20 eV, 0.1 eV steps) around the Mn 2*p*, O 1*s*, C 1*s*, Mn 3*s*, and Mn 3*p* key binding energy features (Figure 9.2). All binding energies were corrected using the signal from adventitious carbon (the carbon film the samples were mounted upon) at 285.0 eV. The main O 1*s* line is detected at approximately 530 eV along with an higher energy shoulder at 531.5 eV. The main peak is attributed

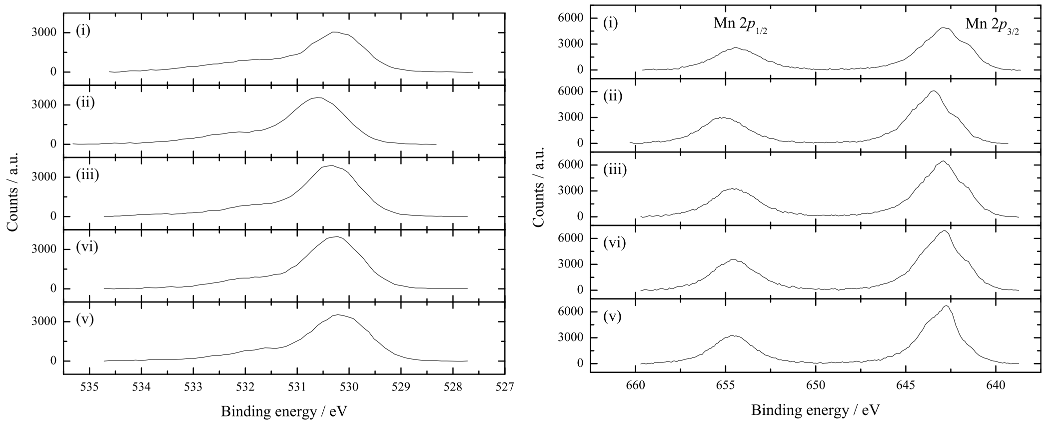

(a) O 1s binding energy.

(b) Mn 2$p_{1/2}$ and 2$p_{3/2}$ binding energy.

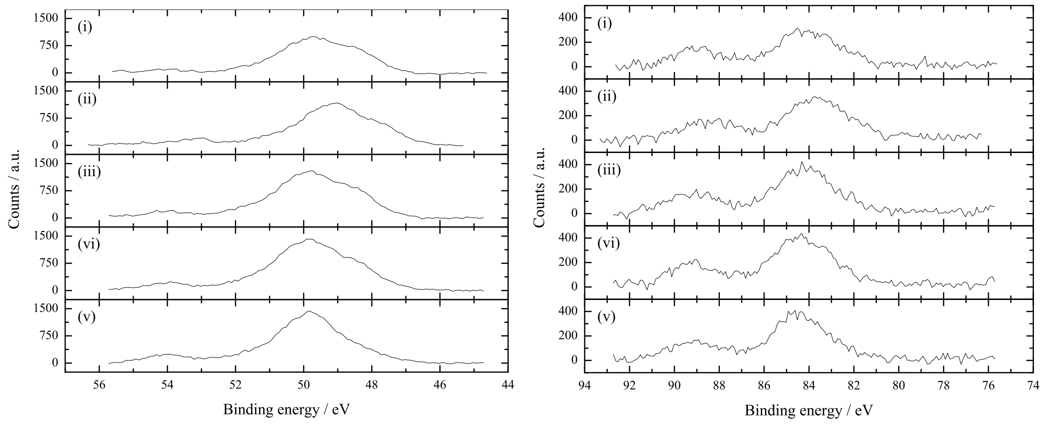

(c) Mn 3p binding energy.

(d) Mn 3s binding energy.

Figure 9.2: XPS scans at key binding energies; (i) bulk $Li_{1.05}Mn_{1.95}O_4$, (ii) bulk $Li_{1.12}Mn_{1.88}O_4$, (iii) nanoparticulate $Li_{1.05}Mn_{1.95}O_4$, (iv) nanoparticulate $Li_{1.12}Mn_{1.88}O_4$, and (v) mesoporous $Li_{1.12}Mn_{1.88}O_4$.

to the binding of O^{2-} ions to metal cations, whereas the shoulder is probably due to water or hydroxides on the surface [144, 145]. The spectrum of manganese is rather complicated and difficult to analyse. The Mn $2p$ spectrum has two main peaks due to spin-orbit coupling effects in the final state, (Mn $2p_{1/2}$ at higher energy and Mn $2p_{3/2}$ at lower energy) separated by approximately 12 eV. The $2p_{3/2}$ peak is expected between 640 and 644 eV. Values of 640.6, 641.9, and 643.2 eV have been reported for Mn^{2+}, Mn^{3+}, and Mn^{4+} respectively. The $2p_{1/2}$ peak is expected between 652.2 and 653.8 for all three oxidation states [146]. It is clear from the observed $2p$ spectra that there is no peak at 640 eV, so the presence of Mn^{2+} can be ruled out. Analysis of the $2p_{3/2}$ peak is complicated due to multiple splitting of the spectrum (up to five emission lines per oxidation state) when there are unpaired electrons in the 3 d valance band (as is the case for high spin Mn^{3+} and Mn^{4+} ions) [145, 147]. The spectra at the Mn $3p$ energy (approximately 50 eV)will also show a Li $1s$ energy at approximately 54 eV [148]. The $3s$ levels in transitions metals display exchange splitting due to interactions between the $3d$ electrons and the XPS induced $3s$ core hole. The amount of splitting depends on the oxidation state of the species involved [149]. For manganese, the splitting energies of the $3s$ levels are approximately 6.5, 5.5, and 4.5 eV for Mn^{2+}, Mn^{3+}, and Mn^{4+} respectively. A plot of these values enables the average oxidation state of the manganese in the samples studied to be deduced.

The peaks in each scan were fitted using Advantage 1.65 software from Thermo Scientific. A Shirley background was applied and deconvolution of the peaks was performed, along with a non-linear least squares fit to determine the peak positions and FWHM. Examples of fits performed on bulk $Li_{1.05}Mn_{1.95}O_4$ are shown in Figure 9.3. For all samples, two peaks were fitted to the O $1s$ spectra, three to the Mn $2p_{3/2}$ and Mn $3p$ spectrums, and two to the Mn $3s$ spectra. Peak positions for each sample are shown in Table 9.1.

The energy gap between the Mn $3s$ doublets can be plotted on a line of known energies for the different oxidation states of the manganese ion. These are 6.5 eV for Mn^{2+}, 5.5 eV for Mn^{3+}, and 4.5 eV for Mn^{4+} [149, 150]. This enables interpolation of the actual average oxidation state of the managnese ions present in the sample (Figure 9.4 and Table 9.2).

9.2 Discussion and summary

XPS measurements have enabled the surface oxidation state of bulk, nanoparticulate, and mesoporous $Li_{1+x}Mn_{1-x}O4$ samples to be probed. These measurements were only performed with a laboratory spectrometer with Al ($K_\alpha = 1486.6$ eV) source. Therefore the results really only tell us about the surface of each sample. No information can

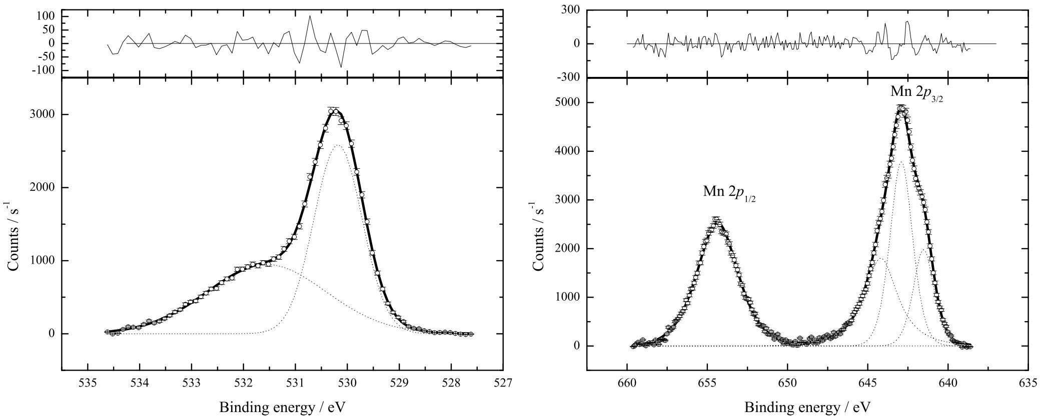

(a) O 1*s* binding energy.

(b) Mn $2p_{1/2}$ and $2p_{3/2}$ binding energy.

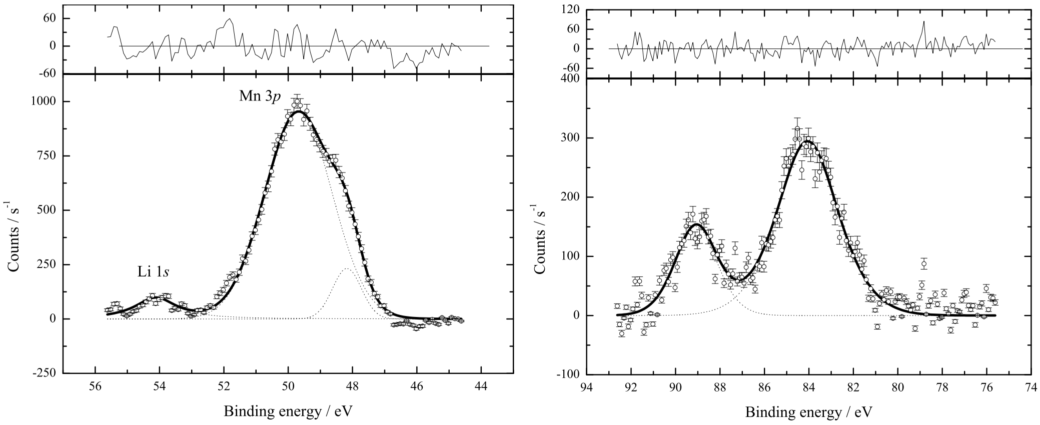

(c) Mn 3*p* binding energy.

(d) Mn 3*s* binding energy.

Figure 9.3: Fits of XPS spectra scans at key binding energies of bulk $Li_{1.05}Mn_{1.95}O_4$. Difference curves between the data and calculated fits are plotted above each spectra.

Sample	O 1s / eV	Mn 2$p_{1/2}$ / eV	Mn 2$p_{3/2}$ / eV	Mn 3s #1 / eV	Mn 3s #2 / eV	Mn 3p / eV
Bulk $Li_{1.05}Mn_{1.95}O_4$	530.6	655.1	643.5	88.7	83.6	49.1
Bulk $Li_{1.12}Mn_{1.88}O_4$	530.2	654.3	642.9	89.1	84.0	49.7
Nanoparticle $Li_{1.05}Mn_{1.95}O_4$	530.3	654.5	643.0	89.4	84.2	49.8
Nanoparticle $Li_{1.12}Mn_{1.88}O_4$	530.3	654.5	642.9	89.3	84.3	49.8
Mesoporous $Li_{1.12}Mn_{1.88}O_4$	530.1	654.6	642.9	89.3	84.4	49.8

Table 9.1: Binding energies in $Li_{1+x}Mn_{2-x}O_4$ samples derived from fitting of the spectra peaks.

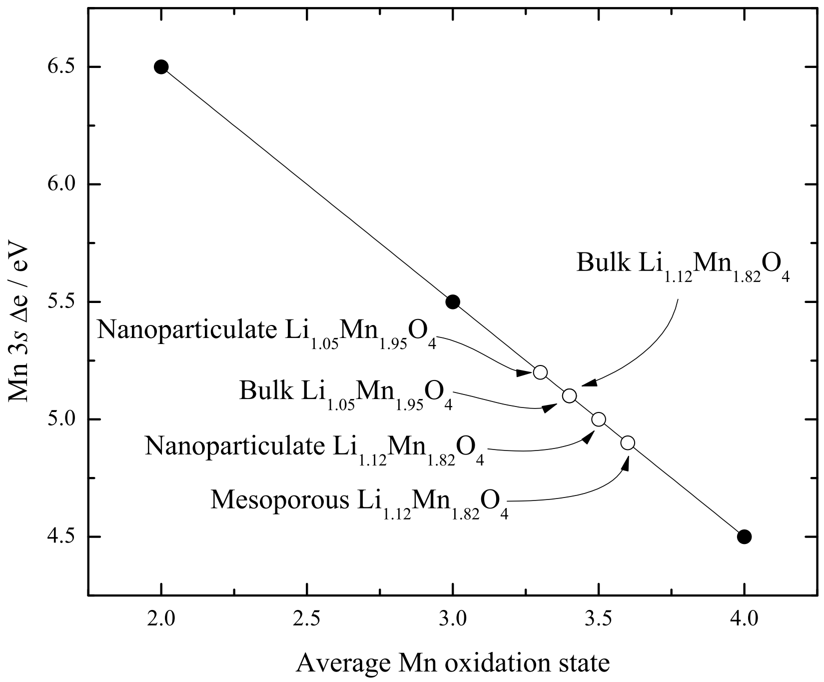

Figure 9.4: Interpolation of known Mn 3s peak splitting for known oxidation states to obtain average oxidation states in the samples analysed.

Sample	Mn 3s peak split / eV	Average oxidation state
Bulk $Li_{1.05}Mn_{1.95}O_4$	5.1	+3.4
Bulk $Li_{1.12}Mn_{1.88}O_4$	5.1	+3.4
Nanoparticle $Li_{1.05}Mn_{1.95}O_4$	5.2	+3.3
Nanoparticle $Li_{1.12}Mn_{1.88}O_4$	5.0	+3.5
Mesoporous $Li_{1.12}Mn_{1.88}O_4$	4.9	+3.6

Table 9.2: Mn 3s peak splitting and derived average oxidation states for the $Li_{1+x}Mn_{2-x}O_4$ samples.

be gained about the overall average oxidation states. Analysis splitting in the Mn 3s peaks can tell us about the average surface oxidation states. The two bulk samples with $x = 0.05$ and 0.12 show identical splitting. This suggests that despite the overall stoichiometry, the surfaces of the materials have the same properties, and the oxidation state is $Mn^{3.4+}$. The nanoparticle samples display slightly different oxidations states. For $x = 0.05$, an oxidation state of $Mn^{3.3+}$ is observed, whereas $Mn^{3.5+}$ is observed for $x = 0.12$. The mesoporous sample ($x = 0.12$) displays the highest surface oxidation state, with a value of $Mn^{3.6+}$. The general trend in increasing oxidation state with smaller amounts of Mn in the spinel samples is what one would expect. Looking at the $x = 0.12$ samples, we can see that the average surface oxidation state is greatest in the mesoporous sample, followed by the nanoparticulate sample, and smallest in the bulk sample. The reason for this could be due to the higher surface areas (90 m^2 g^{-1}, 40 m^2 g^{-1}, and 1.5 m^2 g^{-1} for the mesoporous, nanoparticulate, and bulk samples respectively). The higher surface area material will have a greater proportion of surface defects, which could have different oxidation states, and therefore alter the observed average surface oxidations state.

Chapter 10

Nanoparticulate hausmannite, Mn_3O_4

Previous work on a sample of nanoparticulate core-shell Mn_3O_4-MnO_2 has shown what is believed to be a spin-glass behaviour [151]. The sample synthesis and early characterisation are briefly summarised here.

> $Mn(acac)_2$ (acac = acetylacetonate) was heated to decomposition whilst stirred vigorously in oleylamine. This ensured multiple nucleation, and with the highly viscous oleylamine solution preventing diffusion of the growth species a monodispersed sample of small particles were formed. The particles have a Mn_3O_4 core of approximately 8 nm in diameter surrounded by approximately a 1 nm thick MnO_2 shell. The shell is also capped with an alkyl amine surfactant. HRTEM imaging reveals a spontaneously ordered cubic array of particles, which can be dispersed by the use of a non-polar solvent. XRPD measurements identify the dominant phase as Mn_3O_4. The MnO_2 shell is deduced from XPS measurements of the Mn $2p_{3/2}$, Mn $2p_{1/2}$ and the O $1s$ photoelectron peaks in the sample. The energies of these correlate closer to energies of β-MnO_2, rather than Mn_3O_4.
>
> DC susceptibility measurements show a magnetic transition at just over 40 K. There is a ZFC/FC response splitting below approximately 44 K. The transition at 40 K is believed either to be a superparamagnetic blocking temperature (T_B) or a spin-glass freezing temperature, (T_f). AC susceptibility measurements reveal an increase in the transition temperature with increasing AC frequency. The transition temperature values and applied frequency were used with both an Arrhenius expression (for superparamagnetism) Vogel-Fulcher function (for spin-glasses) to determine what type of magnetic properties the nanoparticles possessed. Values derived pointed towards the latter, a spin-glass material with interactions between the core and shell only.

10.1 Initial nanoparticulate sample

To study this spin-glass, further measurements were carried out upon the previously synthesised sample using muon spin relaxation.

10.1.1 MuSR (ISIS) μSR study

A thin pellet of nanoparticulate $\mathrm{Mn_3O_4}$ sample was prepared and held on a silver sample plate and placed in the cryostat of the MuSR instrument at ISIS [53]. Due to technical difficulties at the ISIS facility at the time of the experiment, these measurements were split into two separate beam time allocations. Initial measurements at temperatures above the freezing temperature derived from magnetic measurements were performed with a 20 G transverse field to determine the forward and backward detector efficiency asymmetries, α. These were determined using the WIMDA analysis program [152] to be 1.102 and 1.122 for the two different experiments (Figure 10.1). Data were collected at varying temperatures on the MuSR instrument cooling through the magnetic transition in applied longitudinal fields of 100, 1000 and 2500 G. The relaxation functions of the muons were modelled with a stretched exponential curve [153] (Equation 10.1) to determine: the initial asymmetry a_0, the characteristic muon relaxation rate λ, and the stretching component β. This expression generally describes muon spin relaxation well in inhomogeneous systems as they are cooled towards a glassy freezing point.

$$a = a_0 \exp\left[-\lambda t^{\beta}\right] \tag{10.1}$$

The stretched exponential form typically has a β value close to 1 (standard exponential) at temperatures well above the glass freezing temperature (where the sample is in a paramagnetic state), suggesting that all muon relaxation going on within the sample is under a dynamic field with a single characteristic time constant. As the sample cools parts of the material slowly start to freeze and create regions where the muon is under a static field and so alters the relaxation function. Different areas in the material will freeze at different times and with different magnetic orientations. It is expected that the β value will drop to approximately $\frac{1}{3}$ of its starting value for a fully frozen spin-glass. For these models it was observed that the % asymmetry (a) generally tended to drop off (but never plateaued out) throughout the time measurement window ($\approx$ 20 µs) so the baseline was set at exactly zero in all fits (Figure 10.2). Derived parameters from the models are shown in Table 10.1 and Table 10.2. The application of static external fields causes a slight decoupling of the muon and the internal field it feels. This can alter the relaxation rates slightly and provide information on strength of the local field the muon experiences.

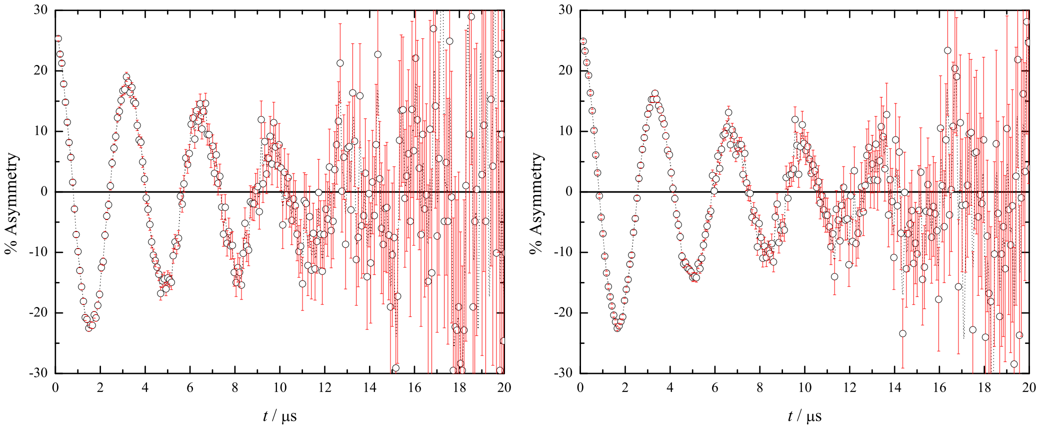

(a) 1st experiment: 20 G transverse field at 100 K .

(b) 2nd experiment: 20 G transverse field at 50 K .

Figure 10.1: Transverse field measurements on nanoparticulate Mn_3O_4 with the MuSR instrument.

Plots of the derived parameters from the first MuSR experiment in a 100 G field are shown in Figure 10.3. These clearly show that there is a sudden transition occurring at 40.0(5) K, in agreement with the initial magnetic susceptibility data. The decrease in initial asymmetry, a_0 indicates that some of the magnetic moments are no longer fluid and have frozen, and therefore alter the proportion of positrons emitted from the decaying muons in the forward and backward directions. The change in relaxation rate, λ indicates a slowing down in the muon relaxation rate, and the change in β from a value close to 1 to a much lower value of ≈ 0.15 suggests there is an increase in static fields present within the sample. The value of 0.15 is a bit lower than expected and probably an artefact. Comparison of these parameters to higher field measurements in the second MuSR experiment indicate that the freezing process is at a higher temperature with higher fields (Figure 10.3(d)). This is expected with this type of material, as the magnetic moments in the glass will need higher energies to overcome the applied magnetic field to move about. Unfortunately, more detailed models of spin-glasses cannot be applied to the data, such as fitting a semiclassical dynamical Kubo-Toyabe model [154, 155]. This is believed to be because the relaxation due to the static component (frozen glass) fields felt by the muons in the material are happening too fast to be resolved in time in the MuSR instrument. Some form of relaxation is occurring at very short times, as can be seen by a sharp drop in asymmetry at times close to 0.5 μs. The application of a magnetic field in this case introduces an additional static component to the field acting on implanted muons, which can be seen in some of the data taken close to and about T_f (Figure 10.4).

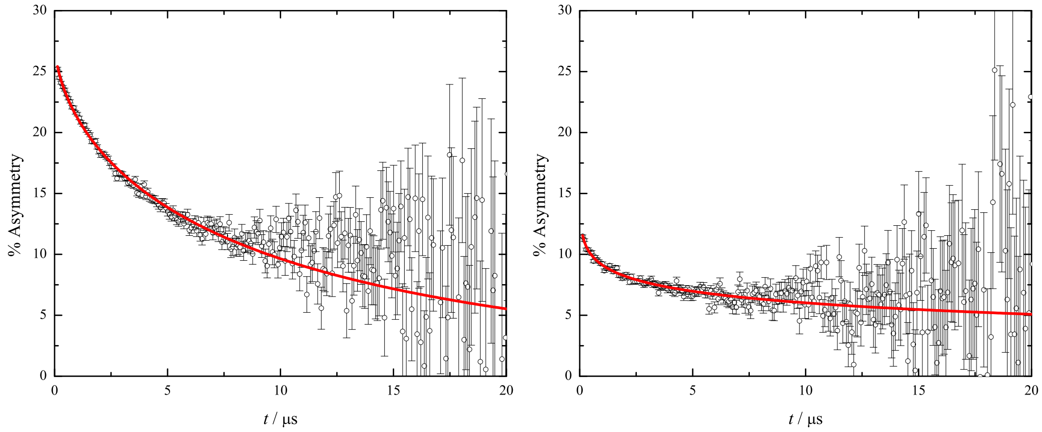

(a) 46 K at 100 G. (b) 36 K at 100 G.

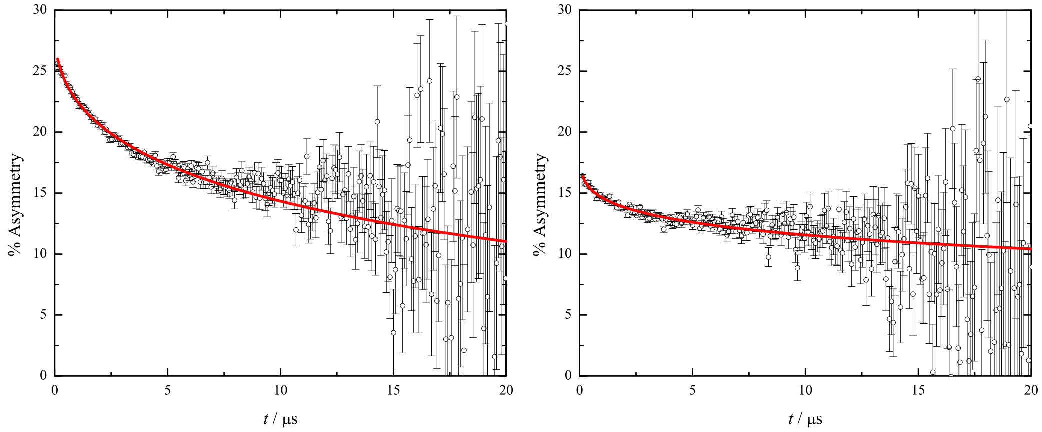

(c) 46 K at 1000 G. (d) 36 K at 1000 G.

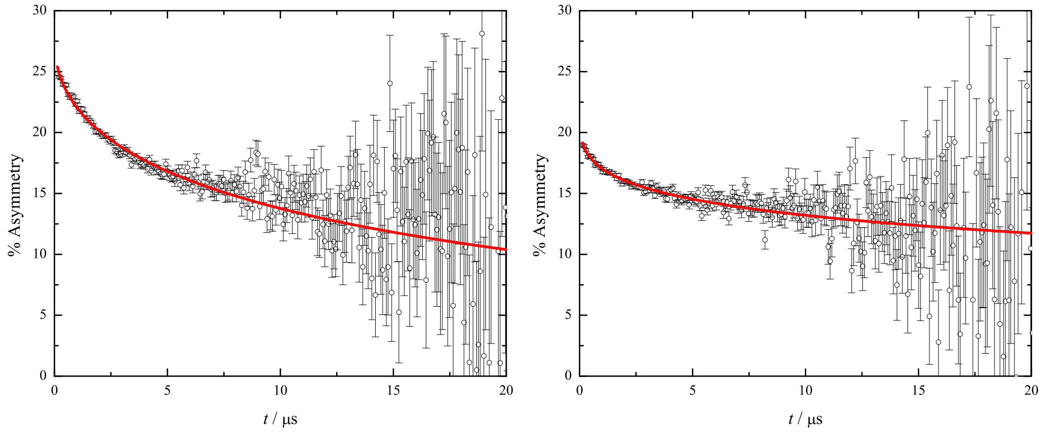

(e) 46 K at 2500 G. (f) 36 K at 2500 G.

Figure 10.2: % Asymmetry relaxation plots from MuSR for nanoparticulate Mn_3O_4 at different longitudinal fields.

T / K	a_0 / %	λ / s^{-1}	β	χ^2
10	18(4)	0.05(6)	0.14(4)	1.454
15	16(2)	0.03(2)	0.17(4)	1.274
20	15.0(13)	0.021(5)	0.21(4)	1.317
25	15.6(15)	0.026(9)	0.20(4)	1.242
30	16.6(16)	0.05(2)	0.20(3)	1.112
32	16.6(14)	0.07(3)	0.21(3)	1.276
34	16.2(13)	0.08(2)	0.23(3)	1.504
35	18(2)	0.15(9)	0.18(3)	1.241
35.5	18(2)	0.17(9)	0.19(3)	1.443
36	18.0(17)	0.15(6)	0.21(3)	1.224
36.5	27(6)	2(2)	0.14(3)	1.210
37	30(7)	3(5)	0.13(3)	1.222
37.5	37(9)	11(23)	0.12(2)	1.350
38	22.32(8)	0.281(19)	0.200(4)	1.477
38.5	26(2)	0.5(2)	0.20(2)	1.356
39	25.3(16)	0.28(8)	0.224(18)	1.656
39.5	22.2(6)	0.147(11)	0.328(16)	1.642
40	22.5(4)	0.122(5)	0.376(15)	1.918
40.5	25.3(3)	0.128(2)	0.478(12)	1.533
41	24.6(3)	0.119(2)	0.479(13)	1.661
42	26.3(2)	0.1208(16)	0.534(11)	1.803
43	27.00(19)	0.1194(14)	0.569(11)	1.529
44	27.24(18)	0.1151(13)	0.584(11)	1.657
45	26.1(2)	0.1055(14)	0.527(12)	1.696
45.5	26.91(16)	0.1070(11)	0.616(11)	1.693
46	27.26(16)	0.1064(11)	0.619(11)	1.699
48	27.19(15)	0.0997(10)	0.643(11)	1.554
50	27.45(14)	0.0950(10)	0.644(12)	1.523
55	26.73(12)	0.0799(10)	0.694(13)	1.683
60	26.73(11)	0.0757(10)	0.717(13)	1.466
70	26.42(10)	0.0644(10)	0.755(15)	1.487
80	26.08(9)	0.0593(11)	0.821(16)	1.232
90	26.13(9)	0.0525(11)	0.807(17)	1.244
100	26.09(8)	0.0518(11)	0.842(18)	1.681

Table 10.1: Derived parameters to Equation 10.1 for 100 G MuSR data (1st experiment). Derived parameters at 36.5–37.5 K can clearly be seen to be highly correlated and have significant errors.

T / K	100 G				1000 G				2500 G			
	a_0 / %	λ / s^{-1}	β	χ^2	a_0 / %	λ / s^{-1}	β	χ^2	a_0 / %	λ / s^{-1}	β	χ^2
34									23.3(11)	0.0054(5)	0.21(3)	1.126
36					19.8(9)	0.0071(7)	0.24(3)	1.311	22.5(7)	0.0097(8)	0.27(3)	1.396
37	34(17)	0(3)	0.08(4)	1.261	20.4(8)	0.0083(7)	0.25(3)	1.271	22.3(6)	0.0101(9)	0.30(3)	1.479
38	28.2(5)	0.041(12)	0.087(3)	1.235	23.6(18)	0.012(3)	0.18(3)	1.327	23.4(6)	0.0137(9)	0.29(2)	1.201
39	41.7(11)	11(4)	0.0616(12)	1.250	23.3(12)	0.0157(18)	0.22(3)	1.272	23.5(5)	0.0191(10)	0.33(2)	1.316
39.5	41.7(11)	11(4)	0.07(4)	1.302	24.0(12)	0.020(2)	0.22(2)	1.093	24.3(5)	0.0227(10)	0.32(2)	1.394
40	26.1(4)	0.039(7)	0.115(4)	1.250	23.5(8)	0.0197(11)	0.26(2)	1.315	24.0(4)	0.0248(11)	0.358(2)	1.379
40.5	22.7(4)	0.0137(16)	0.152(8)	1.681	24.7(8)	0.0246(15)	0.26(2)	1.453	24.9(4)	0.0275(10)	0.353(19)	1.208
41	26.4(3)	0.035(4)	0.145(5)	1.590	25.0(7)	0.0274(12)	0.29(2)	1.217	25.2(3)	0.0328(11)	0.395(17)	1.350
41.5	26.0(3)	0.033(3)	0.163(6)	1.653	24.7(4)	0.0327(10)	0.355(18)	1.326	26.6(4)	0.0338(10)	0.361(17)	1.430
42	27(2)	0.026(8)	0.18(2)	1.744	26.8(5)	0.0311(10)	0.330(17)	1.529	26.6(4)	0.0371(12)	0.398(18)	1.286
42.5					26.7(4)	0.0408(10)	0.382(16)	1.308	27.3(4)	0.0417(12)	0.404(17)	1.491
43	25.5(5)	0.0378(13)	0.323(17)	2.119	27.0(3)	0.0485(11)	0.432(15)	1.596	28.0(4)	0.0437(11)	0.402(17)	1.359
43.5	26.7(5)	0.0456(13)	0.346(16)	1.410	27.6(3)	0.0516(10)	0.438(14)	1.457	27.4(3)	0.0488(12)	0.455(17)	1.427
44	26.5(3)	0.0412(10)	0.391(16)	1.828	28.2(3)	0.0455(10)	0.424(14)	1.951	27.6(3)	0.0521(12)	0.474(16)	1.501
46	27.5(3)	0.0459(10)	0.462(14)	1.505	28.7(3)	0.0433(10)	0.450(14)	1.405	27.7(3)	0.0467(12)	0.480(17)	1.658
48	26.86(19)	0.0485(11)	0.534(15)	1.149	27.8(2)	0.0417(11)	0.502(15)	1.329				
50	27.20(19)	0.0434(11)	0.518(15)	1.582	27.3(18)	0.0438(11)	0.544(15)	1.434				

Table 10.2: Derived parameters to Equation 10.1 for 100, 1000, and 2500 G MuSR data (2nd experiment).

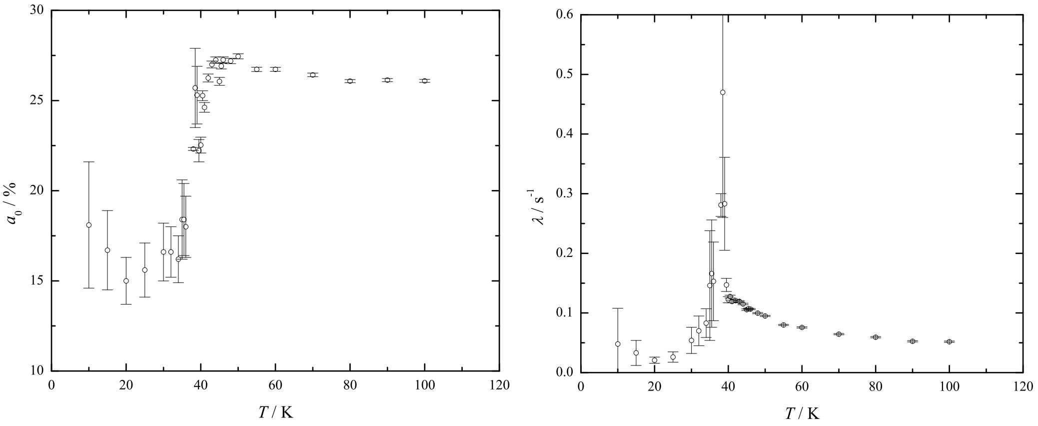

(a) a_0.

(b) λ.

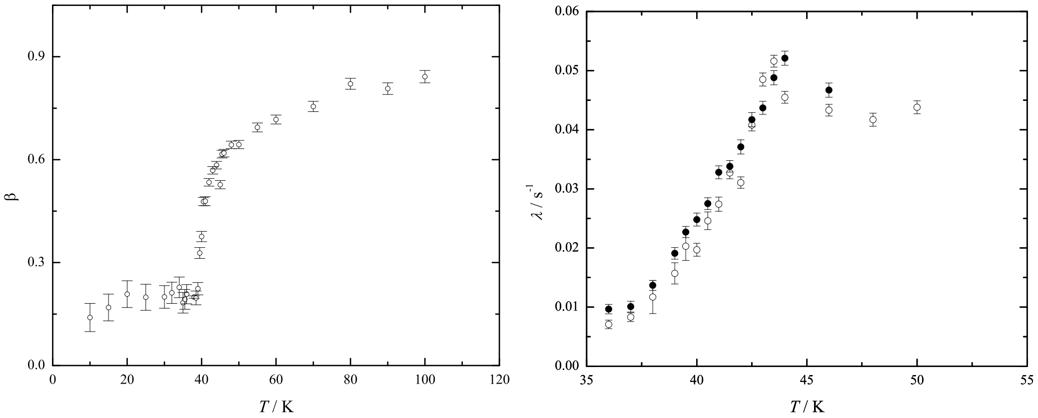

(c) β.

(d) 2nd experiment λ.

Figure 10.3: Plots of stretched exponential parameters from MuSR data taken in 100 G. Data points at 36.5, 37, and 37.5 K have been removed from graphs (a)–(c). (d) shows lambda determined from 1000 G (open symbols) and 2500 G (filled symbols).

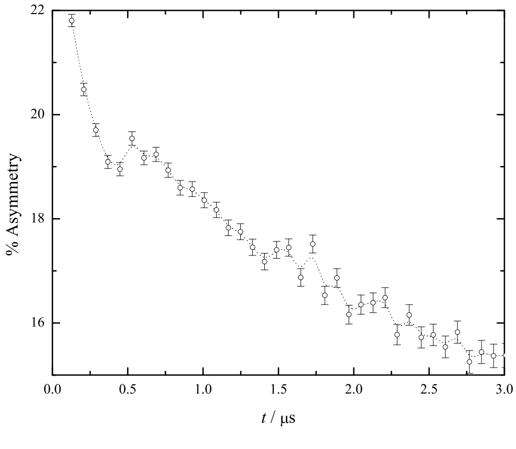

Figure 10.4: Low t relaxation of nanoparticulate Mn_3O_4 on MuSR at 43 K at 100 G.

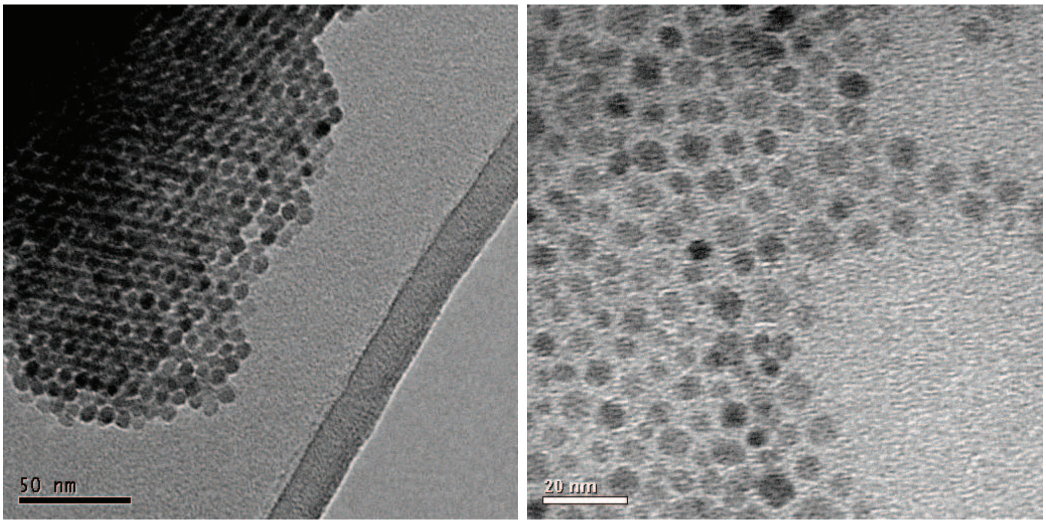

(a) Nanoparticulate Mn_3O_4 array. (b) Disperesd nanoparticulate Mn_3O_4.

Figure 10.5: TEM images of nanoparticulate Mn_3O_4 (Courtesy of Dr Feng Jiao).

10.2 Second nanoparticulate sample

To investigate the muon relaxation further, a second experiment was carried out on the General Purpose Surface (GPS) muon instrument [55] at the Paul Scherrer Institut, Switzerland. The muons at this facility arrive at the instrument in a slightly different way than the setup at ISIS. Here each muon is individually allowed into the sample and then detected, whereas a bunch of muons are implanted and detected at ISIS. This allows a greater time resolution at PSI for fast relaxing muons. For this experiment, a second sample of nanoparticulate Mn_3O_4 was prepared using the same method as previously described by Dr Feng Jiao (Lawrence Berkley Laboratory, USA).

10.2.1 Preliminary characterisation

Preliminary characterisation of the nanoparticulate Mn_3O_4 was carried out on the sample to ensure it had similar properties to the earlier sample. TEM (Figure 10.5) showed the same array of nanoparticles, and XRPD (Figure 10.6) confirmed the hausmannite phase (courtesy of Dr Feng Jiao).

10.2.2 Magnetic measurements

DC susceptibility (Figure 10.7(a)) measurements showed the sample had a similar profile to that reported for the previous sample. The profile shows a ZFC-FC splitting, with a bifurcation point at ≈ 46 K. Below this point, the ZFC profile reaches a maximum

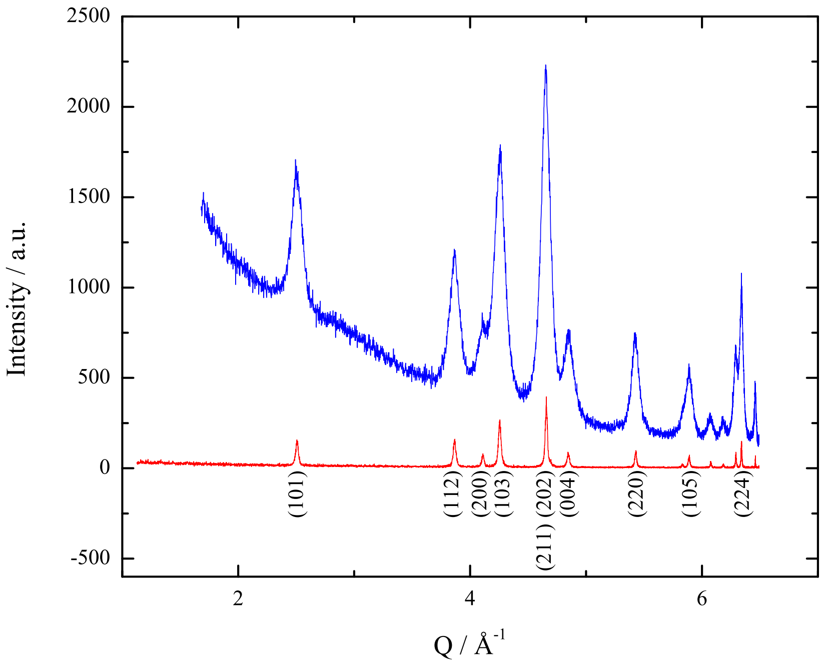

Figure 10.6: XRPD pattern of bulk (lower) and nanoparticulate (upper) Mn_3O_4 measured with a Fe K_α source ($\lambda = 1.93604$ Å). The pattern has been indexed with an $I4_1/amd$ tetragonal cell.

at 33 K, believed to be the spin-glass freezing temperature, T_f. Above the bifurcation point, the ZFC and FC profiles show an almost unchanging susceptibility response to increasing temperature. A Curie-Weiss fit (Equation 2.14) of the ZFC high temperature data ($T > 80$ K, $\chi_0 = 9.8(5) \times 10^{-9}$ mol m^{-3}) has typical parameters to that of a ferro- or ferrimagnet. A positive Weiss temperature of 30.7(15) K is observed, with a Curie constant of 1.16(6) $\times 10^{-5}$ m^3 K mol^{-1}. The Curie temperature can be deduced from a plot of $\frac{d\chi T}{dT}$, (Figure 10.7(c)). This is determined to be 41.5(5) K, in good agreement with literature values of bulk Mn_3O_4 at 42 K [156, 157]. The nature of the core-shell material and its capping layer, make calculating an effective magnetic moment per magnetic ion difficult, because the true mass of Mn present in the sample is not known (due to the alkyl amine capping around each nanoparticle).

The response of the nanoparticles to increasing and decreasing magnetic fields at 5 and 50 K was also measured (Figure 10.8). The 50 K trace shows typical behaviour of a paramagnetic material, that is no hysteresis. The deviation from a horizontal line suggests that there is small amount of diamagnetic material present. The 5 K trace however shows an unusual open hysteresis loop. From this we can make several observations. Firstly, as the loop is open, we know that the material is ferrimagnetic at 5 K. Secondly, the total loop is a sum of all the different magnetic response occurring in

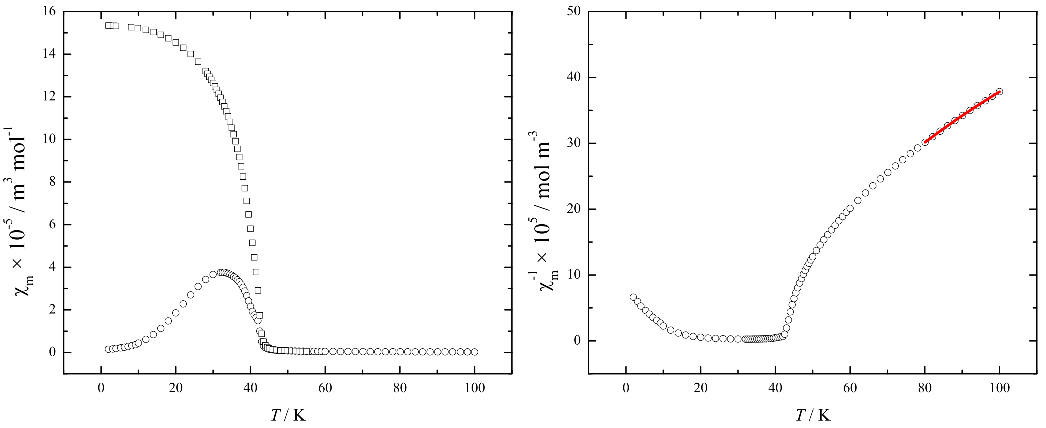

(a) χ_m vs. T. ZFC (circles) and FC (squares).

(b) χ_m^{-1} vs. T with a Curie-Weiss fit for T $\geq$ 80 K.

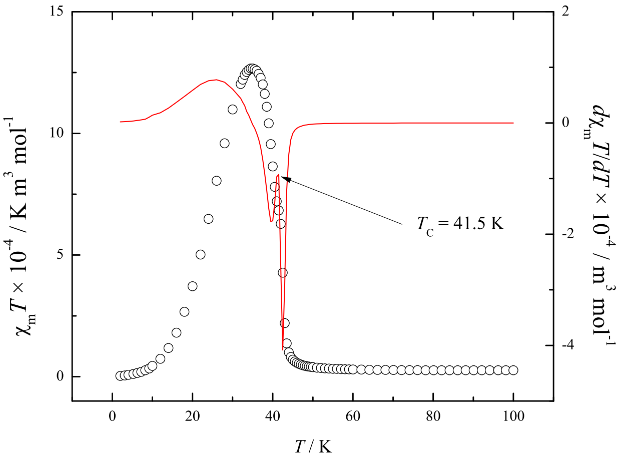

(c) $\chi_m T$ vs. T (data points) and $\frac{d\chi_m T}{dT}$ (line).

Figure 10.7: Graphs of DC susceptibility of nanoparticulate Mn_3O_4.

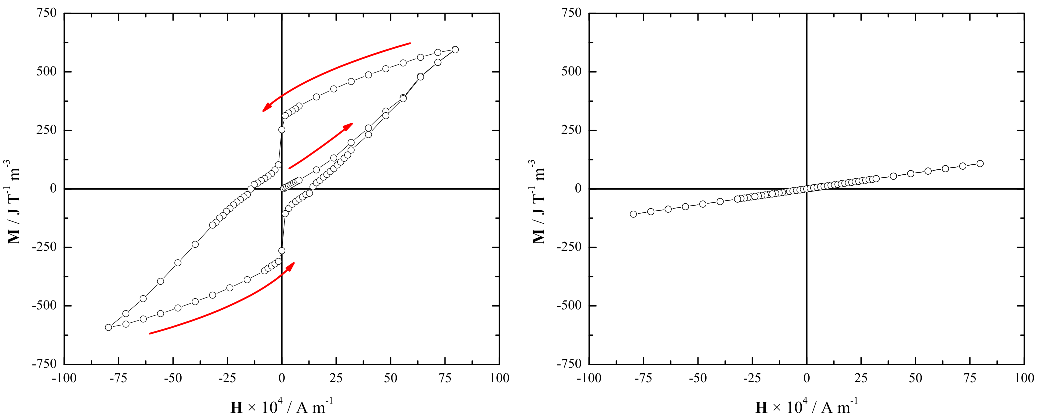

(a) 5 K.

(b) 50 K.

Figure 10.8: Magnetic hysteresis graphs of nanoparticulate Mn_3O_4.

the sample. The shape with quite distinct steps near $\mathbf{H} = 0$ suggests that there are two main components contributing to the total signal: one, a hard magnetic material with a large coercive field which causes the main loop opening; and the second, a soft magnetic material which has a small coercive field enabling spin directions to be reversed easily as soon as the field direction changes. This is consistent with the core-shell model, where it is proposed that the core is ferrimagnetic Mn_3O_4 (a hard magnetic material) and the shell is antiferromagnetic MnO_2.

AC susceptibility measurements were then performed on the material at temperatures around T_f. These were performed at frequencies of: 1, 6, 40, 250, and 997 Hz. The real (χ') and imaginary (χ'') components of the response are shown Figure 10.9. A clear increase of the freezing temperature with higher frequencies can be observed in the real part of the susceptibility. Each trace has been fitted with a gaussian curve (Equation 10.2, where a is the height, b the peak centre, and c the width) to determine the peak maximum, typical examples of which are shown in Figure 10.10. The peak positions are given in Table 10.3.

$$y = y_0 + a \exp\left[-\frac{(x-b)^2}{2c^2}\right] \qquad (10.2)$$

The variation of χ' peak position can be plotted against $\ln \nu$ (frequency). For a superparamagnet, an Arrhenius law can be fitted, (Equation 10.3) to the data. This has been performed, yielding unphysical values for the characteristic relaxation time ($\nu_o \approx 2.4 \times 10^{90}$ Hz) and activation energy to spin reversal ($E_a/k_b = 7000$ K). Physically reasonable values for the former would be in the region of 10^{10}–10^{12} Hz [158]. We can

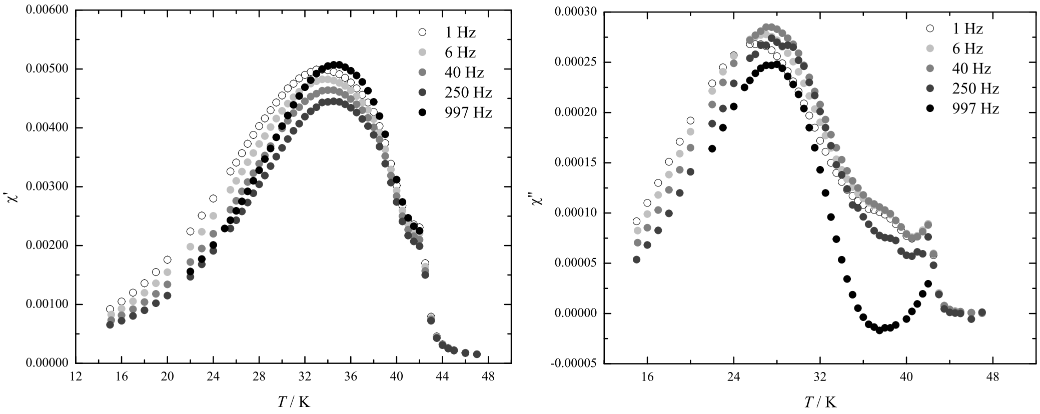

(a) χ'.

(b) χ''.

Figure 10.9: The real and imaginary components of the AC susceptibility of nanoparticulate Mn_3O_4.

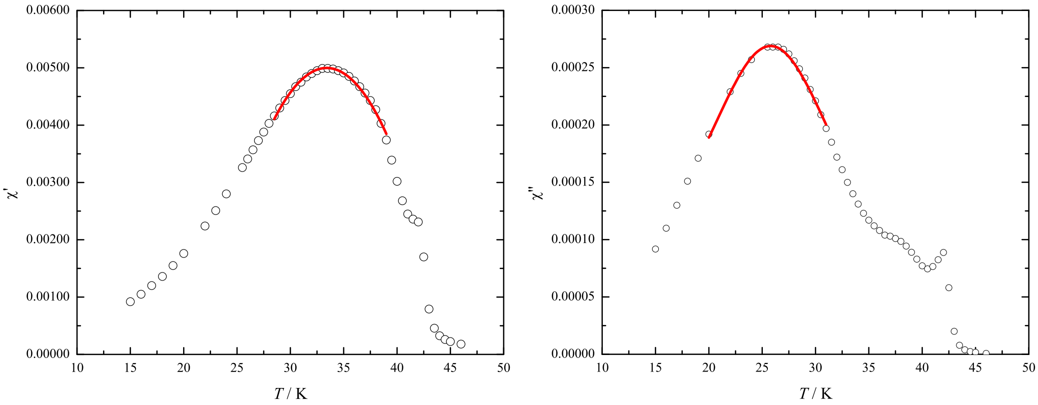

(a) χ'.

(b) χ''.

Figure 10.10: Gaussian fits to AC susceptibility data of nanoparticulate Mn_3O_4 at 1 Hz.

ν / Hz	Peak Position / K χ'	 χ''
1	33.491(10)	25.90(2)
6	33.795(7)	26.46(3)
40	34.087(11)	27.23(3)
250	34.426(10)	27.74(7)
997	34.633(12)	27.27(5)

Table 10.3: AC susceptibility peak positions.

T_o / K	$\ln \nu_0$	E_a/k_b / K	χ^2
32	15.3(11)	23(2)	0.265
31	21.5(11)	54(3)	0.119
30	27.6(11)	97(5)	0.069
29	33.7(12)	152(6)	0.046
28	39.7(12)	219(7)	0.034
27	45.8(12)	298(9)	0.027
26	51.8(13)	390(10)	0.022

Table 10.4: Derived parameters to Equation 10.4 with T_o set at specific values.

therefore assume that the material is not a superparamagnet, and try fitting to an empirical law which describes the viscosity of supercooled liquids, known as the Vogel-Fulcher law (Equation 10.4) [158].

$$\nu = \nu_\text{o} \exp\left[\frac{-E_\text{a}}{k_\text{b} T_\text{f}}\right] \tag{10.3}$$

$$\nu = \nu_\text{o} \exp\left[\frac{-E_\text{a}}{k_\text{b}\left(T_\text{f} - T_\text{o}\right)}\right] \tag{10.4}$$

Here, ν_o is the characteristic relaxation time of the spin-glass, E_a relates to the activation energy barrier of magnetisation reversal, and T_o is believed to be connected to the inter-particle coupling energy. These parameters are highly correlated, therefore making reliable fits very difficult. Initial fits were performed by varying the T_o parameter manually. Derived parameters (with the constrained T_o value) are shown in Table 10.4. Plots of these two types of fits are shown in Figure 10.11 with T_o set at 31 K for the Vogel-Fulcher fit . Allowing all three parameters to refine independently, even starting from suitable values determined from preliminary fits (Table 10.4), was not successful. The characteristic relaxation frequency ν_o settles at $\approx 2.6 \times 10^{63}$ Hz, $T_\text{o} \approx 10$ K, and $E_\text{a}/k_\text{b} = 3000$ K, however the errors observed on all these values is in the order of 2–3 times the value. Further fits were performed by fixing the characteristic relaxation times to physically reasonable values between 10^{10}–10^{12} Hz, allowing T_o and E_a/k_b to refine independently. Derived parameters from this are shown in Table 10.5. Comparisons of data presented in Table 10.4 and Table 10.5 show that the freezing temperature is probably very close to 30 K. However due to the correlation of parameters in the Vogel-Fulcher fit further measurements (such as muon spin relaxation) are required to determine dynamics in the material.

$\ln \nu_0$	T_o / K	$E_\mathrm{a}/k_\mathrm{b}$ / K	χ^2
23.03	30.72(17)	65(4)	0.101
25.33	30.34(17)	80(4)	0.082
27.63	29.97(18)	98(5)	0.068

Table 10.5: Derived parameters to Equation 10.4 with $\ln \nu_0$ set at specific values.

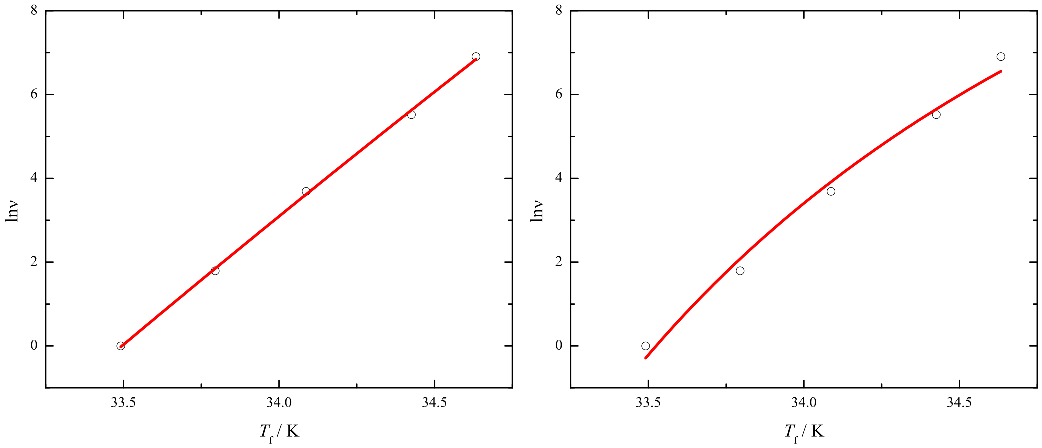

(a) Arrhenius fit.

(b) Vogel-Fulcher fit.

Figure 10.11: $\ln \nu$ vs. T_f for χ' with a fits to Equation 10.3 and Equation 10.4 ($T_\mathrm{o} = 31$ K).

T / K	a_0 / %	λ / s^{-1}	β	χ^2
10	9.4(5)	0.38(7)	0.33(3)	1.216
20	10.4(7)	0.78(19)	0.30(3)	1.193
37	29(3)	14(5)	0.260(16)	1.211
37.5	26.1(18)	8.2(19)	0.290(15)	1.137
38	24.0(10)	5.4(11)	0.312(15)	1.209
38.5	22.3(9)	3.2(4)	0.366(14)	1.158
39	22.6(9)	2.9(3)	0.373(14)	1.286
39.5	21.7(7)	2.07(18)	0.407(14)	1.232
40	23.5(7)	2.12(19)	0.389(12)	1.123
40.5	21.7(5)	1.43(9)	0.453(13)	1.295
41	22.5(5)	1.33(8)	0.447(12)	1.210
42	22.7(4)	1.00(3)	0.552(12)	1.203
43	22.4(2)	0.611(9)	0.758(12)	1.301
50	22.53(17)	0.366(4)	1.02(2)	1.252

Table 10.6: Derived parameters to Equation 10.1 for zero field GPS data.

10.2.3 GPS (PSI) μSR study

Measurements on the GPS instrument were performed by holding the sample in a aluminium foil in the cryostat. A 100 G transverse field measurement was initially performed at 50 K to determine an estimate of the detector efficiency asymmetry using WIMDA [152]. This gave a parameter, $\alpha = 1.105$ (Figure 10.12(a)). Data were then collected at a variety of temperatures for approximately 6 million counts in the forward detector bank. Further patterns were collected with a 200 G longitudinal field. Unfortunately, insufficient experimental time was available to follow the relaxation through the freezing transition, so only a small data set were collected. Each pattern was modelled with a stretched exponential relaxation function (Equation 10.1) to determine: the initial asymmetry a_0, the characteristic muon relaxation time λ, and the stretching component β. For these models, the baseline was set at exactly zero. Derived parameters from the zero field measurements are shown in Table 10.6. Parameters from the field measurements are shown in Table 10.7. Plots of these parameters indicate that the freezing transition (determined from the relaxation function) is lower than in the first sample. As with the MuSR data, application of a magnetic field decouples the muon from the internal field, therefore slowing down the relaxation rate λ, enabling the relaxation behaviour to be observed at very short times (Figure 10.14). It can clearly be seen from the magnetic susceptibility and muon data that the second sample of nanoparticulate Mn_3O_4 has a slightly different magnetic freezing temperature T_f when compared to the original sample studied. This could be due to slightly different synthesis conditions giving rise to a small difference in either particle size or core-shell volume ratio.

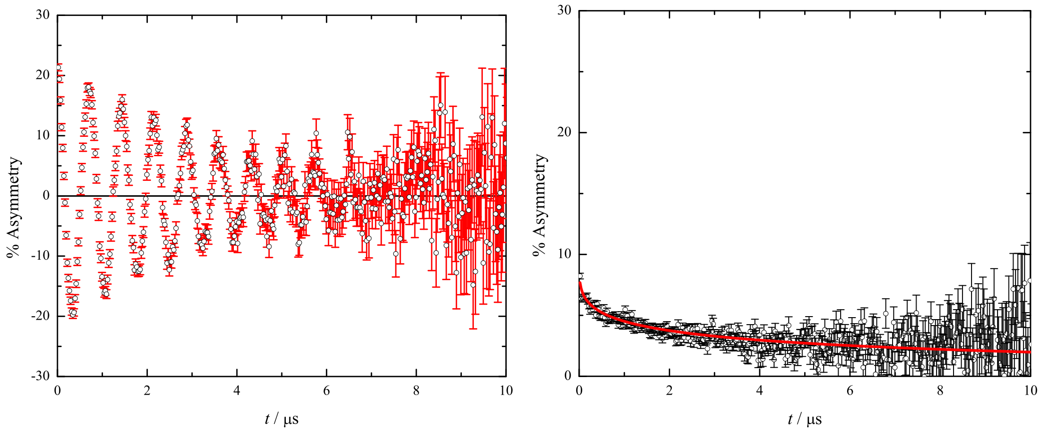

(a) 100 G transverse field at 50 K .

(b) 10 K.

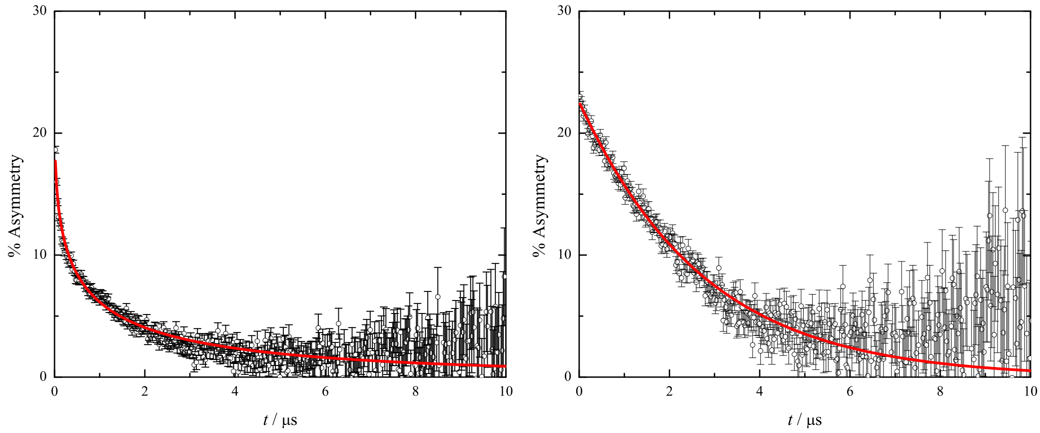

(c) 40 K.

(d) 50 K.

Figure 10.12: Transverse and zero field measurements on nanoparticulate Mn_3O_4 with the GPS instrument. Stretched exponential fits are shown on the zero field data.

T / K	a_0 / %	λ / s^{-1}	β	χ^2
38	38(6)	30(30)	0.164(16)	1.274
39	25.8(17)	2.3(6)	0.240(15)	1.547
40	26.3(14)	1.1(3)	0.249(14)	1.328
41	21.5(5)	0.325(19)	0.383(15)	1.196
42	25.1(5)	0.312(19)	0.359(13)	1.376

Table 10.7: Derived parameters to Equation 10.1 for 200 G field GPS data.

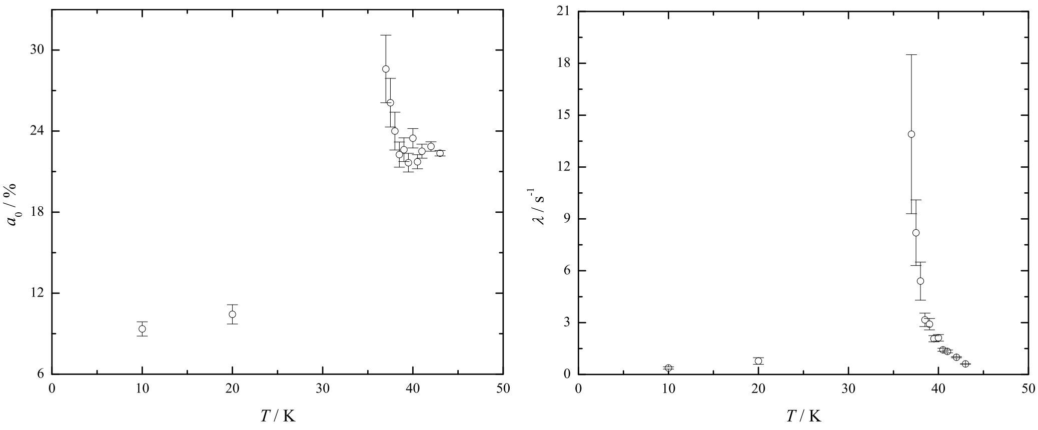

(a) a_0.

(b) λ.

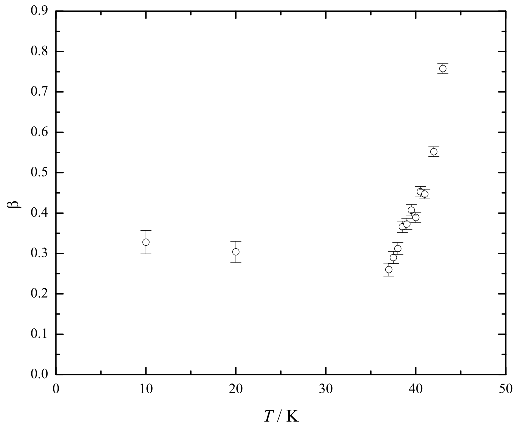

(c) β.

Figure 10.13: Plots of stretched exponential parameters from GPS data taken in 0 G.

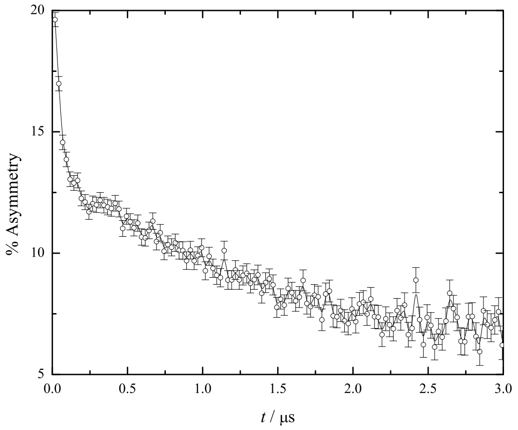

Figure 10.14: Low t relaxation of nanoparticulate Mn_3O_4 on GPS at 40 K at 200 G.

10.3 Summary and discussion

Initial muon studies on the previously synthesised and characterised sample of nanoparticulate Mn_3O_4 show that there is clearly some form of dynamic magnetism in the sample (e.g. Figure 10.2(b)) down to at least 36 K. At high temperatures, the value of the exponent β from Equation 10.1 is quite high, however it is never equal to 1 which would imply it is not a simple paramagnet over the temperature range studied. As the temperature is reduced, β decreases, showing a range of relaxation times. This indicates that the muon senses a range of internal magnetic fields indicating inhomogeneities within the magnetic ordering in the individual nanoparticles (a spin-glass). A sudden change in asymmetry indicates a freezing temperature at $\approx$ 40 K in agreement with AC susceptibility data. Some form of dynamics can be observed at very short t, and a second experiment at PSI on the GPS instrument was carried out to see if these could be studied further. For the second study, a new sample had to be prepared. Magnetic measurements indicated that the material had very similar properties to the first sample, however with a lower freezing temperature of $\approx$ 33 K. GPS measurements showed a freezing temperature again in the 40 K region, though in this case there was a significant reduction to 37 K. Dynamics were also observable at short t. Unfortunately, due to time constraints of the experiment, not many temperature sets were obtained, it is however likely that the dynamic relaxation occurring below 0.5 µs is still too fast for these types of techniques to analyse further. The fast relaxation is due to the considerable magnitude of the static field present from the manganese moments present in the sample.

From all of these measurements we can conclude that the freezing temperature depends upon the applied frequency in magnetometry measurements which indicates a spin-glass state, rather than a superparamagnet. The freezing temperature also depends upon the specific sample as shown by measurements taken in the two different samples over the course of this work. The nanoparticles have been shown to be non-interacting, so the magnetic dynamics must be occurring within the particles themselves. Photoelectron spectroscopy carried out previously suggests that the sample is an example of a core-shell material. The interaction between the Mn_3O_4 core and MnO_2 shell provides a source of the freezing mechanism with a strongly random element. This is because the Mn_3O $_4/MnO_2$ interface is highly unlikely to be uniform around the entire particle. Different areas will have different thicknesses of MnO_2, leading to dislocations and defects. This causes different areas on the surface of each nanoparticle to have slightly different crystallographic and magnetic properties. These will then freeze at slightly different temperatures, creating competing domains within one particle, and lead to a an overall glassy system. Future measurements with very high AC susceptibility measurements could provide further information on the overall dynamics in the particles.

Chapter 11

Conclusions and further work

This thesis has looked for the first time at the magnetic and crystallographic properties of a variety of the first row transition metal oxides in mesoporous forms, as well as a couple of nanoparticle samples. Samples have been analysed with SQUID magnetometry, neutron powder diffraction, X-ray photoelectron spectroscopy and muon spectroscopy to try to understand the collective magnetic properties of the metal ions within the crystal structures. These results are summarised in Table 11.1.

11.1 Conclusions

The first sample to be studied, mesoporous hematite (Chapter 4) has provided the most interesting results so far. Unlike bulk hematite, the mesoporous form does not undergo a well defined first-order magnetic re-orientation transition upon cooling down from room temperature to 2 K. This is due to a perturbation to the fine balance of anisotropy terms in hematite which when all added together determine the spin direction [159–161]. The spin re-orientation at T_{M} arises from a change of sign of the total magnetic anisotropy E_{total} (Equation 11.1).

$$E_{\mathrm{total}} = E_{\mathrm{mca}} + E_{\mathrm{shape}} + E_{\mathrm{surface}} \tag{11.1}$$

This term is made up of several individual contributions; the magnetocrystalline anisotropy E_{mca} (involves non-cubic components of the ligand field in conjunction with spin-orbit coupling), the shape anisotropy E_{shape} (long-range dipolar anisotropy), and the surface anisotropy E_{surface} (lower crystal symmetry and reduced co-ordination numbers). In bulk hematite the two dominant terms are the magnetocrystalline anisotropy and the shape anisotropy. These two terms are very similar in magnitude (2 % difference) but have opposite signs. At low temperatures in bulk hematite, the positive E_{mca} term dominates over the E_{shape} term, causing the magnetic moments to be aligned parallel to the hexagonal axis. As T is raised, the negative E_{shape} term has a greater influence, until it forces the spins to re-orientate into the *ab* plane, causing

Material	Comments
Mesoporous α-Fe_2O_3 *†‡	Suppression of the Morin transition ($T_\mathrm{M} = 259$ K in bulk)
Mesoporous Cr_2O_3 *†	303 K $< T_\mathrm{N} <$ 315 K cf. bulk where 315 K $< T_\mathrm{N} <$ 320 K
Mesoporous Co_3O_4 *†	$T_\mathrm{N} \approx$ 20–26 K cf. bulk where $T_\mathrm{N} \approx$ 28 K
Mesoporous NiO *†	$T_\mathrm{N} \approx$ 500 K cf. bulk where $T_\mathrm{N} \approx$ 525 K
Mesoporous α-MnO_2 *	$T_\mathrm{N} \approx$ 23 K cf. bulk where $T_\mathrm{N} \approx$ 40 K
Nanoscale $Li_{1+x}Mn_{2-x}O_4$ §	Mn oxidation state increase with surface area.
Nanoparticulate Mn_3O_4 *¶	Spin glass material with T_f 37–40 K.

[*] Magnetic susceptibility measurements.
[†] Neutron powder diffraction measurements.
[‡] Inelastic neutron spectroscopy.
[§] X-ray photoelectron spectroscopy.
[¶] Muon spin relaxation spectroscopy.

Table 11.1: Overview of the materials studied in this research.

the Morin transition. In the case of the mesoporous material, it can be deduced that the sign of the E_total term stays negative down to 2 K, similar to what is observed in hematite nanoparticles. For this to happen, either the magnitude of the E_mca term must be reduced (less positive), the magnitude of the E_shape term must be increased (more negative), or the total E_surface must be decreased.

It is known that the shape anisotropy scales with magnetic moment squared $\left(M_s^2\right)$ [162, 163]. As the magnetic moments from the powder diffraction data are comparable between the bulk and mesoporous sample it is unlikely that there is a vast difference between the E_shape values. E_mca will depend largely on the mean distortion of the FeO_6 octahedra from their ideal form. Rietveld refinements of the NPD data suggest that the octahedra in the mesoporous material contains FeO_6 units closer to undistorted octahedra (Appendix B), but precisely how significant this effect will be on the stabilizing one spin structure over another would require precise calculations of E_mca. What is appreciable is the increase in surface area of the mesoporous sample. In the case of nanoparticulate samples of diameter d, it has been shown that T_M scales linearly with $\frac{1}{d}$, implying that surface effects are the dominant influence [164]. This shows that it is the surface anisotropy that really is the important variable, as first postulated by Néel.

The precise nature of such a surface effect has not been examined in detail, but is likely to arise from variations in anisotropy and exchange fields that occur where the co-ordination of iron atoms deviates from that found in bulk material [165] an effect that is likely to be much greater for the mesoporous materials in comparison to bulk compounds. To explore this further requires more detailed knowledge of the nature of the surface itself (for example the specific crystal planes found at the mesopore surfaces, their composition and the extent of disorder) which is beyond the scope of this work. The changes in anisotropy noted in nanoparticles of hematite by inelastic neutron scattering and the similarities noted in the mesoporous hematite sample studied here add further weight to these arguments.

Studies on other mesoporous materials with Néel magnetic ordering occurring at suitable temperatures (at too high temperatures the mesoporous structure will collapse) have also been carried out. T_{N} depends upon the mean exchange coupling energy (J) and also on the mean ligand field. Both of these will be altered by the imposition of mesoporous structure. Mesoporous eskolaite (Chapter 5), which exhibits a Néel ordering temperature lower than that found in bulk material illustrates this. Comparisons of the refined magnetic moments between the bulk and mesoporous samples show only small differences, again enabling the ruling out of significant changes in the shape anisotropy $\left(\propto M_s^2\right)$. This sample as well as the hematite sample are iso-structural with each other and both display a slight expansion in lattice parameters in the mesoporous form. These findings have to be taken with caution however due to the difficulties in accurately determining the position of the broadened Bragg peaks.

Materials such as the mesoporous Co_3O_4 (Chapter 6) and NiO (Chapter 7) upon which parametric NPD studies were carried out also generally display a reduction in Néel ordering temperature in comparison to their bulk counterparts. In the case of Co_3O_4, which has an ordering temperature at approximately 30 K, further analysis of the DC susceptibility profiles was possible. These show that the effective magnetic moment per Co^{2+} site is somewhat higher than in the bulk material. This is probably due to a significantly higher proportion of Co^{2+} ions present on the surface of the mesopores, than in bulk Co_3O_4. The Co^{2+} is probably present in the form of CoO, of which a small amount was detected by NPD. Mesoporous α-MnO_2 (Chapter 8) also displays a lowered Néel temperature, determined by magnetic susceptibility measurements.

X-ray photoelectron spectroscopy measurements of nanoscale $Li_{1+x}Mn_{2-x}O_4$ samples (Chapter 9) reveals some of the complexities that could be present in all the materials studied when a certain amount of site disorder is present and perfect crystal structures are only very basic models. Various oxidation and spin states of the elements in the material are present, making it very difficult to be highly confident in the results. The number of dislocations and bonding combinations on the surfaces of these material types make it very complex to understand the entire system. Until detailed models of what is occurring on the surfaces can be created only broad generalisations are possible.

Magnetisation studies of nanoparticulate Mn_3O_4 (Chapter 10) illustrates the above point very well. Initial beliefs were that the material was purely Mn_3O_4. However this was not compatible with measurements which pointed to a two phase interaction within the particles (magnetic profiles were similar when the nanooparticles were dispersed in hexane and then aggregated together). XPS measurements ([151]) could just make out the presence of MnO_2 as a surface shell, providing the evidence for the second component. Muon spin relaxation studies of this material back up the findings from AC susceptibility measurements that the material is indeed a spin glass, but the dynamics of muon relaxation are too fast for a thorough analysis.

Overall, it can be seen that the imposition of meso-structure upon the metal oxides studied has effects upon the magnetic properties similar to that which has been observed in nanoparticles. This is probably due to an increase in surface anisotropy and an altering of the overall mean exchange energies and ligand fields. The rather visually dramatic suppression of the Morin transition in the mesoporous hematite comes about because of the fine balance of energy terms. It would be of interest to probe this further by making a range of mesoporous hematite samples with gradually decreasing surface areas, and to see when the Morin transition re-appears.

11.2 Future prospects

As well as the measurements presented in this thesis, work has also be carried out upon several other mesoporous transition metal oxides. However, the scheduling of these experiments within the timescale of this doctorate has not enabled the results to be fully analysed and presented here. The experiments carried out are as follows: high resolution powder diffraction studies on the mesoporous NiO samples at ISIS (HRPD), parametric and high resolution studies on mesoporous CuO (tenorite) at the ILL and ISIS (D20 and HRPD), and parametric (E6) and fine-resolution (E9) diffraction of mesoporous samples of Mn_3O_4 and Mn_2O_3 [25] at BENSC (Berlin Neutron Scattering Center, Helmholtz-Zentrum Berlin für Materialien und Energie).

11.2.1 Further analysis

The magnetic and crystallographic measurements performed in this work are one of the first studies of this type on these types of mesoporous transition metal oxides. These have given a valuable insight into the basic properties that these materials possess. However, these measurements and results prompt further questions to be answered. One of particular interest is to determine whether the reduced magnetic moments observed in the materials is due specifically to surface disorder, or an altering of spin and angular orbital momenta which make up the total magnetic moment. To study this, experiments are planned initially on the mesoporous hematite sample using X-ray magnetic circular and linear dichroism (XMCD and XMLD) at the European Synchrotron Radiation Facility (ESRF). From this it will be possible to determine the proportions of orbital and angular momenta on each Fe^{3+} centre. Further planned work is to look at the total scattering profile of the mesoporous materials. This can be done on an instrument such as ID31 at the ESRF (high resolution and intensity beamline). Wavelengths in the region of 0.4 $\AA$ are suitable as this will enable a high range in Q to be studied. Analysis of the total pattern could provide information on the nature of the material at the surfaces (which repeat themselves regularly throughout the mesoporous structure) of the walls.

Another area of interest is to use small angle neutron scattering (SANS) to look at the mesoporous structure of these materials. Reflections similar to those observed using low angle X-ray diffraction would be observed as well as the possibility of magnetic reflections, due to the periodic arrangement of the magnetic correlation across the individual mesoporous particles. The presence of these would help in gaining a fuller picture of the correlation lengths and a greater understanding of how the mesostructure affects the overall magnetic properties.

Due to problems with the synthesis of these materials (Chapter 3) it would be ideal to carry out some in-situ studies during the synthesis steps, to try to achieve a fuller understanding of how the samples are made. This could include looking at the heating steps used to decompose the absorbed salts into oxides.

11.2.2 New materials

An exciting area in this field of mesoporous materials is the possibility of combining two or more materials into one composite. Filling up the pores of one material with that of another would create a very high proportion of closely interacting surfaces. As well as the possibility of novel physical properties, the forced close interaction could combine the individual properties of two different materials not normally found together, such as one material being a good conductor, whilst the other having strong magnetic interactions. This could lead to the development of novel materials. These could still be some way off in the future as it is essential to understand the individual component synthesis and properties first before trying to combine materials.

Appendix A

Units in Magnetometry

There are two widely used systems of units used in magnetometry; the **cgs** and **SI** systems. The cgs system, where distances are measure in centimetres, mass in grams, and time in seconds is the more "traditional" system used, whereas the SI system is more "modern" and uses units recognisable in all other fields of science. A full review of this is given by S. Blundell [166, Appendix A]. However for ease of reference, the key magnetic units and their interconversions between the two systems are listed in Table A.1.

Quantity	Symbol	SI unit	Conversion factor	cgs unit
Length	x	m	$\times 10^{-2} = 1$	cm
Mass	m	kg	$\times 10^{-3} = 1$	g
Force	F	N	$\times 10^{-5} = 1$	dyne
Energy	E	J	$\times 10^{-7} = 1$	erg
Magnetic induction	$\mathbf{B}$	T	$\times 10^{-4} = 1$	G
Magnetic field Strength	$\mathbf{H}$	A m^{-1}	$\times 10^{3}/4\pi = 1$	Oe
Magnetic moment	μ	J T^{-1}	$\times 10^{-3} = 1$	erg G^{-1}
Magnetisation	$\mathbf{M}$	J T^{-1} m^{-3}	$\times 10^{3} = 1$	Oe
Magnetic susceptibility	χ		$\times 4\pi = 1$	emu cm^{-3}
Molar susceptibility	χ_{m}	m^3 mol^{-1}	$\times 4\pi 10^{-6} = 1$	emu mol^{-1}
Mass susceptibility	χ_{g}	m^3 kg^{-1}	$\times 4\pi 10^{-3} = 1$	emu g^{-1}

Table A.1: Units of electromagnetism and their interconversion between the SI and cgs systems. After reference 166.

Atomic magnetic moments are defined in units of the Bohr magneton, μ_{B}. It has a value of 9.274×10^{-24} J T^{-1}. It is derived from an electron (charge e, mass m_e) orbiting a hydrogen nucleus (radius r), creating a current, I.

$$\mu = \pi r^2 I = -\frac{e\hbar}{2m_e} \equiv -\mu_{\mathrm{B}} \tag{A.1}$$

Appendix B

Neutron Diffraction Study of Mesoporous and Bulk Hematite, α-Fe_2O_3

A. H. Hill, F. Jiao, P. G. Bruce, A. Harrison, W. Kockelmann, and C. Ritter.

Reproduced with permission from Chemistry of Materials **20**, 4891 (2008).

Chem. Mater. **2008,** *20,* 4891–4899 4891

Neutron Diffraction Study of Mesoporous and Bulk Hematite, α-Fe_2O_3

A. H. Hill,*[†] F. Jiao,[‡,§] P. G. Bruce,[§] A. Harrison,[†,||] W. Kockelmann,[⊥] and C. Ritter[||]

Centre for Science at Extreme Conditions, Erskine Williamson Building, The King's Buildings, The University of Edinburgh, Mayfield Road, Edinburgh, EH9 3JZ, United Kingdom, School of Chemistry, University of St. Andrews, North Haugh, St. Andrews, Fife, KY16 9ST, United Kingdom, Institut Laue-Langevin, 6 rue Jules Horowitz, 38042 Grenoble Cedex 9, France, and ISIS Facility, Rutherford Appleton Laboratory, Chilton, Didcot, OX11 0QX, United Kingdom

Received January 2, 2008. Revised Manuscript Received May 21, 2008

Variable temperature neutron diffraction was carried out on mesoporous α-Fe_2O_3 (hematite) with a mean pore diameter of 38.5 Å. Data were directly compared to measurements carried out on bulk hematite. Unlike bulk hematite, the mesoporous material does not undergo a spin−flop transition from a weak ferromagnet to a pure antiferromagnet (Morin transition, $T_M = 259.1(2)$). Instead, the material remains a weak ferromagnet down to 2 K with the magnetic moments staying perpendicular to the $R\bar{3}c$ [111] ([003] in the hexagonal cell) direction rather than realigning (to) almost parallel to this direction. The angle of the magnetic Fe^{3+} moments to the [111] direction in the antiferromagnetic state also accurately was obtained for bulk hematite. Using magnetic hysteresis measurements, the canting angle responsible for weak ferromagnetism within the *ab* planes (hexagonal setting) was deduced for the mesoporous material at 12 K and compared to the angle made in bulk hematite above T_M.

Introduction

There is currently a great deal of interest concerning the relationship between the dimensions of a material and its electronic, optical, or magnetic behavior. For example, the collective magnetic properties of materials may be modified strongly when they are prepared in the form of nanoparticles or rods, and this may have important consequences for their technological applications.[1–8] Recently, it was discovered that a wide range of materials may be prepared in mesostructured forms using a variety of templating techniques.[9–13] A particularly interesting development in the context of collective magnetism was the demonstration that transition metal oxides may be prepared in mesostructured forms while retaining a high degree of crystallinity.[14–18] In the case of hematite (α-Fe_2O_3), this was shown to have a profound effect on magnetic behavior in comparison to bulk samples.[17] In this study, we explored the nature of this effect through neutron diffraction studies of magnetic correlations in conventional samples, as well as a sample with a mesostructure imposed on it (mesoporous α-Fe_2O_3).

Hematite possesses a rhombohedral corundum structure (space group $R\bar{3}c$),[19] and upon cooling through the Néel temperature ($T_N = \sim 955$ K) adopts a spin structure containing two ferromagnetic sublattices (Fe and Fe') coupled antiferromagnetically to each other. The moments are aligned approximately perpendicular to the rhombohedral axis (in the basal plane of the hexagonal setting) with a small canting of the magnetic sublattices toward each other caused by a Dzyaloshinsky−Moriya (DM) interaction.[20,21] This gives the material a small, net moment. Upon cooling further, through

---

* Corresponding author. E-mail: a.h.hill@ed.ac.uk.
[†] The University of Edinburgh.
[‡] Current address: Lawrence Berkeley National Laboratory, Berkeley, CA 94720.
[§] University of St. Andrews.
[||] Institut Laue-Langevin.
[⊥] Rutherford Appleton Laboratory.

(1) Bødker, F.; Hansen, M. F.; Koch, C. B.; Lefmann, K.; Mørup, S. *Phys. Rev. B: Condens. Matter Mater. Phys.* **2000**, *61*, 6826.
(2) Klausen, S. N.; Lefmann, K.; Lindgård, P.-A.; Kuhn, L. T.; Bahl, C. R. H.; Frandsen, C.; Mørup, S.; Roessli, B.; Cavadini, N.; Niedermayer, C. *Phys. Rev. B: Condens. Matter Mater. Phys.* **2004**, *70*, 214411.
(3) Zhao, Y. M.; Dunnill, C. W.; Zhu, Y. Q.; Gregory, D. H.; Kockenberger, W.; Li, Y. H.; Hu, W. B.; Ahmad, I.; McCartney, D. G. *Chem. Mater.* **2007**, *19*, 916.
(4) Puntes, V. F.; Krishnan, K. M.; Alivisatos, A. P. *Science (Washington, DC, U.S.)* **2001**, *291*, 2115.
(5) Park, S. J.; Kim, S.; Lee, S.; Khim, Z. G.; Char, K.; Hyeon, T. *J. Am. Chem. Soc.* **2000**, *122*, 8581.
(6) Hyeon, T. *Chem. Commun. (Cambridge, U.K.)* **2003**, 927.
(7) Park, J.; Kang, E. A.; Bae, C. J.; Park, J. G.; Noh, H. J.; Kim, J. Y.; Park, J. H.; Park, J. H.; Hyeon, T. *J. Phys. Chem. B* **2004**, *108*, 13594.
(8) Mørup, S.; Madsen, D. E.; Frandsen, C.; Bahl, C. R. H.; Hansen, M. F. *J. Phys.: Condens. Matter* **2007**, *19*, 213202.
(9) Behrens, P. *Angew. Chem., Int. Ed. Engl.* **1996**, *35*, 515.
(10) Antonelli, D. M.; Ying, J. Y. *Angew. Chem., Int. Ed. Engl.* **1995**, *34*, 2014.
(11) Antonelli, D. M.; Nakahira, A.; Ying, J. Y. *Inorg. Chem.* **1996**, *35*, 3126.
(12) Tian, Z. R.; Tong, W.; Wang, J. Y.; Duan, N. G.; Krishnan, V. V.; Suib, S. L. *Science (Washington, DC, U.S.)* **1997**, *276*, 926.
(13) Yang, P. D.; Zhao, D. Y.; Margolese, D. I.; Chmelka, B. F.; Stucky, G. D. *Nature (London, U.K.)* **1998**, *396*, 152.
(14) Wang, Y. Q.; Yang, C. M.; Schmidt, W.; Spliethoff, B.; Bill, E.; Schüth, F. *Adv. Mater.* **2005**, *17*, 53.
(15) Zhu, K. K.; Yue, B.; Zhou, W. Z.; He, H. Y. *Chem. Commun. (Cambridge, U.K.)* **2003**, 98.
(16) Tian, B. Z.; Liu, X. Y.; Yang, H. F.; Xie, S. H.; Yu, C. Z.; Tu, B.; Zhao, D. Y. *Adv. Mater.* **2003**, *15*, 1370.
(17) Jiao, F.; Harrison, A.; Jumas, J. C.; Chadwick, A. V.; Kockelmann, W.; Bruce, P. G. *J. Am. Chem. Soc.* **2006**, *128*, 5468.
(18) Jiao, F.; Bruce, P. G. *Adv. Mater.* **2007**, *19*, 657.
(19) Izyumov, Y. A.; Ozerov, R. P. *Magnetic Neutron Diffraction*; Plenum Press: New York, 1970.
(20) Dzyaloshinsky, I. *J. Phys. Chem. Solids* **1958**, *4*, 241.
(21) Moriya, T. *Phys. Rev.* **1960**, *120*, 91.

10.1021/cm800009s CCC: \$40.75

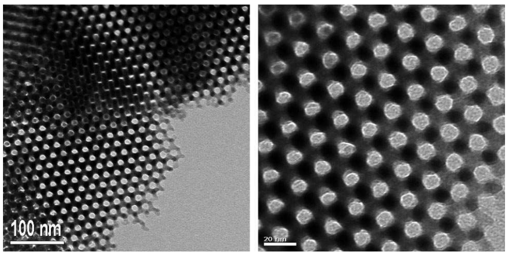

Figure 1. TEM images of mesoporous hematite, α-Fe_2O_3. The mesostructure is a 3-D negative replica of KIT-6.[17]

~260 K, the material undergoes a first order spin reorientation transition, called the Morin transition,[22] where the magnetic moments align themselves along the rhombohedral axis (the *c* axis of the hexagonal setting), and the net magnetic moment is lost. (The description of the magnetic structure of bulk hematite in ref 17 contains an error in the stated directions of the magnetic moments.) The temperature of the Morin transition is denoted as T_M. A slight inclination (tilt) of the moments away from the rhombohedral axis is present, leading to a residual component of the (111) peak in the magnetic diffraction patterns.[23] Analysis of the intensity of this peak enables the angle of tilt to be determined. Previous studies report this angle in the range of 5−15°.[23–25]

A large amount of work has been carried out concerning the relationship between particle size and magnetic ordering, with regard to the suppression of the Morin transition in hematite.[1,26–28] Susceptibility measurements were used recently to show that crystalline mesoporous α-Fe_2O_3 (surface area of 139 $m^2\ g^{-1}$, pore diameter of 38.5 Å) does not show a sharp decrease of the magnetic moment at T_M for the bulk material, or indeed at any temperature down to 2 K, while complementary neutron scattering data taken at 295 K indicate the same type of long-range magnetic order as found in bulk samples.[17] This suggests that the mesostructure leads to a suppression of the Morin transition. In this paper, we present neutron diffraction data taken with the same mesoporous hematite sample (Figure 1) from our previous paper[17] over a much wider range of temperatures. This provides the first thorough characterization of the crystallographic and magnetic structures of this new form of hematite down to 2 K, including the absence of a Morin transition. We also report the evolution of the crystallographic and magnetic structure of bulk hematite for comparison and reference, using data of the same or comparable quality, and allow refinement of the spin structure below T_M with a higher precision than previously was reported.

The synthesis and characterization of the mesoporous hematite sample previously was discussed,[17] so we shall only describe it briefly. An initial mesoporous silica template, KIT-6, was prepared as described by Ryoo and co-workers.[29] This has a 3-D pore structure with a cubic $Ia\bar{3}d$ asymmetric unit. Iron (III) nitrate was allowed to diffuse into the pore structure and was heated to decompose into iron (III) oxide. The silica template was subsequently removed by dissolving in NaOH, leaving a 3-D negative image Fe_2O_3 framework of the original mesoporous silica. TEM images (previously published) show a cubic structure of space group $Ia\bar{3}d$. Low-angle X-ray powder diffraction showed a peak corresponding to the (211) reflection, a_0 of 229 Å. Pore diameter and surface area were calculated from physisorption isotherms.

Experimental Procedures

Bulk hematite was obtained from Acros Organics, 99.999%, 100 mesh (diameter less than ~150 μm). Mesoporous hematite with a surface area of 139 $m^2\ g^{-1}$ and a pore diameter centered at 38.5 Å was prepared using a mesoporous silica template as previously described.[17] Diffraction measurements for bulk hematite were made from 10 to 300 K on a GEM diffractometer with a closed cycle refrigerator using six detector banks at the ISIS Facility. Data for the mesoporous sample were collected from 2 to 295 K on the time-of-flight spectrometer OSIRIS, also at ISIS, contained in a vanadium can and an Orange cryostat. Further neutron diffraction data were collected on diffractometer D1B at the Institut Laue-Langevin on bulk hematite to study in greater detail the evolution of the (111) peak with increasing temperature from 2 to 300 K.

Magnetic hysteresis and magnetization dependence with temperature measurements were performed using polycrystalline samples with a MPMS Quantum Design SQUID magnetometer. The samples were encapsulated in eicosane ($C_{20}H_{42}$, melting point 310 K) in gelatin capsules to prevent grain reorientation in strong magnetic fields.

Results

A $R\bar{3}c$ (hexagonal setting) crystallographic hematite model was fitted to the data sets as a nuclear model for the unit cell, with Fe and O atoms on the 12*c* and 18*e* crystallographic sites, respectively. A second phase consisting of 12 Fe atoms set at the positions generated by the symmetry operations of the $R\bar{3}c$ phase was added with *P*1 symmetry for refinement of the magnetic structure, following the two-phase fit without magnetic symmetry approach summarized by Cui et al.[30] Rietveld refinement[31] of the data was then carried out using the GSAS[32] suite of programs with the EXPGUI interface,[33] using typically 12 point shifted Chebyschev background polynomials for each diffraction pattern.

Bulk Hematite. Crystallographic and magnetic information obtained at the temperatures studied are shown in Table 1. Above T_M, the refinement was carried out with only the magnetic moment in the *x* direction allowed to refine, m_y was set to zero because the direction of the moments in the

---

(22) Morin, F. J. *Phys. Rev.* **1950**, *78*, 819.
(23) Morrish, A. H.; Johnston, G. B.; Curry, N. A. *Phys. Lett.* **1963**, *7*, 177.
(24) Nathans, R.; Pickart, S. J.; Alperin, H. A.; Brown, P. J. *Phys. Rev. A: At., Mol., Opt. Phys.* **1964**, *136*, 1641.
(25) Krén, E.; Molnàr, B.; Svàb, E.; Zsoldos, É. *Solid State Commun.* **1974**, *15*, 1707.
(26) Morrish, A. H. *Canted Antiferromagnetism: Hematite*; World Scientific: London, 1994.
(27) Zysler, R. D.; Fiorani, D.; Testa, A. M.; Suber, L.; Agostinelli, E.; Godinho, M. *Phys. Rev. B: Condens. Matter Mater. Phys.* **2003**, *68*, 212408.
(28) Muench, G. J.; Arajs, S.; Matijevic, E. *Phys. Status Solidi A* **1985**, *92*, 187.
(29) Kleitz, F.; Choi, S. H.; Ryoo, R. *Chem. Commun. (Cambridge, U.K.)* **2003**, 2136.
(30) Cui, J.; Huang, Q.; Toby, B. H. *Powder Diffraction* **2006**, *21*, 71.
(31) Rietveld, H. M. *J. Appl. Crystallogr.* **1969**, *2*, 65.

Table 1. Refined Crystallographic and Magnetic Data for Bulk α-Fe_2O_3[a]

T (K)	a (Å)	c (Å)	Fe^{3+} z coordinate	O^{2-} x coordinate	m_x (μ_B)	m_z (μ_B)	m (μ_B)	R_{wp}	R_p
300	5.035128(4)	13.75809(10)	0.355322(16)	0.30618(6)	4.118(6)	0	4.118(6)	0.0438	0.0419
250	5.034778(3)	13.74857(9)	0.355266(14)	0.30616(6)	1.607(10)	4.026(7)	4.165(7)	0.0411	0.0496
200	5.034516(4)	13.74145(10)	0.355169(15)	0.30615(6)	0.826(14)	4.101(7)	4.183(7)	0.0435	0.0516
150	5.034321(4)	13.73618(11)	0.355155(17)	0.30609(7)	0.785(16)	4.133(8)	4.207(8)	0.0493	0.0549
100	5.034172(4)	13.7321(11)	0.355082(17)	0.30605(7)	0.783(16)	4.164(8)	4.237(8)	0.0503	0.0487
50	5.034172(4)	13.73213(12)	0.355131(18)	0.30615(7)	0.762(18)	4.153(9)	4.223(9)	0.0554	0.0598
10	5.034171(4)	13.73210(11)	0.355080(17)	0.30602(7)	0.781(17)	4.149(9)	4.222(9)	0.0529	0.0520

[a] Data refined in the hexagonal setting of $R\bar{3}c$.

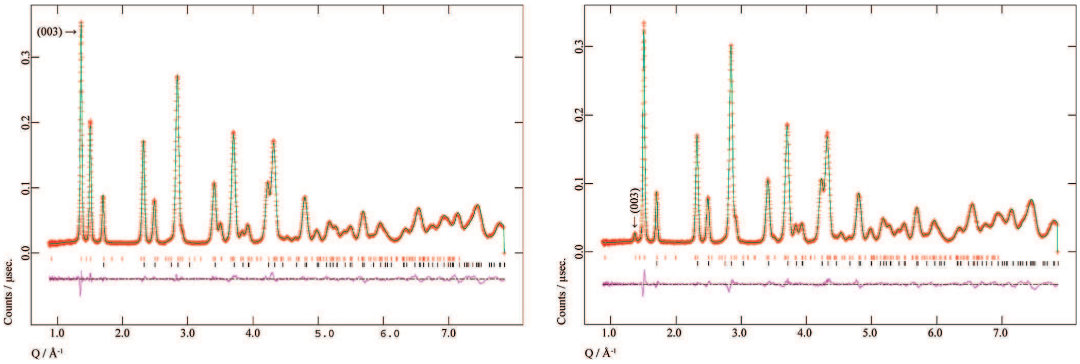

Figure 2. Observed and calculated neutron powder diffraction patterns from detector bank 3 of GEM for bulk α-Fe_2O_3 at 300 K (left) and 10 K (right). The difference pattern is shown below the patterns, with tick marks indicating the Bragg reflection positions from the nuclear, $R\bar{3}c$ (lower), and magnetic, $P1$ (upper), structures. The (003) Bragg reflection is marked.

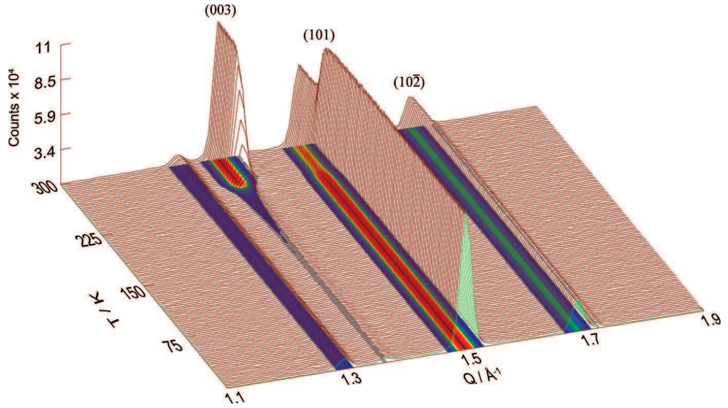

Figure 3. Neutron powder diffraction patterns from D1B of bulk α-Fe_2O_3 from 2 to 300 K. The (003) reflection can be seen at ~1.37 $Å^{-1}$. The peak at 1.3 $Å^{-1}$ is believed to be due to a low concentration of an impurity but does not affect the intensity of the (003) reflection.

hexagonal basal plane remain undetermined due to powder averaging, and m_z was set to zero as refinements with this included turned out to be unstable and diverging. Below T_M, magnetic moments in the x and z directions were allowed to refine (m_y set to zero, again due to powder averaging). Rietveld refinement patterns of neutron diffraction patterns collected on detector bank 3 of GEM above and below T_M, at 300 and 10 K, are shown in Figure 2. Data collected on D1B, tracing the change in Bragg peak intensities, are shown in Figure 3.

Mesoporous Hematite. Because of the limited Q space attainable on the OSIRIS instrument and high correlation between the thermal displacement parameters (U_{iso}) and the magnetic moment, the thermal displacement parameters in the mesoporous refinements were set at the values obtained from the bulk material on GEM. Unit cell parameters, atomic coordinates, and magnetic moments were then allowed to refine independently. These are presented in Table 2, with the omission of the 150 K data set due to a problem in the merging of the data sets, not allowing a full range of Q values in a continuous manner. Rietveld refinement patterns of neutron diffraction patterns collected at 295 and 2 K are

---

(32) Larson, A. C.; Von Dreele, R. B. *General Structure Analysis System (GSAS), Report No. LAUR 86-748*; Los Alamos National Laboratory: Los Alamos, NM, 2004.

(33) Toby, B. H. *J. Appl. Crystallogr.* **2001**, *34*, 210.

Table 2. Refined Crystallographic and Magnetic Data for Mesoporous α-Fe_2O_3[a]

T (K)	a (Å)	c (Å)	Fe^{3+} z coordinate	O^{2-} x coordinate	m_x (μ_B)	m_z (μ_B)	m (μ_B)	R_{wp}	R_p
295	5.03599(3)	13.7816(9)	0.35510(6)	0.3090(3)	4.05(2)	0	4.05(2)	0.0248	0.0188
250	5.036201(17)	13.7873(5)	0.35493(5)	0.3098(3)	3.98(2)	0	3.98(2)	0.0265	0.0190
100	5.035521(16)	13.7687(4)	0.35493(5)	0.3100(2)	4.192(18)	0	4.192(18)	0.0266	0.0224
50	5.035469(16)	13.7673(4)	0.35485(5)	0.3097(2)	4.208(18)	0	4.208(18)	0.0271	0.0231
2	5.035476(16)	13.7676(4)	0.35485(5)	0.3097(3)	4.224(18)	0	4.224(18)	0.0274	0.0235

[a] Data refined in hexagonal setting of $R\bar{3}c$. N.B. 295 K data sets were collected without the use of a cryostat. Because of different off-center sample displacements on the OSIRIS diffractometer for the two experimental settings (with and without cryostat), the lattice parameters for the mesoporous sample at 295 K are omitted in Figure 8.

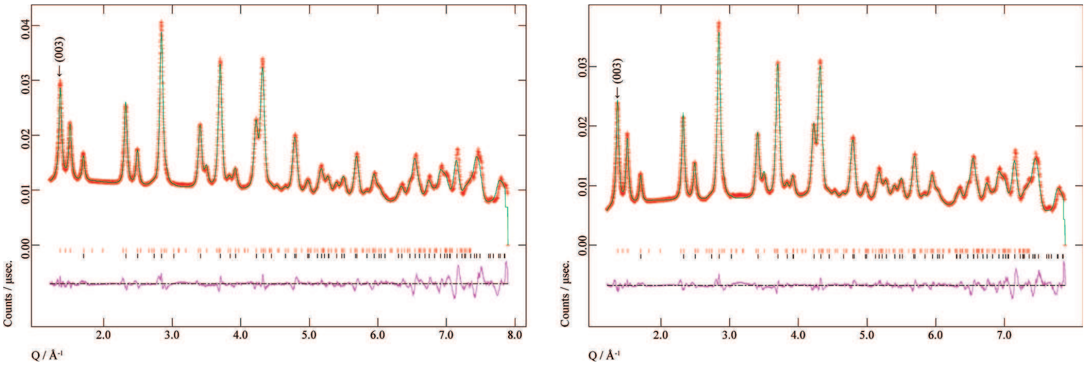

Figure 4. Observed and calculated neutron powder diffraction patterns from OSIRIS for mesoporous α-Fe_2O_3 at 295 K (left) and 2 K (right). The difference pattern is shown below the diffraction patterns, with tick marks indicating the Bragg reflection positions from the nuclear, $R\bar{3}c$ (lower), and magnetic, $P1$ (upper), structures. The (003) Bragg reflection is marked.

shown in Figure 4. For all data, the magnetic moments were refined as previously described for the bulk hematite sample above T_M.

Discussion

Bulk Hematite. From Figure 2, it can clearly be seen that as the temperature goes below T_M, the intensity of the (003) peak (in the rhombohedral setting, this corresponds to the (111) peak) changes dramatically to a much smaller finite value. The plot of integrated peak intensity (the FWHM of the (003) peaks in the D1B data was determined by fitting a Gaussian function to the peak with the ABFFIT software[34]) is shown in Figure 5, together with the refined moment on the Fe^{3+} ions from GEM data. The temperature at which the intensity of the (003) Bragg peak is halved from its maximum value is just above 254 K. This corresponds well to data taken in 0.01 T (cooled in zero field) with a MPMS Quantum Design SQUID magnetometer (Figure 5), which show T_M to be between 259.0 and 259.2 K (calculated to be the temperature at which the susceptibility is half that of the maximum value).

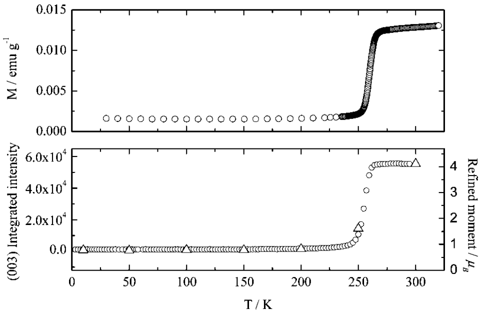

Figure 5. Magnetization (1 emu g^{-1} = 1 J T^{-1} kg^{-1}) of bulk α-Fe_2O_3 (upper) measured in 0.01 T (cooled in 0 T) and integrated peak intensity of the (003) Bragg peak of bulk α-Fe_2O_3 from D1B data (lower), showing the Morin transition. The calculated magnetic moment from refinement of GEM data in the *ab* plane also is shown (triangles). Error bars are of similar size as the data point symbols.

Above T_M, the magnetic structure was refined with no component along the c axis. As the intensity of the (003) reflection does not decrease to zero below T_M, it appears that there is a component of the magnetic moment on Fe^{3+} in the basal plane at a base temperature (Figure 6, produced with the VESTA program[35]). Rietveld refinement of a structure with such a component of that moment in the basal plane gave an estimate of the angle at which the moments tilt out away from the [111] direction. This angle was found to be 10.7(2)° at 10 K, which is in good agreement with, but more precise than, the previously published value of 15(10)°.[25] The values of the magnetic moments of the Fe^{3+} ions (m = 4.22(1) μ_B), calculated from the Rietveld refinements, are lower than that expected for the quantized z component of the spin-only moment of Fe^{3+}, 5.00 μ_B, but is of a similar value to previously refined values.[36] This is due to the α-Fe_2O_3 system being a charge transfer insulator

---

(34) Antoniadis, A.; Berruyer, J.; Filhol, A. *Acta Crystallogr., Sect. A: Found. Crystallogr.* **1990**, *46*, 692.

(35) Momma, K.; Izumi, F. *Commission Crystallogr. Comput., IUCr Newslett.* **2006**, *7*, 106.

(36) Baron, V.; Gutzmer, J.; Rundlöf, H.; Tellgren, R. *Solid State Sci.* **2005**, *7*, 753.

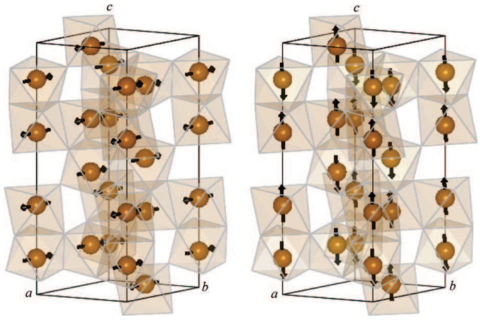

Figure 6. Arrangement of magnetic lattices in bulk hematite on either side of the Morin transition at 300 K (left) and 10 K (right).

rather than a Mott−Hubbard insulator[37,38] with a p−d band gap. Hence, there is a small amount of Fe−O σ-type bonding due to charge back transfer: $2p(O^{2-}) \rightarrow 3d(Fe^{3+})$. This therefore reduces the effective charge on the Fe^{3+} ions, producing a lower magnetic moment. This was observed with spherical neutron polarimetry in the case of isostructural eskolaite, Cr_2O_3.[39] No net magnetization is seen on the oxygen anions, due to an equal fraction of up and down spin gain from its up and down spin chromium cation neighbors.

Magnetic hysteresis loops of bulk hematite (Figure 7) carried out below and above T_M at 12 and 295 K show what is expected for the material. At 12 K, no hysteresis loop is observed, in line with what is expected for a simple antiferromagnet. At 295 K, hysteresis is observed, due to the weak ferromagnetic state of the material. Extrapolation of the high-field region of the $\mathbf{M}(\mathbf{H})$ curve (where saturation occurs) provides a spontaneous magnetization, $\mathbf{M}_r$, of 0.28 emu g^{-1}. This is of a similar magnitude to values previously reported.[26,40–42] In combination with the μ_B value obtained at the corresponding temperature by neutron diffraction, an *ab* plane canting angle λ of 0.06° can be calculated, corresponding to a canting component of 0.004 μ_B per Fe^{3+} ion, again agreeing with previous literature.[24] These results are summarized in Table 3.

Mesoporous Hematite. Rietveld refinement of the data for mesoporous hematite shows that no spin−flop transition occurs down to 2 K. This is made obvious by the (003) peak not diminishing in intensity (Figure 4). As with bulk hematite, the values of the calculated magnetic moments are lower than those expected for a free ion, again due to a loss of magnetic moment into the surrounding oxygen ligands; note too that iron at the surface of hematite has been shown to have a greatly reduced moment,[43] and the collective magnetic properties of hematite films have been observed to depart from those of bulk materials when their thickness is as much as 200 Å.[44]

When the temperature is reduced from 250 to 2 K, there is a considerable reduction in the background fit in the diffraction patterns, shown by a plot of background intensities (12 point shifted Chebyschev fit) over Q (Figure 8). A clear minimum can be seen in the lower temperature plots at ~2.5 $Å^{-1}$; at lower Q, the background rises, due to slight overcompensation into the broadened Bragg peaks, which have the largest magnetic contribution.

Extraction of integrated peak intensities of the two purely magnetic (003) and (101) (the latter corresponding to the (100) peak in the rhombohedral setting) Bragg reflections using the CMPR program[45] shows an increase in area with cooling, corresponding to the reduction of the paramagnetic background (Figure 9). Despite problems with combining the full d-range of the 150 K data set for full Rietveld refinement, it was still possible to extract the peak areas. There are no components of the magnetic moments of Fe^{3+} ions in the [003] direction observable in any of the Rietveld refinements; all moments are 90° to this direction, in the basal plane. The material is, however, still a weak ferromagnet due to the DM interactions, causing a slight canting of the magnetic moments, distorting the alignment of the antiferromagnetic planes. Although this small ferromagnetic component of moment cannot be observed in our neutron diffraction patterns, it has been seen down to 2 K in magnetization measurements taken with the SQUID magnetometer.[17] As with bulk hematite, the canting angle can be calculated from the magnetic hysteresis curves (Figure 7) and with the calculated moments from the neutron diffraction data. At 12 K, the canting angle θ is 0.11°, corresponding to a spontaneous moment of 0.008 μ_B per Fe^{3+} ion (Table 3). What is particularly striking with the mesoporous material is that it is a much harder magnet at low temperatures. At 12 K, it has a coercive field ($\mathbf{H}_c$) of ~0.36 T, as compared to ~0.028 T at 295 K. This is similar to observations made in nanoparticulate hematite, where the higher coercive field was related to the existence of a higher anisotropy within the particles.[46] At room temperature, however, the bulk material is a harder magnet than the mesoporous material, $\mathbf{H}_c$ = ~0.17 T.

Analysis of the refined lattice parameters of bulk and mesoporous hematite show that overall, the lattices of both bulk and mesoporous α-Fe_2O_3 contract upon cooling by approximately the same magnitude (0.02 and 0.2% along the *a* and *c* axes, respectively, in the bulk and 0.01 and 0.1% in the same respective directions in the mesoporous material). There is, however, a noticeable difference between the lattice parameters of the bulk and mesoporous samples. The lattice parameters are ~0.03 and 0.3% greater in the mesoporous material along the *a* and *c* axes, respectively, than in bulk material throughout the temperature range studied (Figure 10). This gives a 0.2% increase in the *c*/*a* ratio for the mesoporous sample. Such lattice expansions previously were

---

(37) Catti, M.; Valerio, G.; Dovesi, R. *Phys. Rev. B: Condens. Matter Mater. Phys.* **1995**, *51*, 7441.

(38) Rollmann, G.; Rohrbach, A.; Entel, P.; Hafner, J. *Phys. Rev. B: Condens. Matter Mater. Phys.* **2004**, *69*, 165107.

(39) Brown, P. J.; Forsyth, J. B.; Lelievre-Berna, E.; Tasset, F. *J. Phys.: Condens. Matter* **2002**, *14*, 1957.

(40) Andersen, D. H. *Phys. Rev.* **1966**, *151*, 247.

(41) Goya, G. F.; Veith, M.; Rapalavicuite, R.; Shen, H.; Mathur, S. *Appl. Phys. A: Mater. Sci. Process.* **2005**, *80*, 1523.

(42) Flanders, P. J.; Remeika, J. P. *Philos. Mag.* **1965**, *11*, 1271.

(43) Wang, X. G.; Weiss, W.; Shaikhutdinov, S. K.; Ritter, M.; Petersen, M.; Wagner, F.; Schlögl, R.; Scheffler, M. *Phys. Rev. Lett.* **1998**, *81*, 1038.

(44) Kamzin, A. S.; Vcherashnii, D. B. *JETP Lett. (Engl. Transl.)* **2002**, *75*, 575.

(45) Toby, B. H. *J. Appl. Crystallogr.* **2005**, *38*, 1040.

(46) Zysler, R. D.; Winkler, E.; Vasquez Mansilla, M. V.; Fiorani, D. *Physica B* **2006**, *384*, 277.

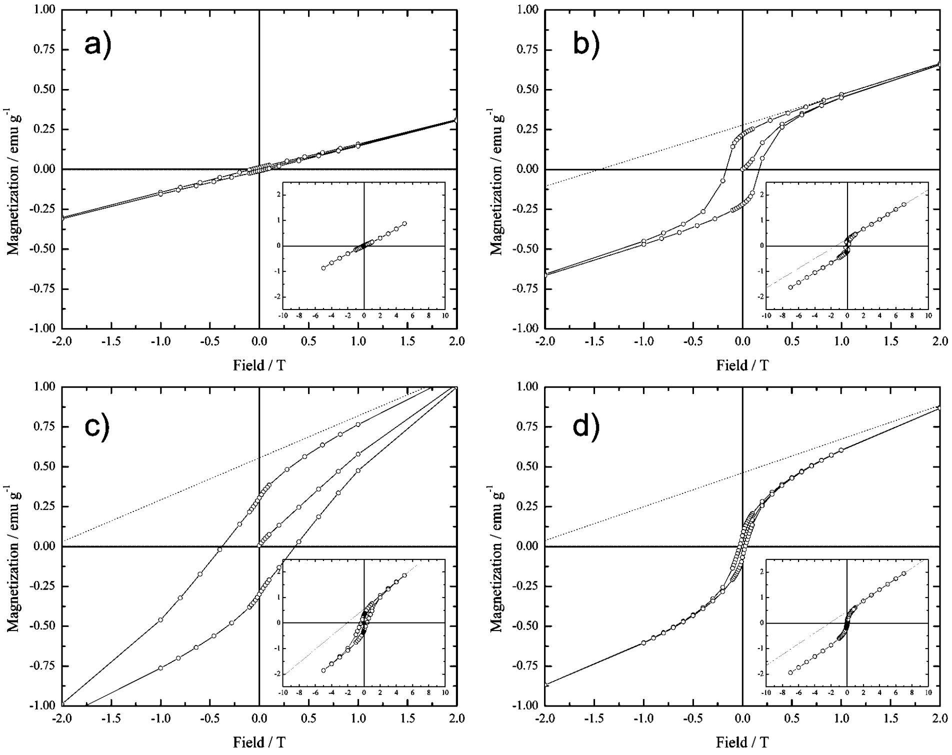

Figure 7. Magnetic hysteresis in bulk (a and b) and mesoporous (c and d) hematite at 12 K (a and c) and 295 K (b and d). All graphs are on the same scale for ease of comparison. Insets show full hysteresis loops. Dashed lines are linear fits to the high-field data to determine the remnant magnetizations in the weakly ferromagnetic states, $\mathbf{M}_r$.

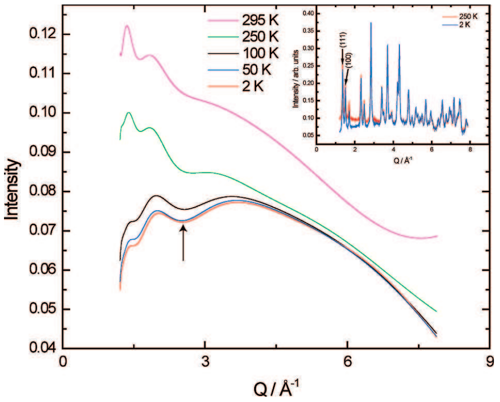

Figure 8. Plots of background functions for mesoporous α-Fe_2O_3 ranging from 295 K (top) to 2 K (bottom). The minimum marked with an arrow corresponds to a value of $Q = \sim 2.5$ Å^{-1}. Inset shows powder diffraction patterns of mesoporous α-Fe_2O_3 collected at 250 K (red upper pattern at low Q) and 2 K (blue lower pattern) with the pure magnetic (003) and (101) Bragg reflections marked. At low Q, a decrease of the paramagnetic background upon cooling is observed.

noted in microcrystalline hematite particles,[47–49] where a suppression of the Morin transition also was observed. Figure 11a shows as to how O−Fe−O angles in the FeO_6 octahedra change with temperature in both samples. The angles (Figure 12) are ∼78° (octahedral share a face along *c* between Fe and Fe') and 102° (no face sharing between Fe and Fe'). The dominant superexchange coupling is between spins on the two different antiferromagnetic sublattices (Fe and Fe'), which depend both on the Fe−O−Fe' bridging angle and Fe−O bond lengths. There are four different such Fe−O−Fe' bridging angles in the hematite cell;[37] two of ∼131°, one of ∼120°, and one of ∼86°; the corresponding Fe−O bond lengths are in the region of 3.7, 3.4, and 2.9 Å, respectively (Figure 12). The bridge closest to 90° is expected to have the weakest superexchange based on the Goodenough−Kanamori rules,[50] which are likely to override the fact that the corresponding bond lengths are the shortest.

When the unit cell dimensions *a* and *c* change, the angles and distances in the superexchange pathways will change. Expansion in *a* will lower the three angles that dominate the superexchange mechanism and increase the Fe−Fe' distances, both of which will reduce the superexchange. However, an expansion along *c* increases bridging angles (increasing superexchange), and bonds lengths (decreasing superexchange), with the effect that net antiferromagnetic

---

(47) Yamamoto, N. *J. Phys. Soc. Jpn.* **1968**, *24*, 23.
(48) Nininger, R. C.; Schroeer, D. *J. Phys. Chem. Solids* **1978**, *39*, 137.
(49) Schroeer, D.; Nininger, R. C. *Phys. Rev. Lett.* **1967**, *19*, 632.
(50) Goodenough, J. B. *Magnetism and the Chemical Bond*; Wiley Interscience: New York, 1963; p 15.

Table 3. Data from M(H) Curves and Calculated Canting Properties

sample	bulk Fe_2O_3 295 K	meso Fe_2O_3 295 K	meso Fe_2O_3 100 K	meso Fe_2O_3 12 K[a]
$\mathbf{H}_c$/T (estimated)	0.167	0.028	0.087	0.363
$\mathbf{M}_r$ (emu g^{-1})	0.278(3)	0.462(8)	0.54(2)	0.556(17)
θ (deg)	0.0554(8)	0.0934(20)	0.106(5)	0.108(2)
m_x/μ_B	4.118(6)	4.05(2)	4.192(18)	4.224(18)
m_y/μ_B	0.00380(6)	0.00661(17)	0.0078(4)	0.0079(2)

[a] Angle calculated using refined moment at 2 K.

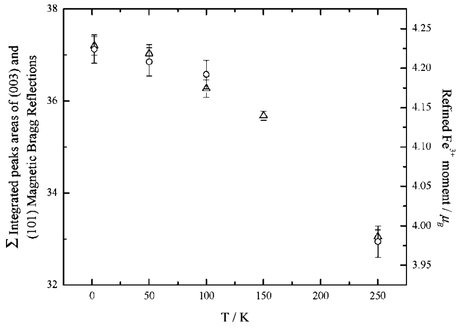

Figure 9. Sum of extracted integrated (003) and (101) Bragg peak intensities (triangles) and refined magnetic moment (circles) of mesoporous hematite, showing an increase in magnetic ordering with cooling.

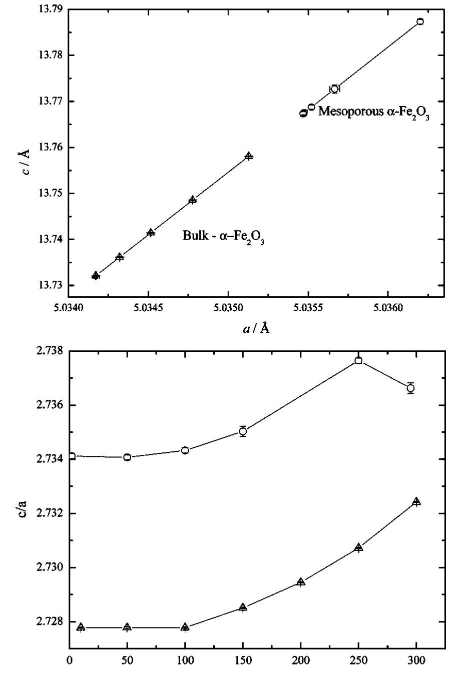

Figure 10. Plot of lattice parameters *c* and *a* (top) for bulk (triangles) and mesoporous (circles) hematite and variance of *c*/*a* ratio with temperature.

coupling is more sensitive to expansion along *a* than along *c*; if the ratio *c*/*a* is increased at a constant unit cell volume, antiferromagnetic coupling will become stronger. Figure 10 shows that *c*/*a* is larger for the mesoporous sample, while the volume of the unit cell is also larger at a given temperature, so it is unclear as to what the net effect will be.

The variation of geometry of these individual bridges with temperature and sample are presented graphically in Figure 11b−d. The strongest superexchange interaction is likely to propagate through the pathway with the largest bridging angle, whose properties are shown in Figure 11b: The angle in the bulk material is larger than in the mesoporous sample, while the length of this pathway is smaller. These two factors conspire to create a weaker superexchange interaction in the mesoporous material. However, when we take the other pathways into consideration, the picture is less clear. In general, bond lengths are greater at a particular temperature in the mesoporous sample, but there is no clear trend in the Fe−O−Fe' bridging angle, so it is difficult to say as to what the overall trend will be in the strength of the superexchange interaction with regard to the nature of the sample.

The diffraction patterns show clear Scherrer broadening of both magnetic and structural Bragg peaks of the mesoporous sample. This could be due to disruption of the repetition of the crystallographic and magnetic cell over long ranges by the mesostructure. Using TOF profile 2 in GSAS[32] (an incorporation of the Ikeda−Carpenter function[51] with a pseudo-Voigt linear combination of a Lorentzian and Gaussian function), the γ_2 variables of the Lorentzian part of the peak profile were allowed to refine independently between nuclear and magnetic phases. The nuclear and magnetic correlation lengths in the material were calculated using the Scherrer equation. Over the temperature range studied, the average values for the nuclear and magnetic correlation lengths were calculated to be 152.8(6) and 137.6(6) Å, respectively, in the mesoporous material. These are much shorter than those found in a sample of bulk α-Fe_2O_3 studied with the same experimental settings (300 and 150 K) with values of 529(4) and 594(5) Å for the nuclear and magnetic phases.

The spin orientation in bulk crystalline hematite is determined by a number of interactions in the material. The spin Hamiltonian can be expressed as follows:[52]

$$\mathcal{H} = \sum_{\langle ij\rangle} \{J_{ij}(\mathbf{S}_i \cdot \mathbf{S}_j) + \mathbf{D}[\mathbf{S}_i \times \mathbf{S}_j] + \mathbf{S}_i \cdot K_{ij} \cdot \mathbf{S}_j\} + \sum_i \{D\mathbf{S}_{iz}^2 + \mu_B \mathbf{S}_i \cdot g_i \cdot \mathbf{H}\} \quad (1)$$

The first term includes the Heisenberg exchange interaction, the Dzyaloshinsky−Moriya interaction, and the magnetic dipolar interactions. The second term concerns the single ion anisotropy and the Zeeman energies.

---

(51) Ikeda, S.; Carpenter, J. M. *Nucl. Instrum. Methods Phys. Res., Sect. A* **1985**, *239*, 536.

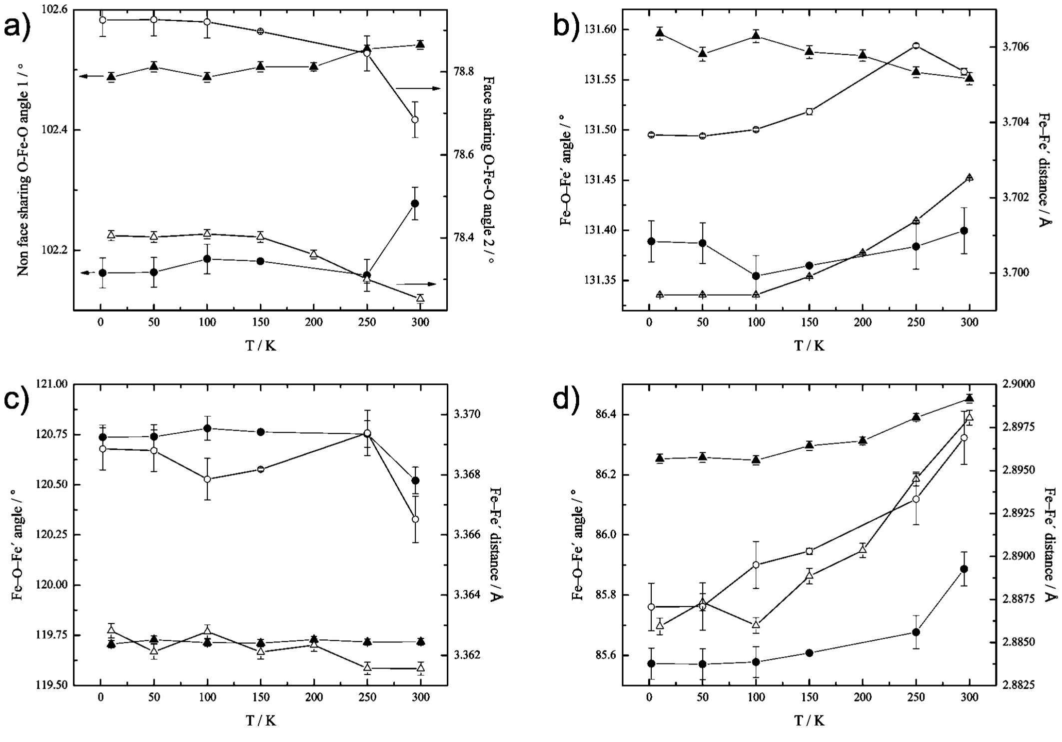

Figure 11. Structural characteristics of FeO_6 coordination polyhedra and Fe−O−Fe’ exchange pathways for mesoporous (circles) and bulk (triangles) hematite. (a) O−Fe−O angles for face sharing (solid symbols) and nonface sharing (open symbols) parts of FeO_6 octahedra (see Figure 12). (b−d) Calculated Fe−O−Fe’ angles (solid symbols) and Fe−Fe’ distances (open symbols). Data points are connected purely to guide the eye.

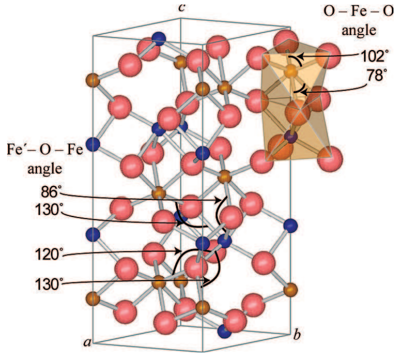

Figure 12. Hexagonal unit cell of hematite showing the Fe−O−Fe’ angles for the different dominant superexchange pathways, as well as the O−Fe−O angles within each FeO_6 octahedra. The large spheres represent O^{2-}, and the small spheres represent the two different spin sublattices of Fe^{3+}: Fe (dark blue) and Fe’ (light brown) (after Catti et al.[37]).

The spin reorientation at T_M arises from a change of sign of the total magnetic anisotropy E_{mag}.[26,53–55] This term is made up of several individual contributions; the magnetocrystalline anisotropy E_{mca} (involves noncubic components of the ligand field in conjunction with spin−orbit coupling), the shape anisotropy E_s (long-range dipolar anisotropy), and the surface anisotropy $E_{surface}$ (lower crystal symmetry and reduced coordination numbers)

$$E_{mag} = E_{mca} + E_s + E_{surface} \qquad (2)$$

In bulk hematite, the two dominant terms are the magnetocrystalline anisotropy and the shape anisotropy. These two terms are very similar in magnitude (2% difference) but have opposite signs. At low temperatures in bulk hematite, the positive E_{mca} term dominates over the E_s term, causing the magnetic moments to be aligned parallel to the hexagonal axis. As T is raised, the negative E_s term has a greater influence, until it forces the spins to reorientate into the *ab* plane, causing the Morin transition. In the case of the mesoporous material, it can be deduced that the sign of the E_{total} term stays negative down to 2 K, similar to what is observed in hematite nanoparticles.[2] For this to happen, either the magnitude of the E_{mca} term must be reduced (less positive), the magnitude of the E_s term must be increased (more negative), or the total $E_{surface}$ must be decreased.

It is known that the shape anisotropy scales with M_s^2.[56,57] As the magnetic moments from the powder diffraction data

---

(52) Moriya, T., Weak ferromagnetism. In *Magnetism*; Rado, G. T., Suhl, H., Eds.; Academic Press: San Diego, 1963; Vol. 1, p 85.

(53) Artman, J. O.; Murphy, J. C.; Foner, S. *Phys. Rev.* **1965**, *138*, 912.

(54) Harrison, R. J.; McEnroe, S. A.; Robinson, P.; Carter-Stiglitz, B.; Palin, E. J.; Kasama, T. *Phys. Rev. B: Condens. Matter Mater. Phys.* **2007**, *76*, 174436.

(55) Wu, R., Theory of magnetocrystalline anisotropy and magnetoelasticity. In *Handbook of Magnetism and Advanced Magnetic Materials*; Kronmüller, H., Parkin, S., Eds.; John Wiley and Sons: New York, 2007; Vol. 1, p 423.

(56) Yoshida, K. *Prog. Theor. Phys.* **1951**, *6*, 691.

are comparable between bulk and mesoporous samples, it is unlikely that there is a vast difference between the E_s values. E_{mca} depends largely on the mean distortion of FeO_6 octahedra from their ideal form: The data presented in Figure 11a suggest that over most of the temperature range studied, the mesoporous material contains FeO_6 units closer to undistorted octahedra, but precisely as to how significant this effect will be on the stabilizing one spin structure over another would require precise calculations of E_{mca}. What is appreciable is the increase in surface area of the mesoporous sample. The effect of surface anisotropy was first postulated by Néel.[58] It has been shown that in thin metal films, the surface anisotropy can have a significant effect for thicknesses up to 600 Å.[52] Theoretical studies have shown how important the surface anisotropy is in nanoparticles and how this can vary with respect to the crystal plane at the surface.[59–61] Experimental observations of increased coercive fields (indicative of an increased surface anisotropy) also were reported in hematite nanoparticles.[46,62] In the case of nanoparticulate samples of diameter *d*, it has been shown that T_M scales linearly with 1/*d*, implying that surface effects are the dominant influence.[27] Particles in the 80−200 Å diameter range have been shown to have no Morin transition even down to 4 K.[1,63–68]

The precise nature of such a surface effect has not been examined in detail but is likely to arise from variations in anisotropy and exchange fields that occur where the coordination of iron atoms deviates from that found in bulk material:[46] an effect that is likely to be much greater for the mesoporous materials in comparison to bulk compounds. To explore this further requires more detailed knowledge of the nature of the surface itself (i.e., the specific crystal planes found at the mesopore surfaces, their composition, and the extent of disorder), which is beyond the scope of this work.

Neutron scattering studies of collective magnetic excitations in hematite particles of 160 Å in diameter indicate that in contrast to bulk material, the sign of the magnetic anisotropy does not change from 300 K down to at least 50 K.[2] Studies of the magnetic excitations in mesoporous material by inelastic neutron scattering to obtain the magnetic anisotropy value would be desirable to unravel the various competing interactions and their variations with temperature.

Conclusion

From the variable temperature neutron diffraction of mesoporous α-Fe_2O_3, we have shown that this material does not undergo a first order spin reorientation transition down to 2 K. This is clearly evident from the (003) magnetic Bragg peak intensity not decreasing at low temperatures. If the Morin transition were to exist, it would be expected that the (003) Bragg peak would drop drastically, as seen in the bulk α-Fe_2O_3 reference sample at 259.1(2) K. Rietveld refinement of data taken from the bulk material below this temperature provides the most precise estimate to date of the canting of moments on Fe^{3+} ions from the hexagonal *c* axis, with a value of 10.7(2)° at 10 K. In the case of the mesoporous α-Fe_2O_3 sample, the spin structure at 2 K does not deviate from the one found above the Morin transition in the bulk material. It also was observed that the paramagnetic scattering from the mesoporous sample increased significantly with increasing temperature, despite the sample still being below the Néel ordering temperature (~955 K in bulk α-Fe_2O_3,). No such increase in paramagnetic scattering was seen in the bulk material over a comparable temperature range. This suggests that there is rising surface disorder of the magnetic spins in the mesostructured material as the temperature is raised. Moreover, this suggests that the surface plays a key role in the magnetic properties of such mesoporous magnets. More detailed insights into the effect of temperature and mesostructure on the magnetic behavior of mesoporous hematite may be revealed by inelastic neutron scattering measurements of the magnetic excitations, in turn providing a measure of the changing contributions of competing terms in the Hamiltonian.

Acknowledgment. A.H.H. thanks Drs. A. J. Williams and J. A. Rodgers for their guidance with Rietveld refinements and Prof. J. P. Attfield and Drs. I. D. H. Oswald and S. A. J. Kimber for their useful input and suggestions. We also thank the referees for their very helpful suggestions.

CM800009S

---

(57) Tachiki, M.; Nagamiya, T. *J. Phys. Soc. Jpn.* **1958**, *13*, 452.
(58) Néel, L. *J. Phys. Radium* **1954**, *15*, 225.
(59) Zhang, K.; Fredkin, D. R. *J. Appl. Phys.* **1996**, *79*, 5762.
(60) Huang, Z.; Chen, Z.; Li, S.; Feng, Q.; Zhang, F.; Du, Y. *Eur. Phys. J. B* **2006**, *51*, 65.
(61) Restrepo, J.; Labaye, Y.; Greneche, J. M. *Physica B* **2006**, *384*, 221.
(62) Zysler, R. D.; Vasquez Mansilla, M.; Fiorani, D. *Eur. Phys. J. B* **2004**, *41*, 171.
(63) Kündig, W.; Bömmel, H.; Constabaris, G.; Lindquist, R. H. *Phys. Rev.* **1966**, *142*, 327.
(64) Amin, N.; Arajs, S. *Phys. Rev. B: Condens. Matter Mater. Phys.* **1987**, *35*, 4810.
(65) de Boer, C. B.; Mullender, T. A. T.; Dekkers, M. J. *Geophys. J. Int.* **2001**, *146*, 201.
(66) Gee, S. H.; Hong, Y. K.; Sur, J. C.; Erickson, D. W.; Park, M. H.; Jeffers, F. *IEEE Trans. Magn.* **2004**, *40*, 2691.
(67) Dang, M. Z.; Rancourt, D. G.; Dutrizac, J. E.; Lamarche, G.; Provencher, R. *Hyperfine Interact.* **1998**, *117*, 271.
(68) Wu, C. Z.; Yin, P.; Zhu, X.; OuYang, C. Z.; Xie, Y. *J. Phys. Chem. B* **2006**, *110*, 17806.

Appendix C

Mesoporous single-crystal Co_3O_4 templated by cage-containing mesoporous silica

W. Yue, A. H. Hill, A. Harrison, and W. Zhou.

Reproduced with permission from Chemical Communications, pp. 2518–2520 (2007).

COMMUNICATION www.rsc.org/chemcomm | ChemComm

Mesoporous single-crystal Co_3O_4 templated by cage-containing mesoporous silica

Wenbo Yue,[a] Adrian H. Hill,[b] Andrew Harrison[bc] and Wuzong Zhou*[a]

Received (in Cambridge, UK) 5th January 2007, Accepted 21st February 2007
First published as an Advance Article on the web 15th March 2007
DOI: 10.1039/b700185a

Mesoporous single-crystal Co_3O_4 was obtained using cage-containing mesoporous silicas, FDU-12 and SBA-16, as templates and characterised by XRD, HRTEM and nitrogen adsorption–desorption while SQUID magnetometry was used to probe the magnetic character.

In our previous papers and the reports from others,[1–5] it has been demonstrated that crystal growth of transition metal oxides inside the pores of mesoporous silica, SBA-15 and KIT-6, leads to mesoporous single-crystal oxides, which may be developed into new forms of catalysts with high activity and selectivity, and new materials with some interesting physical properties. The porous oxides produced can be regarded as negative replicas of the mesoporous silicas and, therefore, the morphology of the building unit has the same shape of the original pores in the silica template. Both the pore structures of SBA-15[6] and KIT-6[7] contain cylindrical pore units. As a result, the building unit in the porous crystals of oxides templated by them is a piece of nanorod. In SBA-15, some small subchannels connecting the principal channels must be available for crystal expansion. Otherwise, individual nanowires instead of three dimensional porous crystals are produced.[8]

Unlike the formation of mesoporous silicas, where the silicate species and surfactant molecules may aggregate simultaneously,[9] the hard templates are prepared first for the porous metal oxides. Therefore, an important step is to impregnate the templating pores with the precursor. This can be achieved in different ways. In the first method, the inner surface of mesoporous silica is functionised *via* aminosilylation of the silanols and then anchoring the acidic precursor (*e.g.* $H_2Cr_2O_7$, $H_3PW_{12}O_{40}$) molecules.[1] The second method is the so-called "two solvents" impregnation method. For example, a suspension of mesoporous silica in dry hexane is mixed with an aqueous solution of metal nitrate. The precursor molecules will then move into the pores during a stirring.[2] Recently, some porous crystals of oxides were fabricated *via* an evaporation method, *i.e.* simply dissolving the nitrate precursor in ethanol. It was expected that the precursor molecules would enter the pores during the evaporation of ethanol by a capillary action.[3] The impregnation can also be achieved by a solid-state grinding route if a suitable precursor is used.[10] In the present work, we synthesized porous Co_3O_4 crystals by using this latter method and using some cage-containing mesoporous silicas as templates.

Co_3O_4 has potential applications[11] in electrochromic devices, gas sensors, Li-ion rechargeable battery, semiconductors, solar energy absorbers and heterogeneous catalysts. Mesoporous Co_3O_4 crystals may have improved properties for these applications because of their large specific surface areas and shape selectivity.

Both SBA-16[12] and FDU-12[13] have mesoporous networks built by spherical nanocages connected by some windows. SBA-16 has a body-centred cubic structure (space group $Im\bar{3}m$) and FDU-12 is face-centred cubic (space group $Fm\bar{3}m$). Accordingly, each spherical nanocage is 8 coordinated by the neighbouring nanocages in SBA-16, but 12 coordinated in FDU-12. When porous crystals of Co_3O_4 form in these two silica phases, we expect the structures of the products to be three dimensional arrangements of solid nanospheres connected to each other by some very short nanorods as shown in Fig. 1.

SBA-16 and FDU-12 were synthesized according to the established methods.[12,13] For FDU-12, the windows connecting the spherical nanocages could be tuned from 4 to 7.5 nm while the change of diameter of the nanocages was not so significant (from 10 to 12 nm), mainly by changing the maturing temperature.[13] In the present work, the hydrothermal conditions of 100 °C for small windows (4 nm) were selected. The metal oxide $Co(NO_3)_3\cdot 6H_2O$ was impregnated within the mesoporous silica using a solid–liquid method. 1 mmol of $Co(NO_3)_3\cdot 6H_2O$ was mixed with 0.15 g of SBA-16 or FDU-12, and was ground for a few minutes. The mixture was then placed in a crucible and heated in a muffle furnace. The temperature was increased slowly (1 $^\circ C\ min^{-1}$) from room temperature up to 500 °C. The specimen was kept at 500 °C for 5 h before cooling down.

In this method, a mixture of two solids was heated directly without using any solvent. The essential condition for this method is that the melting point of $Co(NO_3)_2\cdot 6H_2O$ (55 °C) is lower than its decomposition temperature (74 °C). When $Co(NO_3)_2\cdot 6H_2O$ melted at 55 °C, the liquid phase covered the external surface of

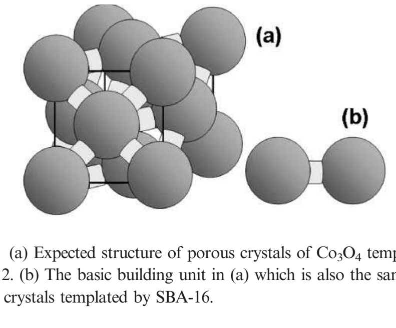

Fig. 1 (a) Expected structure of porous crystals of Co_3O_4 templated by FDU-12. (b) The basic building unit in (a) which is also the same in the porous crystals templated by SBA-16.

---

[a] *School of Chemistry, University of St. Andrews, St. Andrews, Fife, UK KY16 9ST. E-mail: wzhou@st-andrews.ac.uk; Fax: +44 (0)1334 463808; Tel: +44 (0)1334 467276*
[b] *School of Chemistry and EaStChem, The University of Edinburgh, The King's Buildings, West Mains Rd., Edinburgh, UK EH9 3JJ*
[c] *Institut Laue-Langevin, 6, rue Jules Horowitz BP, 156 - 38042, Grenoble, France*

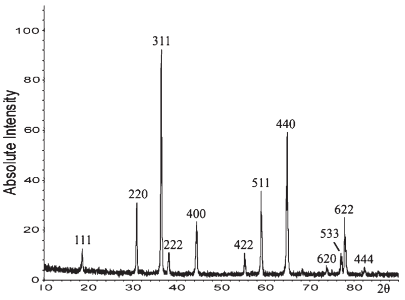

Fig. 2 XRD pattern of porous Co_3O_4 crystals templated by SBA-16, indexed onto the cubic unit cell with $a = 0.8085$ nm.

the silica particles and moved into the pores under capillary action. The precursor was then decomposed step by step with increasing temperature, forming intermediate compounds, such as $Co(NO_3)_2\cdot 2H_2O$ by losing $4H_2O$, and $Co(NO_3)(OH)\cdot H_2O$ by further losing HNO_3. Crystalline Co_3O_4 formed at the final stage. This process is different from one outside the mesopores due to a confinement effect. The silica template was then removed with a 10 wt% HF aqueous solution. A black powder product of mesoporous Co_3O_4 crystals was obtained by centrifugation and washed with distilled water thrice.

Initial characterisation of the specimens was by X-ray powder diffraction (XRD). Both XRD patterns of the cobalt oxides templated by SBA-16 and FDU-12 indicate that the products are cubic Co_3O_4, space group $Fd\bar{3}m$ (Fig. 2).

Further investigation of the products was carried out by selected area electron diffraction (SAED), transmission electron microscopy (TEM) and high resolution TEM (HRTEM) on JEOL-JEM-2011 microscope operated at 200 kV. Fig. 3a shows a TEM image of a FDU-12 particle whose spherical cavities have been partially filled with Co_3O_4 crystals (the dark areas). The size of these particles is variable. For example, the particle in the centre of Fig. 3a is about 150 nm in diameter, while at the top right corner, there is a much larger particle. The silica particles cannot be entirely filled by Co_3O_4, because even it is fully filled at beginning by $Co(NO_3)_2\cdot 6H_2O$, the volume of the cobalt compound will be significantly reduced when it decomposes and forms Co_3O_4.

Fig. 3b shows porous Co_3O_4 crystals after the template was removed. The pore system in FDU-12 has been replicated by the metal oxide. The diameter of the main particle is about 600 nm and some small particles nearby are only about 100 nm in diameter.

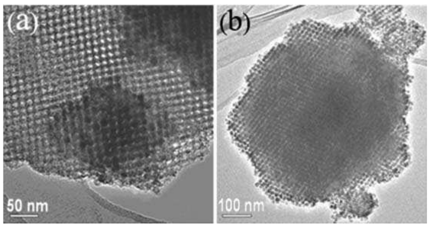

Fig. 3 (a) TEM image of a particle of FDU-12 containing some cobalt oxide nanospheres. (b) Porous cobalt oxide crystals after removing the silica template.

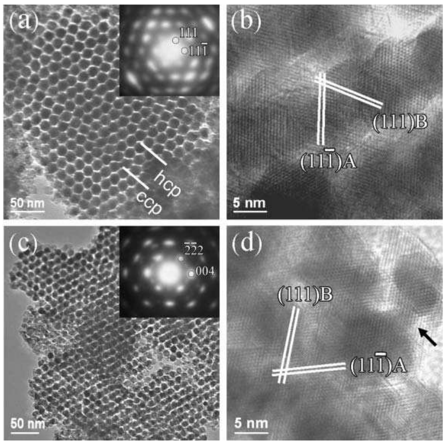

Fig. 4 TEM images of porous Co_3O_4 templated by (a) FDU-12 and (c) SBA-16. In (a), irregular intergrowth of ccp and hcp stackings is indicated. The insets in (a) and (c) are SAED patterns from these two samples of crystalline Co_3O_4. (b) and (d) HRTEM images of Co_3O_4 templated by FDU-12 and SBA-16, respectively. The arrow in (d) points to the bridge connecting two nanospheres. The *d*-spacings of the marked fringes are *ca.* 0.467 nm, corresponding to the {111} planes of Co_3O_4.

The chemical composition of the specimen was examined by energy dispersive X-ray spectroscopy (EDX). The EDX spectra from cobalt oxide with the FDU-12 template show the elements cobalt, oxygen and silicon. After the template was dissolved, no silicon was present in the samples.

TEM images with higher magnifications of the porous Co_3O_4 crystals templated by FDU-12 and SBA-16 (Fig. 4) indicated that the porous crystals were both made of nanoballs connected by nanobridges. Such bridges can be observed at the edge of the particles as indicated by an arrow in Fig. 4(d). In the FDU-12 templated Co_3O_4, the nanospheres are in a cubic close packed arrangement and some stacking faults, also commonly seen in FDU-12, namely irregular intergrowth of cubic close-packing (ccp) and hexagonal close-packing (hcp), are often observed. In the SBA-16 templated porous oxide, the nanospheres are in a body centred arrangement and such defects do not form.

SAED patterns from large areas show the single-crystal property and can be indexed to the cubic Co_3O_4 structure, as shown in the insets in Fig. 4 (a) and (c). HRTEM images of the porous Co_3O_4 crystals further confirm the single-crystal property (Fig. 4(b) and (d)). Since the crystal orientation of Co_3O_4 has no relation with the orientation of the mesopore network, it is difficult to find a viewing direction parallel to a principal orientation in both the Co_3O_4 crystal and the mesopore system. Consequently, when we found a good projection for the mesopore network, *e.g.* shown in Fig. 4(a) and (c), we missed a principal crystal orientation of Co_3O_4. Similarly, when we approached a principal orientation of the crystal as shown in Fig. 4(b) and (d), the arrangement of the nanospheres could not be clearly revealed.

Fig. 5 shows the nitrogen adsorption–desorption isotherms of the porous Co_3O_4 products. The isotherms of Co_3O_4 porous crystals are both type IV with a hysteresis loop, indicating the mesoporous property. The specific surface areas of Co_3O_4 crystals

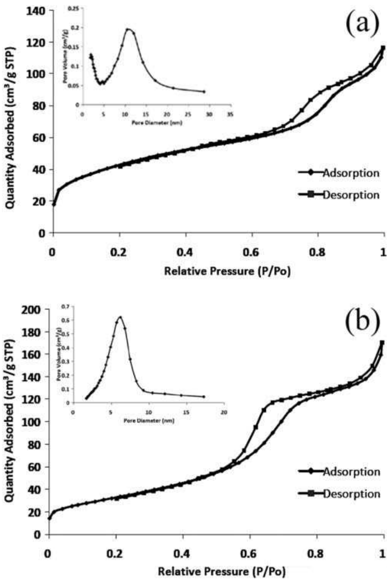

Fig. 5 Nitrogen adsorption–desorption isotherms measured at 77 K from porous crystals of Co_3O_4 templated by (a) FDU-12 and (b) SBA-16. Insets: pore size distribution of the corresponding crystals.

templated by FDU-12 and SBA-16 are 151(1) and 122.4(6) $m^2\ g^{-1}$, respectively, which are larger than the surface area of Co_3O_4 templated by KIT-6 (92 $m^2\ g^{-1}$).[3] For a comparison with the surface areas in FDU-12 (410 $m^2\ cm^{-3}$) and in SBA-16 (686 $m^2\ cm^{-3}$), the above values were altered to 450 (FDU-12 templated, pore volume is 0.171 $cm^3\ g^{-1}$) and 298 $m^2\ cm^{-3}$ (SBA-16 templated, pore volume is 0.246 $cm^3\ g^{-1}$) when the densities of 2.2 g cm^{-3} (SiO_2) and 6.07 g cm^{-3} (Co_3O_4) were used. The diameters of the nanospheres in these two specimens are similar as seen in Fig. 4. and the average pore size of the SBA-16 templated Co_3O_4 (6.6 nm) is slightly larger than that in the FDU-12 templated sample (6.1 nm). The large specific surface areas in the samples also indicate high yields.

Finally, preliminary magnetic characterisation of a Co_3O_4 sample templated with SBA-16 was performed by SQUID magnetometry. Measurements were made from 2–340 K in 0.01 T after cooling to base temperature in zero field. The temperature-dependent susceptibility and effective magnetic moment are displayed in Fig. 6, revealing behaviour similar to that seen in bulk Co_3O_4 (Aldrich, 99.995%). The results of the measurements on the bulk material are displayed in the same figure for comparison, and these observations and interpretation may also be compared with those of similar work on another form of mesoporous Co_3O_4.[14]

WZ thanks St Andrews University for an EaStCHEM studentship for WY and AH thanks the University of Edinburgh for a studentship for AHH.

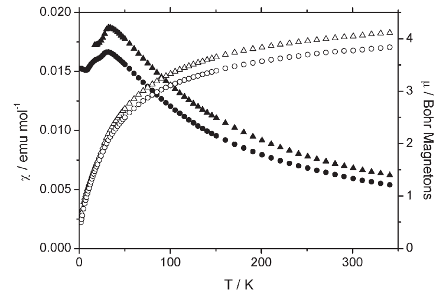

Fig. 6 Temperature dependence of magnetic susceptibility (solid circles) and effective magnetic moment (open circles) of Co_3O_4 templated by SBA-16 and measured in 0.01 T after cooling to base temperature in zero field. The behaviour of bulk Co_3O_4 is depicted by triangles—open and closed as for the mesoporous form.

Notes and references

1 K. K. Zhu, B. Yue, W. Z. Zhou and H. Y. He, *Chem. Commun.*, 2003, 98; B. Yue, H. L. Tang, Z. P. Kong, K. K. Zhu, C. Dickinson, W. Z. Zhou and H. Y. He, *Chem. Phys. Lett.*, 2005, **407**, 83.
2 K. Jiao, B. Zhang, B. Yue, Y. Ren, S. X. Liu, S. R. Yan, C. Dickinson, W. Z. Zhou and H. Y. He, *Chem. Commun.*, 2005, 5618.
3 C. Dickinson, W. Z. Zhou, R. P. Hodgkins, Y. F. Shi, D. Y. Zhao and H. Y. He, *Chem. Mater.*, 2006, **18**, 3088.
4 B. Z. Tian, X. Y. Liu, H. F. Yang, S. H. Xie, C. Z. Yu, B. Tu and D. Y. Zhao, *Adv. Mater.*, 2003, **15**, 1370; B. Z. Tian, X. Y. Liu, L. A. Solovyov, Z. Liu, H. F. Yang, Z. D. Zhang, S. H. Xie, F. Q. Zhang, B. Tu, C. Z. Yu, O. Terasaki and D. Y. Zhao, *J. Am. Chem. Soc.*, 2004, **126**, 865.
5 F. Jiao, A. Harrison, J. C. Jumas, A. V. Chadwick, W. Kockelmann and P. G. Bruce, *J. Am. Chem. Soc.*, 2006, **128**, 5468.
6 D. Y. Zhao, J. L. Feng, Q. S. Huo, N. Melosh, G. H. Fredrickson, B. F. Chmelka and G. D. Stucky, *Science*, 1998, **279**, 548.
7 F. Kleitz, S. H. Choi and R. Ryoo, *Chem. Commun.*, 2003, 2136.
8 K. K. Zhu, H. Y. He, S. H. Xie, X. A. Zhang, W. Z. Zhou, S. L. Jin and B. Yue, *Chem. Phys. Lett.*, 2003, **377**, 317.
9 C. F. Cheng, H. Y. He, W. Z. Zhou and J. Klinowski, *Chem. Phys. Lett.*, 1995, **244**, 117; W. Z. Zhou and J. Klinowski, *Chem. Phys. Lett.*, 1998, **292**, 207.
10 Y. M. Wang, Z. Y. Wu, H. J. Wang and J. H. Zhu, *Adv. Funct. Mater.*, 2006, **16**, 2374.
11 F. Švegl, B. Orel and M. Hutchins, *J. Sol-Gel Sci. Technol.*, 1997, **8**, 765; W. Y. Li, L. N. Xu and J. Chen, *Adv. Funct. Mater.*, 2005, **15**, 851; J. Wollenstein, M. Burgmair, G. Plescher, T. Sulima, J. Hildenbrand, H. Bottner and I. Eisele, *Sens. Actuators, B*, 2003, **93**, 442; P. Poizot, S. Laruelle, S. Grugeon, L. Dupont and J. M. Tarascon, *Nature*, 2000, **407**, 496; S. A. Needham, G. X. Wang, K. Konstantinov, Y. Tournayre, Z. Lao and H. K. Liu, *Electrochem. Solid State Lett.*, 2006, **9**, A315; C. S. Cheng, M. Serizawa, H. Sakata and T. Hirayama, *Mater. Chem. Phys.*, 1998, **53**, 225; A. G. Avila, E. C. Barrera, L. A. Huerta and S. Muhl, *Sol. Energy Mater. Sol. Cells*, 2004, **82**, 269; D. Mehandjiev and E. Nikolovazhecheva, *J. Catal.*, 1980, **65**, 475; L. Yan, X. M. Zhang, T. Ren, H. P. Zhang, X. L. Wang and J. S. Suo, *Chem. Commun.*, 2002, 860.
12 D. Y. Zhao, Q. S. Huo, J. L. Feng, B. F. Chmelka and G. D. Stucky, *J. Am. Chem. Soc.*, 1998, **120**, 6024.
13 J. Fan, C. Z. Yu, F. Gao, J. Lei, B. Z. Tian, L. M. Wang, Q. Luo, B. Tu, W. Z. Zhou and D. Y. Zhao, *Angew. Chem., Int. Ed.*, 2003, **42**, 3146; J. Fan, C. Z. Yu, J. Lei, Q. Zhang, T. C. Li, B. Tu, W. Z. Zhou and D. Y. Zhao, *J. Am. Chem. Soc.*, 2005, **127**, 10794.
14 Y. Q. Wang, C. M. Yang, W. Schmidt, B. Spliethoff, E. Bill and F. Schuth, *Adv. Mater.*, 2005, **17**, 53.

Appendix D

Synthesis of Ordered Mesoporous NiO with Crystalline Walls and a Bimodal Pore Size Distribution

F. Jiao, A. H. Hill, A. Harrison, A. Berko, A. V. Chadwick, and P. G. Bruce.

Reproduced with permission from Journal of the American Chemical Society **30**, 5262 (2008).

J|A|C|S
ARTICLES

Synthesis of Ordered Mesoporous NiO with Crystalline Walls and a Bimodal Pore Size Distribution

Feng Jiao,† Adrian H. Hill,‡ Andrew Harrison,‡,§ Aaron Berko,¶ Alan V. Chadwick,¶
and Peter G. Bruce*,†

*EaStChem and School of Chemistry, University of St. Andrews, St. Andrews,
Fife KY16 9ST, U.K., EaStChem and School of Chemistry, University of Edinburgh, Joseph
Black Building, West Mains Road, Edinburgh EH9 3JJ, U.K., Institut Laue-Langevin 6, rue
Jules Horowitz, BP 156-38042 Grenoble Cedex 9, France, and Centre for Materials Research,
School of Physical Sciences, University of Kent, Canterbury, Kent CT2 7NR, U.K.*

Received December 5, 2007; E-mail: p.g.bruce@st-andrews.ac.uk

Abstract: A mesoporous solid with crystalline walls and an ordered pore structure exhibiting a bimodal pore size distribution (3.3 and 11 nm diameter pores) has been synthesized. Previous attempts to synthesize solids with large ordered mesopores by hard templating focused on the preparation of templates with thick walls (the thick walls become the pores in the target materials), something that has proved difficult to achieve. Here the large pores (11 nm) do not depend on the synthesis of a template with thick walls but instead on controlling the microporous bridging between the two sets of mesopores in the KIT-6 template. Such control determines the relative proportion of the two pore sizes. The wall thickness of the 3D cubic NiO mesopore has also been varied. Preliminary magnetic characterization indicates the freezing of uncompensated moments or blocking of superparamagnetism.

Introduction

Interest in mesoporous solids (pore size 2–50 nm) has become intense in recent years.[1–9] The advent of hard templating, where one mesoporous solid (often a mesoporous silica) is used as a template within which to grow another mesoporous solid (e.g., a transition metal oxide), has proved a powerful tool with which to synthesize a wide range of mesoporous materials combining an ordered pore structure and crystalline walls.[10–14] However, the method, as originally exploited, has its limitations. For example, it can be challenging to synthesize mesopores exhibiting mixed valency or with oxidation states that are difficult to stabilize in solution or that contain Li.[15,16] Previously, we reported the synthesis of the mesoporous spinel Fe_3O_4 and lithium containing compound $LiCoO_2$ by post-template redox reaction and post-template reaction with a lithium source, respectively, thus demonstrating access to a wider range of mesoporous solids.[16–18]

Another limitation is the pore sizes that may be obtained for mesoporous solids with an ordered pore structure and crystalline walls.[7,10,11,19,20] Silica xerogels or carbon aerogels have been used as hard templates to produce inorganic solids with a pore size up to 18 nm, but the pores are disordered.[20–22] To obtain ordered mesoporous oxides with crystalline walls, mesoporous silicas with an ordered pore structure, such as SBA-15, SBA-16, and KIT-6, are used as hard templates, but such a route limits the pore size to less than 7 nm.[16,23–30] Efforts to prepare large and ordered porous solids by hard templating have focused

---

† University of St. Andrews.
‡ University of Edinburgh.
§ Institut Laue-Langevin 6.
¶ University of Kent.

(1) Kresge, C. T.; Leonowicz, M. E.; Roth, W. J.; Vartuli, J. C.; Beck, J. S. *Nature* **1992**, *359*, 710.
(2) Huo, Q. S.; Margolese, D. I.; Stucky, G. D. *Chem. Mater.* **1996**, *8*, 1147.
(3) Sayari, A. *Chem. Mater.* **1996**, *8*, 1840.
(4) Corma, A. *Chem. Rev.* **1997**, *97*, 2373.
(5) Yang, P. D.; Zhao, D. Y.; Margolese, D. I.; Chmelka, B. F.; Stucky, G. D. *Nature* **1998**, *396*, 152.
(6) Ying, J. Y.; Mehnert, C. P.; Wong, M. S. *Angew. Chem., Int. Ed.* **1999**, *38*, 56.
(7) Schuth, F. *Chem. Mater.* **2001**, *13*, 3184.
(8) Davis, M. E. *Nature* **2002**, *417*, 813.
(9) Antonietti, M.; Ozin, G. A. *Chem.—Eur. J.* **2004**, *10*, 29.
(10) Yang, H. F.; Zhao, D. Y. *J. Mater. Chem.* **2005**, *15*, 1217.
(11) Lu, A. H.; Schuth, F. *Adv. Mater.* **2006**, *18*, 1793.
(12) Joo, S. H.; Choi, S. J.; Oh, I.; Kwak, J.; Liu, Z.; Terasaki, O.; Ryoo, R. *Nature* **2001**, *412*, 169.
(13) Kleitz, F.; Choi, S. H.; Ryoo, R. *Chem. Commun.* **2003**, 2136.
(14) Ryoo, R.; Joo, S. H.; Kruk, M.; Jaroniec, M. *Adv. Mater.* **2001**, *13*, 677.
(15) Brezesinski, T.; Groenewolt, M.; Antonietti, M.; Smarsly, B. *Angew. Chem., Int. Ed.* **2006**, *45*, 781.
(16) Jiao, F.; Shaju, K. M.; Bruce, P. G. *Angew. Chem., Int. Ed.* **2005**, *44*, 6550.
(17) Jiao, F.; Jumas, J. C.; Womes, M.; Chadwick, A. V.; Harrison, A.; Bruce, P. G. *J. Am. Chem. Soc.* **2006**, *128*, 12905.
(18) Jiao, F.; Harrison, A.; Hill, A. H.; Bruce, P. G. *Adv. Mater.* **2007**, *19*, 4063.
(19) Valdes-Solis, T.; Fuertes, A. B. *Mater. Res. Bull.* **2006**, *41*, 2187.
(20) Fuertes, A. B. *J. Phys. Chem. Solids* **2005**, *66*, 741.
(21) Li, W. C.; Lu, A. H.; Weidenthaler, C.; Schuth, F. *Chem. Mater.* **2004**, *16*, 5676.
(22) Li, W. C.; Lu, A. H.; Schmidt, W.; Schuth, F. *Chem.—Eur. J.* **2005**, *11*, 1658.
(23) Yue, W. B.; Zhou, W. Z. *J. Mater. Chem.* **2007**, *17*, 4947.
(24) Wang, Y. Q.; Yang, C. M.; Schmidt, W.; Spliethoff, B.; Bill, E.; Schuth, F. *Adv. Mater.* **2005**, *17*, 53.
(25) Tian, B. Z.; Liu, X. Y.; Solovyov, L. A.; Liu, Z.; Yang, H. F.; Zhang, Z. D.; Xie, S. H.; Zhang, F. Q.; Tu, B.; Yu, C. Z.; Terasaki, O.; Zhao, D. Y. *J. Am. Chem. Soc.* **2004**, *126*, 865.

10.1021/ja710849r CCC: $40.75

on the synthesis of ordered porous templates with thick walls (the walls of the template become the pores of the target mesoporous materials). Such synthesis has proved difficult.[10,11]

Here we show that it is possible to produce an ordered mesoporous solid with crystalline walls, specifically NiO, and with a pore diameter up to 11 nm. The resulting mesoporous NiO exhibits a bimodal pore size distribution (3.3 and 11 nm diameter). A bimodal pore size distribution has been observed previously using hard template routes and explained by insufficient impregnation of the precursor or infiltration of the precursor in the space between the particles of the template.[22,27,31,32] In this paper, we demonstrate, for the first time, that by disconnecting the two sets of mesopores in the KIT-6 template a bimodal pore size distribution may be generated and the proportion of the two sizes (3.3 and 11 nm) may be varied by controlling the temperature of the hydrothermal reaction used to form the KIT-6 silica template. Furthermore, this is the first example of a 3D mesoporous NiO with a cubic mesoporous symmetry.

Experimental Procedures

Preparation of the mesoporous silica, KIT-6, has been reported previously.[13,33] A typical synthesis procedure was as follows: 10 g of poly(ethylene glycol)−block−poly(propylene glycol)−block−poly(ethylene glycol) P123 (average $M_n \sim 5800$, Aldrich) was mixed with 282.5 mL of water and 16.75 mL of concentrated HCl (37 wt %, Fisher) in a beaker. The mixture was stirred at 35 °C until a homogeneous solution was obtained. Then, 10 g of *n*-butanol (99.4+%, Aldrich) was added, and this mixture was stirred for 1 h before 21.5 g of tetraethyl orthosilicate (TEOS, 98%, Aldrich) was added. After stirring at 35 °C for 24 h, the mixture was transferred into autoclaves which were sealed and maintained at three different temperatures, 80, 100, and 130 °C, for another 24 h. The resulting mixtures were filtered and dried at 60 °C, then added to 300–400 mL of ethanol and 20–30 mL of concentrated HCl (37 wt %, Fisher) in an 800 mL beaker. After stirring at room temperature for 1–2 h, the mixture was filtered and washed with water and ethanol several times. The final sample was dried at 60 °C and calcined at 500 °C for 3 h under air to remove the polymer template. The resulting three mesoporous silicas (KIT-6) were characterized by N_2 adsorption and transmission electron microscopy (TEM) analysis before being used as a hard template in the following procedure.

A typical synthesis of mesoporous NiO was as follows: 4 g of $Ni(NO_3)_2 \cdot 6H_2O$ (96%, Aldrich) was dissolved in 150 mL of ethanol, followed by addition of 5 g of mesoporous silica KIT-6. After stirring at room temperature in a fume cupboard until all the solution had been absorbed, the powder was redispersed in 100 mL of dry *n*-hexane under stirring in an open beaker. After all the solvent had evaporated, the sample was heated slowly to 550 °C and calcined at that temperature for 3 h. The resulting sample was treated twice with a hot aqueous solution of 2 M NaOH to remove the silica template, followed by washing with water several times and then drying at 60 °C. Mesoporous NiO prepared by using KIT-6 at 80, 100, and 130 °C was denoted as NiO-80, NiO-100, and NiO-130, respectively.

TEM studies were carried out by using a JEOL JEM-2011. This TEM uses a LaB6 filament as the electron source, and the accelerate voltage is 200 keV. TEM and HRTEM images were both recorded by a Gatan CCD camera in a digital format. Wide-angle powder X-ray diffraction data were collected in a Stoe STADI/P powder diffractometer operating in transmission mode and with a low-angle position-sensitive detector. Incident radiation was generated using a Fe Kα_1 source ($\lambda = 1.936$ Å). Low-angle powder X-ray diffraction data were collected using a Rigaku/MSC, D/max-rB with Cu Kα_1 radiation ($\lambda = 1.541$ Å) operating in reflection mode and a scintillation detector. N_2 adsorption−desorption analysis was carried out using a Micromeritics ASAP 2020. The typical sample weight used in the measurement was 100–200 mg. The outgas condition was set to 180 min at 120 °C under vacuum, and all adsorption−desorption measurements were carried out under liquid nitrogen temperature. Oxidation states were verified by XANES, and local structure was probed by EXAFS on Station 9.3 at the CCLRC Daresbury Laboratory SRS, U.K. The magnetic measurements were taken using a MPMS Quantum Design SQUID magnetometer. Weighed samples were encapsulated in gelatin and then placed in a diamagnetic straw, attached to the sample holder, which was connected to the SQUID system. Data were collected in an applied field of 0.01 T, first after cooling from 320 to 1.8 K in zero field (zfc) and then after cooling through the same temperature range in a field of 0.01 T (fc).

Results and Discussion

In order to produce a material with a highly ordered mesoporous structure throughout, it is essential to achieve a high degree of infiltration and wetting of the precursor solution within the pore structure of the hard template KIT-6. This was achieved in the case of mesoporous NiO by infiltrating a solution of $Ni(NO_3)_2$ in ethanol rather than water and by redispersing in hexane. In this way, it was possible to achieve a very high degree of pore filling.

The three 3D mesoporous NiO materials were examined by transmission electron microscopy (TEM). All three samples show a highly ordered pore structure (Figure 1). By examining many particles, it has been demonstrated that this highly ordered mesoporous structure is present throughout each material, confirming the high level of infiltration achieved by the solution precursor. The symmetry of the mesostructure for NiO-80, NiO-100, and NiO-130 is that of the 3D template KIT-6, *Ia*3*d*. The cubic lattice parameters, a_0, extracted from the TEM data are 213, 230, and 258 Å for NiO-80, NiO-100, and NiO-130, respectively. The wall thicknesses for NiO-80, NiO-100, and NiO-130 estimated from TEM results are 5.5, 6.8, and 7.8 nm, respectively. These values are in good agreement with the pore sizes of the corresponding mesoporous silica templates, which are 5.3, 7.1, and 8.0 nm (Table 1), respectively (the pores of the template become the walls of the mesoporous NiO materials).[13,33] The NiO particles are of typical diameter, 0.2–0.5 μm, and are approximately spherical, consistent with a 3D process of nucleation and growth within the isotropic pore structure of the KIT-6 template.

The pore structures of mesoporous NiO were examined by N_2 adsorption−desorption measurements, the results of which are presented in Figure 2 and summarized in Table 1. The isotherms with H1 hysteresis loops, observed for all three mesoporous NiO (Figure 2a), are similar in shape to those observed previously for many other mesoporous transition metal

---

(26) Shen, W. H.; Dong, X. P.; Zhu, Y. F.; Chen, H. R.; Shi, J. L. *Microporous Mesoporous Mater.* **2005**, *85*, 157.

(27) Jiao, K.; Zhang, B.; Yue, B.; Ren, Y.; Liu, S. X.; Yan, S. R.; Dickinson, C.; Zhou, W. Z.; He, H. Y. *Chem. Commun.* **2005**, 5618.

(28) Jiao, F.; Bruce, P. G. *Adv. Mater.* **2007**, *19*, 657.

(29) Tian, B. Z.; Liu, X. Y.; Yang, H. F.; Xie, S. H.; Yu, C. Z.; Tu, B.; Zhao, D. Y. *Adv. Mater.* **2003**, *15*, 1370.

(30) Salabas, E. L.; Rumplecker, A.; Kleitz, F.; Radu, F.; Schuth, F. *Nano Lett.* **2006**, *6*, 2977.

(31) Shi, Y. F.; Meng, Y.; Chen, D. H.; Cheng, S. J.; Chen, P.; Yang, T. F.; Wan, Y.; Zhao, D. Y. *Adv. Funct. Mater.* **2006**, *16*, 561.

(32) Zhou, L.; Li, H. Q.; Yu, C. Z.; Zhou, X. F.; Tang, J. W.; Meng, Y.; Xia, Y. Y.; Zhao, D. Y. *Carbon* **2006**, *44*, 1601.

(33) Kim, T. W.; Kleitz, F.; Paul, B.; Ryoo, R. *J. Am. Chem. Soc.* **2005**, *127*, 7601.

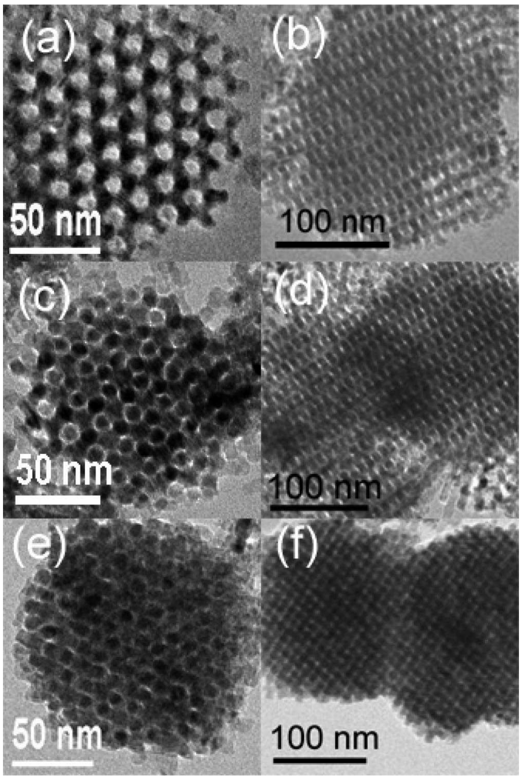

Figure 1. TEM images for mesoporous (a, b) NiO-80, (c, d) NiO-100, and (e, f) NiO-130 recorded along different directions.

Table 1. Summary of BET Surface Areas, Pore Diameters, and Wall Thicknesses for KIT-6 Synthesized Hydrothermally at 80, 100, and 130 °C (Denoted as KIT-6-80, KIT-6-100, and KIT-6-130, Respectively) and Corresponding Mesoporous NiO Replicas

	BET surface area (m^2/g)	pore diameter[a] (nm)	wall thickness[b] (nm)
KIT-6-80	820	5.3	3.6
KIT-6-100	816	7.1	3.4
KIT-6-130	787	8	3.3
NiO-80	108.6	3.1/11.1/31	5.5
NiO-100	94.1	3.15/11.3/33	6.8
NiO-130	81.8	3.3/29	7.8

[a] The pore size distribution is calculated from the desorption isotherm by the BJH method. [b] The wall thickness is estimated by TEM analysis.

oxides synthesized by the hard template route.[24,27,28,34] The pore size distributions calculated from the desorption isotherms by the BJH method are shown as a plot of the relative pore filling versus pore size in Figure 2b. The first peak at 3.1, 3.15, and 3.3 nm for NiO-80, NiO-100, and NiO-130, respectively, is in agreement with the wall thickness (~3.3 nm) of KIT-6 (see Table 1). For NiO-80 and NiO-100, but not NiO-130, there is also a peak at 11 nm; that is, NiO-80 and NiO-100 exhibit a bimodal pore size distribution. The TEM image of this large pore is shown in Figure 1a.

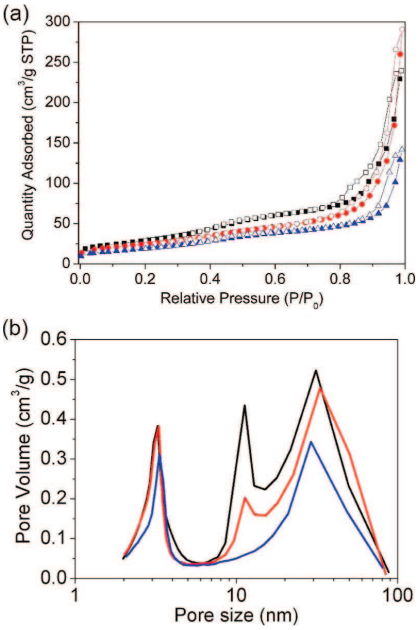

Figure 2. (a) N_2 adsorption−desorption isotherms for NiO-80 (black), NiO-100 (red), and NiO-130 (blue). (b) Pore size distributions calculated from desorption isotherms by the BJH method for NiO-80 (black), NiO-100 (red), and NiO-130 (blue).

Scheme 1. Mechanism By Which Two Pore Sizes in Mesoporous NiO Can Occur

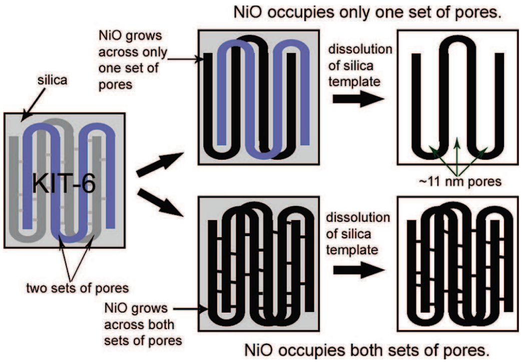

KIT-6 is composed of two sets of interpenetrating mesopores. Whereas early reports indicated that each set of mesopores was independent, recent studies have contradicted this view, suggesting that they are interconnected by micropores, as in SBA-15.[33,35] If NiO growing within the pores of KIT-6 can do so across both sets of pores, then the resulting mesoporous NiO will have a wall thickness equivalent to the size of the KIT-6 mesopores (5–8 nm) and a pore diameter equivalent to the KIT-6 wall thickness (~3.3 nm). If, on the other hand, NiO grows within only one set of the KIT-6 mesopores, then the resulting

---

(34) Zhu, K. K.; Yue, B.; Zhou, W. Z.; He, H. Y. *Chem. Commun.* **2003**, 98.

(35) Sakamoto, Y.; Kim, T. W.; Ryoo, R.; Terasaki, O. *Angew. Chem., Int. Ed.* **2004**, *43*, 5231.

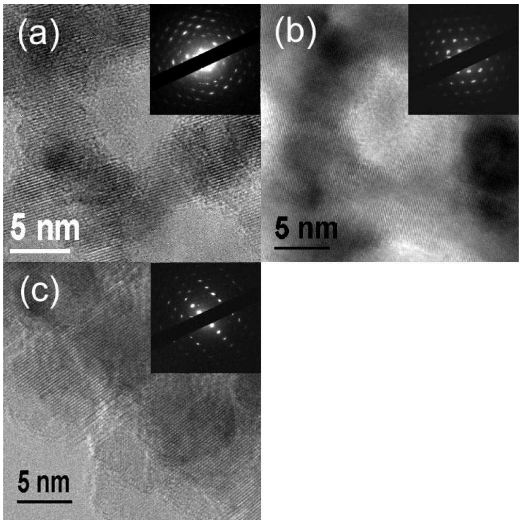

Figure 3. HRTEM images and selected area electron diffractions (insets) for (a) NiO-80, (b) NiO-100, and (c) NiO-130.

mesoporous NiO will still have a wall thickness of 5–8 nm but the pore diameter will be greater than before (~11 nm), equivalent to the dimensions of two walls plus a pore of KIT-6 (Scheme 1).

The differences observed in the mesostructures for the three NiO materials reflect the differences in the connectivity between the two sets of mesopores in KIT-6. For NiO-130, mesoporous NiO must grow across both sets of the mesopores in KIT-6 since only ~3.3 nm pores are observed in NiO; that is, the two sets of mesopores in KIT-6 must be connected by micropores. Examination of HRTEM images for NiO-130 shows coherence of the lattice fringes throughout the particles, and selected area electron diffraction on a single particle indicates a single-crystal-like structure, consistent with structural coherence across the two sets of pores (Figure 3c). For KIT-6 synthesized below 130 °C, the micropores must be less well developed, leading to less connectivity between the two sets of mesopores and hence the appearance of the 11 nm pores in NiO-80 and NiO-100. Figure 3a,b shows that there is structural coherence across the particles for NiO-80 and NiO-100. The relative intensities of the peaks in Figure 2b corresponding to the 3.3 and 11 nm pores differ between NiO-80 and NiO-100, demonstrating a difference in the proportions of the two pore sizes. The proportion of the 11 nm pores decreases with increasing temperature, and the 11 nm pores disappear entirely for NiO-130. These results are consistent with the change in the microporous connectivity of KIT-6 achieved by changing the temperature used to prepare the template.[33] The results show that it is possible to control the appearance and proportion of large (11 nm) pores in 3D mesoporous NiO by varying the KIT-6 synthesis temperature. The BET surface areas for NiO-80, NiO-100, and NiO-130, calculated from the sorption data, are 108.6, 94.1, and 81.8 m^2 g^{-1} (Table 1) and are similar to the surface areas of other mesoporous transition metal oxides templated by KIT-6.[17,26,27,36,37]

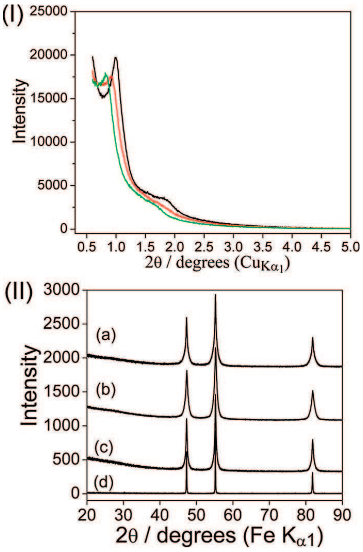

Figure 4. (I) Low-angle PXRD patterns for NiO-80 (black line), NiO-100 (red line), and NiO-130 (green line). (II) Powder X-ray diffraction patterns for (a) NiO-80, (b) NiO-100, (c) NiO-130, and (d) bulk NiO.

The results described above were obtained at a $Ni(NO_3)_2$ to KIT-6 weight ratio of 0.8 and a calcination temperature of 550 °C. The effect of varying the impregnation ratio, $Ni(NO_3)_2$ to KIT-6, and the calcination temperature on the bimodal pore size distribution has also been investigated. The $Ni(NO_3)_2$/KIT-6 weight ratio was varied from 0.5 to 2. For NiO-80 and NiO-100, there is a slight increase in the ratio of 11 to 3.3 nm pores at low $Ni(NO_3)_2$/KIT-6 weight ratios, while there is a small decrease in the ratio of 11 to 3.3 nm pores when more $Ni(NO_3)_2$ is added. In the case of NiO-130, no significant change was observed. These results indicate that, although previous studies suggested that insufficient impregnation of the precursor may result in a bimodal pore size distribution, this is not observed in the present study.[32] The influence of varying the calcination temperature was also examined. A sample was heated at different temperatures from 400 to 800 °C, but no significant change in the pore size distribution of NiO was observed.

The 3D mesoporous NiO samples were examined by low-angle powder X-ray diffraction (Figure 4I). The data show one sharp peak at 0.8–1.0° and another broad peak at 1.5–1.8° (Cu $K\alpha_1$). These peaks may be indexed as the (211) and (332) reflections of the cubic unit cell with lattice parameters of $a_0 =$ 216, 236, and 263 Å for NiO-80, NiO-100, and NiO-130, respectively, consistent with the a_0 values obtained from the TEM data.

Wide-angle powder X-ray diffraction data for mesoporous NiO are shown in Figure 4II, where they are compared with data for bulk NiO. The peaks of all phases are coincident, demonstrating that the simple cubic rock salt structure ($Fm\bar{3}m$) dominates the walls of the mesoporous solid.

The three mesoporous NiO materials were examined by XANES/EXAFS and compared with bulk NiO (99% pure, Aldrich, color green); see Figure S1 in Supporting Information. The XANES data demonstrate that the oxidation state is Ni^{2+} in all the samples. The EXAFS data for mesoporous and bulk NiO are shown in Figure S2. The agreement between the major

---

(36) Jiao, F.; Harrison, A.; Jumas, J. C.; Chadwick, A. V.; Kockelmann, W.; Bruce, P. G. *J. Am. Chem. Soc.* **2006**, *128*, 5468.

(37) Laha, S. C.; Ryoo, R. *Chem. Commun.* **2003**, 2138.

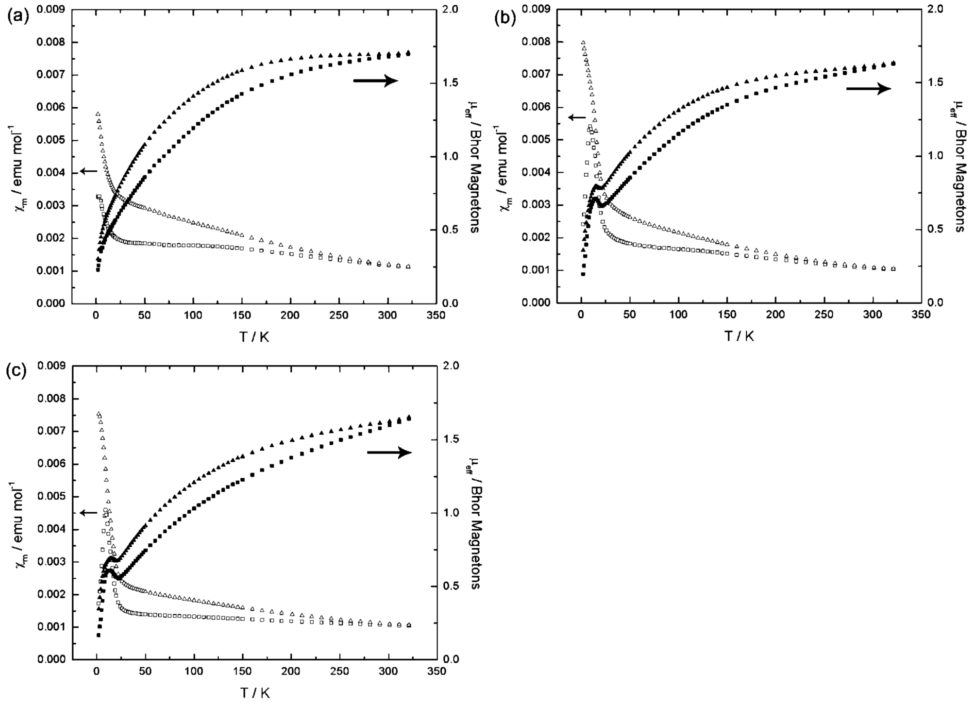

Figure 5. Molar susceptibility (open symbols) and effective magnetic moment (filled symbols) curves of (a) NiO-80, (b) NiO-100, and (c) NiO-130. The samples were measured in 0.01 T, after being cooled in both zero field (squares) and 0.01 T (triangles). Arrows on the graphs indicate the relevant axes for the data.

peaks in the four data sets confirms that the four materials possess the same basic structure (i.e., that of crystalline NiO).

Magnetization measurements were carried out on polycrystalline powder samples of mesoporous NiO with field and zero field cooling, as described in the Experimental Section. The data are presented in Figure 5, expressed both as the molar susceptibility and the effective moment ($\mu_{\mathrm{eff}} = (8\chi_{\mathrm{m}}T)^{1/2}$, where χ_{m} is expressed in emu mol^{-1}). The values of μ_{eff} for the mesoporous samples tend toward that of a spin ½ system (1.73 μ_{B}) rather than the value one would expect for a system with $S = 1$ (2.828 μ_{B}), as is the case in NiO.[38] The XANES experiments indicate that there is a negligible level of Ni^{3+} (which would have $S = ½$), so it is likely that our observations are intrinsic to the mesoporous NiO. Our observation of a reduced moment on Ni^{3+} compared to the value for a paramagnet at the same temperature indicates that a significant fraction freezes to some form of long-range order above the highest temperature of our measurements (bulk NiO has a Néel temperature of 523 K).[39] The remaining moments, perhaps located at sites of lower connectivity (for example, at walls or dislocations in the material), might then freeze at lower temperatures. The divergence of the fc and zfc susceptibility data from the highest temperature indicates the freezing of uncompensated moments or blocking of superparamagnetism. A more detailed understanding of the magnetic behavior observed for mesoporous NiO requires more detailed studies beyond the scope of the present paper.

Conclusion

Mesoporous NiO has been synthesized with crystalline walls and an ordered 3D pore structure, exhibiting a bimodal pore size distribution composed of small (3.3 nm) and large (11 nm) diameter pores. The presence of large pores does not depend on synthesizing a template with thick walls (an approach which has proved difficult to realize) but instead arises because one or the other of the two sets of mesopores in the template KIT-6 are filled (a large pore is composed of two walls and a pore of KIT-6). By varying the KIT-6 synthesis conditions, hence the degree of microporous bridging between the two sets of mesopores, it is possible to control the bimodal pore size distribution. More bridging leads to fewer large pores until only small pores remain. Preliminary magnetic data are compatible with a significant fraction of the moments freezing at a relatively high temperature, with further freezing on cooling. Further measurements, particularly with neutrons, are required to explore the changing character of such correlations with temperature.

Acknowledgment. P.G.B. is indebted to the EPSRC and the EU for financial support.

Supporting Information Available: Additional supporting figures. This material is available free of charge via the Internet at http://pubs.acs.org.

JA710849R

---

(38) Richardson, J. T.; Yiagas, D. I.; Turk, B.; Forster, K.; Twigg, M. V. *J. Appl. Phys.* **1991**, *70*, 6977.

(39) Vernon, M. W. *Phys. Status Solidi* **1970**, *37*, K1.

Appendix E

Synthesis of Ordered Mesoporous Li–Mn–O Spinel as a Positive Electrode for Rechargeable Lithium Batteries

F. Jiao, J. Bao, A. H. Hill, and P. G. Bruce.

Reproduced with permission from Angewandte Chemie International Edition **47**, 9711 (2008).

Angewandte Chemie

Mesoporous Cathodes

DOI: 10.1002/anie.200803431

Synthesis of Ordered Mesoporous Li–Mn–O Spinel as a Positive Electrode for Rechargeable Lithium Batteries**

*Feng Jiao, Jianli Bao, Adrian H. Hill, and Peter G. Bruce**

$LiMn_2O_4$ spinel is one of the most important intercalation electrodes for rechargeable lithium batteries at the present time.[1–4] It combines the highest intrinsic rate capability of the well-known intercalation cathodes with high safety, low toxicity, and low cost, making it attractive for high-power applications, such as hybrid electric vehicles.[5–11] However, the drawback of this electrode is its slow dissolution in the electrolyte present in the lithium-ion battery. To mitigate such dissolution, recent interest has focused on highly lithium-rich compositions in the region of $Li_{1.12}Mn_{1.88}O_4$ ($Li[Li_{0.12}Mn_{1.88}]O_4$) because of their high average oxidation state (presence of less soluble Mn^{3+}), despite compromising theoretical capacity.[11,12] Consequently, high rate capability becomes even more important to ensure high utilization of the reduced theoretical capacity. Here we describe the synthesis of an ordered mesoporous $Li_{1.12}Mn_{1.88}O_4$ spinel and show that it combines higher rate capability than the corresponding bulk material (50 % higher specific capacity at a rate of 30C, 3000 mA g^{-1}) at ambient temperature with good stability at elevated temperatures, despite a high surface area of 90 $m^2 g^{-1}$ and without the need for deliberate coating or doping with foreign ions.[13,14] Furthermore, when cycled over a wide voltage range (including the 3 V and 4 V plateaus) the mesoporous material exhibits improved capacity retention compared to the bulk spinel. This capacity retention is because of the nanometer thin walls between the pores that render the cubic/tetragonal phase transformation more facile in the mesoporous spinel than in the bulk phase. The potential advantages of using nanostuctured electrode materials, in this case mesoporous solids, over nanoparticles are discussed.

Ordered mesoporous $Li_{1+x}Mn_{2-x}O_4$ spinel is synthesized for the first time, as described in detail in the Experimental Section, by a hard templating route with post-template treatment.[15–19] Briefly, an aqueous solution of $Mn(NO_3)_2$ was infiltrated into the ordered 3D pore structure of the mesoporous silica, KIT-6. Heating in air converted the precursor into Mn_2O_3. Following the removal of the SiO_2 template, the replica 3D mesoporous Mn_2O_3 was transformed to Mn_3O_4 spinel by heating in a reducing atmosphere, which then reacted with LiOH to form mesoporous $LiMn_2O_4$ spinel (Figure 1). It is remarkably that throughout the solid-state transformations $Mn_2O_3 \rightarrow Mn_3O_4 \rightarrow LiMn_2O_4$, the ordered 3D mesoporous structure was preserved (Figure 1), demonstrating that the thin walls of the mesopore (7 nm thick) can accommodate the strain of multiple solid–solid phase transformations. The mesoporous structure exists throughout the material, as demonstrated by examining many particles using

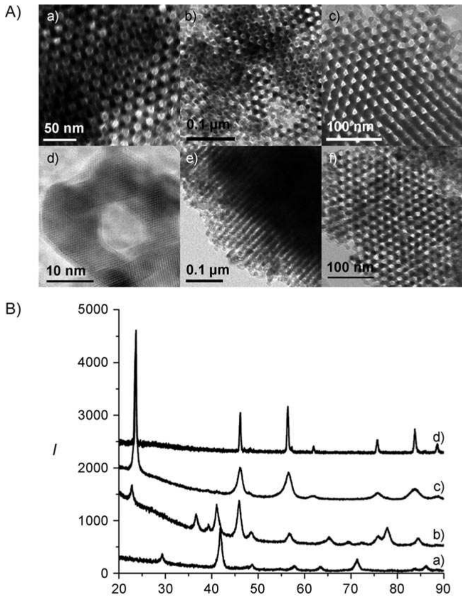

Figure 1. A) TEM images of mesoporous a) Mn_2O_3, b) Mn_3O_4, and c) $Li_{1.12}Mn_{1.88}O_4$. d) High-resolution TEM image of mesoporous $Li_{1.12}Mn_{1.88}O_4$. e,f) TEM images of mesoporous $Li_{1.12}Mn_{1.88}O_4$ e) after 20 cycles between 3–4.3 V and f) after 30 cycles between 2–4.5 V. B) Powder XRD patterns of mesoporous a) Mn_2O_3, b) Mn_3O_4, c) $Li_{1.12}Mn_{1.88}O_4$, broadened owing to nanometer-thin walls, and d) bulk $Li_{1.12}Mn_{1.88}O_4$.

---

[*] Dr. F. Jiao,[+] J. Bao, Prof. P. G. Bruce
EaStChem and School of Chemistry, University of St. Andrews
The Purdie Building, North Haugh, St Andrews KY16 9ST (UK)
E-mail: g.bruce@st-and.ac.uk
A. H. Hill
School of Chemistry and EaStChem, University of Edinburgh,
Joseph Black Building
West Mains Road, Edinburgh EH9 3JJ (UK)
[+] Current address: Physical Biosciences Division, Lawrence Berkeley National Laboratory
1 Cyclotron Rd, Berkeley, CA 94720 (USA)

[**] P.G.B. is indebted to the EPSRC (SUPERGEN) and the EU for financial support. A.H.H. would like to thank Dr. Ronald Brown for the assistance with the XPS setup.

Supporting information for this article is available on the WWW under http://dx.doi.org/10.1002/anie.200803431.

TEM. The strategy of post-template reduction followed by solid-state reaction with LiOH permitted the synthesis of a mixed-valence lithium-containing compound that could otherwise not be easily synthesized directly within the template. Control of the oxygen partial pressure within the pores of the SiO_2 template to control the mixed-valance state, would have proved difficult, and introduction of a lithium precursor within the silica template would, on heating, have led to its reaction with the silica. Circumventing the latter problem has been demonstrated only once before by synthesizing the low temperature (LT) form of $LiCoO_2$.[16] However, LT-$LiCoO_2$ is a poor cathode with low capacity, and in contrast to manganese spinel, is of limited interest.[3,4]

The mesoporous spinel has the same cubic mesostructure as KIT-6 (space group *Ia3d*). An a_0 lattice parameter of 24.1 nm for the spinel was extracted from the TEM data. N_2 sorption measurements conducted on the mesoporous spinel (see Supporting Information) show a type IV isotherm, as observed in mesoporous materials. Barrett–Joyner–Halenda (BJH) analysis of the desorption isotherm indicated a pore size distribution with a peak centered at 4.1 nm. Such a pore diameter for the mesoporous spinel is in good agreement with the dimensions of the walls of the KIT-6 template, which become the pores of the replica spinel structure. The BET surface area for mesoporous $Li_{1.12}Mn_{1.88}O_4$ is 90 m^2g^{-1}, which is similar to that of other mesoporous transition metal oxides templated by KIT-6.[20–25]

Chemical/oxidation state analysis (see Experimental Section) indicated that the composition of the spinel phase was $Li_{1.12}Mn_{1.88}O_4$. The powder XRD pattern shown in Figure 1 B (c), confirms the spinel structure and is in agreement with that of the bulk $Li_{1.12}Mn_{1.88}O_4$, although the mesoporous material exhibits peak broadening as expected for a nanomaterial.[26] Although using the highest temperature commensurate with retention of the mesostructure (400 °C), and strong reducing conditions (H_2 gas), it was not possible to synthesize a more reduced spinel with a composition closer to stoichiometric $LiMn_2O_4$.

Lithium manganese oxide spinel may be cycled over 3 V and 4 V plateaus.[1,2,27] Cycling in the more technologically relevant 4 V region will be considered first, and thereafter the effect of the mesostructure on cycling over both plateaus.

Mesoporous $Li_{1.12}Mn_{1.88}O_4$ was incorporated into a composite electrode as described in the Experimental Section. Additional electrodes were constructed identically (same composition and active mass), except for replacement of the mesoporous spinel with bulk spinel of the same composition. Another bulk spinel, $Li_{1.05}Mn_{1.95}O_4$, with a composition regarded as within the range for optimum performance has also been used.[8–10] Both bulk materials were prepared by a solid-state reaction (Experimental Section). To compare directly the rate capabilities of the three different spinel materials, their discharge capacities on the first cycle were expressed as a percentage of their capacity at a rate of 30 mAg^{-1} (0.30C; 1C equates to discharge of the theoretical capacity of $Li_{1.12}Mn_{1.88}O_2$, 98 mAg^{-1}, in 1 h) and plotted versus current density in Figure 2 A. Use of the same loading of active material per unit area in each case resulted in a thicker mesoporous electrode because of the lower density of the porous material. As can be seen from the Figure 2 A, the mesoporous material exhibits the best capacity retention at

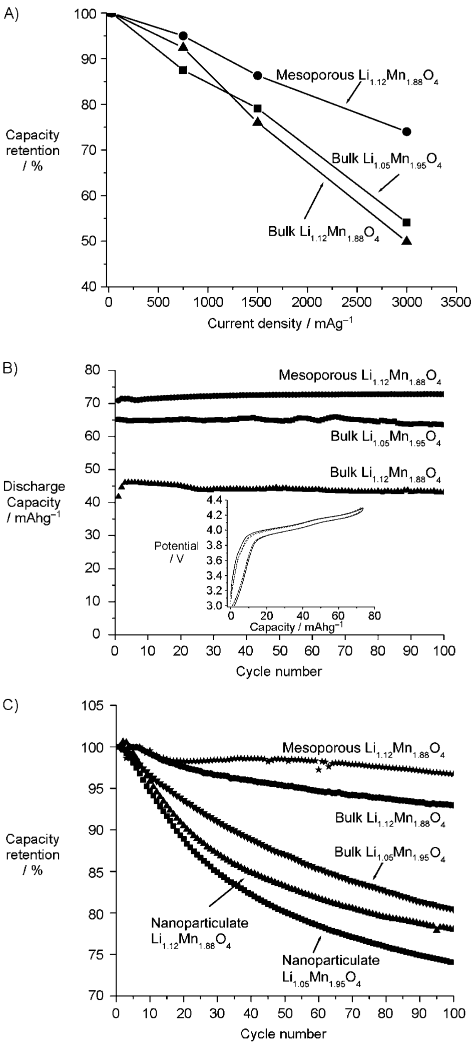

Figure 2. A) Rate capability for mesoporous $Li_{1.12}Mn_{1.88}O_4$ (●), bulk $Li_{1.05}Mn_{1.95}O_4$ (■), and bulk $Li_{1.12}Mn_{1.88}O_4$ (▲); capacity retention expressed as percentage capacity at 30 mAg^{-1} (0.30C). B) Cycling data for mesoporous $Li_{1.12}Mn_{1.88}O_4$ (●), bulk $Li_{1.05}Mn_{1.95}O_4$ (■), and bulk $Li_{1.12}Mn_{1.88}O_4$ (▲) between 3–4.3 V at a rate of 3000 mAg^{-1} (30C). The inset shows the load curves, 5th cycle (——), 25th cycle (– – –), and 50th cycle (•••••) for mesoporous $Li_{1.12}Mn_{1.88}O_4$. C) Cycling data for mesoporous $Li_{1.12}Mn_{1.88}O_4$ (⋆), bulk $Li_{1.12}Mn_{1.88}O_4$ (●), bulk $Li_{1.05}Mn_{1.95}O_4$ (▼), nanoparticulate $Li_{1.12}Mn_{1.88}O_4$ (▲),and nanoparticulate $Li_{1.05}Mn_{1.95}O_4$ (■) at 50 °C at 30 mAg^{-1} (0.30C) between 3–4.3 V.

high rates, despite having a thicker electrode. Its capacity retention is 50% higher than the equivalent $Li_{1.12}Mn_{1.88}O_2$ bulk phase at a rate of 3000 mA g^{-1} (30C), demonstrating the superior rate capability obtained by using a mesoporous spinel. No attempt has been made to optimize the electrode construction, and thus we do not claim that these are the best performances that can be obtained for spinel electrodes.[10] Rather, all the electrodes are constructed identically to facilitate back-to-back comparison of the effect of mesoporosity on the performance, not to demonstrate the best possible performance.

The superior rate capability of the mesoporous material may be due to a number of factors. The higher surface area in contact with the electrolyte (BET surface area for mesoporous $Li_{1.12}Mn_{1.88}O_4$ is 90 m^2 g^{-1} compared with 1.5 m^2 g^{-1} for the bulk forms of the two compositions) and the thin walls, resulting in short diffusion lengths of approximately 3.5 nm (wall thickness 7 nm), are clearly important. However, in addition, the ordered cubic pore structure ensures that the pores are of uniform size and uniformly interconnected in all directions, thus helping to promote efficient and equal access of the electrolyte to the internal surface throughout the electrode.

The conventional approach to optimizing the power (rate) of an electrode is to reduce the particle size to a few nanometers. It is interesting to compare the rate performance of the electrodes consisting of nanoparticles with those in which the particles are mesoporous and are of micrometer dimensions, the internal walls being a few nanometers thick. Ultimately, obtaining high power (rate) in any electrode requires porosity to ensure a ready supply of ions from the electrolyte and thus sacrificing volumetric capacity is the inevitable price to pay for high rate. If this is achieved by deliberately designing porosity inside the particles, as in the mesoporous solids, then an optimum pore size may be selected such that volume of the solid will not be unnecessarily wasted, as in the case of solids with random porosity (random in size and shape). Random porosity also gives rise to situations in a composite electrode made of nanoparticles, in which some pores will be too small, too large, or occluded. As the particles of the mesoporous solid are of micron dimensions, they maintain a similar interparticle contact to that of bulk materials and will pack more densely within the composite electrode than nanoparticles. It is recognized that fabricating electrodes from nanoparticles is difficult because of the low tap density and problem of maintaining particle contact. Of course a potential disadvantage is that preparing mesoporous materials may be more difficult than simple nanoparticles. Comparison between mesoporous $Li_{1.12}Mn_{1.88}O_4$ and an electrode constructed identically with bulk $Li_{1.05}Mn_{1.95}O_4$, indicates that the rate capability of the mesoporous material is also superior to this bulk composition (Figure 2A).

Recent interest in Li–Mn–O spinel arises from its high rate capability and thus its usefulness for high-rate applications. Thus, the focus was on cycling at high rate (power). The absolute capacities for the three materials at the high rate of 3000 mA g^{-1} (30C) are shown in Figure 2B, from which it may be seen that the specific capacity of the mesoporous material is significantly higher than its bulk equivalent (by 50–60%) and somewhat higher than bulk $Li_{1.05}Mn_{1.95}O_4$ despite a lower theoretical capacity for $Li_{1.12}Mn_{1.88}O_2$ because of its more lithium-rich composition. Considering the effect of the mesoporosity on the volumetric capacity, the density of mesoporous $Li_{1.12}Mn_{1.88}O_4$ is 35% lower than the corresponding bulk material, which translates into a 25% reduction in volumetric capacity of the composite electrode, as only a proportion of the composite electrode is the active material. Thus, based on the total volume of the electrode, those constructed using mesoporous $Li_{1.12}Mn_{1.88}O_4$ have a higher gravimetric and slightly higher volumetric energy density than those fabricated using the corresponding bulk material. The inset in Figure 2B shows the load curves for 3 cycles (5, 25, and 50) of the mesoporous Li-1.12 phase. The difficulty in resolving one cycle from another emphasizes the stability of the load curves on cycling. Retention of the mesostructure on cycling is demonstrated by the TEM data in Figure 1A (e).

Having considered the performance at 30°C it is interesting to examine the performance at elevated temperatures. It is well known that Mn^{3+} disproportionation into Mn^{2+} and Mn^{4+}, followed by Mn^{2+} dissolution in the electrolyte, is one of the main causes of spinel electrodes losing capacity with time/cycling in cells operated at elevated temperatures of circa. 50°C. Lowering of the cell capacity is particularly severe if graphite electrodes are employed.[13,14,28] To alleviate such the capacity lowering, Li–Mn–O spinels may be doped with foreign ions, for example F^-, or coated with metal oxides, such as ZnO.[29,30] As a result, mesoporous $Li_{1.12}Mn_{1.88}O_4$, with its high surface area and without such modifications, might have been expected to exhibit severed capacity loss on cycling at elevated temperatures.

To investigate the elevated temperature stability of the mesoporous phase, the variation of discharge capacity with cycle number at 50°C is shown in Figure 2C for 1) mesoporous, 2) nanoparticle, 3) bulk $Li_{1.12}Mn_{1.88}O_4$, 4) nanoparticle, and 5) bulk $Li_{1.05}Mn_{1.95}O_4$. The capacities are presented as a percentage of their theoretical values, to provide direct comparison of the lowering of the capacity on cycling for the different materials. A low rate of 30 mA g^{-1} was selected to provide a more severe test of capacity fading on cycling than would be the case if high rates were employed. The rapid loss of capacity on cycling the bulk $Li_{1.05}Mn_{1.95}O_4$ is evident in Figure 2C and is in accord with previous studies of such optimized nonstoichiometric spinels in the absence of foreign ion dopants or coatings.[10,13,31] Nanoparticles of $Li_{1.05}Mn_{1.95}O_4$ (BET surface area of 40 m^2 g^{-1} compared with 1.5 m^2 g^{-1} for the bulk material) result in even more severe capacity fading (Figure 2C). Nanoparticles of $Li_{1.12}Mn_{1.88}O_4$ (40 m^2 g^{-1}) show lowering of the capacity to some extent and the lowering takes place presumably because of the higher average oxidation state leading to a higher Mn^{4+}/Mn^{3+} ratio at the surface. Thus, the Mn^{3+} disproportionation reaction is lowered leading to lesser Mn^{2+} dissolution in the electrolyte. However, the mesoporous $Li_{1.12}Mn_{1.88}O_4$ material exhibits roughly comparable capacity retention to the corresponding bulk material (surface area 1.5 m^2 g^{-1}; Figure 2C), despite the former having a surface area twice that of the $Li_{1.12}Mn_{1.88}O_4$ nanoparticles (90 m^2 g^{-1} compared with 40 m^2 g^{-1}). This could be in part due to the micrometer-sized particles of the mesoporous material, which may maintain better interparticle contact than the nanoparticles on cycling. However, we suggest that the comparable capacity retentions of the mesoporous and the bulk $Li_{1.12}Mn_{1.88}O_4$ are due to the internal surface of the former being more stable than the outer surface, a conjecture that is reinforced by the results of dissolution measurements reported below. We do not, at this stage, have an explanation for the slight dip then rise in capacity within the first few cycles for the mesoporous $Li_{1.12}Mn_{1.88}O_4$; powder-XRD data show no evidence of structural changes on cycling.

To explore whether the superior capacity retention of the mesoporous $Li_{1.12}Mn_{1.88}O_4$ compared with the other materials is associated with less manganese dissolution, equal masses of the mesoporous, bulk, and nanoparticulate $Li_{1.12}Mn_{1.88}O_4$ and the bulk $Li_{1.05}Mn_{1.95}O_4$ were placed into equal volumes of electrolyte at 50 °C for 4 days, and the quantity of manganese in each solution was determined (see Experimental Section). The manganese concentrations in the mesoporous $Li_{1.12}Mn_{1.88}O_4$, bulk $Li_{1.12}Mn_{1.88}O_4$, nanoparticulate $Li_{1.12}Mn_{1.88}O_4$, and bulk $Li_{1.05}Mn_{1.95}O_4$ are 3.7, 6.3, 26, and 9.5 ppm, respectively. These results demonstrate that the mesoporous $Li_{1.12}Mn_{1.88}O_4$ is more stable at elevated temperatures than the other materials. Importantly, they reinforce the conclusions from Figure 2C that the stability of the mesoporous $Li_{1.12}Mn_{1.88}O_4$ is slightly greater than the equivalent bulk phase, despite the former having a much higher surface area. The results of the dissolution experiments support the view expressed above that the internal surface of the mesoporous $Li_{1.12}Mn_{1.88}O_4$ is more stable towards disproportionation/dissolution of the manganese than the external surface, explaining the superior cycling stability at elevated temperatures compared with nanoparticles. It is difficult to study directly the internal surfaces of mesoporous solids. XPS measurements carried out on the bulk and mesoporous $Li_{1.12}Mn_{1.88}O_4$ (see Supporting Information Figure 3S) give an average oxidation state of +3.65 for manganese on the outer surface, that is, the surface is not Li_2MnO_3.

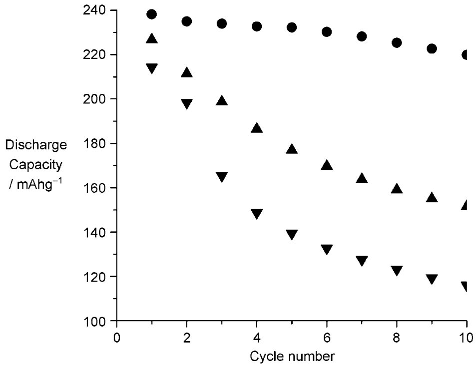

Figure 3. Discharge capacity versus cycle number for the mesoporous $Li_{1.12}Mn_{1.88}O_4$ (●), bulk $Li_{1.05}Mn_{1.95}O_4$ (▲), and bulk $Li_{1.12}Mn_{1.88}O_4$ (▼) at a rate of 30 $mA\,g^{-1}$ (0.30C) between 2–4.5 V.

Cycling over the 3 and 4 V plateaus were also considered. Although not as technologically relevant as the 4 V region, it is interesting to explore the effect that mesostructuring has on such cycling. The variation of the discharge capacity with the cycle number, where cycling is carried out between 2 and 4.5 V, is shown in Figure 3 for the bulk $Li_{1.05}Mn_{1.95}O_4$, and the mesoporous and bulk $Li_{1.12}Mn_{1.88}O_4$. Even within 10 cycles the severe capacity fading of the bulk materials is evident, whereas the mesoporous $Li_{1.12}Mn_{1.88}O_4$ exhibits much better capacity retention. To consider this effect in more detail the load curves for each of the three materials as a function of cycle number were examined. It is known that the capacity loss suffered on cycling bulk spinel with the composition $Li_{1.05}Mn_{1.95}O_4$ between 3 and 4 V plateaus is related to the difficulty of reversing the cubic ($LiMn_2O_4$)/tetragonal-($Li_2Mn_2O_4$) phase transition associated with the 3 V plateau.[32,33] As a result, although capacity lowering occurs at both 3 and 4 V, the most severe loss of capacity is associated with the 3 V plateau for the bulk $Li_{1.05}Mn_{1.95}O_4$ (Figure 4A). This is also the case for the bulk $Li_{1.12}Mn_{1.88}O_4$ material (Figure 4B), although in this case there is more loss of capacity at 4 V than for the $Li_{1.05}Mn_{1.95}O_4$ electrode. In contrast, the load curves for the mesoporous $Li_{1.12}Mn_{1.88}O_4$ presents a more optimistic situation (Figure 4C). The most

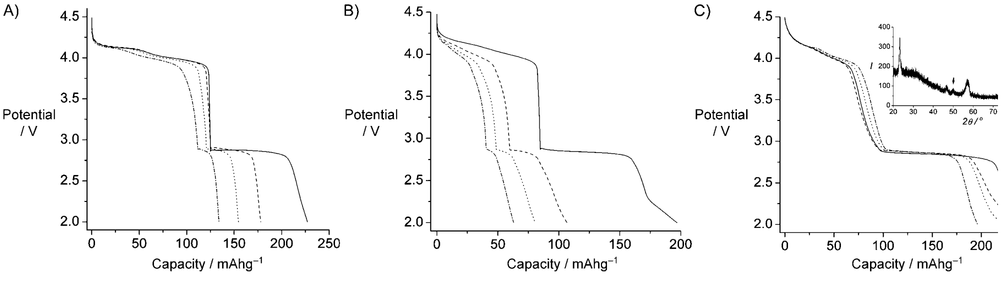

Figure 4. Load curves showing the first discharge (——), fifth discharge (– – –), tenth discharge (•••••) and 20th discharge (–•–•) for A) bulk $Li_{1.05}Mn_{1.95}$ B) bulk $Li_{1.12}Mn_{1.88}O_4$, and C) mesoporous $Li_{1.12}Mn_{1.88}O_4$. The inset in (C) is the powder XRD pattern for mesoporous $Li_{1.12}Mn_{1.88}O_4$ after discharging to arrows indicate peaks for the tetragonal phase.

dramatic difference occurs at 3 V, where the capacity retention is far better than for either of the bulk materials, implying that the cubic/tetragonal phase transformation is far more facile for the mesoporous material than the bulk. The capacity retention at 4 V is also somewhat better for the mesoporous material. The inset in Figure 4 C shows powder XRD data collected at the end of discharge demonstrating the presence of the tetragonal phase at the end of the 3 V plateau.

TEM data collected after cycling over the 3 and 4 V plateaus demonstrate retention of the mesostructure (Figure 1 A (f)). As the nanometer-sized walls in the mesoporous materials lead to the relief of strain during the structural phase transitions, these materials undergo the transitions in a more facile fashion than their bulk counterparts.[15] Indeed the transformations from Mn_2O_3 to Mn_3O_4 and then to $LiMn_2O_4$, associated with the formation of the mesoporous material discussed herein, while retaining the mesostructure throughout, are a testimony to the ease with which the phase transformations can occur in mesoporous materials. It appears that this same effect has rendered more facile the cubic/tetragonal phase transition than is the case for the bulk materials. These results are in agreement with previous studies on spinels. On cycling layered $LiMnO_2$, it coverts to a spinel material that exhibits a nanodomain structure, in which the domains can spontaneously switch between cubic and tetragonal phases, with strain being relieved at the domain wall boundaries.[32,33] Furthermore, ball-milling $LiMn_2O_4$ can induce a similar nanodomain structure with a consequent improvement in cycling over the 3 V plateau.[34]

In conclusion, a mesoporous lithium manganese oxide spinel has been synthesized for the first time. By combining a mesoporous structure with the composition $Li_{1.12}Mn_{1.88}O_4$, superior rate capability at ambient temperature (50 % higher specific capacity and marginally higher volumetric capacity at 3000 mA h g^{-1}, 30C) compared with the corresponding bulk material have been demonstrated. Comparable stability to the bulk material at elevated temperatures is observed despite a surface area of 90 m^{2}g^{-1} for the mesopore and without recourse to the introduction of foreign ion dopants or the application of metal oxide coatings, suggesting that the internal surfaces of the mesopore are more stable than the external surface. In addition, the mesoporous material can be cycled over both the 3 and 4 V plateaus with improved capacity retention compared with bulk materials. This improvement is due to the nanometer-sized walls better accommodating the strain of the cubic/tetragonal phase transformation that occurs at 3 V.

Experimental Section

Preparations of electrode materials: Preparation of the mesoporous silica (KIT-6) has been described previously.[35] Typical synthesis of mesoporous $Li_{1.12}Mn_{1.88}O_4$: $Mn(NO_3)_2 \cdot 6H_2O$ (98 %, Aldrich; 30 g) was dissolved in distilled water (ca. 20 mL) and this saturated $Mn(NO_3)_2$ solution (5 mL) was added slowly with stirring to mesoporous KIT-6 (5 g) dispersed in *n*-hexane (200 mL). The mixture was stirred overnight, filtered, and dried at room temperature, followed by heating at 600 °C for 3 h. The resulting material was treated twice with a hot NaOH solution (2 M) in water to remove the silica template, followed by washing with water and drying at 60 °C. This procedure results in mesoporous Mn_2O_3 free from SiO_2, as demonstrated by chemical analysis. Reduction of mesoporous Mn_2O_3 to Mn_3O_4 was achieved by heating at 280 °C for 3 h under a H_2 atmosphere (H_2/Ar = 5:95). Thereafter, mesoporous Mn_3O_4 (1 g) was mixed with $LiOH \cdot H_2O$ (1.5 g) in water (10 mL), stirred until dry, and was heated slowly at 350 °C for 1 h. After the calcination, the sample was cooled to room temperature at a rate of 3 °C min^{-1}, and the resulting material was washed with water then dried at 120 °C.

Bulk $Li_{1.05}Mn_{1.95}O_4$ and $Li_{1.12}Mn_{1.88}O_4$: stoichiometric ratios of lithium acetate and manganese acetate were ball-milled for 15 min before heating at 400 °C in air for 3 h. The resulting powder was ball-milled again for 15 min and then heated at 900 °C in air for 5 h. After the calcination, the sample was cooled to room temperature at a rate of 3 °C min^{-1}.

Nanoparticles of $Li_{1.05}Mn_{1.95}O_4$ and $Li_{1.12}Mn_{1.88}O_4$ were synthesized from lithium acetate and manganese acetate following a previously reported procedure.[36]

The materials were characterized by transmission electron microscopy (TEM, Jeol JEM-2011), powder-XRD diffraction (PXRD, Stoe STADI/P diffractometer operating in transmission mode with $Fe_{K\alpha_1}$ radiation, $\lambda = 1.936$ Å), and N_2 sorption (Hiden IGA porosimeter) techniques. Oxidation states were determined by redox titration using ferrous ammonium sulfate/$KMnO_4$, as described previously.[37] Atomic absorption measurements were carried out on a Pye Unicam AAS spectrometer.

Manganese dissolution studies: spinel material (0.1 g) was sealed in a glass bottle with LP-30 electrolyte (10 mL) and stored at 50 °C for 4 days. After filtering, the liquid was collected and analyzed by atomic absorption.

Electrochemical cells were constructed by mixing the active material, Kynar (a copolymer based on poly(vinylidene fluoride)), and Super S carbon in the weight ratios 80:10:10. The mixture was cast onto aluminum foil from acetone using the doctor-blade technique. After solvent evaporation at room temperature and heating at 80 °C under vacuum for 8 h, the electrodes were assembled into cells with a lithium electrode (99.9 %, Aldrich; a disc with a diameter of 8 mm and a thickness of ca. 0.7 mm) and LP-30 electrolyte (Merck; 1 M $LiPF_6$ in 1:1 v/v ethylene carbonate/dimethyl carbonate). The cells were constructed and handled in an argon-filled MBraun glovebox. Electrochemical measurements were carried out using a MACCOR Series 4200 cycler. High-rate measurements were performed on two and three electrode cells, but no difference was found, demonstrating that the polarization was dominated by the cathode. Hence two-electrode results are reported here.

Received: July 15, 2008

Keywords: electrodes · intercalation · lithium batteries · mesoporous materials · spinel phases

---

[1] M. M. Thackeray, W. I. F. David, P. G. Bruce, J. B. Goodenough, *Mater. Res. Bull.* **1983**, *18*, 461.
[2] J. M. Tarascon, E. Wang, F. K. Shokoohi, W. R. McKinnon, S. Colson, *J. Electrochem. Soc.* **1991**, *138*, 2859.
[3] W. A. van Schalkwijk, B. Scrosati, *Advances in Lithium-ion Batteries*, Kluwer Academic/Plenum, New York, **2002**.
[4] G. A. Nazri, G. Pistoia, *Lithium Batteries: Science and Technology*, Kluwer Academic, Boston, **2004**.
[5] J. M. Tarascon, M. Armand, *Nature* **2001**, *414*, 359.
[6] A. S. Aricò, P. Bruce, B. Scrosati, J. M. Tarascon, W. Van Schalkwijk, *Nat. Mater.* **2005**, *4*, 366.
[7] P. G. Bruce, B. Scrosati, J. M. Tarascon, *Angew. Chem.* **2008**, *120*, 2972; *Angew. Chem. Int. Ed.* **2008**, *47*, 2930.
[8] R. J. Gummow, A. Dekock, M. M. Thackeray, *Solid State Ionics* **1994**, *69*, 59.

[9] Y. Y. Xia, M. Yoshio, *J. Electrochem. Soc.* **1997**, *144*, 4186.
[10] G. Amatucci, J. M. Tarascon, *J. Electrochem. Soc.* **2002**, *149*, K31.
[11] K. Ariyoshi, E. Iwata, M. Kuniyoshi, H. Wakabayashi, T. Ohzuku, *Electrochem. Solid-State Lett.* **2006**, *9*, A557.
[12] Z. H. Chen, K. Amine, *J. Electrochem. Soc.* **2006**, *153*, A1279.
[13] A. Du Pasquier, A. Blyr, P. Courjal, D. Larcher, G. Amatucci, B. Gerand, J. M. Tarascon, *J. Electrochem. Soc.* **1999**, *146*, 428.
[14] Y. Y. Xia, Y. H. Zhou, M. Yoshio, *J. Electrochem. Soc.* **1997**, *144*, 2593.
[15] F. Jiao, J. C. Jumas, M. Womes, A. V. Chadwick, A. Harrison, P. G. Bruce, *J. Am. Chem. Soc.* **2006**, *128*, 12905.
[16] F. Jiao, K. M. Shaju, P. G. Bruce, *Angew. Chem.* **2005**, *117*, 6708; *Angew. Chem. Int. Ed.* **2005**, *44*, 6550.
[17] A. H. Lu, F. Schuth, *Adv. Mater.* **2006**, *18*, 1793.
[18] R. Ryoo, S. H. Joo, M. Kruk, M. Jaroniec, *Adv. Mater.* **2001**, *13*, 677.
[19] H. F. Yang, D. Y. Zhao, *J. Mater. Chem.* **2005**, *15*, 1217.
[20] F. Jiao, P. G. Bruce, *Adv. Mater.* **2007**, *19*, 657.
[21] F. Jiao, A. Harrison, J. C. Jumas, A. V. Chadwick, W. Kockelmann, P. G. Bruce, *J. Am. Chem. Soc.* **2006**, *128*, 5468.
[22] C. Dickinson, W. Z. Zhou, R. P. Hodgkins, Y. F. Shi, D. Y. Zhao, H. Y. He, *Chem. Mater.* **2006**, *18*, 3088.
[23] J. Y. Luo, J. J. Zhang, Y. Y. Xia, *Chem. Mater.* **2006**, *18*, 5618.
[24] A. Rumplecker, F. Kleitz, E. L. Salabas, F. Schuth, *Chem. Mater.* **2007**, *19*, 485.
[25] W. H. Shen, X. P. Dong, Y. F. Zhu, H. R. Chen, J. L. Shi, *Microporous Mesoporous Mater.* **2005**, *85*, 157.
[26] C. Masquelier, M. Tabuchi, K. Ado, R. Kanno, Y. Kobayashi, Y. Maki, O. Nakamura, J. B. Goodenough, *J. Solid State Chem.* **1996**, *123*, 255.
[27] M. M. Thackeray, P. J. Johnson, L. A. Depicciotto, P. G. Bruce, J. B. Goodenough, *Mater. Res. Bull.* **1984**, *19*, 179.
[28] Y. M. Chiang, D. R. Sadoway, Y. I. Jang, B. Y. Huang, H. F. Wang, *Electrochem. Solid-State Lett.* **1999**, *2*, 107.
[29] W. Choi, A. Manthiram, *J. Electrochem. Soc.* **2007**, *154*, A614.
[30] Y. K. Sun, K. J. Hong, J. Prakash, *J. Electrochem. Soc.* **2003**, *150*, A970.
[31] Y. Y. Xia, M. Yoshio, *J. Power Sources* **1997**, *66*, 129.
[32] A. D. Robertson, A. R. Armstrong, P. G. Bruce, *Chem. Mater.* **2001**, *13*, 2380.
[33] H. F. Wang, Y. I. Jang, Y. M. Chiang, *Electrochem. Solid-State Lett.* **1999**, *2*, 490.
[34] S. H. Kang, J. B. Goodenough, L. K. Rabenberg, *Chem. Mater.* **2001**, *13*, 1758.
[35] F. Kleitz, S. H. Choi, R. Ryoo, *Chem. Commun.* **2003**, 2136.
[36] A. Caballero, M. Cruz, L. Hernan, M. Melero, J. Morales, E. R. Castellon, *J. Power Sources* **2005**, *150*, 192.
[37] M. J. Katz, R. C. Clarke, W. F. Nye, *Anal. Chem.* **1956**, *28*, 507.

Appendix F

Mesoporous Mn_2O_3 and Mn_3O_4 with Crystalline Walls

F. Jiao, A. H. Hill, A. Harrison, and P. G. Bruce.

Reproduced with permission from Advanced Materials **19**, 4063 (2007).

ADVANCED MATERIALS

DOI: 10.1002/adma.200700336

Mesoporous Mn_2O_3 and Mn_3O_4 with Crystalline Walls**

By *Feng Jiao, Andrew Harrison, Adrian H. Hill, and Peter G. Bruce**

Mesoporous transition metal oxides have attracted much attention recently.[1] The synthesis of mesoporous solids usually demands a templating approach.[1,2] Soft templates (surfactants) yield ordered mesopores with non-crystalline walls.[2,3] The use of hard templates (e.g., mesoporous silica) results in sufficiently high processing temperatures to yield ordered mesopores with crystalline walls.[4,5] However, when used to synthesize transition metal oxides, both methods are restricted in the oxidation states that are accessible.[6] Here we describe, for the first time, the synthesis of ordered mesoporous Mn_3O_4 with crystalline walls by first synthesizing highly ordered mesoporous Mn_2O_3, then reducing it to form highly crystalline Mn_3O_4, while retaining the ordered pore structure. The magnetic properties of both materials are discussed.

The preparation of mesoporous Mn_2O_3 and Mn_3O_4 with highly crystalline walls is described in detail in the methods section. Briefly, an aqueous solution of a Mn^{2+} salt is impregnated into the mesoporous silica, KIT-6, with a 3D pore structure by a 'bi-solvent' method. Drying and heating at 600 °C converts the precursor to Mn_2O_3. The mesoporous silica is removed by dissolution using a hot aqueous solution of 2 M NaOH. Heating at 280 °C under a H_2–Ar (5 % H_2, 95 % Ar) atmosphere converts the ordered mesoporous Mn_2O_3 to ordered mesoporous Mn_3O_4 without destroying the mesostructure.

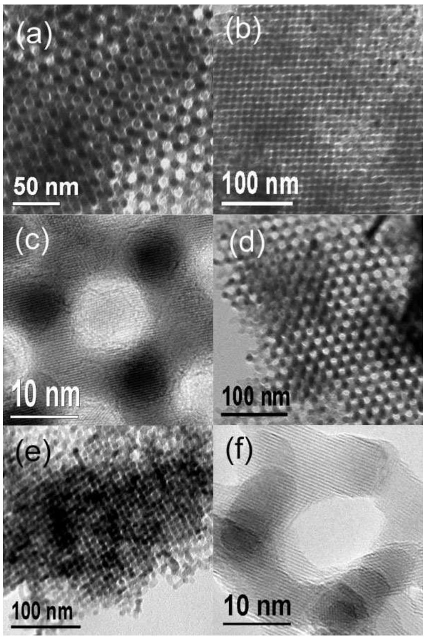

Figure 1. TEM images for mesoporous Mn_2O_3 recorded along a) [111] and b) [110] directions, HRTEM image for mesoporous Mn_2O_3; TEM images for mesoporous Mn_3O_4 recorded along d) [111] and e) [110] directions, HRTEM image for mesoporous Mn_3O_4.

TEM data, Figure 1, confirm the formation of an ordered pore structure for Mn_2O_3 and its retention on conversion to Mn_3O_4. The pore structure replicates that of the KIT-6 template, space group *Ia*-3*d*. Examining many different particles demonstrated that the mesoporous structure is presented throughout each material. The unit cell parameters, a_0, extracted from the TEM data, are 25.1 and 24.9 nm for mesoporous Mn_2O_3 and Mn_3O_4, respectively. These data indicate that the mesostructure is preserved despite conversion from Mn_2O_3 to Mn_3O_4. Low-angle powder X-ray diffraction (PXRD) patterns (Figure 2) for both mesoporous materials exhibit one sharp peak at ~ 0.9°, which could be indexed as the [211] reflection in the *Ia*-3*d* space group and one broad peak at 1.7–1.8°, further demonstrating the ordered mesostructures. The d-values calculated from the first peak are 101.2 and 101.0 Å, which correspond to the unit cell parameters, a_0, 24.8 and 24.7 nm for mesoporous Mn_2O_3 and Mn_3O_4, respectively. These values are in good agreement with the TEM results.

The mesostructures were further confirmed by nitrogen adsorption-desorption measurements. Type IV isotherms (Fig. 3a and b) were obtained for both materials, consistent with the mesoporosity observed by TEM and low angle PXRD. The Brunauer–Emmett–Teller (BET) surface areas for mesoporous Mn_2O_3 and Mn_3O_4 are 138.7 m^2 g^{-1} and

---

[*] Prof. P. G. Bruce, F. Jiao
School of Chemistry and EaStChem, University of St Andrews
St Andrews, Fife KY16 9ST (UK)
E-mail: pgb1@st-andrews.ac.uk
Prof. A. Harrison,[+] A. H. Hill
School of Chemistry and EaStChem, University of Edinburgh,
Joseph Black Building
West Mains Road, Edinburgh EH9 3JJ (UK)

[+] Current address: Institut Laue-Langevin 6, rue Jules Horowitz, BP 156 – 38042 Grenoble Cedex 9, France.

[**] P.G.B. is grateful to the Royal Society, EU and the EPSRC for financial support.

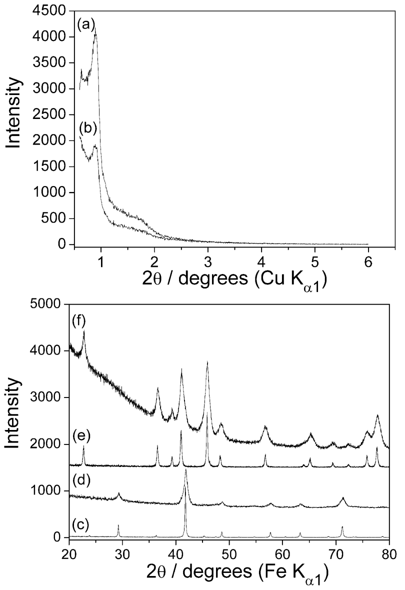

Figure 2. Low angle PXRD patterns for a) mesoporous Mn_2O_3 and b) mesoporous Mn_3O_4. Wide-angle PXRD patterns for c) bulk Mn_2O_3, (d) mesoporous Mn_2O_3, e) bulk Mn_3O_4, and (f) mesoporous Mn_3O_4.

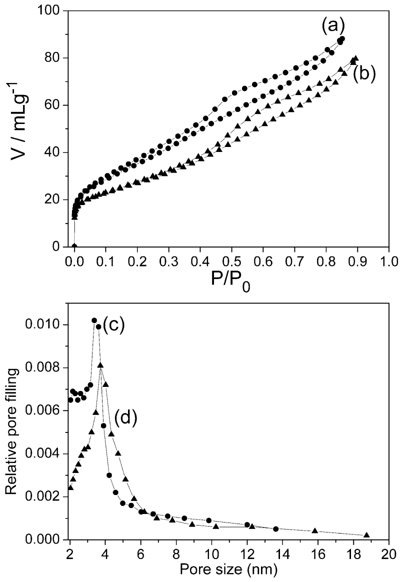

Figure 3. N_2 adsorption-desorption isotherms for a) mesoporous Mn_2O_3 and b) mesoporous Mn_3O_4; the pore size distributions for c) mesoporous Mn_2O_3 and d) mesoporous Mn_3O_4.

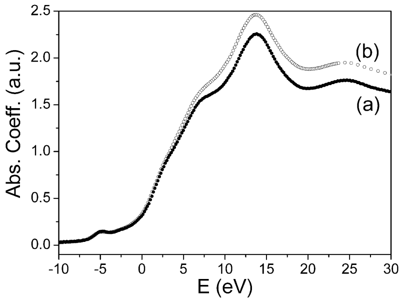

Figure 4. XANES data for a) bulk Mn_3O_4 and b) mesoporous Mn_3O_4.

99.7 $m^2\ g^{-1}$, respectively. The pore size distributions, calculated from desorption isotherms, are shown in Figure 3c and d and exhibit a narrow distribution centred at 3.56 nm for mesoporous Mn_2O_3 and a slightly larger pore size (3.75 nm) for mesoporous Mn_3O_4, respectively.

The high-resolution TEM (HRTEM) images (Fig. 1c and f) show the detailed structures of the pores. It is evident that the basic pore sharp is retained on conversion from Mn_2O_3 to Mn_3O_4, although the pore size for mesoporous Mn_3O_4 (Fig. 1f) is slightly larger than that for Mn_2O_3 (Fig. 1c), consistent with the nitrogen adsorption-desorption results. HRTEM results also indicate that the walls are crystalline in both cases, which is further confirmed by the wide-angle PXRD results (Fig. 2c–f). Peaks corresponding to the crystal structures of Mn_2O_3 and Mn_3O_4 (JCPDS Nos. 24-508 and 24-734, respectively) are present in the figures. Further evidence supporting the conversion of Mn_2O_3 to Mn_3O_4 has been obtained by XANES. The XANES results (Fig. 4) clearly confirm the oxidation state of Mn in mesoporous Mn_3O_4 is +2.67.

Conversion of Mn_2O_3 (corrundum structure) to Mn_3O_4 (spinel structure) involves a significant loss of oxygen and change of structure from hexagonal of cubic close packing. Such a transformation requires shearing of the AB stacked planes (hcp) to the ABC stacking (ccp). The ability to do so while preserving the mesoporous structure demonstrates that the thin (< 8 nm thick) walls can accommodate the strain of such a structural transformation without severe fracture. The loss of oxygen on transformation results in shrinkage of the walls (i.e., larger pores) while preserving the basic pore shape, further testifying to the flexibility of the mesostructure in its accommodation of structural change.

The imposition of a mesostructure on a material may influence its magnetic properties; as a result we performed SQUID magnetometry measurements to explore the magnetic properties of mesoporous Mn_2O_3 and Mn_3O_4. Figure 5a displays the susceptibility of the mesoporous Mn_2O_3 measured in an applied field of 0.01 T first after cooling in zero field (zfc) and then after cooling in a field of 0.01 T (fc). The same measurements were also conducted on the mesoporous Mn_3O_4 as well as bulk Mn_3O_4 (Aldrich, 97 %), and the results are shown in Figure 5c.

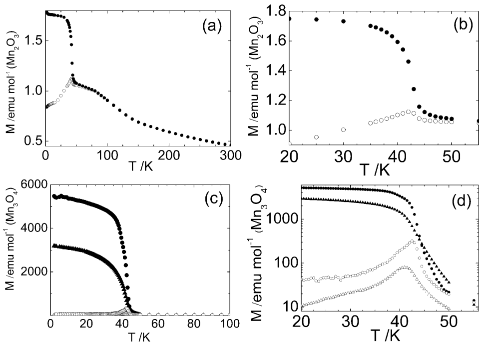

Figure 5. a) Magnetisation data for mesoporous Mn_2O_3 with crystalline walls taken in 0.01 T after first cooling in zero field (zfc, open circles) and then in an applied field of 0.01 T (fc, closed circles), b) the data in greater detail centred around 40 K; c) Magnetisation data for mesoporous Mn_3O_4 with crystalline walls taken in 0.01 T after first cooling in zero field (zfc, open circles) and then in an applied field of 0.01 T (fc, closed circles); the results of the same measurement on bulk Mn_3O_4 with the same heating treatment are shown as triangles with the same distinction between open (zfc) and closed (fc) forms as for the data for the mesoporous sample. d) The data in greater detail centred around 40 K, with the y-axis on a logarithmic scale to accentuate the zfc behaviour.

It is known that bulk α-Mn_2O_3 orders antiferromagnetically at a temperature that is variously reported in the range 80–100 K and the dependence on temperature of the magnetic susceptibility possesses a broad maximum in this region.[7] In addition to such a feature, we also observe in the mesoporous Mn_2O_3, a distinct divergence of the fc and zfc magnetisation just above 40 K, Figure 5a and b. The simplest interpretation of this behaviour is that it arises from a small amount of Mn_3O_4 in the sample. A rough estimate of the amount of such a phase may be obtained from the low-temperature fc response, indicating that it is of the order of 0.05 % and hence not detected in PXRD pattern of mesoporous Mn_2O_3. Similar behaviour has been seen in work on α-Mn_2O_3 nanoparticles, though there is disagreement on the origin of the fc-zfc divergence above 40 K.[8,9] One interpretation assigns the feature to traces of Mn_3O_4,[8] while a more detailed magnetic study argues that it is inherent to the Mn_2O_3 nanoparticles.[9]

Bulk Mn_3O_4 is known to undergo long-range magnetic ordering to a collinear ferrimagnetic array on cooling through $T_c = 42$ K; on further cooling this transforms to a spiral spin structure at 39 K, and finally a canted spin array is formed at 33 K.[10] Whilst the highest-temperature transition is very distinct in both samples, and there is a hint of a transition a 39 K in the zfc data of the bulk sample, no other transitions are marked by distinct features in Figure 5b in either sample for either fc or zfc data. There are two clear differences between the two samples apparent in Figure 5c: the transition above 40 K is broader for the mesoporous form, and for the zfc data it is centred at a lower temperature; the saturation magnetisation is lower for the mesoporous sample. A simple interpretation of both observations may be based on the greater fraction of manganese atoms at the surface of the mesoporous sample, and the likely lower degree of crystallinity of such samples. The former will reduce the mean exchange field, and perhaps also increase the distribution of sites, with an increasing fraction not possessing the same number of nearest-neighbour with which to undergo magnetic exchange; the latter will also have an influence on the homogeneity of the mean exchange field.

Ordered mesoporous Mn_2O_3 and Mn_3O_4 with crystalline walls have been successfully synthesized. Mesoporous Mn_2O_3 was converted to Mn_3O_4 in a reducing atmosphere without destroying the ordered mesostructure. This is the first synthesis of mesoporous Mn_3O_4 or any reduced mesoporous manganese oxide, something that is unlikely to be achieved by direct template synthesis. The ordered mesostructures are demonstrated by TEM, N_2 adsorption-desorption, and low-angle PXRD measurements. The successful synthesis of mesoporous Mn_3O_4 with crystalline walls is confirmed by HRTEM, wide-angle PXRD, and XANES data. The magnetic properties of mesoporous Mn_2O_3 and Mn_3O_4 have been characterized by SQUID measurements.

Experimental

Preparation of mesoporous silica KIT-6 and bi-solvent method have been described previously [11]. In a typical synthesis of Mn_3O_4, 30 g of $Mn(NO_3)_2 \cdot 6H_2O$ (98 %, Aldrich) was dissolved in ~ 20 mL of water to form a saturated $Mn(NO_3)_2$ solution. 5 g of mesoporous KIT-6 was dispersed in 200 mL of dried n-hexane. After stirring at room temperature for 3 h, 5 mL of the saturated $Mn(NO_3)_2$ solution was added slowly with stirring. The mixture was stirred overnight, filtered and dried at room temperature until a completely dried powder was obtained. The sample was heated slowly to 600 °C, calcined at that temperature for 3 h and the resulting material treated twice with a 2 M hot NaOH solution in water, to remove the silica template, followed by washed with water several times, and then drying at 60 °C. This procedure results in mesoporous Mn_2O_3. Reduction of mesoporous Mn_2O_3 was achieved by heating at 280 °C for 3 h under a 5 % H_2–95 % Ar atmosphere.

The materials were characterized by transmission electron microscopy (TEM, Jeol JEM-2011), powder X-ray diffraction (PXRD, Stoe STADI/P diffractometer operating in transmission mode with Fe Kα_1 radiation, $\lambda = 1.936$ Å), low angle X-ray diffraction (Rigaku/MSC, D/max-rB with Cu Kα_1 radiation, $\lambda = 1.541$ Å) and N_2 adsorption (Hiden IGA porosimeter). Oxidation states were verified by XANES on Station 9.3 at the CCLRC Daresbury Laboratory SRS, U.K. Magnetisation measurements were made on a Quantum Design $MPMS_2$ SQUID magnetometer in a field of 0.01 T.

Received: February 7, 2007

---

[1] a) U. Bach, D. Lupo, P. Comte, J. E. Moser, F. Weissortel, J. Salbeck, H. Spreitzer, M. Grätzel, *Nature* **1998**, *395*, 583. b) U. Ciesla, F. Schuth, *Microporous Mesoporous Mater.* **1999**, *27*, 131. c) M. E. Davis, *Nature* **2002**, *417*, 813.

[2] a) P. D. Yang, D. Y. Zhao, D. I. Margolese, B. F. Chmelka, G. D. Stucky, *Nature* **1998**, *396*, 152. b) G. J. D. Soler-Illia, C. Sanchez, B. Lebeau, J. Patarin, *Chem. Rev.* **2002**, *102*, 4093. c) J. Y. Ying, C. P. Mehnert, M. S. Wong, *Angew. Chem. Int. Ed.* **1999**, *38*, 56.

[3] a) D. M. Antonelli, J. Y. Ying, *Angew. Chem. Int. Ed. Engl.* **1995**, *34*, 2014. b) D. M. Antonelli, J. Y. Ying, *Angew. Chem. Int. Ed. Engl.* **1996**, *35*, 426. c) F. Jiao, P. G. Bruce, *Angew. Chem. Int. Ed.* **2004**, *43*, 5958.

[4] a) H. F. Yang, D. Y. Zhao, *J. Mater. Chem.* **2005**, *15*, 1217. b) A. H. Lu, F. Schuth, *Adv. Mater.* **2006**, *18*, 1793.

[5] a) B. Z. Tian, X. Y. Liu, L. A. Solovyov, Z. Liu, H. F. Yang, Z. D. Zhang, S. H. Xie, F. Q. Zhang, B. Tu, C. Z. Yu, O. Terasaki, D. Y. Zhao, *J. Am. Chem. Soc.* **2004**, *126*, 865. b) B. Z. Tian, X. Y. Liu, H. F. Yang, S. H. Xie, C. Z. Yu, B. Tu, D. Y. Zhao, *Adv. Mater.* **2003**, *15*, 1370. c) F. Jiao, A. Harrison, J. C. Jumas, A. V. Chadwick, W. Kockelmann, P. G. Bruce, *J. Am. Chem. Soc.* **2006**, *128*, 5468. d) Y. Q. Wang, C. M. Yang, W. Schmidt, B. Spliethoff, E. Bill, F. Schuth, *Adv. Mater.* **2005**, *17*, 53. e) K. K. Zhu, B. Yue, W. Z. Zhou, H. Y. He, *Chem. Commun.* **2003**, 98. f) K. Jiao, B. Zhang, B. Yue, Y. Ren, S. X. Liu, S. R. Yan, C. Dickinson, W. Z. Zhou, H. Y. He, *Chem. Commun.* **2005**, 5618. g) H. J. Shin, R. Ryoo, Z. Liu, O. Terasaki, *J. Am. Chem. Soc.* **2001**, *123*, 1246.

[6] a) F. Jiao, J. C. Jumas, M. Womes, A. V. Chadwick, A. Harrison, P. G. Bruce, *J. Am. Chem. Soc.* **2006**, *128*, 12905. b) T. Brezesinski, M. Groenewolt, M. Antonietti, B. Smarsly, *Angew. Chem. Int. Ed.* **2006**, *45*, 781. c) F. Jiao, K. M. Shaju, P. G. Bruce, *Angew. Chem. Int. Ed.* **2005**, *44*, 6550.

[7] a) J. Cable, M. Wilkinson, E. Woolan, W. Koehler ORNL-2302, *Phys. Prog. Rep.* **1957**, 43. b) R. R. Chevalier, G. Roult, E. F. Bertaut, *Solid State Commun.* **1967**, *5*, 7. c) R. W. Grant, S. Geller, J. A. Cape, G. P. Espinosa, *Phys. Rev.* **1968**, *175*, 686. d) M. Regulski, R. Przenioslo, I. Sosnowska, D. Howhlwein, R. Schneider, *J. Alloys Compd.* **2004**, *362*, 236.

[8] T. Ahmad, K. V. Ramanujachary, S. E. Lofland, A. K. Ganguli, *J. Mater. Chem.* **2004**, *14*, 3406.

[9] S. Mukherjee, A. K. Pal, S. Bhattacharya, J. Raittila, *Phys. Rev. B* **2006**, *74*, 104413.

[10] a) K. Dwight, N. Menyuk, *Phys. Rev. B* **1960**, *199*, 1470. b) G. B. Jensen, O. V. Nielsen, *J. Phys. C* **1974**, *7*, 409. c) G. Srinivasan, M. S. Seehra, *Phys. Rev. B* **1983**, *28*, 1. d) I. S. Jacobs, *J. Phys. Chem. Solids* **1959**, *11*, 1.

[11] a) F. Kleitz, S. H. Choi, R. Ryoo, *Chem. Commun.* **2003**, 2136. b) M. Imperor-Clerc, D. Bazin, M. D. Appay, P. Beaunier, A. Davidson, *Chem. Mater.* **2004**, *16*, 1813.

Nomenclature

bcc Body centred cubic

BENSC Berlin Neutron Scattering Center, Helmholtz-Zentrum Berlin für Materialien und Energie

BET Brunauer-Emmett-Teller method for surface area analysis

BJH Barrett-Joyner-Halenda for pore size distribution analysis

CSEC Centre for Science at Extreme Conditions

EaStCHEM Edinburgh and St Andrews Research School of Chemistry

EPSRC Engineering and Physical Sciences Research Council

ESRF European Synchrotron Radiation Facility

FC Field cooled magnetic measurements

FWHM Full width at half maximum

GPS General purpose surface-muon instrument (PSI)

GSAS General structure and analysis system

HR(TEM) (High resolution) transmission electron microscopy/microscope

ILL Institut Laue Langevin, high flux neutron reactor, Grenoble, France

INS Inelastic neutron scattering

ISIS The UK neutron and muon pulsed source

KIT-6 Cubic mesoporous silica, space group $Ia\bar{3}d$

LAXRD Low angle X-ray diffraction

MPMS Magnetic property measurement system

μSR	Muon spin relaxation/rotation/resonance
MuSR	64-detector μSR spectrometer
NPD	Neutron powder diffraction
PSD	Pore size distribution
PSI	Paul Scherrer Institut, Switzerland
SANS	Small angle neutron scattering
SBA-16	Cubic mesoporous silica, space group $Im\bar{3}m$
SQUID	Superconducting quantum interface device
$\boldsymbol{T}_{\mathrm{B}}$	Superparamgnetic blocking temperature
$\boldsymbol{T}_{\mathrm{C}}$	Curie temperature
$\boldsymbol{T}_{\mathrm{f}}$	spin-glass freezing temperature
$\boldsymbol{T}_{\mathrm{M}}$	Morin transition temperature
$\boldsymbol{T}_{\mathrm{N}}$	Néel temperature
TOF	Time-of-flight
XANES	X-ray absorption near edge spectroscopy
XMCD	X-ray magnetic circular dichroism
XMLD	X-ray magnetic linear dichroism
XPS	X-ray photoelectron spectroscopy
XRPD	X-ray powder diffraction
ZFC	Zero field cooled magnetic measurements

Bibliography

[1] A. D. McNaught and A. Wilkinson, *IUPAC Compendium of Chemical Terminology* (Blackwell Science, Oxford, UK, 1997), 2nd ed.

[2] M. Davis, C. Saldarriaga, C. Montes, J. Garces, and C. Crowder, Zeolites **8**, 362 (1988).

[3] C. T. Kresge, M. E. Leonowicz, W. J. Roth, J. C. Vartuli, and J. S. Beck, Nature **359**, 710 (1992).

[4] J. S. Beck, J. C. Vartuli, W. J. Roth, M. E. Leonowicz, C. T. Kresge, K. D. Schmitt, C. T.-W. Chu, D. H. Olson, E. W. Sheppard, S. B. McCullen, J. B. Higgins, and J. L. Schlenker, J. Am. Chem. Soc. **114**, 10834 (1992).

[5] D. Zhao, J. Feng, Q. Huo, N. Melosh, G. H. Fredrickson, B. F. Chmelka, and G. D. Stucky, Science **279**, 548 (1998).

[6] M. Impéror-Clerc, I. Grillo, A. Y. Khodakov, D. Durand, and V. L. Zholobenko, Chem. Commun. pp. 834–836 (2007).

[7] F. Kleitz, S. H. Choi, and R. Ryoo, Chem. Commun. pp. 2136–2137 (2003).

[8] Q. Huo, D. I. Margolese, U. Ciesla, P. Feng, T. E. Gier, P. Sieger, R. Leon, P. M. Petroff, F. Schüth, and G. D. Stucky, Nature **368**, 317 (1994).

[9] D. M. Antonelli, A. Nakahira, and J. Y. Ying, Inorg. Chem. **35**, 3126 (1996).

[10] D. M. Antonelli and J. Y. Ying, Curr. Opin. Colloid Interface Sci. **1**, 523 (1996).

[11] A. Sayari and P. Liu, Microporous Mater. **12**, 149 (1997).

[12] U. Ciesla and F. Schüth, Microporous Mesoporous Mater. **27**, 131 (1999).

[13] D. E. De Vos, M. Dams, B. F. Sels, and P. A. Jacobs, Chem. Rev. **102**, 3615 (2002).

[14] G. J. de A. A. Soler-Illia, C. Sanchez, B. Lebeau, and J. Patarin, Chem. Rev. **102**, 4093 (2002).

[15] P. Yang, D. Zhao, D. I. Margolese, B. F. Chmelka, and G. D. Stucky, Nature **396**, 152 (1998).

[16] Z.-R. Tian, W. Tong, J.-Y. Wang, N.-G. Duan, V. V. Krishnan, and S. L. Suib, Science **276**, 926 (1997).

[17] R. Ryoo, S. H. Joo, and S. Jun, J. Phys. Chem. B **103**, 7743 (1999).

[18] S. Jun, S. H. Joo, R. Ryoo, M. Kruk, M. Jaroniec, Z. Liu, T. Ohsuna, and O. Terasaki, J. Am. Chem. Soc. **122**, 10712 (2000).

[19] S. H. Joo, S. J. Choi, I. Oh, J. Kwak, Z. Liu, O. Terasaki, and R. Ryoo, Nature **412**, 169 (2001).

[20] H. J. Shin, R. Ryoo, Z. Liu, and O. Terasaki, J. Am. Chem. Soc. **123**, 1246 (2001).

[21] K. Zhu, B. Yue, W. Zhou, and H. He, Chem. Commun. pp. 98–99 (2003).

[22] F. Jiao and P. G. Bruce, Angew. Chem. Int. Ed. **43**, 5958 (2004).

[23] F. Jiao, A. Harrison, J. C. Jumas, A. V. Chadwick, W. Kockelmann, and P. G. Bruce, J. Am. Chem. Soc. **128**, 5468 (2006).

[24] W. Yue, A. H. Hill, A. Harrison, and W. Zhou, Chem. Commun. pp. 2518–2520 (2007).

[25] F. Jiao, A. Harrison, A. H. Hill, and P. G. Bruce, Adv. Mater. **19**, 4063 (2007).

[26] L. Zhou, Q. Ren, X. Zhou, J. Tang, Z. Chen, and C. Yu, Microporous Mesoporous Mater. **109**, 248 (2008).

[27] F. Jiao, A. H. Hill, A. Harrison, A. Berko, A. V. Chadwick, and P. G. Bruce, J. Am. Chem. Soc. **130**, 5262 (2008).

[28] N. F. Mott, Proc. Phys. Soc. A **62**, 416 (1949).

[29] J. Hubbard, Proc. R. Soc. Lond., A, Math. Phys. Sci. **277**, 237 (1964).

[30] D. V. Dimitrov, G. C. Hadjipanayis, V. Papaefthymiou, and A. Simopoulos, J. Magn. Magn. Mater. **188**, L8 (1998).

[31] R. H. Kodama, S. A. Makhlouf, and A. E. Berkowitz, Phys. Rev. Lett. **79**, 1393 (1997).

[32] L. Néel, C. R. Hebd. Seances Acad. Sci. **252**, 4075 (1961).

[33] L. Néel, C. R. Hebd. Seances Acad. Sci. **253**, 9 (1961).

[34] L. Néel, C. R. Hebd. Seances Acad. Sci. **253**, 1286 (1961).

[35] W. Yue and W. Zhou, Prog. Nat. Sci. **18**, 1329 (2008).

[36] G. L. Squires, *Introduction to the Theory of Thermal Neutron Scattering* (Dover Publications, Mineola, USA, 1996).

[37] R. Scherm and B. Fåk, *Neutron and X-ray Spectroscopy* (Springer, Dordrecht, Netherlands, 2006), chap. Inelastic neutron scattering: introduction, pp. 361–381.

[38] C. Giacovazzo, *Fundementals of Crystallography* (Oxford University Press, Oxford, UK, 2005), chap. The Diffraction of X-rays by Crystals, pp. 153–225, 2nd ed.

[39] H. M. Rietveld, J. Appl. Crystallogr. **2**, 65 (1969).

[40] R. A. Young, *The Rietveld Method* (Oxford University Press, Oxford, UK, 1993), chap. Introduction to the Rietveld method, pp. 1–38, International Union of Crystallography monographs on crystallography; 5.

[41] A. C. Larson and R. B. Von Dreele, Tech. Rep. LAUR 86-748, Los Alamos National Laboratory, USA (2004).

[42] B. H. Toby, J. Appl. Crystallogr. **34**, 210 (2001).

[43] K. S. W. Sing, D. H. Everett, R. A. W. Haul, L. Moscou, R. A. Pierotti, J. Rouquérol, and T. Siemieniewska, Pure Appl. Chem. **57**, 603 (1985).

[44] S. Brunauer, P. H. Emmett, and E. Teller, J. Am. Chem. Soc. **60**, 309 (1938).

[45] E. P. Barrett, L. G. Joyner, and P. P. Halenda, J. Am. Chem. Soc. **73**, 373 (1951).

[46] M. Kruk, M. Jaroniec, and A. Sayari, Langmuir **13**, 6267 (1997).

[47] D. Martien, *Introduction to: Ac susceptibility*, Quantum Design brouchure.

[48] D. B. Williams and C. B. Carter, *Transmission Electron Microscopy: A Textbook for Materials Science* (Plenum Press, London, UK, 1996).

[49] D. Briggs and J. T. Grant, eds., *Surface analysis by Auger and x-ray photoelectron spectroscopy* (IMPublications, Chichester, UK, 2003), 2nd ed.

[50] J. H. Brewer and R. Cywinski, eds., *Muon Science: Muons in Physics, Chemistry and Materials* (SUSSP Publications and Institute of Physics Publishing, Edinburgh and Bristol, UK, 1999).

[51] S. J. Blundell, Contemp. Phys. **40**, 175 (1999).

[52] J. S. Lord, J. Phys.: Conference Series **17**, 81 (2005).

[53] A. D. Hillier, P. J. C. King, S. P. Cottrell, and J. S. Lord., *The MuSR User Guide*, ISIS Facility, STFC, Rutherford Appleton Laboratory, UK (2005).

[54] G. Eaton, A. Carne, S. Cox, J. Davies, R. de Renzi, O. Hartmann, A. Kratzer, C. Ristori, C. Scott, G. Stirling, and T. Sundqvist, Nucl. Instrum. Methods Phys. Res., Sect. A **269**, 483 (1988).

[55] A. Amato, *GPS User Guide*, Laboratory for Muon Spectroscopy, Paul Scherrer Institut, Switzerland (2007).

[56] R. M. Grudzien, B. E. Grabicka, and M. Jaroniec, J. Mater. Chem. **16**, 819 (2006).

[57] A. H. Hill, F. Jiao, P. G. Bruce, A. Harrison, W. Kockelmann, and C. Ritter, Chem. Mater. **20**, 4891 (2008).

[58] D. Martín y Marero and D. Engberg, Physica B **267–268**, 134 (1999).

[59] W. G. Williams, R. M. Ibberson, P. Day, and J. E. Enderby, Physica B **241–243**, 234 (1997).

[60] J. Cui, Q. Huang, and B. H. Toby, Powder Diffr. **21**, 71 (2006).

[61] F. J. Morin, Phys. Rev. **78**, 819 (1950).

[62] E. Krén, B. Molnàr, E. Svàb, and E. Zsoldos, Solid State Commun. **15**, 1707 (1974).

[63] V. Baron, J. Gutzmer, H. Rundlöf, and R. Tellgren, Solid State Sci. **7**, 753 (2005).

[64] M. Catti, G. Valerio, and R. Dovesi, Phys. Rev. B **51**, 7441 (1995).

[65] G. Rollmann, A. Rohrbach, P. Entel, and J. Hafner, Phys. Rev. B **69**, 165107 (2004).

[66] P. J. Brown, J. B. Forsyth, E. Lelièvre-Berna, and F. Tasset, J. Phys.: Condens. Matter **14**, 1957 (2002).

[67] A. H. Morrish, *Canted Antiferromagnetism: Hematite* (World Scientific, London, UK, 1994).

[68] D. H. Andersen, Phys. Rev. **151**, 247 (1966).

[69] G. F. Goya, M. Veith, R. Rapalavicuite, H. Shen, and S. Mathur, Appl. Phys. A **80**, 1523 (2005).

[70] P. J. Flanders and J. P. Remeika, Philos. Mag. **11**, 1271 (1965).

[71] R. Nathans, S. J. Pickart, H. A. Alperin, and P. J. Brown, Phys. Rev. **136**, A1641 (1964).

[72] S. Ikeda and J. M. Carpenter, Nucl. Instrum. Methods Phys. Res., Sect. A **239**, 536 (1985).

[73] D. Schroeer and R. C. Nininger Jr., Phys. Rev. Lett. **19**, 632 (1967).

[74] N. Yamamoto, J. Phys. Soc. Jpn. **24**, 23 (1968).

[75] R. C. Nininger Jr. and D. Schroeer, J. Phys. Chem. Solids **39**, 137 (1978).

[76] M. F. Hansen, F. Bødker, S. Mørup, K. Lefmann, K. N. Clausen, and P.-A. Lindgård, Phys. Rev. Lett. **79**, 4910 (1997).

[77] F. Bødker, M. F. Hansen, C. B. Koch, K. Lefmann, and S. Mørup, Phys. Rev. B **61**, 6826 (2000).

[78] S. N. Klausen, K. Lefmann, P.-A. Lindgård, K. N. Clausen, M. F. Hansen, F. Bødker, S. Mørup, and M. Telling, J. Magn. Magn. Mater. **266**, 68 (2003).

[79] S. N. Klausen, K. Lefmann, P.-A. Lindgård, L. T. Kuhn, C. R. H. Bahl, C. Frandsen, S. Mørup, B. Roessli, N. Cavadini, and C. Niedermayer, Phys. Rev. B **70**, 214411 (2004).

[80] C. Frandsen, C. R. H. Bahl, B. Lebech, K. Lefmann, L. T. Kuhn, L. Keller, N. H. Andersen, M. von Zimmermann, E. Johnson, S. N. Klausen, and S. Mørup, Phys. Rev. B **72**, 214406 (2005).

[81] L. T. Kuhn, K. Lefmann, C. R. H. Bahl, S. N. Ancona, P.-A. Lindgård, C. Frandsen, D. E. Madsen, and S. Mørup, Phys. Rev. B **74**, 184406 (2006).

[82] B. N. Brockhouse, J. Chem. Phys. **21**, 961 (1953).

[83] L. M. Corliss, J. M. Hastings, R. Nathans, and G. Shirane, J. Appl. Phys. **36**, 1099 (1965).

[84] C. Dickinson, W. Zhou, R. P. Hodgkins, Y. Shi, D. Zhao, and H. He, Chem. Mater. **18**, 3088 (2006).

[85] C. Dickinson, Phd. thesis, University of St Andrews, UK (2007).

[86] T. R. McGuire, E. J. Scott, and F. H. Grannis, Phys. Rev. **102**, 1000 (1956).

[87] C. Kittel, *Introduction to Solid State Physics* (John Wiley & Sons, Inc., New York, USA, 1996), chap. Ferromagnetism and antiferromagnetism, pp. 441–484, 7th ed.

[88] M. R. Fitzsimmons, J. A. Eastman, R. A. Robinson, A. C. Lawson, J. D. Thompson, R. Movshovich, and J. Satti, Phys. Rev. B **48**, 8245 (1993).

[89] Y. A. Izyumov and R. P. Ozerov, *Magnetic Neutron Diffraction* (Plenum Press, New York, USA, 1970).

[90] P. J. Brown, A. G. Fox, E. N. Maslen, M. A. O'Keefe, and B. T. M. Willis, *International Tables for Crystallography* (Kluwer Academic Publishers, Dordrecht, Netherlands, 2004), vol. C, chap. Intensity of diffracted intensities, pp. 554–595, 3rd ed.

[91] S. Greenwald, Nature **177**, 286 (1956).

[92] M. Baster, F. Bourée, A. Kowalska, and Z. Latacz, J. Alloys Compd. **296**, 1 (2000).

[93] E. J. Samuelsen, M. T. Hutchings, and G. Shirane, Physica **48**, 13 (1970).

[94] R. A. Alikhanov, Ž. Dimitrijević, A. Kowalska, S. Kraśnicki, H. Rżany, J. Todorović, and A. Wanic, Phys. Status Solidi B **32**, 41 (1969).

[95] J. B. Goodenough, Phys. Rev. **117**, 1442 (1960).

[96] J. B. Goodenough, *Magnetism and the Chemical Bond* (Interscience, New York, USA, 1963).

[97] H. L. Alberts, J. Phys. Soc. Jpn. **38**, 1541 (1975).

[98] H. L. Alberts and J. C. A. Boeyens, J. Magn. Magn. Mater. **2**, 327 (1976).

[99] T. G. Worlton, R. M. Brugger, and R. B. Bennion, J. Phys. Chem. Solids **29**, 435 (1968).

[100] W. L. Roth, J. Phys. Chem. Solids **25**, 1 (1964).

[101] P. Dutta, M. S. Seehra, S. Thota, and J. Kumar, J. Phys.: Condens. Matter **20**, 015218 (2008).

[102] L. M. Khriplovich, E. V. Kholopov, and I. E. Paukov, J. Chem. Thermodyn. **14**, 207 (1982).

[103] H. T. Zhu, J. Luo, J. K. Liang, G. H. Rao, J. B. Li, J. Y. Zhang, and Z. M. Du, Physica B **403**, 3141 (2008).

[104] E. L. Salabas, A. Rumplecker, F. Kleitz, F. Radu, and F. Schüth, Nano Lett. **6**, 2977 (2006).

[105] E. L. Salabas, F. Radu, H. Tysüsz, and M. J. Benitez, Experimental report 36189, Institut Laue-Langevin, France (2008).

[106] P. Cosse, J. Inorg. Nucl. Chem. **8**, 483 (1958).

[107] R. L. Carlin, *Magnetochemistry* (Springer-Verlag, Berlin, Germany, 1986).

[108] K. Venkateswara Rao and C. S. Sunandana, Solid State Commun. **148**, 32 (2008).

[109] A. H. Morrish, *The Physical Principles of Magnetism* (Wiley-IEEE Press, New York, USA, 2001).

[110] A. Aharoni, *Introduction to the Theory of Ferromagnetism* (Claredon Press, Oxford, UK, 1996).

[111] D. Scheerlinck and S. Hautecler, Phys. Status Solidi B **73**, 223 (1976).

[112] W. Jauch, M. Reehuis, H. J. Bleif, F. Kubanek, and P. Pattison, Phys. Rev. B **64**, 052102 (2001).

[113] A. Antoniadis, J. Berruyer, and A. Filhol, Acta Crystallogr., Sect. A: Found. Crystallogr. **46**, 692 (1990).

[114] Y. Sakamoto, T.-W. Kim, R. Ryoo, and O. Terasaki, Angew. Chem. Int. Ed. **43**, 5231 (2004).

[115] C. G. Shull, W. A. Strauser, and E. O. Wollan, Phys. Rev. **83**, 333 (1951).

[116] W. L. Roth, Phys. Rev. **111**, 772 (1958).

[117] W. L. Roth, Phys. Rev. **110**, 1333 (1958).

[118] L. C. Bartel and B. Morosin, Phys. Rev. B **3**, 1039 (1971).

[119] H. P. Rooksby, Acta Crystallogr. **1**, 226 (1948).

[120] D. Rodic, V. Spasojevic, V. Kusigerski, R. Tellgren, and H. Rundlof, Phys. Status Solidi B **218**, 527 (2000).

[121] V. Fernandez, C. Vettier, F. de Bergevin, C. Giles, and W. Neubeck, Phys. Rev. B **57**, 7870 (1998).

[122] G. Srinivasan and M. S. Seehra, Phys. Rev. B **28**, 6542 (1983).

[123] E. Winkler, R. D. Zysler, M. Vasquez Mansilla, D. Fiorani, D. Rinaldi, M. Vasilakaki, and K. N. Trohidou, Nanotechnology **19**, 185702 (2008).

[124] T. C. Hansen, P. F. Henry, H. E. Fischer, J. Torregrossa, and P. Convert, Meas. Sci. Technol. **19**, 034001 (2008).

[125] J.-M. Moreau, C. Michel, R. Gerson, and W. J. James, Acta Crystallogr., Sect. B: Struct. Sci. **26**, 1425 (1970).

[126] J. T. Richardson and W. O. Milligan, Phys. Rev. **102**, 1289 (1956).

[127] N. Kijima, T. Ikeda, K. Oikawa, F. Izumi, and Y. Yoshimura, J. Solid State Chem. **177**, 1258 (2004).

[128] M. H. Rossouw, D. C. Liles, M. M. Thackeray, W. . I. F. David, and S. Hull, Mater. Res. Bull. **27**, 221 (1992).

[129] Y. Muraoka, H. Chiba, T. Atou, M. Kikuch, K. Hiraga, Y. Syono, S. Sugiyama, S. Yamamoto, and J.-C. Grenier, J. Solid State Chem. **144**, 136 (1999).

[130] N. Yamamoto, T. Endo, M. Shimada, and T. Takada, Jpn. J. Appl. Phys. **13**, 723 (1974).

[131] L. Li, Y. Pan, L. Chen, and G. Li, J. Solid State Chem. **180**, 2896 (2007).

[132] J. Ge, L. Zhuo, F. Yang, B. Tang, L. Wu, and C. Tung, J. Phys. Chem. B **110**, 17854 (2006).

[133] M. E. Fisher, Philos. Mag. **7**, 1731 (1962).

[134] E. E. Bragg and M. S. Seehra, Phys. Rev. B **7**, 4197 (1973).

[135] X.-F. Shen, Y.-S. Ding, J. Liu, Z.-H. Han, J. I. Budnick, W. A. Hines, and S. L. Suib, J. Am. Chem. Soc. **127**, 6166 (2005).

[136] S. L. Brock, N. Duan, Z. R. Tian, O. Giraldo, H. Zhou, and S. L. Suib, Chem. Mater. **10**, 2619 (1998).

[137] D. Reinen, U. Kesper, and D. Belder, J. Solid State Chem. **116**, 355 (1995).

[138] P. Bruce, Chem. Commun. pp. 1817–1824 (1997).

[139] B. Scrosati, S. Panero, P. Reale, D. Satolli, and Y. Aihara, J. Power Sources **105**, 161 (2002).

[140] C. Sides, N. Li, C. Patrissi, B. Scrosati, and C. Martin, Mater. Res. Soc. Bull. **27**, 605 (2002).

[141] J. C. Arrebola, A. Caballero, L. Hernán, and J. Morales, J. Power Sources **183**, 310 (2008).

[142] F. Jiao, J. Bao, A. H. Hill, and P. G. Bruce, Angew. Chem. Int. Ed. **47**, 9711 (2008).

[143] A. Caballero, M. Cruz, L. Hernán, M. Melero, J. Morales, and E. R. Castellón, J. Power Sources **150**, 192 (2005).

[144] B. P. Löchel and H.-H. Strehblow, J. Electrochem. Soc. **131**, 713 (1984).

[145] Q.-H. Wu, J.-M. Xu, Q.-C. Zhuang, and S.-G. Sun, Solid State Ionics **177**, 1483 (2006).

[146] M. Oku, K. Hirokawa, and S. Ikeda, J. Electron. Spectrosc. Relat. Phenom. **7**, 465 (1975).

[147] R. P. Gupta and S. K. Sen, Phys. Rev. B **10**, 71 (1974).

[148] J. Tsuji, M. Fujita, Y. Haruyama, K. Kanda, S. Matsui, N. Ozawa, T. Yao, and K. Taniguchi, Anal. Sci. **21**, 779 (2005).

[149] D. A. Shirley, Phys. Scr. **11**, 117 (1975).

[150] V. A. M. Brabers, F. M. van Setten, and P. S. A. Knapen, J. Solid State Chem. **49**, 93 (1983).

[151] F. Jiao, A. Harrison, and P. G. Bruce, Angew. Chem. Int. Ed. **46**, 3946 (2007).

[152] F. L. Pratt, Physica B **289–290**, 710 (2000).

[153] A. Keren, P. Mendels, I. A. Campbell, and J. Lord, Phys. Rev. Lett. **77**, 1386 (1996).

[154] A. Keren, Phys. Rev. B **50**, 10039 (1994).

[155] R. S. Hayano, Y. J. Uemura, J. Imazato, N. Nishida, T. Yamazaki, and R. Kubo, Phys. Rev. B **20**, 850 (1979).

[156] G. Srinivasan and M. S. Seehra, Phys. Rev. B **28**, 1 (1983).

[157] G. B. Jensen and O. V. Nielsen, J. Phys. C: Solid State Phys. **7**, 409 (1974).

[158] J. A. Mydosh, *Spin glasses: an experimental introduction* (Taylor & Francis, London, UK, 1993).

[159] J. O. Artman, J. C. Murphy, and S. Foner, Phys. Rev. **138**, A912 (1965).

[160] R. J. Harrison, S. A. McEnroe, P. Robinson, B. Carter-Stiglitz, E. J. Palin, and T. Kasama, Phys. Rev. B **76**, 174436 (2007).

[161] R. Wu, *Handbook of Magnetism and Advanced Magnetic Materials* (John Wiley & Sons, Chichester, UK, 2007), vol. 1, chap. Theory of Magnetocrystalline Anisotropy and Magnetoelasticity, pp. 423–434.

[162] K. Yosida, Prog. Theor. Phys. **6**, 691 (1951).

[163] M. Tachiki and T. Nagamiya, J. Phys. Soc. Jpn. **13**, 452 (1958).

[164] R. D. Zysler, D. Fiorani, A. M. Testa, L. Suber, E. Agostinelli, and M. Godinho, Phys. Rev. B **68**, 212408 (2003).

[165] R. D. Zysler, E. Winkler, M. Vasquez Mansilla, and D. Fiorani, Physica B **384**, 277 (2006).

[166] S. Blundell, *Magnetism in Condensed Matter* (Oxford University Press, Oxford, UK, 2001).

Publications

F. Jiao, J. Bao, A. H. Hill, and P. G. Bruce.
Synthesis of Ordered Mesoporous Li–Mn–O Spinel as a Positive Electrode for Rechargeable Lithium Batteries.
Angewandte Chemie International Edition, **47**, 9711 (2008).

A. H. Hill, F. Jiao, P. G. Bruce, A. Harrison, W. Kockelmann, and C. Ritter.
Neutron Diffraction Study of Mesoporous and Bulk Hematite, α-Fe_2O_3.
Chemistry of Materials, **20**, 4891 (2008).

F. Jiao, A. H. Hill, A. Harrison, A. Berko, A. V. Chadwick, and P. G. Bruce.
Synthesis of ordered mesoporous NiO with crystalline walls and a bimodal pore size distribution.
Journal of the American Chemical Society, **130**, 5262 (2008).

F. Jiao, A. Harrison, A. H. Hill, and P. G. Bruce.
Mesoporous Mn_2O_3 and Mn_3O_4 with crystalline walls.
Advanced Materials, **19**, 4063 (2007).

W. Yue, A. H. Hill, A. Harrison, and W. Zhou.
Mesoporous single-crystal Co_3O_4 templated by cage-containing mesoporous silica.
Chemical Communications, pp. 2518–2520 (2007).